

NAME

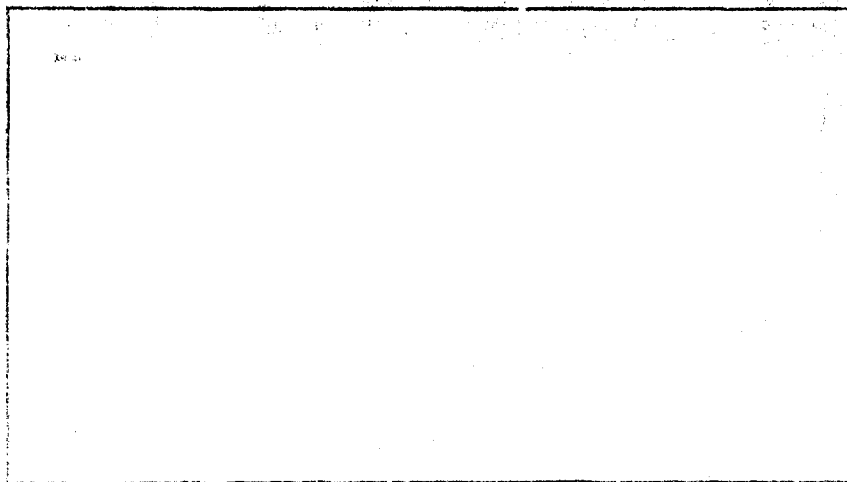
0

LEVEL II

AIR FORCE INSTITUTE OF TECHNOLOGY



AIR UNIVERSITY
UNITED STATES AIR FORCE



DTIC
UNCLASSIFIED

SCHOOL OF ENGINEERING

Best Available Copy

AD A100 825

AFIT/GE/EE/80D-38

Accession For	
NTIS GRA&I	<input checked="checked" type="checkbox"/>
DTIC TAB	<input type="checkbox"/>
Unannounced	<input type="checkbox"/>
Justification	
By _____	
Distribution/	
Availability Codes	
Dist	Avail and/or Special
A	

(6)

SENSITIVITY STUDY
OF STRAPDOWN INERTIAL SENSORS
IN HIGH PERFORMANCE APPLICATIONS

(7) Master's THESIS

(14) AFIT/GE/EE/80D-38 ✓ (30) John E. Ryan
Capt USAF

(11) Dec 80

(12) 225

DTIC
ELECTE
JUL 1 1981
S D

Approved for public release; distribution unlimited.

012225

AFIT/GE/EE/80D-38

SENSITIVITY STUDY
OF STRAPDOWN INERTIAL SENSORS
IN HIGH PERFORMANCE APPLICATIONS

THESIS

Presented to the Faculty of the School of Engineering
of the Air Force Institute of Technology
Air University (ATC)
in Partial Fulfillment of the
Requirements for the Degree of
Master of Science

by

John E. Ryan, B.S.
Capt USAF

Graduate Electrical Engineering

December 1980

Approved for public release; distribution unlimited.

Preface

The goal of this study was to gain some insight into the propagation of errors through a strapdown inertial reference system as a result of highly dynamic flight profiles. This was to be done using modern estimation theory and stochastic models of state-of-the-art sensors. Since a simulation package was not available to achieve this objective, a generalized simulation program, SOFE, was used as a basis to develop the desired software package.

A large portion of this thesis was directed toward implementing and validating the software required to perform the error analysis. It is my belief that credible results can be achieved only when painstaking effort is used in setting up the problem.

I would like to thank my thesis advisor, Dr Peter S. Maybeck, for his enthusiastic help throughout this study. Also, the well documented software and generous assistance provided by Stanton H. Musick of the Air Force Avionics Laboratory was of great benefit and made this task considerably easier. Finally, I sincerely thank my wife, Elaine, for her excellent typing and patient endurance.

Contents

	Page
Preface.....	ii
List of Figures.....	vi
List of Tables.....	xi
Abstract.....	xii
I. Introduction.....	1
Background.....	1
Problem.....	2
Scope.....	3
Development.....	3
II. Error Model Development.....	5
Basic Error Differential Equations.....	5
Coordinate Systems.....	9
Altitude Channel Mechanization.....	11
Gyro Error Model.....	13
Accelerometer Error Model.....	19
Gravity Error Model.....	22
Barometric Altimeter Error Model.....	23
Complete Truth Model.....	23
Initial Conditions.....	35
III. Software.....	40
SOFE.....	40
PROFGEN.....	41
SOFEPL.....	43
IV. Program Validation.....	44
Pinson Error Model Verification.....	44
Covariance Analysis Versus Monte Carlo Simulation.....	45
Number of Monte Carlo Runs.....	57
Baro-Inertial Gains.....	57
State-of-the-Art Error Model.....	61
V. Flight Profiles.....	69
Performance.....	69
Combat Flight Profile.....	71
Training Flight Profile.....	78

Contents

	<u>Page</u>
VI. Error Budget.....	84
Accelerometer Errors.....	97
Accelerometer Bias.....	99
Accelerometer Scale Factor Error.....	101
Accelerometer Misalignment.....	101
Accelerometer Second Order Errors.....	102
Accelerometer Correlated Noise.....	103
Accelerometer White Gaussian Noise.....	103
Gyro Errors.....	104
Gyro Bias.....	107
Gyro Scale Factor Error.....	107
Gyro Misalignment.....	108
Gyro White Gaussian Noise.....	109
Gyro Scale Factor Nonlinearity.....	110
Barometric Altimeter Errors.....	110
Gravity Errors.....	111
Short Alignment Time.....	112
Error Budget Conclusions.....	113
VII. Error Analysis.....	115
Errors Generated from Pitch Changes.....	115
Errors Generated from Turns.....	117
Errors Generated from Rolls.....	120
Errors Generated from Acceleration Along Flight Path....	121
Errors Generated Using the Training Flight Profile.....	121
Error Analysis Conclusions.....	128
VIII. Conclusions and Recommendations.....	132
Conclusions.....	132
Recommendations.....	133
Bibliography.....	136
Appendix A: SOFE.....	138
Appendix B: SOFE Subroutines for Error Analysis.....	141
Appendix C: PROFGEN.....	153
Appendix D: PROFGEN Update for Roll Only Maneuver.....	157
Appendix E: Older Generation Error Models.....	161

Contents

	<u>Page</u>
Appendix F: SOFE Subroutines for Truth Model.....	162
Appendix G: SOFE Subroutines for Filter Model.....	172
Appendix H: Plots of Error States as a Result of Specific Sensor Errors.....	186
Vita.....	209

List of Figures

<u>Figure</u>	<u>Page</u>
1 Pinson 9-State Error Model $F(t)$ Matrix Partition.....	7
2 Body and Navigation Coordinate Frames.....	10
3 Scale Factor Nonlinearity (Nominal Scale Factor 131328.387 pulses/rad).....	16
4 F Matrix for a 60 State Inertial Reference System Truth Model in the form of $\dot{\underline{x}} = \underline{F}\underline{x} + \underline{w}$	27
5 Latitude Error for I.C. of $x(6) = 1$ ft/sec.....	46
6 Longitude Error for I.C. of $x(6) = 1$ ft/sec.....	46
7 Longitude Error Mean and Standard Deviations from 50 Runs.....	48
8 Longitude Error Square Root of Variance.....	48
9 Latitude Error Mean and Standard Deviations from 50 Runs.....	49
10 Latitude Error Square Root of Variance.....	49
11 Altitude Error Mean and Standard Deviations from 50 Runs.....	50
12 Altitude Error Square Root of Variance.....	50
13 East Velocity Error Mean and Standard Deviations from 50 Runs.....	51
14 East Velocity Error Square Root of Variance.....	51
15 North Velocity Error Mean and Standard Deviations from 50 Runs.....	52
16 North Velocity Error Square Root of Variance.....	52
17 Up Velocity Error Mean and Standard Deviations from 50 Runs.....	53
18 Up Velocity Error Square Root of Variance.....	53
19 East Tilt Error Mean and Standard Deviations from 50 Runs.....	54
20 East Tilt Error Square Root of Variance.....	54

List of Figures

<u>Figure</u>	<u>Page</u>
21 North Tilt Error Mean and Standard Deviations from 50 Runs.....	55
22 North Tilt Error Square Root of Variance.....	55
23 Azimuth Error Mean and Standard Deviations from 50 Runs.....	56
24 Azimuth Error Square Root of Variance.....	56
25 Up Velocity Error Mean and Standard Deviations from 20 Runs.....	58
26 Azimuth Error Mean and Standard Deviations from 20 Runs.....	58
27 Altitude Error Using Gains in Equation (35).....	60
28 Up Velocity Error Using Gains in Equation (35).....	60
29 Longitude Error from F4 Trajectory.....	62
30 Latitude Error from F4 Trajectory.....	62
31 East Velocity Error from F4 Trajectory.....	63
32 North Velocity Error from F4 Trajectory.....	63
33 Altitude Error from F4 Trajectory.....	64
34 Up Velocity Error from F4 Trajectory.....	64
35 East Tilt Error from F4 Trajectory.....	65
36 North Tilt Error from F4 Trajectory.....	65
37 Azimuth Error from F4 Trajectory.....	66
38 Longitude Error with Linear Gyro Scale Factor.....	67
39 East Velocity Error with Linear Gyro Scale Factor.....	67
40 Longitude Error from Large Scale Factor Nonlinearity.....	68
41 East Velocity Error from Large Scale Factor Nonlinearity....	68
42 Acceleration Tolerance During Combat.....	72
43 Latitude/Longitude from Combat Flight Profile.....	73

List of Figures

<u>Figure</u>		<u>Page</u>
44	Altitude from Combat Flight Profile.....	73
45	Roll from Combat Flight Profile.....	74
46	Pitch from Combat Flight Profile.....	74
47	Yaw from Combat Flight Profile.....	75
48	Latitude/Longitude from Training Flight Profile.....	79
49	Altitude from Training Flight Profile.....	79
50	Roll from Training Flight Profile.....	80
51	Pitch from Training Flight Profile.....	80
52	Yaw from Training Flight Profile.....	81
53	Longitude Error State from Initial Conditions.....	85
54	Latitude Error State from Initial Conditions.....	85
55	East Velocity Error State from Initial Conditions.....	86
56	North Velocity Error State from Initial Conditions.....	86
57	Altitude Error State from Initial Conditions.....	87
58	Up Velocity Error State from Initial Conditions.....	87
59	East Tilt Error State from Initial Conditions.....	88
60	North Tilt Error State from Initial Conditions.....	88
61	Azimuth Error State from Initial Conditions.....	89
62	Longitude Error State from All Noise Sources.....	90
63	Latitude Error State from All Noise Sources.....	90
64	East Velocity Error State from All Noise Sources.....	91
65	North Velocity Error State from All Noise Sources.....	91
66	Altitude Error State from All Noise Sources.....	92
67	Up Velocity Error State from All Noise Sources.....	92
68	East Tilt Error State from All Noise Sources.....	93

List of Figures

<u>Figure</u>		<u>Page</u>
69	North Tilt Error State from All Noise Sources.....	93
70	Azimuth Error State from All Noise Sources.....	94
71	Longitude Error State from Training Profile.....	122
72	Latitude Error State from Training Profile.....	122
73	East Velocity Error State from Training Profile.....	123
74	North Velocity Error State from Training Profile.....	123
75	Altitude Error State from Training Profile.....	124
76	Up Velocity Error State from Training Profile.....	124
77	East Tilt Error State from Training Profile.....	125
78	North Tilt Error State from Training Profile.....	125
79	Azimuth Error State from Training Profile.....	126
H-1	Longitude Error State from Accelerometer Noise.....	187
H-2	Latitude Error State from Accelerometer Noise.....	187
H-3	East Velocity Error State from Accelerometer Noise.....	188
H-4	North Velocity Error State from Accelerometer Noise.....	188
H-5	Altitude Error State from Accelerometer Noise.....	189
H-6	Up Velocity Error State from Accelerometer Noise.....	189
H-7	East Tilt Error State from Accelerometer Noise.....	190
H-8	North Tilt Error State from Accelerometer Noise.....	190
H-9	Azimuth Error State from Accelerometer Noise.....	191
H-10	Longitude Error State from Gyro Noise.....	192
H-11	Latitude Error State from Gyro Noise.....	192
H-12	East Velocity Error State from Gyro Noise.....	193
H-13	North Velocity Error State from Gyro Noise.....	193
H-14	Altitude Error State from Gyro Noise.....	194

List of Figures

<u>Figure</u>	<u>Page</u>
H-15 Up Velocity Error State from Gyro Noise.....	194
H-16 East Tilt Error State from Gyro Noise.....	195
H-17 North Tilt Error State from Gyro Noise.....	195
H-18 Azimuth Error State from Gyro Noise.....	196
H-19 East Velocity Error State from Gyro Bias.....	197
H-20 North Velocity Error State from Gyro Bias.....	197
H-21 East Tilt Error State from Gyro Scale Factor.....	198
H-22 North Tilt Error State from Gyro Scale Factor.....	198
H-23 Azimuth Error State from Gyro Scale Factor.....	199
H-24 East Velocity Error State from Gyro Misalignment.....	200
H-25 North Velocity Error State from Gyro Misalignment.....	200
H-26 East Tilt Error State from Gyro Misalignment.....	201
H-27 North Tilt Error State from Gyro Misalignment.....	201
H-28 Azimuth Error State from Gyro Misalignment.....	202
H-29 East Tilt Error State from Gyro White Noise.....	203
H-30 North Tilt Error State from Gyro White Noise.....	203
H-31 Azimuth Error State from Gyro White Noise.....	204
H-32 East Tilt Error State from Gyro Scale Factor Nonlinearity....	205
H-33 North Tilt Error State from Gyro Scale Factor Nonlinearity....	205
H-34 Azimuth Error State from Gyro Scale Factor Nonlinearity.....	206
H-35 Altitude Error State from Gravity Error Sources.....	207
H-36 Up Velocity Error State from Gravity Error Sources.....	207
H-37 East Velocity Error State from Short Alignment.....	208
H-38 North Velocity Error State from Short Alignment.....	208

List of Tables

<u>Table</u>	<u>Page</u>
1 States of the Nine Dimensional Pinson Error Model.....	6
2 Notation Used in Figures 1 and 4.....	8
3 GG1342 Laser Gyro Performance Characteristics.....	15
4 Gyro Scale Factor Nonlinearity.....	18
5 Bell Model XI Accelerometer Error Model.....	19
6 Contribution of Accelerometer Error Sources.....	22
7 Model for Gravity Variations (Ref 17).....	23
8 Error States and Initial Standard Deviations.....	24
9 Notation Used in Figure 4.....	33
10 Standard Deviations of the Non-Zero Elements of the Diagonal Q Matrix for Driving Noise <u>w</u>	34
11 PROFGEN Output.....	42
12 Representative Fighter Maximum Performance.....	70
13 Combat Flight Profile.....	76
14 Training Flight Profile.....	82
15 Percent Contribution to Total Error.....	95
16 Percent Contribution to Initial Conditions.....	98
17 Percent Contribution of Accelerometer Errors to Total Error...	100
18 Percent Contribution of Gyro Errors to Total Error.....	106

Abstract

This study uses a computer simulation of a strapdown laser gyro inertial reference system to analyze the errors generated as a result of highly dynamic flight profiles. A stochastic error model using state-of-the-art inertial sensors is developed in detail and implemented in software. SOFE, a generalized simulation program, was used to implement both a Monte Carlo simulation and a covariance analysis. The Monte Carlo method was selected to perform the error analysis.

Two highly dynamic flight trajectories were developed using the flight profile generator, PROFGEN. The PROFGEN program itself was modified to include an aircraft roll time constant and a roll-only maneuver. The errors generated in the inertial reference system as a result of these flight trajectories were investigated. Both an error budget and an analysis of the maneuvers inducing these errors were accomplished.

Gyro error sources induced the most system error and coupled the dynamics of the flight trajectory into the variations of the error. Misalignment was found to be the major cause of both the accelerometer and gyro induced error. Successive maneuvers were found that reinforced system errors and other maneuvers were found that cancelled these errors. Also, some cases were found where the amount of system error varied with a change in heading.

SENSITIVITY STUDY OF STRAPDOWN INERTIAL SENSORS IN HIGH PERFORMANCE APPLICATIONS

I. Introduction

Background

Strapdown inertial reference systems eliminate many of the mechanical complexities of gimbalede systems since they have fewer moving parts. This leads to smaller components, improved reliability, easier maintenance, and less cost. But, these systems also have some disadvantages.

In a strapdown system the gyros and accelerometers are mounted (through vibration dampers) directly to the airframe. The gyros supply angular velocity directly to the navigation computer. The computer, in turn, uses the angular information to resolve the direction of the sensed acceleration. This additional computation is not present in a gimbalede system, since these systems use the gyros directly to maintain the accelerometers in a known orientation. However, increased computational requirements are no longer a serious drawback considering the current availability of low cost minicomputers.

A factor of greater concern in a strapdown reference system is that the inertial sensors are subjected to a more dynamic environment than sensors in a gimbalede system. This is especially true in high performance fighter aircraft. The gyros and accelerometers are subjected to both the faster dynamics of aircraft attitude changes and motion over a wider dynamic range: not only must they withstand a harsher environment, they must provide precise outputs over vastly differing regimes.

The development of the ring laser gyro has enhanced interest in strapdown inertial reference systems. This type of gyro measures rotation by detecting differences in the frequency of light travelling in opposite directions within a rotating cavity and is essentially a solid state device (Ref 1). Since it has no moving parts, it is not susceptible to acceleration-induced errors and is well suited to the highly dynamic environment of a strapdown system. Its mechanical simplicity also makes it adaptable to mass production techniques which can lead to lower acquisition costs.

Problem

Present strapdown ring laser gyro strapdown reference systems provide acceptable accuracy in the relatively benign environment of transport or commercial aircraft. However, these systems do not provide the desired accuracy when used in a highly dynamic environment such as that of a modern air superiority fighter aircraft.

One of the first steps in refining the accuracy of a strapdown system is to develop a full understanding of the propagation of sensor errors through the system. The problem undertaken in this study will be to develop a computer simulation of a state-of-the-art strapdown inertial reference system followed by an analysis of the impact of individual sensor errors upon overall system errors. Highly dynamic flight profiles will be used to generate the inertial reference system errors.

A deterministic analysis of the effects of sensor errors on strapdown inertial reference system performance was accomplished in a previous thesis by Lt Richard H. Reynolds (Ref 14). Although this deterministic approach provides valuable baseline information, it does not

accurately portray the uncertainties in the system model, nor does it account for uncertain initial conditions and noise-corrupted inputs.

The probabilistic approach undertaken here utilizes stochastic models to account for uncertainties in the inertial reference system. Stochastic process and modern estimation theories will also be used to characterize the initial conditions, forcing functions, and the resulting system outputs.

Scope

The focus of this study will be to identify the relative effect of each error source on the overall system error. Also, the severity of errors induced by specific flight profiles will be investigated so that maneuvers that degrade performance can be identified.

Error models characterizing the dominant sources of errors of state-of-the-art inertial sensors will be used in the simulation. The Bell Model XI accelerometer (Ref 5) was chosen for this application because of its wide use in current high-accuracy inertial reference systems, while the Honeywell GG1342 ring laser gyro was chosen because it is currently available and has been flight tested in the A-7E using highly dynamic flight profiles.

Flight profiles will be generated based upon the performance characteristics of an F15 aircraft. In its air superiority role, the F15 represents the most dynamic environment that an aircraft inertial system currently encounters.

Development

The initial portion of this study entails the development of the software and models to perform the error analysis. First, a set of error differential equations for a ring laser gyro strapdown inertial

reference system will be developed based upon the general formulation used by Widhall and Grundy (Ref 17). These equations will then be implemented in a digital simulation program called SOFE (Ref 12). SOFE will be used to generate statistics by the methods of Monte Carlo simulation and also by covariance propagation for the linearized error equation model of the strap-down inertial reference system.

In addition, two supporting computer programs, a flight profile generator, PROFGEN (Ref 11), and a post processor for generating sample statistics and plots, SOFEPL (Ref 6), will be used in conjunction with the basic simulation program.

Validation of the implementation of the basic error differential equations will be accomplished by duplicating error standard deviation plots shown in Reference 17 for a simpler model. Further validation of the complete augmented state equations will be accomplished by comparing the results of the two different approaches, the Monte Carlo simulation and the covariance analysis.

Representative F15 flight profiles will then be developed, followed by an analysis of the errors generated in the strapdown system as a result of the highly dynamic profiles. In addition to determining the error budget for each flight profile, the sources of system error induced by specific high dynamic maneuvers will be sought.

II. Error Model Development

Basic Error Differential Equations

In order to analyze the performance of a reference system using modern linear estimation theory, a stochastic system error model is often expressed in the form of linearized first order differential equations. These equations are of the form

$$\dot{\underline{x}} = \underline{F}\underline{x} + \underline{B}\underline{u} + \underline{w} \quad (1)$$

where

\underline{F} = Fundamental Matrix

\underline{B} = Control Input Matrix

\underline{x} = Error State Vector

\underline{u} = Deterministic Forcing Function

\underline{w} = White Gaussian Driving Noise

Britting showed that the same basic equations could be used for both gimbale and strapdown systems (Ref 4). These consist of a system-independent nine-by-nine matrix Pinson error model (Ref 13) augmented by system-dependent error forcing functions. The first three states represent errors in position, states four through six are velocity errors, and states seven through nine are tilt errors. These states are defined in Table 1. The nine-by-nine matrix for the Pinson model is shown in Figure 1 with corresponding notation shown in Table 2. Widnall and Grundy developed first order error equations for a strapdown reference system in this fashion (Ref 17), so many of their results will be applied in the development of the model used here.

State	Meaning	Units
x(1)	Error in east longitude	radians
x(2)	Error in north latitude	radians
x(3)	Error in altitude	feet
x(4)	Error in east velocity	ft/sec
x(5)	Error in north velocity	ft/sec
x(6)	Error in vertical velocity	ft/sec
x(7)	Attitude error east component	radians
x(8)	Attitude error north component	radians
x(9)	Attitude error up component	radians

Table 1. States of the Nine Dimensional Pinson Error Model

	1	2	3	4	5	6	7	8	9
1	0	$\rho_u/\cos L$	$-\rho_n/(R\cos L)$	$1/(R\cos L)$	0	0	0	0	0
2	0	0	ρ_e/R	0	$1/R$	0	0	0	0
3	0	0	0	0	0	1	0	0	0
4	0	F_{42}	F_{43}	F_{44}	$\omega_u + \Omega_u$	$-\omega_n - \Omega_n$	0	$-f_u$	f_n
5	0	F_{52}	F_{53}	$-2\omega_u$	$-K_z$	ρ_e	f_u	0	$-f_e$
6	0	$-2\Omega_u v_e$	F_{63}	$2\omega_n$	$-2\rho_e$	0	$-f_n$	f_e	0
7	0	0	$-\rho_e/R$	0	$-1/R$	0	0	ω_u	$-\omega_n$
8	0	$-\Omega_u$	$-\rho_n/R$	$1/R$	0	0	$-\omega_u$	0	ω_e
9	0	F_{92}	$-\rho_u/R$	$(\tan L)/R$	0	0	ω_n	$-\omega_e$	0
	1	2	3	4	5	6	7	8	9

Figure 1. Pinson Nine State Error Model $F(t)$ Matrix Partition

Symbol and Value	Meaning
L	Latitude
$\Omega = 7.2921151 \times 10^{-5}$ rad/sec	Earth Rotation Rate
R = 20925640 ft	Radius of Earth
g = 32.0881576	Magnitude of gravity vector
v_e, v_n, v_u	Vel. in local nav frame (e,n,u)
f_e, f_n, f_u	Specific Force in nav frame
$\Omega_n = \Omega \cos L$	North Component of Earth Rate
$\Omega_u = \Omega \sin L$	Up Component of Earth Rate
$\rho_e = -v_n/R$ $\rho_n = v_e/R$ $\rho_u = (v_e \tan L)/R$	Components of Angular Velocity of Nav Frame with respect to Earth
$\omega_e = \rho_e$ $\omega_n = \rho_n + \Omega_n$ $\omega_u = \rho_u + \Omega_u$	Components of Angular Velocity of Nav Frame with respect to Inertial Space
$K_z = v_u/R$	
$F_{42} = 2(\Omega_n v_n + \Omega_u v_u)$ $+ \rho_n v_n / \cos^2 L$	
$F_{43} = \rho_u \rho_e + \rho_n K_z$	
$F_{44} = -\rho_e \tan L - K_z$	
$F_{52} = -2\Omega_n v_e - \rho_n v_e / \cos^2 L$	
$F_{53} = \rho_n \rho_u - \rho_e K_z$	
$F_{63} = 2g/R - (\rho_n^2 + \rho_e^2)$	
$F_{92} = \omega_n + \rho_u \tan L$	

Table 2. Notation used in Figures 1 and 4

Coordinate Systems

The basic Pinson error model is often implemented in an east-north-up (e,n,u) navigation coordinate frame. However, the gyro and accelerometer sensitive axes are assumed to be nominally aligned along the axes of an aircraft body frame orientated in a nose, right-wing, down (x,y,z) direction. Therefore, it will be necessary to transform the sensor noises derived in the body frame to the navigation frame prior to using them as a driving force for the basic error differential equations. Using the notation

ϕ = Roll Euler Angle

θ = Pitch Euler Angle

ψ = Yaw Euler Angle

and referring to Figure 2, the transformation from the body frame to the navigation frame, C_b^n , is

$$C_b^n = \begin{pmatrix} C_{ex} & C_{ey} & C_{ez} \\ C_{nx} & C_{ny} & C_{nz} \\ C_{ux} & C_{uy} & C_{uz} \end{pmatrix} \quad (2)$$

where

$$C_{ex} = \sin\psi \cos\theta$$

$$C_{nx} = \cos\psi \cos\theta$$

$$C_{ux} = \sin\theta$$

$$C_{ey} = \sin\psi \sin\theta \sin\phi + \cos\psi \cos\phi$$

$$C_{ny} = \cos\psi \sin\theta \sin\phi - \sin\psi \cos\phi$$

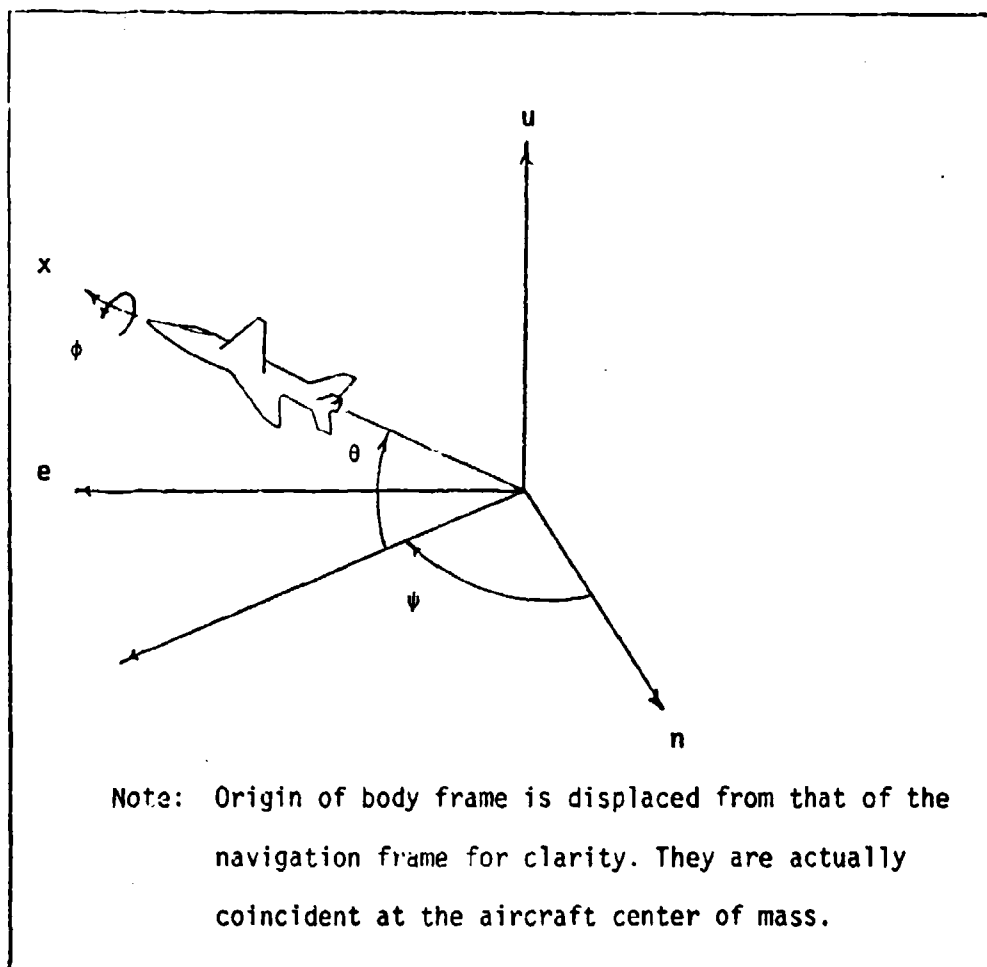


Figure 2. Body and Navigation Coordinate Frames

$$\begin{aligned}
C_{uy} &= -\cos\theta \sin\phi \\
C_{ez} &= -\cos\psi \sin\phi + \sin\psi \sin\theta \cos\phi \\
C_{nz} &= \cos\psi \sin\theta \cos\phi + \sin\psi \sin\phi \\
C_{uz} &= -\cos\theta \cos\phi
\end{aligned}$$

In addition to the above transformation, the output of the flight profile generator, PROFGEN, will also have to be transformed to the navigation and body frames. The necessary transformation from the PROFGEN frame to the navigation frame used here, C_p^n , is

$$C_p^n = \begin{pmatrix} 0 & -1 & 0 \\ 1 & 0 & 0 \\ 0 & 0 & 1 \end{pmatrix} \quad (3)$$

This transformation is done implicitly in the simulation by equating the west components of PROFGEN's output to the respective negative east components in the error model.

After transforming to the proper navigation frame, both specific force and angular velocity must also be transformed to the body frame. This transformation is the inverse of that given in Equation (2) and is defined as

$$C_n^b = \begin{pmatrix} C_{xe} & C_{xn} & C_{xu} \\ C_{ye} & C_{yn} & C_{yu} \\ C_{ze} & C_{zn} & C_{zu} \end{pmatrix} = \begin{pmatrix} C_{ex} & C_{ey} & C_{ez} \\ C_{nx} & C_{ny} & C_{nz} \\ C_{ux} & C_{uy} & C_{uz} \end{pmatrix}^T \quad (4)$$

Altitude Channel Mechanization

Since a three-accelerometer reference system will be used, and

the vertical channel of an unaided inertial reference system is inherently unstable, external aiding will be used in the vertical computations. (Ref 17:13) To minimize the vertical error, a barometric altimeter input will be implemented in a third order feedback loop. The error aiding equations used here are

$$u_h = -K_1(\delta h - \delta h_{ref}) \quad (5)$$

$$u_{vu} = -K_2(\delta h - \delta h_{ref}) \quad (6)$$

$$\dot{\delta a} = K_3(\delta h - \delta h_{ref}) \quad (7)$$

where

u_h = rate of correction of indicated altitude

u_{vu} = rate of correction of vertical vel. error

δh = indicated altitude error, State $x(3)$

δh_{ref} = barometric altitude error

δa = difference of integral of indicated and barometric altitude, used as an additional state, $x(10)$

Equations (5) and (6) are used as additional driving forces for the differential equations of states $x(3)$ and $x(6)$ respectively, and Equation (7) is added to the system as an additional state, $x(10)$. The altitude channel equations, including these aiding equations, then become

$$\dot{x}(3) = x(6) - K_1(x(6) - \delta h_{ref}) \quad (8)$$

$$\begin{aligned} \dot{x}(6) = & -2\omega_u v_e x(2) + F_{63} x(3) - K_2(x(6) - \delta h_{ref}) \\ & + 2\omega_n x(4) - 2p_e x(5) - f_n x(7) + f_e x(8) - x(10) \end{aligned} \quad (9)$$

$$\dot{x}(10) = K_3(x(6) - \delta h_{ref}) \quad (10)$$

The value of the gains K_1 , K_2 , and K_3 have been arbitrarily chosen so that the characteristic equation of the baro-altitude loop has a triple pole at $s = -.01 \text{ sec}^{-1}$ which provides stable feedback in a loop with a time constant of about 100 seconds. Such a design was used in the Litton CAINS inertial navigator (Ref 17:16). These values are

$$K_1 = 3 \times 10^{-2} \text{ sec}^{-1}$$

$$K_2 = 3 \times 10^{-4} \text{ sec}^{-2}$$

$$K_3 = 1 \times 10^{-6} \text{ sec}^{-3}$$

The results of using these gains will be discussed in the verification section to follow.

Gyro Error Model

The Honeywell GG1342 ring laser gyro was chosen as a representative state-of-the-art gyro to be used in this simulation. It is a 0.63 micron (visible red) wavelength gyro with a 34.5 centimeter path length and uses body dither for lock-in compensation. Mechanical dithering is accomplished by piezoelectric transducers oscillating the lasing block through a small angle to minimize dwell time in the lock-in zone. As the block passes through lock-in a residual error, random rate noise, is introduced which should be accounted for in the development of the error model.

This type of gyro was recently flight tested by the Naval Air Development Center in the A-7E aircraft. Benign maneuvers as well as air-to-air combat maneuvers were performed during these tests. Results showed a median of an ensemble of radial position error rates of less than 0.75 nautical miles per hour could be achieved using only a six

minute alignment. Ground tests showed that the six minute alignment produced an RMS alignment error in azimuth of 3.75 arc min (Ref 2).

For the investigation undertaken here, one of these gyros will be assumed to be nominally aligned along each of the pitch, roll, and yaw axis of the aircraft. This is a simplification for analysis purposes. In general, a better gyro is used for the roll axis, or the greater dynamic range of the roll axis is distributed by canting the input axes of the gyros in relation to the roll axis. The performance characteristics assumed for each gyro are listed in Table 3.

Bias stability, scale factor stability, and input axis orthogonality errors will be achieved in the simulation by augmenting the basic ten-by-ten error model with additional states. These states will be derived from differential equations of the form

$$\dot{\mathbf{x}} = 0 \quad (11)$$

That is, they will be modelled as random biases, and obtained as the output of integrators with no input, but with an initial condition modelled as a Gaussian random variable based upon the given standard deviations (Ref 8).

Random drift of the laser gyro will be modelled as a white Gaussian noise driving the attitude tilt error states of the Pinson error model.

In addition to the error model characteristics shown in Table 3, a scale factor nonlinearity typical of all dithered laser gyros (Ref 1) will be inserted in the model. A describing function for this nonlinearity was obtained from Dr. Jack W. Bell of the Air Force Avionics Laboratory (Ref 3) as

Error Source	Standard Deviation
Bias Stability	0.008 deg/hr
Random Drift	0.002 deg/ $\sqrt{\text{hr}}$
Scale Factor Stability	5 PPM
Input Axis Misalignment	25 μrad

Table 3. GG1342 Laser Gyro Performance Characteristics

$$\text{GSF}_{\text{out}} = \text{GSF}_{\text{in}} + A\omega^2 - B|\omega| + C \quad (12)$$

where

GSF = Gyro Scale Factor (GSF_{in} is nominally 131328.387)

ω = Input Axis Angular Velocity in deg/sec

$A = 19.444 \times 10^{-3} \text{ (pulses/rad)(sec/deg)}^2$

$B = 4.277777 \text{ (pulses/rad)(sec/deg)}$

$C = 217.78622 \text{ pulses/rad}$

The describing function is valid for the region

$$80 \text{ deg/sec} < |\omega| < 140 \text{ deg/sec}$$

and is based upon a nominal scale factor of 131328.387 pulses/rad.

Outside the above region of application the scaling is assumed to be linear. The error contribution of this describing function is plotted in Figure 3.

To convert this function so that it may be applied to the error model used here it is necessary to divide through by the nominal scale factor and convert the region of application from deg/sec to

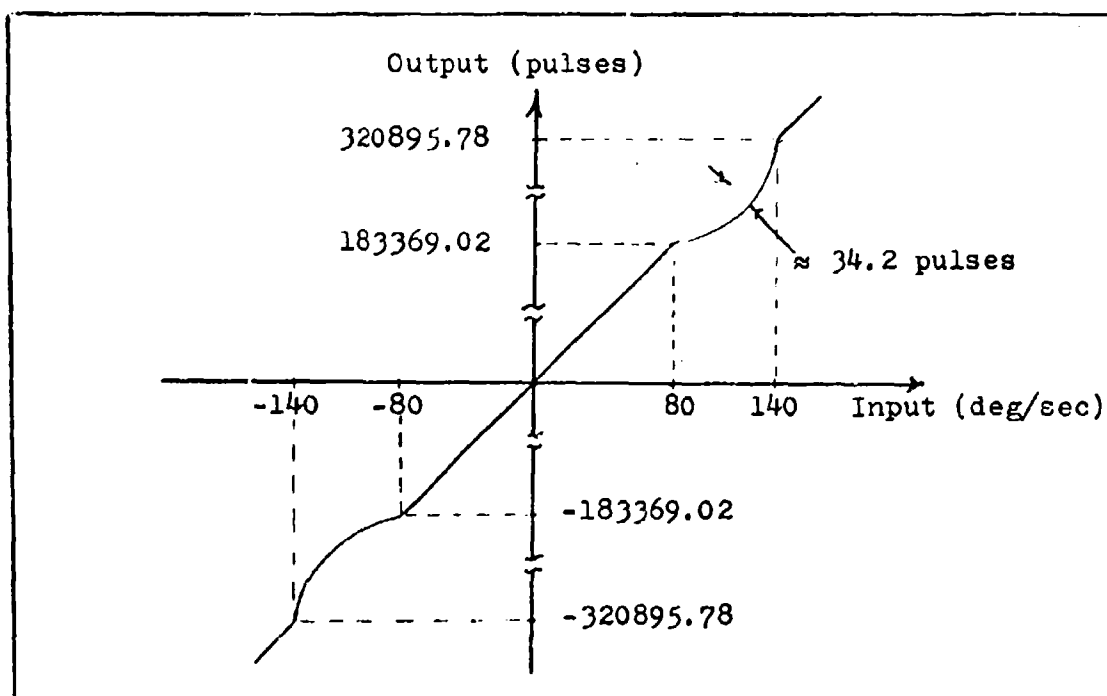


Figure 3. Scale Factor Nonlinearity (Nominal Scale Factor 131328.387 pulses/rad)

rad/sec. This results in the function

$$GSF_{out} = GSF_{in} + A'\omega^2 - B'|\omega| + C' \quad (13)$$

where

GSF = Gyro Scale Factor (GSF_{in} is nominally 1)

ω = Input Axis Angular Velocity in rad/sec

$A' = 4.86039 \times 10^{-4} \text{ (sec/rad)}^2$

$B' = 1.8663 \times 10^{-3} \text{ sec/rad}$

$C' = 1.65833 \times 10^{-3}$

This function is valid in the region

$$1.3963 \text{ rad/sec} < |\omega| < 2.4435 \text{ rad/sec}$$

The contribution of the scale factor nonlinearity to the overall scale factor error is shown in Table 4 for selected input rates. Although Figure 3 does represent the form of the nonlinearity described in Reference 1, the magnitude of the error contribution shown in the third column of Table 4 appears to be high. Scale factor linearities for three Honeywell GG1342 gyros discussed in Reference 2 are given as 3.1, 2.5, and 1.1 PPM. Based on these figures, the describing function for the nonlinearity given in Equation (13) will be scaled down such that its maximum value will be equal to the midvalue, 2.5 PPM. This reduced error contribution is shown in the fourth column of Table 4. The effect of this and alternative choices will be shown in the subsequent validation section.

Angular Rate		Error contribution	
deg/sec	rad/sec	$A'\omega^2 - B' \omega + C'$	2.5 PPM Maximum
± 80	1.3962634	4.3098×10^{-8}	8.08683×10^{-10}
± 90	1.5707963	-7.3992×10^{-5}	-1.38837×10^{-6}
± 100	1.7453292	-1.1841×10^{-4}	-2.22182×10^{-6}
± 110	1.9198621	-1.3323×10^{-4}	-2.5×10^{-6}
± 120	2.0943951	-1.1847×10^{-4}	-2.22295×10^{-6}
± 130	2.268928	-7.4065×10^{-5}	-1.38973×10^{-6}
± 140	2.4434609	-4.38595×10^{-8}	-8.22972×10^{-10}

Table 4. Gyro Scale Factor Nonlinearity

Error Source	Standard Deviation
Bias	
Repeatability	10 μg
White Noise	5 $\mu\text{g}/\sqrt{\text{sec}}$
Correlated Noise ($\tau = 60 \text{ sec}$)	7 μg
Scale Factor	
Stability	15 PPM
Quadratic	0.09 $\mu\text{g}/\text{g}^2$
Cross Axes	0.20 $\mu\text{g}/\text{g}^2$
Cubic	0.0007 $\mu\text{g}/\text{g}^3$
Orthogonality	10 arc sec
Gain Change Stability	
Bias	10 μg
Scale Factor	5 PPM

Table 5. Bell Model XI Accelerometer Error Model

Accelerometer Error Model

Although the Systron Donner accelerometer is currently used in the Honeywell ring laser gyro navigator (RLGN), the Bell Model XI accelerometer was chosen for this study because of its better and more state-of-the-art performance characteristics. The Bell Model XI accelerometer is a single axis, pendulous proofmass, force rebalance device which uses a capacitive bridge pickoff to detect specific force. The parameters for the basic error model for this accelerometer are shown in Table 5. Long term errors, temperature compensation errors, and errors induced from a specific onboard computer implementat-

ion were not considered in this model. It is assumed that temperature compensation and computer processing will be designed such that the dominant short term errors will be those listed in Table 5.

Bias stability will be modeled as a random constant with a standard deviation based upon the RMS value of the two terms given in the table

$$\sqrt{(10\mu g)^2 + (10\mu g)^2} = 14.14 \mu g = 4.55376 \times 10^{-4} \text{ ft/sec}^2 \quad (14)$$

This value will be the basis of the random initial condition of an undriven integrator used to generate the random constant.

The white Gaussian noise given in the model will directly drive the differential equations for the three velocity states in the basic Pinson error model. Transformation from the body frame to the navigation frame is not necessary because the strength of the noise is the same for all three axes. Since the noise is spherically distributed, a rotation of the reference frame still results in the same statistical characteristics for the noise driving each axis.

The correlated noise bias will be modeled as a stationary first order Gauss-Markov process (Ref 8:183). That is, the differential equation for the state will be that of a first order lag driven by white Gaussian noise of strength Q where

$$Q = 2\sigma^2/\tau = 2(7\mu g)^2/(60\text{sec}) = 1.6935 \times 10^{-9} \text{ ft}^2/\text{sec}^3 \quad (15)$$

The remaining error sources will be modeled as random constants. The scale factor stability terms will be combined to obtain a standard deviation of

$$\sqrt{(15 \text{ PPM})^2 + (5 \text{ PPM})^2} = 1.5811388 \times 10^{-5} \quad (16)$$

The placard acceleration limit for the F15 is 7.5 g. This value was used to determine the relative contribution of each error source with the acceleration applied both along the input axis and 45 degrees between axes. The equation used to calculate indicated acceleration, A_i , is

$$\begin{aligned} A_i = & K_b + K_i a_i + K_{ii} a_i^2 + K_{pp} a_p^2 + K_{oo} a_o^2 \\ & + K_{ip} a_i a_p + K_{io} a_i a_o + K_{po} a_p a_o \\ & + K_{iii} a_i^3 + K_{ppp} a_p^3 + K_{ooo} a_o^3 \end{aligned} \quad (17)$$

where

a_i, a_p, a_o = acceleration along input, pendulous
or output axis

K_b = bias coefficient

K_i = scale factor coefficient

K_{ii}, K_{pp}, K_{oo} = quadratic nonlinearity coefficients

K_{io}, K_{po}, K_{ip} = cross axis nonlinearity coefficients

$K_{iii}, K_{ooo}, K_{ppp}$ = cubic nonlinearity coefficients

As shown in Table 6, the contribution of the cubic error is an order of magnitude less than the other error sources. Thus, it will not be included in the error model used in this simulation.

Therefore, for the accelerometers to be modeled, eleven additional states will be added to the basic error model for each accelerometer. One state will generate correlated noise, while ten states will represent random constants.

Error (μg)	7.5 g Along Input Axis	7.5 g 45° between axes
Bias	14.14	14.14
Scale Factor	118.5854	83.8525
Quadratic	5.0625	2.53
Cross Axes	0.0	5.625
Cubic	0.295	0.1044

Table 6. Contribution of Accelerometer Error Sources

Gravity Error Model

The gravity error model consists of local variations of the gravity vector which are not normally compensated for in inertial reference systems. Both gravity deflections and gravity anomaly are modeled as first order Gauss-Markov processes with the correlation time derived from the vehicle speed and spatial correlation distance (Ref 17). This is shown by

$$\dot{x} = -\frac{v}{d}x + w \quad (18)$$

where

v = Vehicle Ground Speed

d = Correlation Distance

x = Error State

w = White Noise of Strength Q

$$Q = 2\sigma^2 v/d$$

The gravity variation model given in Reference 17 for the western

Gravity Error	Standard Deviation	Distance
East-West Deflection	26 μg	10 nm
North-South Deflection	17 μg	10 nm
Anomaly	35 μg	60 nm

Table 7. Model for Gravity Variations (Ref 17)

United States is shown in Table 7.

Barometric Altimeter Error Model

The barometric altimeter is used in this simulation to stabilize the vertical velocity and altitude. Two sources of error will be modeled, the scale factor error due to nonstandard temperature and the error due to the variation in altitude of a constant pressure surface.

The nonstandard temperature error will be modeled as a random constant with a standard deviation of 0.03. The variation of the pressure surface will be modeled as a spatial first order Gauss-Markov process with a correlation distance of 250 nm and a standard deviation of 500 feet (Ref 17).

Complete Truth Model

The complete truth model of the errors for the strapdown inertial reference system consists of 60 error states basically of the form

$$\dot{\underline{x}} = \underline{F} \underline{x} + \underline{w} \quad (19)$$

Each of these states, \underline{x} , are defined in Table 8. The fundamental matrix, \underline{F} , for the truth model is shown in Figure 4 with an explanation of its entries in Tables 2 and 9. The strengths of driving white Gaussian noise terms, \underline{w} , are given in Table 10.

State	Meaning	σ_0
Basic Altitude Damped INS		
x(1)	Error in East Longitude	5.7735×10^{-2} arc min
x(2)	Error in North Latitude	5.7735×10^{-2} arc min
x(3)	Error in Altitude	Equation (21)
x(4)	Error in East Velocity	1 ft/sec
x(5)	Error in North Velocity	1 ft/sec
x(6)	Error in Vertical Velocity	0.1 ft/sec
x(7)	Attitude Error East Component	Equation (23)
x(8)	Attitude Error North Component	Equation (25)
x(9)	Attitude Error Up Component	Equation (27)
x(10)	Altitude Stabilization Error	Equation (29)
Gyro Error States		
x(11)	x Gyro Bias	0.008 deg/hr
x(12)	y Gyro Bias	0.008 der/hr
x(13)	z Gyro Bias	0.008 deg/hr
x(14)	x Gyro Scale Factor Error	5 PPM
x(15)	y Gyro Scale Factor Error	5 PPM
x(16)	z Gyro Scale Factor Error	5 PPM
x(17)	x Gyro Misalign about y	25 μ rad
x(18)	x Gyro Misalign about z	25 μ rad
x(19)	y Gyro Misalign about x	25 μ rad
x(20)	y Gyro Misalign about z	25 μ rad

Table 8. Error States and Initial Standard Deviations

State	Meaning	σ_0
x(21)	z Gyro Misalign about x	25 μ rad
x(22)	z Gyro Misalign about y	25 μ rad
	Accelerometer Error States	
x(23)	x Accelerometer Bias	14.14 μ g
x(24)	y Accelerometer Bias	14.14 μ g
x(25)	z Accelerometer Bias	14.14 μ g
x(26)	x Accel. Correlated Noise	7 μ g
x(27)	y Accel. Correlated Noise	7 μ g
x(28)	z Accel. Correlated Noise	7 μ g
x(29)	x Accel. Input Quadratic	0.09 μ g/g ²
x(30)	y Accel. x Cross Quadratic	0.09 μ g/g ²
x(31)	z Accel. x Cross Quadratic	0.09 μ g/g ²
x(32)	x Accel. y Cross Quadratic	0.09 μ g/g ²
x(33)	y Accel. Input Quadratic	0.09 μ g/g ²
x(34)	z Accel. y Cross Quadratic	0.09 μ g/g ²
x(35)	x Accel. z Cross Quadratic	0.09 μ g/g ²
x(36)	y Accel. z Cross Quadratic	0.09 μ g/g ²
x(37)	z Accel. Input Quadratic	0.09 μ g/g ²
x(38)	x Accel. x, y Cross Scale Factor	0.2 μ g/g ²
x(39)	y Accel. x, y Cross Scale Factor	0.2 μ g/g ²
x(40)	z Accel. x, y Cross Scale Factor	0.2 μ g/g ²

Table 8. (continued)

State	Meaning	σ_0
x(41)	x Accel. x, z Cross Scale Factor	0.2 $\mu\text{g/g}^2$
x(42)	y Accel. x, z Cross Scale Factor	0.2 $\mu\text{g/g}^2$
x(43)	z Accel. x, z Cross Scale Factor	0.2 $\mu\text{g/g}^2$
x(44)	x Accel. y, z Cross Scale Factor	0.2 $\mu\text{g/g}^2$
x(45)	y Accel. y, z Cross Scale Factor	0.2 $\mu\text{g/g}^2$
x(46)	z Accel. y, z Cross Scale Factor	0.2 $\mu\text{g/g}^2$
x(47)	x Accelerometer Scale Factor	15 PPM
x(48)	y Accelerometer Scale Factor	15 PPM
x(49)	z Accelerometer Scale Factor	15 PPM
x(50)	x Accel. Misalign about y	10 arc sec
x(51)	x Accel. Misalign about z	10 arc sec
x(52)	y Accel. Misalign about x	10 arc sec
x(53)	y Accel. Misalign about z	10 arc sec
x(54)	z Accel. Misalign about x	10 arc sec
x(55)	z Accel. Misalign about y	10 arc sec
Altimeter Error States		
x(56)	Barometric Pressure Error	0.03
x(57)	Barometric Scale Factor Error	500 ft
Gravity Model Error State		
x(58)	East Deflection of Gravity	26 μg
x(59)	North Deflection of Gravity	17 μg
x(60)	Gravity Anomaly	35 μg

Table 8. (continued)

	1	2	3	4	5	6	7	8	9	10
1	0	$\rho_u/\cos L$	$-\rho_n/(R\cos L)$	$1/(R\cos L)$	0	0	0	0	0	0
2	0	0	ρ_e/R	0	$1/R$	0	0	0	0	0
3	0	0	$-K_1$	0	0	1	0	0	0	0
4	0	F_{42}	F_{43}	F_{44}	$\omega_u + \Omega_u$	$-\omega_n - \Omega_n$	0	$-f_u$	f_n	0
5	0	F_{52}	F_{53}	$-2\omega_u$	$-K_z$	ρ_e	f_u	0	$-f_e$	0
6	0	$-2\Omega_u v_e$	$F_{63} - K_2$	$2\omega_n$	$-2\rho_e$	0	$-f_n$	f_e	0	-1
7	0	0	$-\rho_e/R$	0	$-1/R$	0	0	ω_u	$-\omega_n$	0
8	0	$-\Omega_u$	$-\rho_n/R$	$1/R$	0	0	$-\omega_u$	0	ω_e	0
9	0	F_{92}	$-\rho_u/R$	$(\tan L)/R$	0	0	ω_n	$-\omega_e$	0	0
10	0	0	K_3	0	0	0	0	0	0	0

Figure 4b. Matrix F_i , Pinson Error Model Augmented with a Tenth State for Vertical Stabilization (Notation used here is shown in Table 2)

	23	24	25	26	27	28	
4	C_{ex}	C_{ey}	C_{ez}	C_{ex}	C_{ey}	C_{ez}	4
5	C_{nx}	C_{ny}	C_{nz}	C_{nx}	C_{ny}	C_{nz}	5
6	C_{ux}	C_{uy}	C_{uz}	C_{ux}	C_{uy}	C_{uz}	6
	23	24	25	26	27	28	

Figure 4c. Matrix F_2

	29	30	31	32	33	34	35	36	37
4	$C_{ex}^f f_x$	$C_{ey}^f f_x$	$C_{ez}^f f_x$	$C_{ex}^f f_y$	$C_{ey}^f f_y$	$C_{ez}^f f_y$	$C_{ex}^f f_z$	$C_{ey}^f f_z$	$C_{ez}^f f_z$
5	$C_{nx}^f f_x$	$C_{ny}^f f_x$	$C_{nz}^f f_x$	$C_{nx}^f f_y$	$C_{ny}^f f_y$	$C_{nz}^f f_y$	$C_{nx}^f f_z$	$C_{ny}^f f_z$	$C_{nz}^f f_z$
6	$C_{ux}^f f_x$	$C_{uy}^f f_x$	$C_{uz}^f f_x$	$C_{ux}^f f_y$	$C_{uy}^f f_y$	$C_{uz}^f f_y$	$C_{ux}^f f_z$	$C_{uy}^f f_z$	$C_{uz}^f f_z$
	29	30	31	32	33	34	35	36	37

Figure 4d. Matrix F_3

	38	39	40	41	42	43	44	45	46
4	C_{ex}^f	C_{ey}^f	C_{ez}^f	C_{ex}^f	C_{ey}^f	C_{ez}^f	C_{ex}^f	C_{ey}^f	C_{ez}^f
5	C_{nx}^f	C_{ny}^f	C_{nz}^f	C_{nx}^f	C_{ny}^f	C_{nz}^f	C_{nx}^f	C_{ny}^f	C_{nz}^f
6	C_{ux}^f	C_{uy}^f	C_{uz}^f	C_{ux}^f	C_{uy}^f	C_{uz}^f	C_{ux}^f	C_{uy}^f	C_{uz}^f
	38	39	40	41	42	43	44	45	46

Figure 4e. Matrix F_4

	47	48	49	50	51	52	53	54	55
4	C_{ex}^f	C_{ey}^f	C_{ez}^f	$-C_{ex}^f$	C_{ex}^f	C_{ey}^f	$-C_{ey}^f$	$-C_{ez}^f$	C_{ez}^f
5	C_{nx}^f	C_{ny}^f	C_{nz}^f	$-C_{nx}^f$	C_{ex}^f	C_{ny}^f	$-C_{ny}^f$	$-C_{nz}^f$	C_{nz}^f
6	C_{ux}^f	C_{uy}^f	C_{uz}^f	$-C_{ux}^f$	C_{ux}^f	C_{uy}^f	$-C_{uy}^f$	$-C_{uz}^f$	C_{uz}^f
	47	48	49	50	51	52	53	54	55

Figure 4f. Matrix F_5

	56	57	58	59	60	
3	K_1	$K_1 h$	0	0	0	3
4	0	0	1	0	0	4
5	0	0	0	1	0	5
6	K_2	$K_2 h$	0	0	1	6
7	0	0	0	0	0	7
8	0	0	0	0	0	8
9	0	0	0	0	0	9
10	$-K_3$	$-K_3 h$	0	0	0	10
	56	57	58	59	60	

Figure 4g. Matrix F_6

	11	12	13	14	15	16	
7	C_{ex}	C_{ey}	C_{ez}	$C_{ex}^{\omega_x}$	$C_{ey}^{\omega_y}$	$C_{ez}^{\omega_z}$	7
8	C_{nx}	C_{ny}	C_{nz}	$C_{nx}^{\omega_x}$	$C_{ny}^{\omega_y}$	$C_{nz}^{\omega_z}$	8
9	C_{ux}	C_{uy}	C_{uz}	$C_{ux}^{\omega_x}$	$C_{uy}^{\omega_y}$	$C_{uz}^{\omega_z}$	9
	11	12	13	14	15	16	

Figure 4h. Matrix F_7

	17	18	19	20	21	22	
7	$C_{ex}^{\omega z}$	$-C_{ex}^{\omega y}$	$-C_{ey}^{\omega z}$	$C_{ey}^{\omega x}$	$C_{ez}^{\omega y}$	$-C_{ez}^{\omega x}$	7
8	$C_{nx}^{\omega z}$	$-C_{nx}^{\omega y}$	$-C_{ny}^{\omega z}$	$C_{ny}^{\omega x}$	$C_{nz}^{\omega y}$	$-C_{nz}^{\omega x}$	8
9	$C_{ux}^{\omega z}$	$-C_{ux}^{\omega y}$	$-C_{uy}^{\omega z}$	$C_{uy}^{\omega x}$	$C_{uz}^{\omega y}$	$-C_{uz}^{\omega x}$	9
	17	18	19	20	21	22	

Figure 4i. Matrix F_8

	26	27	28	
26	$-1/\tau_1$	0	0	26
27	0	$-1/\tau_2$	0	27
28	0	0	$-1/\tau_3$	28
	26	27	28	

Figure 4j. Matrix F_9 ($\tau_1 = \tau_2 = \tau_3$)

	56	57	58	59	60	
56	$-v/d_1$	0	0	0	0	56
57	0	0	0	0	0	57
58	0	0	$-v/d_2$	0	0	58
59	0	0	0	$-v/d_3$	0	59
60	0	0	0	0	$-v/d_4$	60
	56	57	58	59	60	

Figure 4k. Matrix F_{10}

Symbol and Value	Meaning
$K_1 = 3 \times 10^{-2} \text{ sec}^{-1}$ $K_2 = 3 \times 10^{-4} \text{ sec}^{-2}$ $K_3 = 1 \times 10^{-6} \text{ sec}^{-3}$	Gains for Altitude Channel Aiding Equations
f_x, f_y, f_z	Specific Force in Body Frame
$\omega_x, \omega_y, \omega_z$	Angular Rate in Body Frame
h	Altitude
$\begin{pmatrix} C_{ex} & C_{ey} & C_{ez} \\ C_{nx} & C_{ny} & C_{nz} \\ C_{ux} & C_{uy} & C_{uz} \end{pmatrix}$	C_b^n , the Transformation from the Body Frame to the Nav Frame
$\tau_1 = 60 \text{ sec}$ $\tau_2 = 60 \text{ sec}$ $\tau_3 = 60 \text{ sec}$	Accelerometer Correlation Times
$v = \sqrt{v_e^2 + v_n^2}$	Ground Speed
$d_1 = 250 \text{ nm}$	Accelerometer Correlation Distance
$d_2 = 10 \text{ nm}$ $d_3 = 10 \text{ nm}$ $d_4 = 60 \text{ nm}$	Correlation Distances for Gravity Model

Table 9. Notation used in Figure 4.

(See Table 2 for notation used in Figure 4b)

Element	Noise Source	Standard Deviation
w(4)	Accelerometer White Noise	$5 \mu g/\sqrt{\text{sec}}$
w(5)	Accelerometer White Noise	$5 \mu g/\sqrt{\text{sec}}$
w(6)	Accelerometer White Noise	$5 \mu g/\sqrt{\text{sec}}$
w(7)	Gyro Random Drift	$0.002 \text{ deg}/\sqrt{\text{hr}}$
w(8)	Gyro Random Drift	$0.002 \text{ deg}/\sqrt{\text{hr}}$
w(9)	Gyro Random Drift	$0.002 \text{ deg}/\sqrt{\text{hr}}$
w(27)	x Accelerometer Correlated Noise	$\sqrt{2(7\mu g)^2/(60\text{sec})}$
w(28)	y Accelerometer Correlated Noise	$\sqrt{2(7\mu g)^2/(60\text{sec})}$
w(29)	z Accelerometer Correlated Noise	$\sqrt{2(7\mu g)^2/(60\text{sec})}$
w(56)	Barometric Pressure	$\sqrt{2(0.03)^2_v/(250\text{nm})}$
w(58)	East Deflection of Gravity	$\sqrt{2(26\mu g)^2_v/(10\text{nm})}$
w(59)	North Deflection of Gravity	$\sqrt{2(17\mu g)^2_v/(10\text{nm})}$
w(60)	Gravity Anomaly	$\sqrt{2(35\mu g)^2_v/(60\text{nm})}$

Table 10. Standard Deviations of the Non-zero Elements of the Diagonal Q Matrix for Driving Noise \underline{w} where

$$E(\underline{w}(t)\underline{w}(t + \tau)^T) = Q\delta(\tau)$$

Initial Conditions

The initial conditions for the first ten states will be based upon a ground alignment at a random alignment heading. It will also be assumed that the baro-inertial vertical channel has already reached a steady state condition.

Initial longitude and latitude error, $x(1)_0$ and $x(2)_0$ will be based upon the accuracy of the input data available from the pilot. It is assumed that data can be entered through the inertial reference system's control panel to within ± 0.1 arc min. The standard deviation for this uniformly distributed random variable, σ_0 , is

$$\sigma_0 = (0.2 \text{ arc min})/\sqrt{12} = 5.7735 \times 10^{-2} \text{ arc min} \quad (20)$$

For each run of the Monte Carlo simulation, a random sample of $x(1)_0$ and $x(2)_0$ will be approximated by a Gaussian distributed variable based upon the standard deviation given in Equation (20).

The initial altitude error, $x(3)_0$, will be used to minimize the start-up transient response of the baro-inertial loop by offsetting initial barometric altimeter errors. The relationship between these variables is given in the third row of the fundamental matrix in Figure 4 as

$$0 = -K_1 x(3)_0 + K_1 x(56)_0 + K_1 x(57)_0 h$$

or

$$x(3)_0 = x(56)_0 + x(57)_0 h \quad (21)$$

Values that are typically obtained from a ground alignment will be used to specify the initial standard deviations of the east ($\sigma(4)_0$),

north $(\sigma(5))_0$, and up $(\sigma(6))_0$ velocities. The values used in Reference 17 are

$$\sigma(4)_0 = 1 \text{ ft/sec}$$

$$\sigma(5)_0 = 1 \text{ ft/sec}$$

$$\sigma(6)_0 = 0.1 \text{ ft/sec}$$

East and north attitude errors, $x(7)_0$ and $x(8)_0$, depend upon initial accelerometer and gravity errors. During alignment, the transformation matrix from the platform reference frame (the body frame in this case) to the navigation frame will be rotated into alignment with the sensed gravity vector. This results in initial attitude errors that correspond to errors in the sensed gravity vector. The contribution of each sensor to the system error depends upon the alignment heading of the aircraft.

The relationship between initial east tilt error, $x(7)_0$, and acceleration errors can be derived from row five of the fundamental matrix shown in Figure 4. With the aircraft at rest, the terms of interest are

$$0 = x(7)_0 f_u + (x(23))_0 + x(26)_0 + x(35)_0 f_z f_z - x(50)_0 f_z) C_{nx} \\ + (x(24))_0 + x(27)_0 + x(36)_0 f_z f_z + x(52)_0 f_z) C_{ny} + x(59)_0 \quad (22)$$

but $f_u = -f_z = g$, and assuming alignment at a random heading ψ_R we have

$$x(7)_0 = -(x(23))_0/g + x(26)_0/g + x(35)_0 g + x(50)_0) \cos \psi_R \\ + (x(24))_0/g + x(27)_0/g + x(36)_0 g - x(52)_0) \sin \psi_R \\ - x(59)_0/g \quad (23)$$

Similarly, the fourth row of the fundamental matrix provides the

relationship for initial north tilt errors

$$0 = -x(8)_0 f_u + (x(24)_0 + x(27)_0 + x(36)_0 f_z f_z + x(52)_0 f_z) c_{ey} \\ + (x(23)_0 + x(26)_0 + x(35)_0 f_z f_z - x(50)_0 f_z) c_{ex} + x(58) \quad (24)$$

Using the same substitution as in Equation (23) results in

$$x(8)_0 = (x(24)_0/g + x(27)_0/g + x(36)_0 g - x(52)_0) \cos \psi_R \\ + (x(23)_0/g + x(26)_0/g + x(35)_0 g + x(50)_0) \sin \psi_R \\ + x(58)_0/g \quad (25)$$

East gyro errors will cause an initial azimuth error since a ground alignment seeks to null east angular velocity. From the components of the east tilt rate differential equation, row seven in the fundamental matrix shown in Figure 4, the relationship is found to be

$$0 = x(8)_0 \omega_u - x(9)_0 \omega_n \\ + (x(11)_0 + x(14)_0 \omega_x + x(17)_0 \omega_z - x(18)_0 \omega_y) c_{ex} \\ + (x(12)_0 + x(15)_0 \omega_y - x(19)_0 \omega_z + x(20)_0 \omega_x) c_{ey} \quad (26)$$

Since the aircraft is at rest and aligned at a random heading

$$\omega_u = -\omega_z = \Omega_n \\ \omega_x = \Omega_n \cos \psi_R \\ \omega_y = -\Omega_n \sin \psi_R$$

Substituting these values into Equation (26) gives

$$x(9)_0 = (x(8)_0 \Omega_n + (x(11)_0 + x(14)_0 \Omega_n \cos \psi_R \\ - x(17)_0 \Omega_n + x(18)_0 \Omega_n \sin \psi_R) \sin \psi_R \\ + (x(12)_0 - x(15)_0 \Omega_n \sin \psi_R + x(19)_0 \Omega_n \\ + x(20)_0 \Omega_n \cos \psi_R) \cos \psi_R) / \Omega_n \quad (27)$$

The initial value of the azimuth error shown in Equation (27) will apply for longer alignment times (6 minutes or longer). An additional Gaussian sample based on a standard deviation of 3 arc min will be added to Equation (27) to simulate a shorter alignment period (approximately 3 minutes). These values correspond to RMS azimuth errors compiled for alignments during the A-7E flight tests (Ref 2).

The random alignment heading, ψ_R , will be realized at the start of each Monte Carlo run by approximating the heading's uniform distribution from $-\pi$ to π by a Gaussian distribution with a standard deviation, σ_R , of

$$\sigma_R = 2\pi/\sqrt{12} = 1.8137993 \text{ rad}$$

Although the Gaussian distribution will result in a north bias, this type of random variable generator was used because it is included in the basic simulation program, SOFE. Use of it will introduce the desired variation into aircraft heading during alignment, and will reflect the fact the aircraft are not normally parked in an entirely random fashion.

It is assumed that the vertical channel is in steady state; therefore the initial value of state $x(10)$, the integral of the difference between computed and barometric altitude, will be set to compensate for initial vertical velocity errors. The relationship between these variables can be obtained from the sixth row of the fundamental matrix

$$\begin{aligned} 0 = & x(3)_0 F_{63} - x(10)_0 + (x(25)_0 + x(28)_0 + x(37)_0) f_z f_z \\ & + x(49)_0 f_z C_{uz} - K_2(x(3)_0 - x(56)_0 - x(57)_0 h) + x(60)_0 \end{aligned} \quad (28)$$

but initially

$$x(3)_0 = x(56)_0 + x(57)_0 h$$

$$f_z = -g$$

$$C_{uz} = -1$$

$$F_{63} = 2g/R$$

Substituting these relationships into Equation (28) results in

$$\begin{aligned} x(10)_0 &= x(3)_0 2g/R - x(25)_0 - x(28)_0 - x(37)_0 g^2 \\ &+ x(49)_0 g + x(60)_0 \end{aligned} \quad (29)$$

III. Software

The primary program used in this study is a generalized digital simulation program developed by the Air Force Avionics Laboratory called SOFE (Ref 12). Two additional programs used in conjunction with SOFE are a flight profile generator called PROFGEN (Ref 11) and a post-processor called SOFEPL (Ref 6).

SOFE

This section will show how SOFE was implemented for this simulation. Refer to Appendix A for a brief discussion of the program itself. Normally SOFE is used to implement both a complete truth model and a reduced order Kalman filter model. However, SOFE was used here with the order of the filter model equal to the truth model. No measurements are provided to the filter model so that its computed covariance is the unconditional state covariance.

The truth model is propagated through many runs and is used as the basis of a Monte Carlo simulation where data is accumulated such that the standard deviation of the error states can be calculated. The filter model is propagated through one run and used as the basis of a covariance analysis. Here, the square roots of the diagonal elements of the covariance matrix are computed for comparison to the standard deviations generated by the truth model and Monte Carlo sample statistics generation.

In a subsequent validation section of this study, the results of both a Monte Carlo simulation and a covariance analysis for a strapdown inertial reference system will be compared. Based on this comparison, the Monte Carlo simulation method was chosen to accomplish the error analysis since it required less time. A second reason for using a Monte

Carlo simulation is that the scale factor nonlinearity for the laser gyro can be implemented more directly than in a covariance analysis.

The subroutines and data for SOFE that implement the truth model of error state equations developed in the previous section are listed in Appendix B. Although a subroutine, TRAJ, is available in SOFE for programming of trajectory data, an external flight profile generator, PROFGEN, was used to simplify programming and enhance versatility in developing trajectories.

PROFGEN

A discription of PROFGEN is included in Appendix C. PROFGEN was programmed to construct an F4 flight profile during the development of the simulation package, followed by construction of two basic F15 flight profiles for use in the error analysis. The F4 flight profile was developed and is currently used by the Air Force Avionics Laboratory, while the F15 flight profiles were developed for this study and will be discussed in a subsequent section.

The output variables of PROFGEN that drive the simulation program are listed in Table 11. PROFGEN uses a north-west-up navigation frame which is implicitly transformed to the east-north-up frame used here by equating the corresponding components of each vector.

Several of PROFGEN's output variables require transformations prior to being used as driving functions in the error model. Specific force is transformed to the body frame from the navigation frame using C_n^b from Equation (4) as shown in

$$\begin{pmatrix} f_x \\ f_y \\ f_z \end{pmatrix} = \begin{pmatrix} C_{xe} & C_{xn} & C_{xu} \\ C_{ye} & C_{yn} & C_{yu} \\ C_{ze} & C_{zn} & C_{zu} \end{pmatrix} \begin{pmatrix} f_e \\ f_n \\ f_u \end{pmatrix} \quad (30)$$

Symbol	Meaning	Units
t	Time	seconds
L	Latitude	radians
l	Longitude	radians
α	Heading	radians
h	Altitude	feet
ϕ	Roll	radians
θ	Pitch	radians
ψ	Yaw	radians
v_n	North Velocity	ft/sec with respect to earth in the nav frame
$-v_e$	Minus East Velocity	
v_u	Up Velocity	
f_n	Specific Force Along North Axis	ft/sec ²
$-f_e$	Specific Force Along West Axis	ft/sec ²
f_u	Specific Force Along Up Axis	ft/sec ²
$\dot{\phi}$	Roll Rate	rad/sec
$\dot{\theta}$	Pitch Rate	rad/sec
$\dot{\psi}$	Yaw Rate	rad/sec

Table 11. PROFGEN Output

Angular velocity of the body frame with respect to inertial space is found from the sum of the angular velocity of the navigation frame with respect to the earth and the angular velocity of the earth with respect to inertial space. Coordinatizing this in the body frame results in

$$\begin{pmatrix} \omega_x \\ \omega_y \\ \omega_z \end{pmatrix} = \begin{pmatrix} C_{xe} & C_{xn} & C_{xu} \\ C_{ye} & C_{yn} & C_{yu} \\ C_{ze} & C_{zn} & C_{zu} \end{pmatrix} \begin{pmatrix} \omega_e \\ \omega_n \\ \omega_u \end{pmatrix} + \begin{pmatrix} \dot{\phi} \\ \dot{\theta} \\ \dot{\psi} \end{pmatrix} \quad (31)$$

using

$$\omega_e = -v_n/R \quad (32)$$

$$\omega_n = v_e/R + \Omega \cos L \quad (33)$$

$$\omega_u = (v_e \tan L)/R + \Omega \sin L \quad (34)$$

where

$$R = 20925640 \text{ ft}$$

$$\Omega = 7.2921151 \times 10^{-3} \text{ rad/sec}$$

SOFEPPL

SOFEPPL is the post processor which is used in conjunction with SOFE (Ref 6). This program is used to compute ensemble averages and standard deviations of the error states. The graphics package, DISSPLA, is used by SOFEPL to generate a plot file. Actual plots are obtained by using the DISSPLA post processor that corresponds to the desired output device.

IV. Program Validation

The error model for the strapdown inertial reference system was developed in detail in Section II and implemented in software as described in Section III. It remains now to verify that the error state equations and their implementation are correct, and that the results obtained from the simulation are accurate.

Two approaches are to be used to verify the error model. First, the implementation of the basic Pinson error model is to be checked by comparing plots of the error states to those obtained in a previously published report (Ref 17). Then, the entire error model will be implemented in two different manners, a truth model for Monte Carlo simulations and a filter model for covariance computations (assuming no input measurements, as described previously), and the results will be compared.

In addition, the number of runs required to perform a Monte Carlo simulation will be ascertained, and the stability of the baro-inertial altitude channel will be investigated.

Pinson Error Model Verification

The response of an unstable pure inertial reference system and a typical stable baro-inertial system to various initial conditions was investigated by Widnall and Grundy (Ref 17:45-53). They showed plots of responses of an unstable system to an initial altitude error of 10 ft and of a stable system to initial errors of 100 ft in altitude and 1 ft/sec in vertical velocity.

These results were duplicated by selecting the proper initial conditions and setting to zero all the driving noises and noise states in the augmented truth model leaving the basic 10 dimensional error model.

In addition, the baro-inertial aiding gains (K_1 , K_2 , K_3) were set to zero to verify the unstable system response. Typical plots that were obtained are shown in Figures 5 and 6. Latitude and longitude errors resulting from an initial vertical velocity error of 1 ft/sec are plotted over a 2 hour period. As expected, a small amplitude oscillation occurs at the Schuler frequency.

Covariance Analysis versus Monte Carlo Simulation

Verification of the complete augmented error model, including driving noises, was done by comparing the results of a Monte Carlo simulation and a covariance analysis implemented through SOFE as described in Appendix A. Rather than use the state-of-the-art model for the laser gyro and accelerometer developed in Section II, error characteristics of older generation sensors were used (Ref 7). Essentially, this results in the same basic error equations but different initial conditions and driving noise strength. These error model values are listed in Appendix E. The benefit of using sensors with higher noise characteristics is that it allows for easier comparison of results and also provides a baseline whereby the introduction of better sensors should cause improved performance in the simulation. Another consideration in using the older filter model is that the gyro scale factor nonlinearity error is not addressed in that model, thus allowing for a more meaningful comparison of covariance computations and Monte Carlo statistics.

Both the truth model and the filter model of the strapdown inertial reference system were driven by the same highly dynamic flight trajectory. This flight profile was developed by the Air Force Avionics Laboratory and simulates an F4 in combat. The system's response to the specific profile was not considered; rather, the differences between the filter

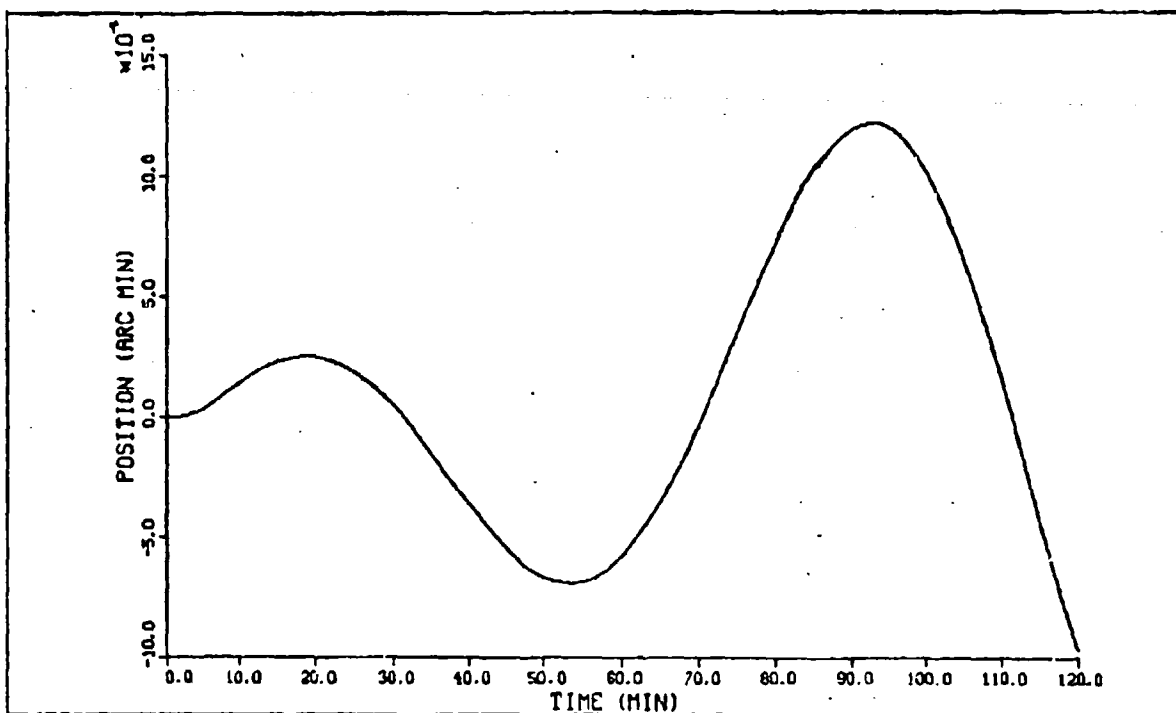


Figure 5. Latitude error for I.C. of $x(6) = 1$ ft/sec

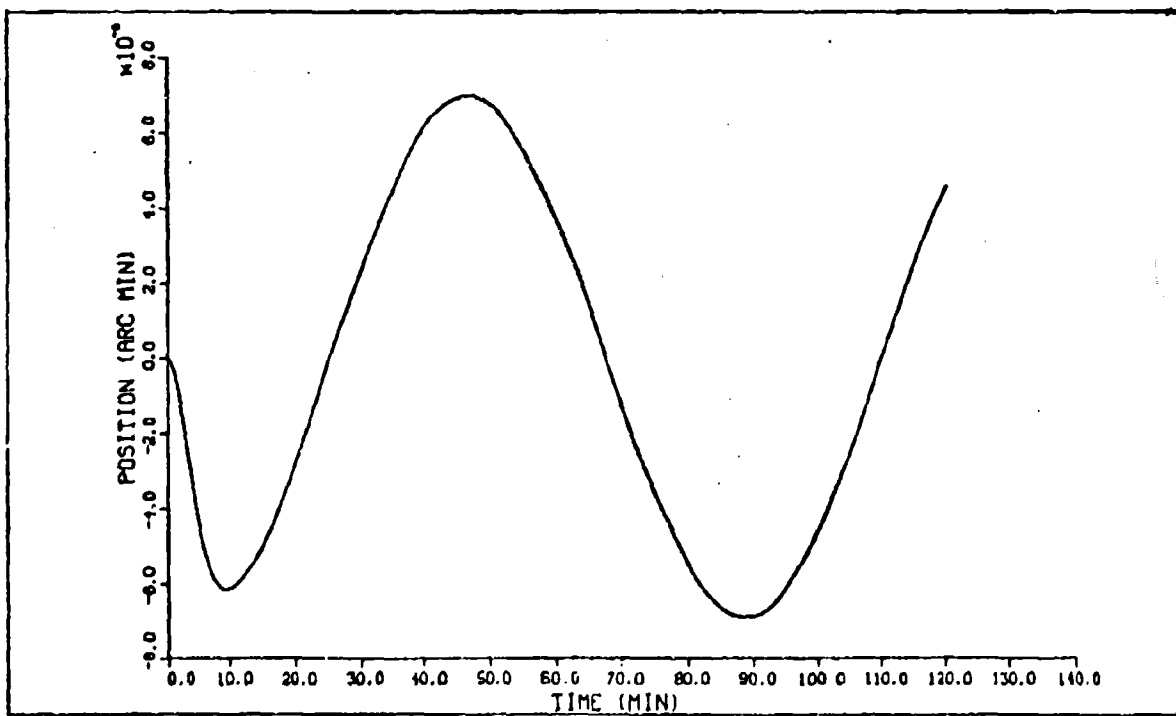


Figure 6. Longitude error for I.C. of $x(6) = 1$ ft/sec

model and the truth model responses were compared. Plots of position, velocity, and tilt errors resulting from a 50 run Monte Carlo simulation using the truth model, and the covariance matrix of the filter model are shown in Figures 7 through 24. For the truth model plots, the dashed lines represent the average plus or minus one standard deviation, and the solid line represents that ensemble average itself. The dashed lines on the filter model plots represent the square root of the diagonal element of the covariance matrix associated with that error state, added to or subtracted from the assumed mean of zero.

Comparison of the plots obtained from each model shows that, although, there are some higher frequency variations in the truth model, the basic trends of each model are nearly identical. It is presumed that, in the limit, as the number of Monte Carlo runs is increased, the differences between the results obtained from the two models will vanish. However, for the purposes of the study undertaken here, the errors present in the 50 run Monte Carlo simulation should be entirely acceptable. Also, after comparing the plots from each model it was concluded that the error models had been implemented correctly since two different methods of implementation of the same system error model produced essentially the same results.

Since comparable statistics were obtained from both Monte Carlo and covariance propagation, other factors must be weighed in the selection of one of these models to perform the error analysis. Although the filter model requires only one run to generate the error statistics, approximately the same amount of computer time is needed to generate a 50 run Monte Carlo simulation. Since these run times are relatively large, a significant savings could be achieved by using the Monte Carlo

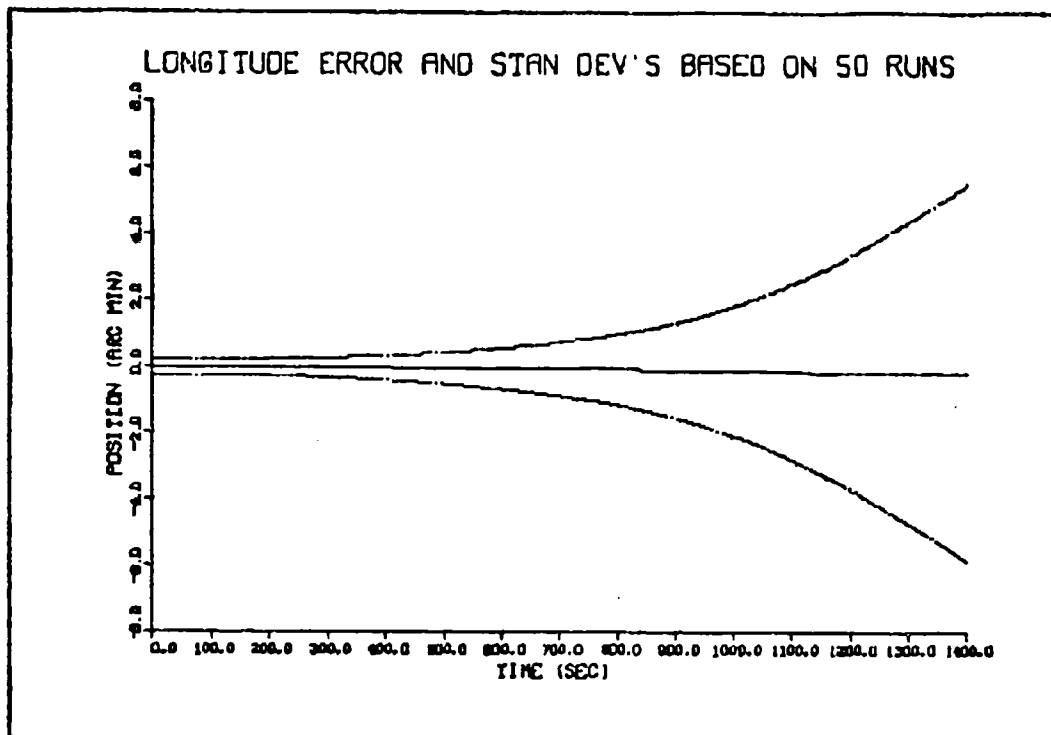


Figure 7. Mean and Standard Deviations from 50 Runs

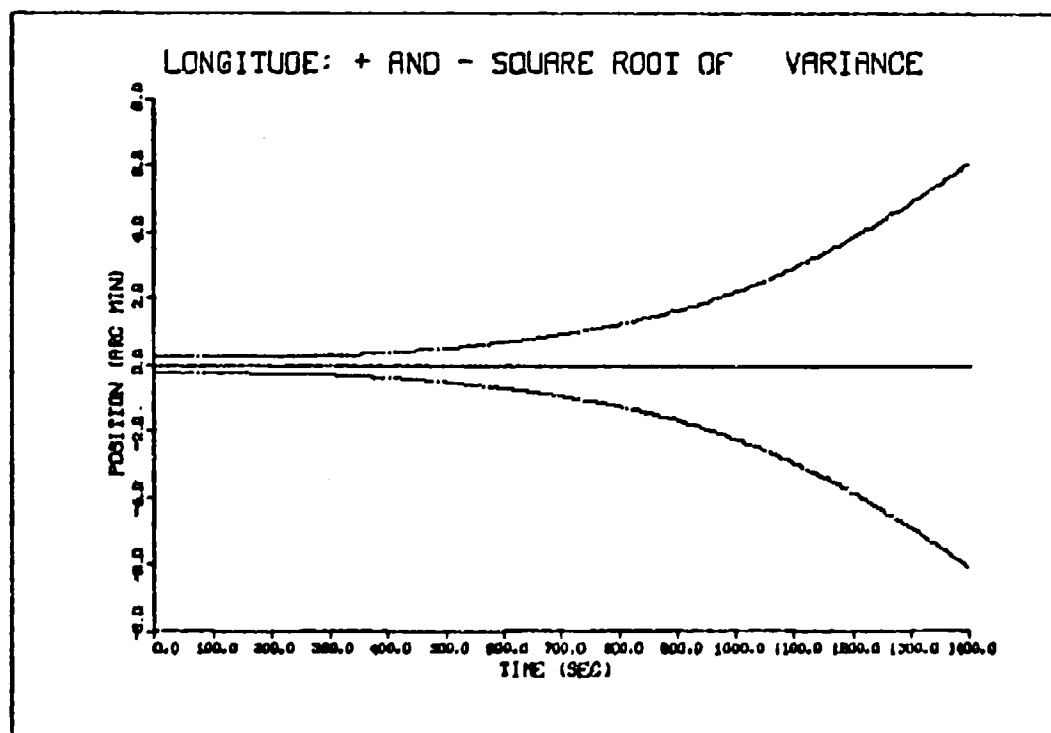


Figure 8. Square Root of Variance

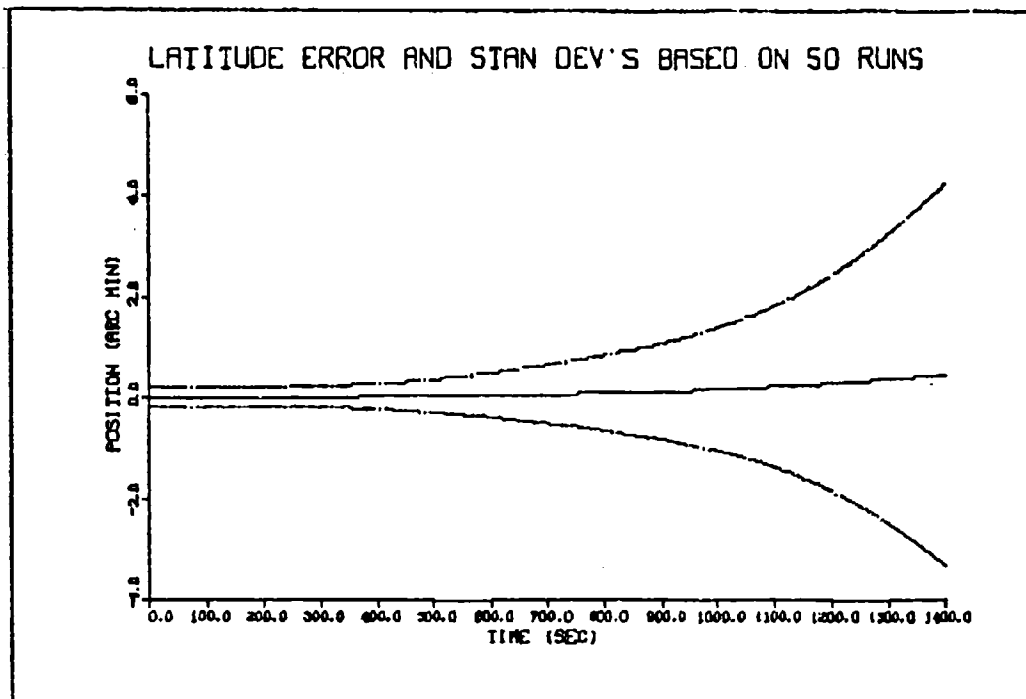


Figure 9. Mean and Standard Deviations from 50 Runs

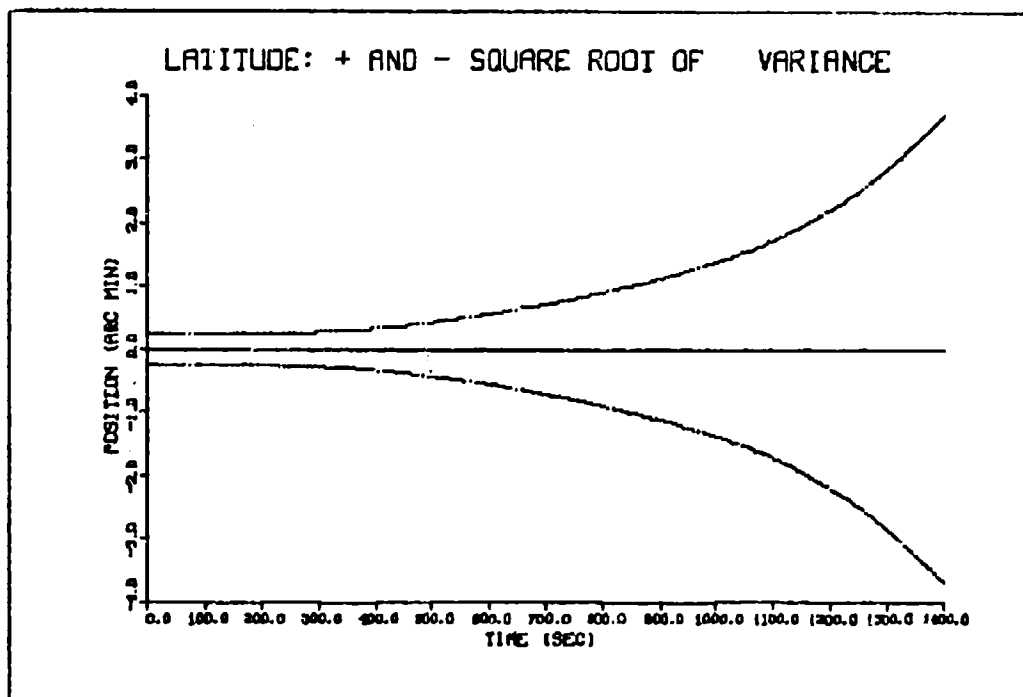


Figure 10. Square Root of Variance

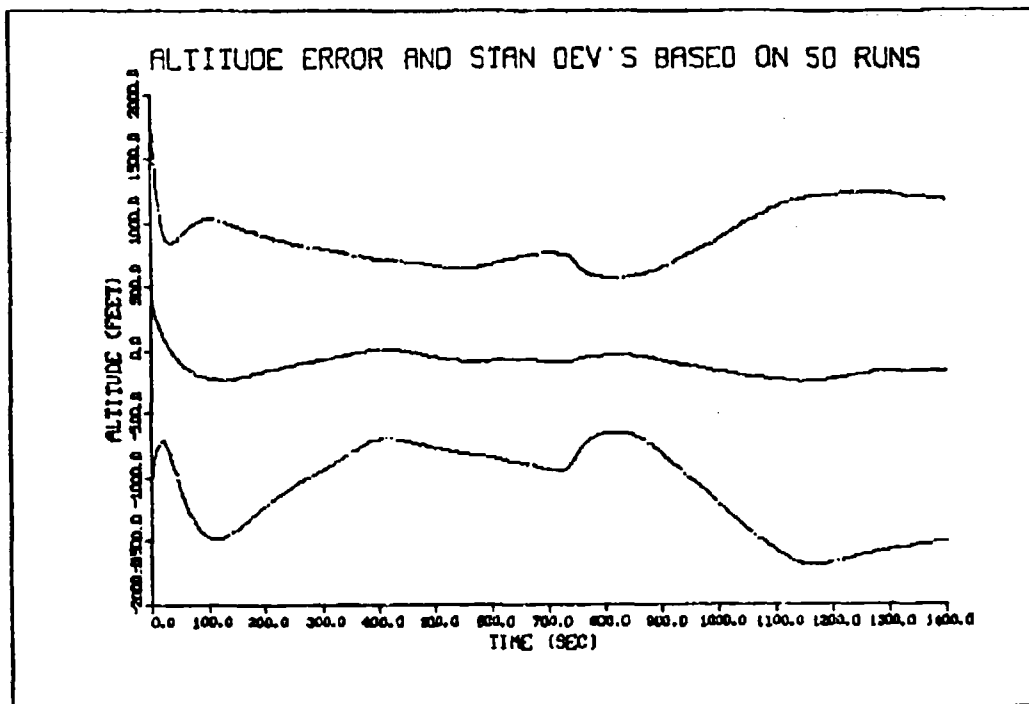


Figure 11. Mean and Standard Deviations from 50 Runs

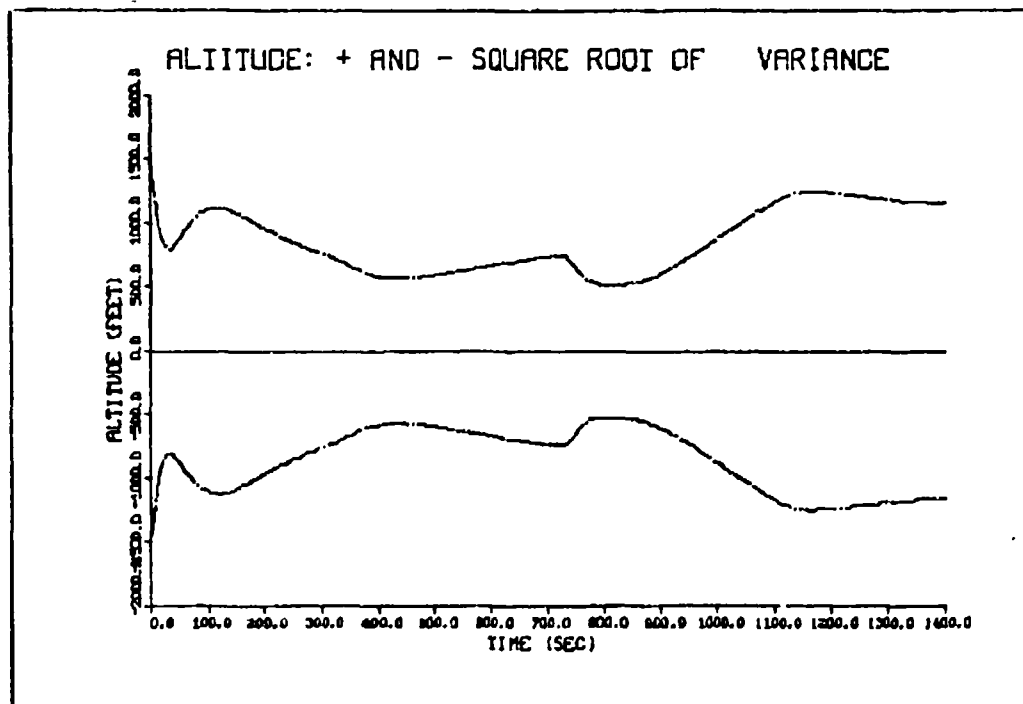


Figure 12. Square Root of Variance

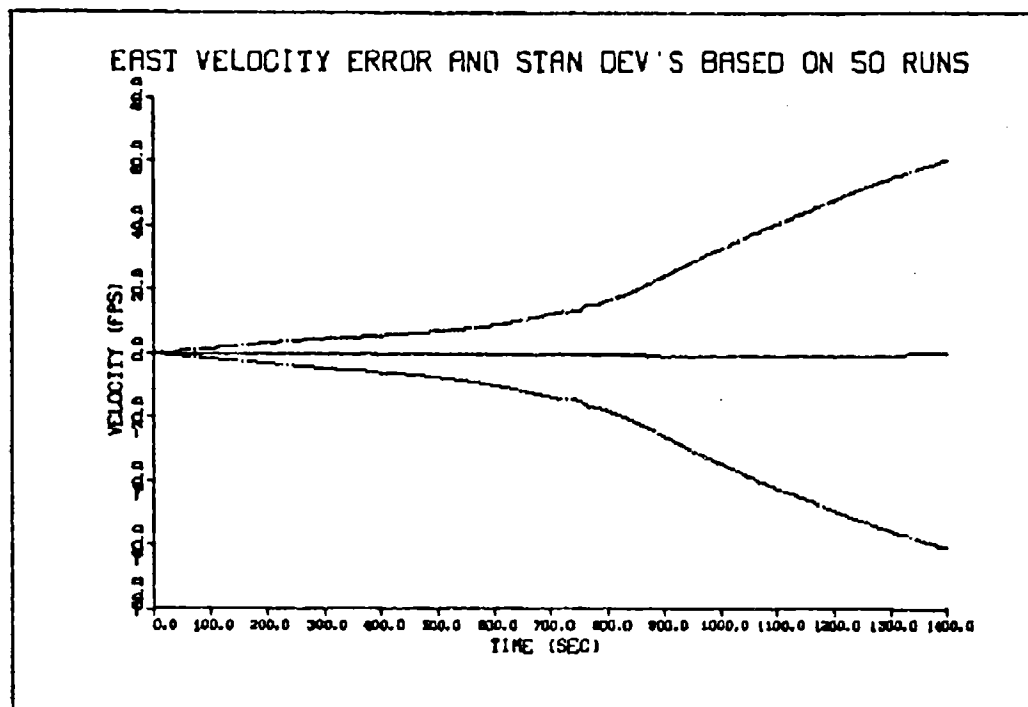


Figure 13. Mean and Standard Deviations from 50 Runs

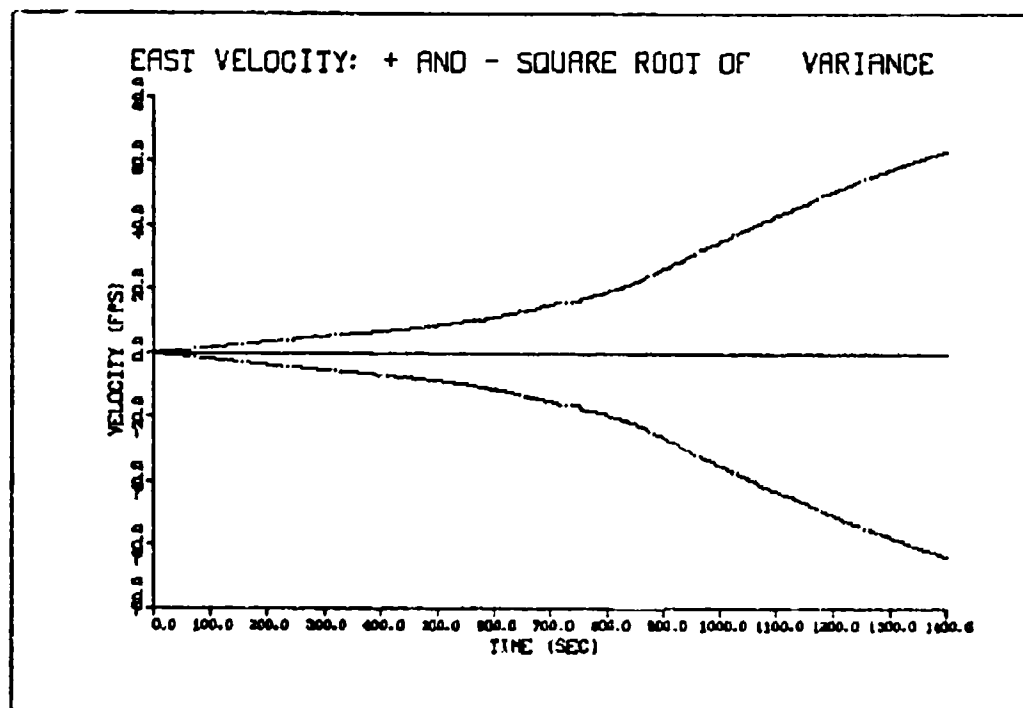


Figure 14. Square Root of Variance

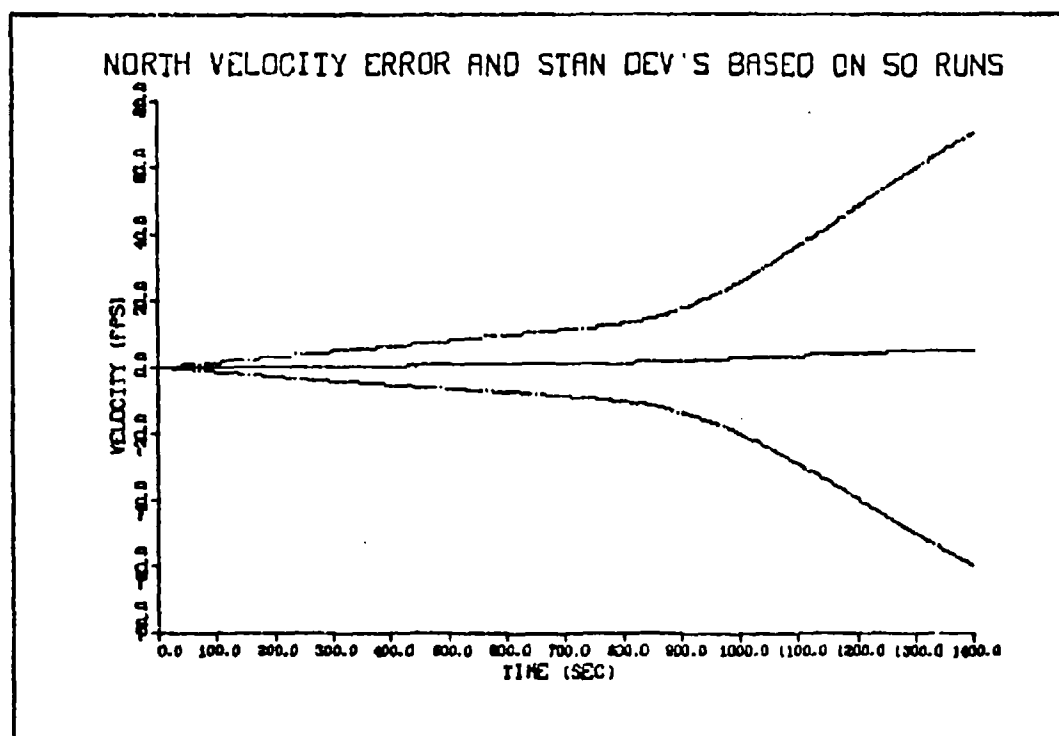


Figure 15. Mean and Standard Deviations from 50 Runs

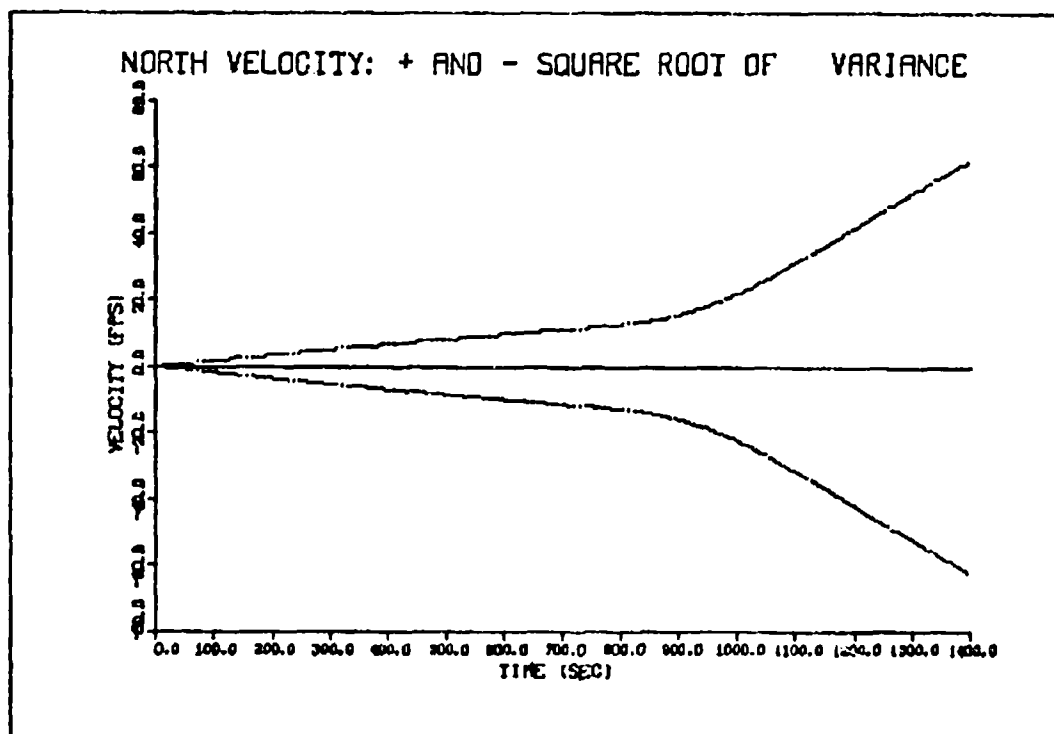


Figure 16. Square Root of Variance

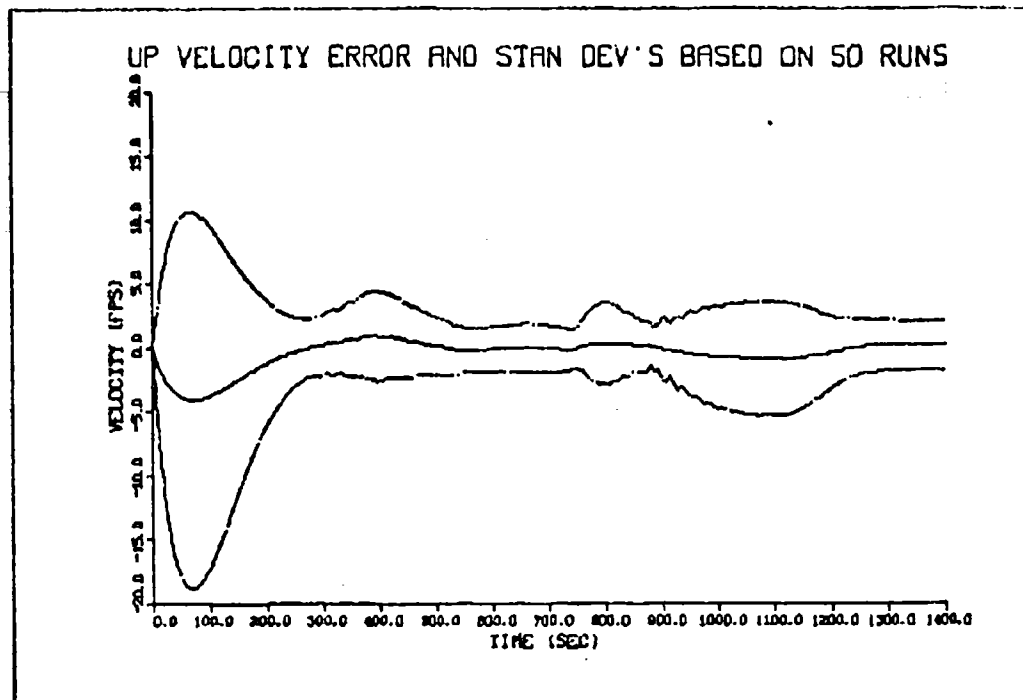


Figure 17. Mean and Standard Deviations from 50 Runs

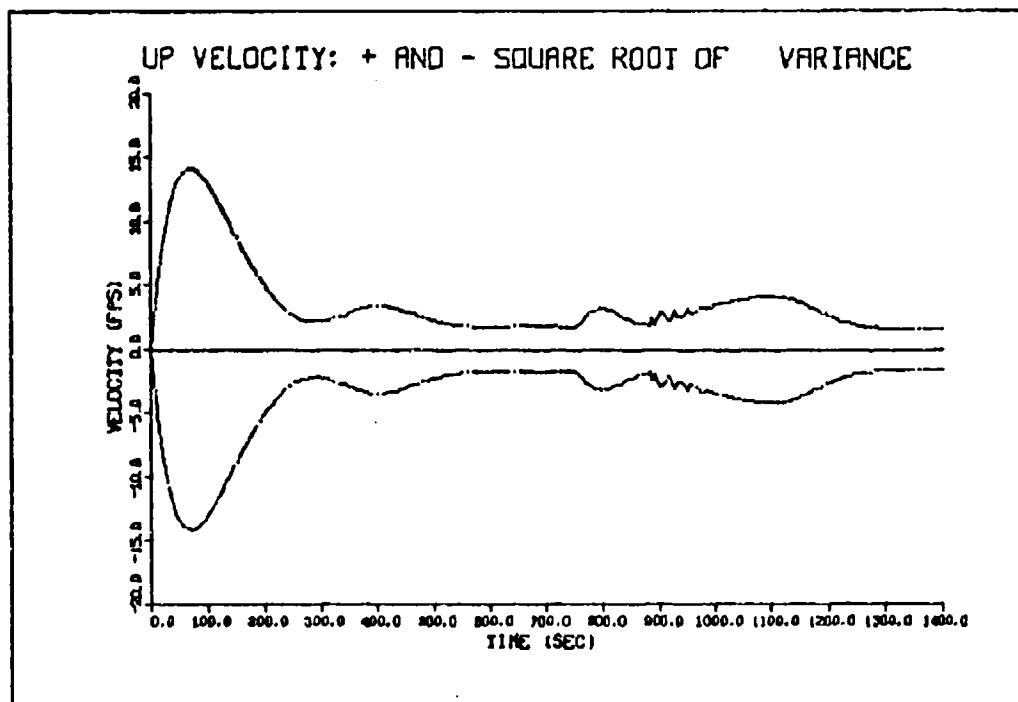


Figure 18. Square Root of Variance

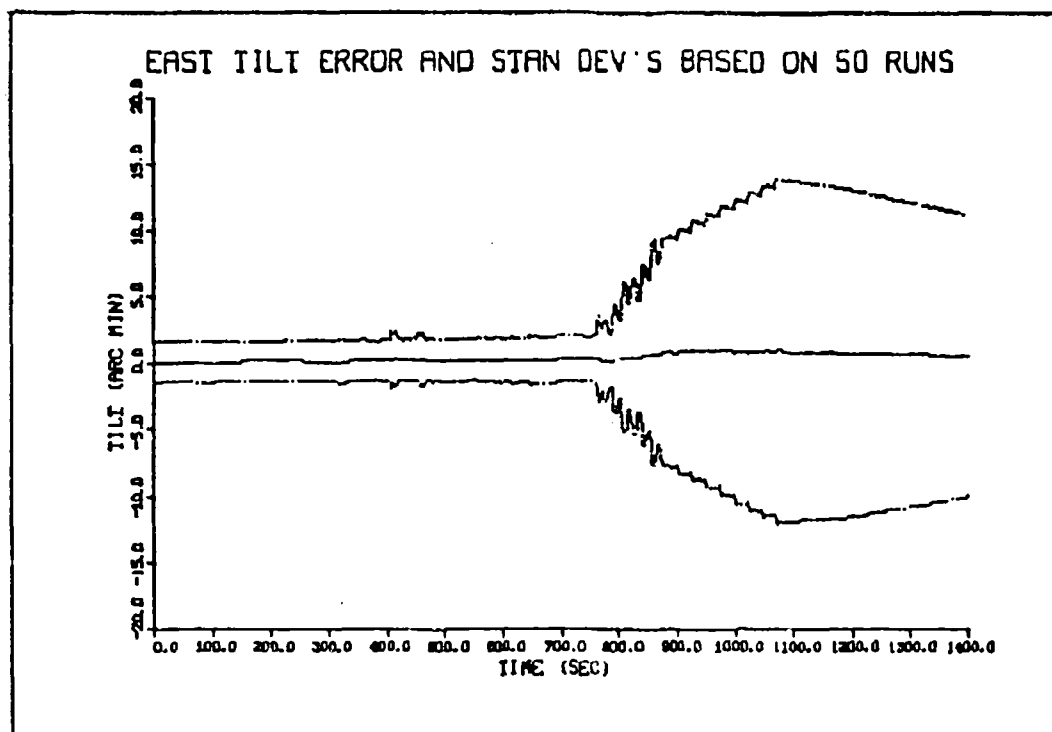


Figure 19. Mean and Standard Deviations from 50 Runs

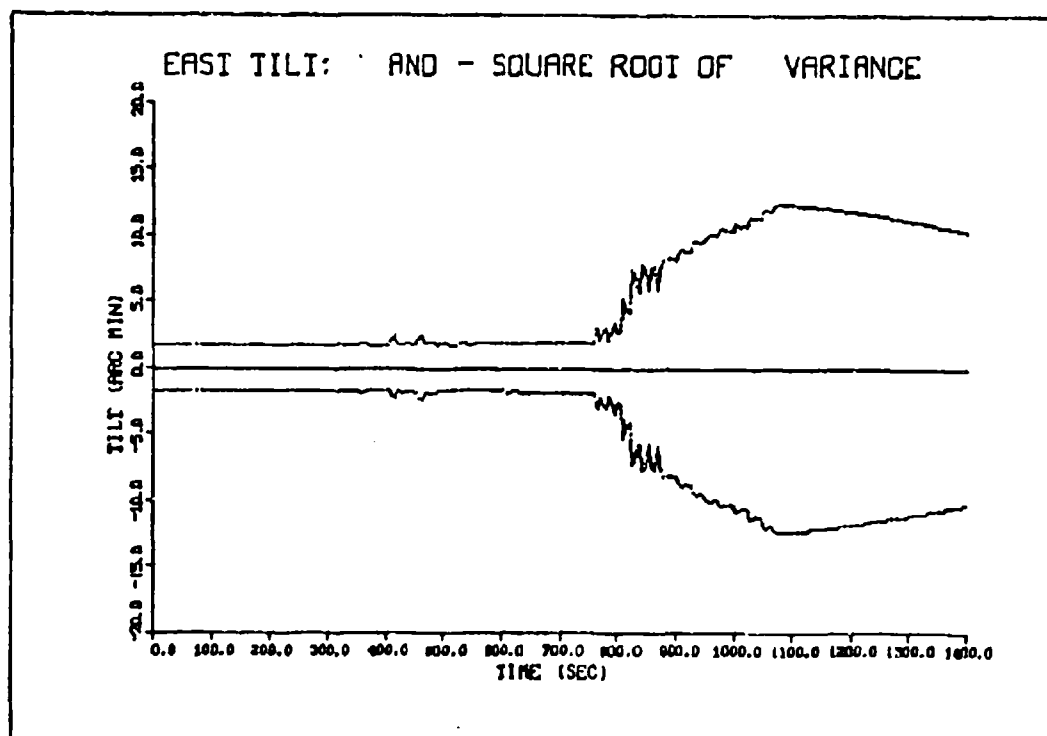


Figure 20. Square Root of Variance

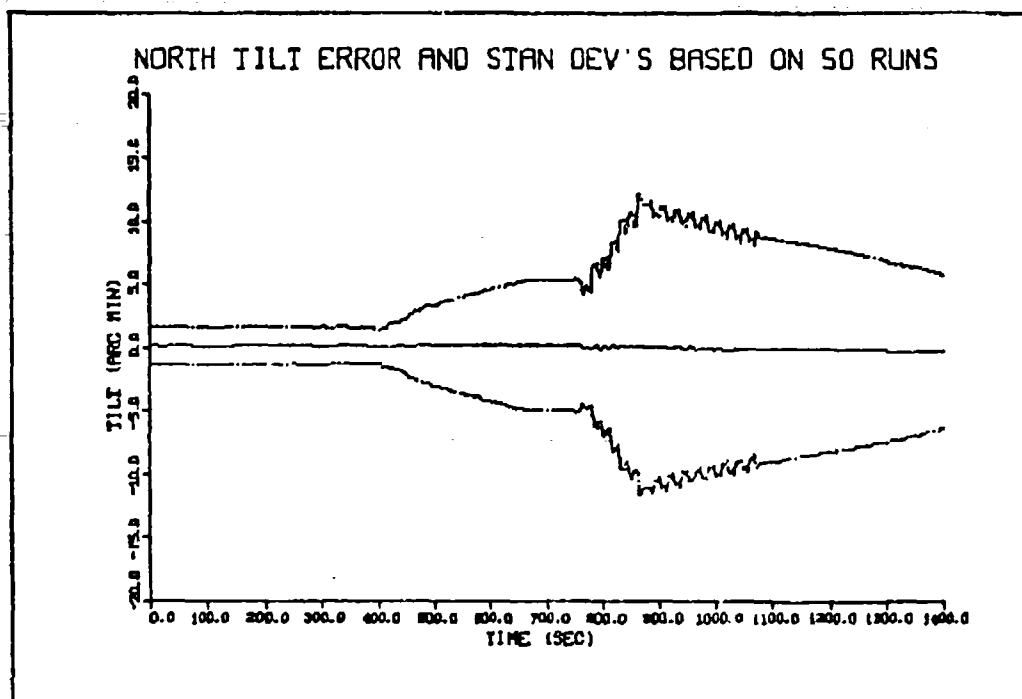


Figure 21. Mean and Standard Deviations from 50 Runs

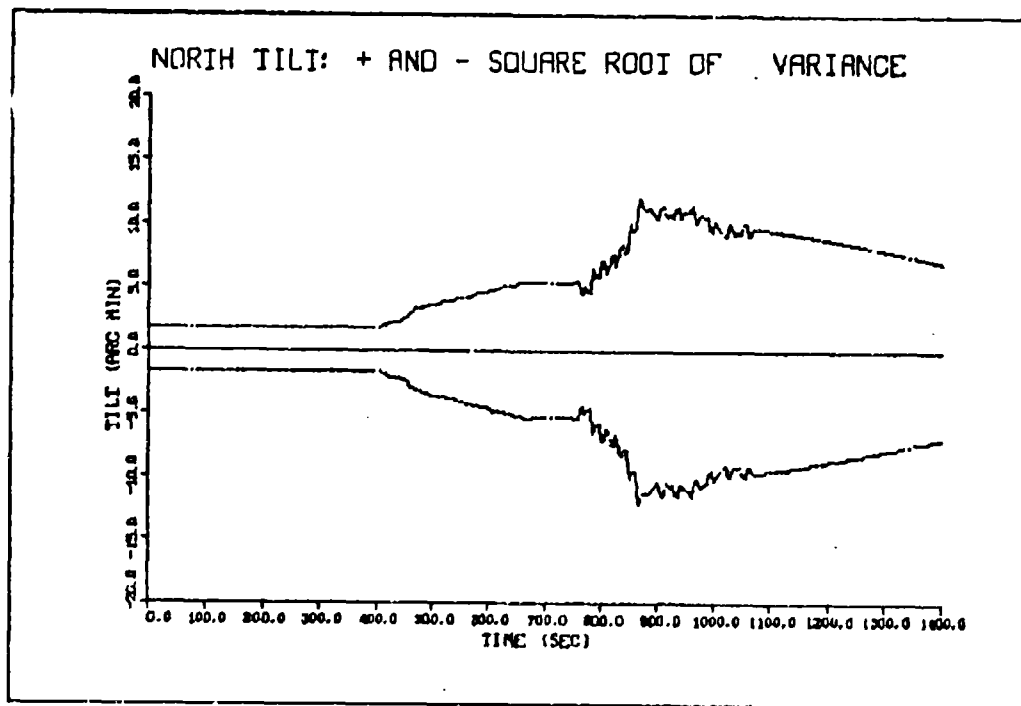


Figure 22. Square Root of Variance

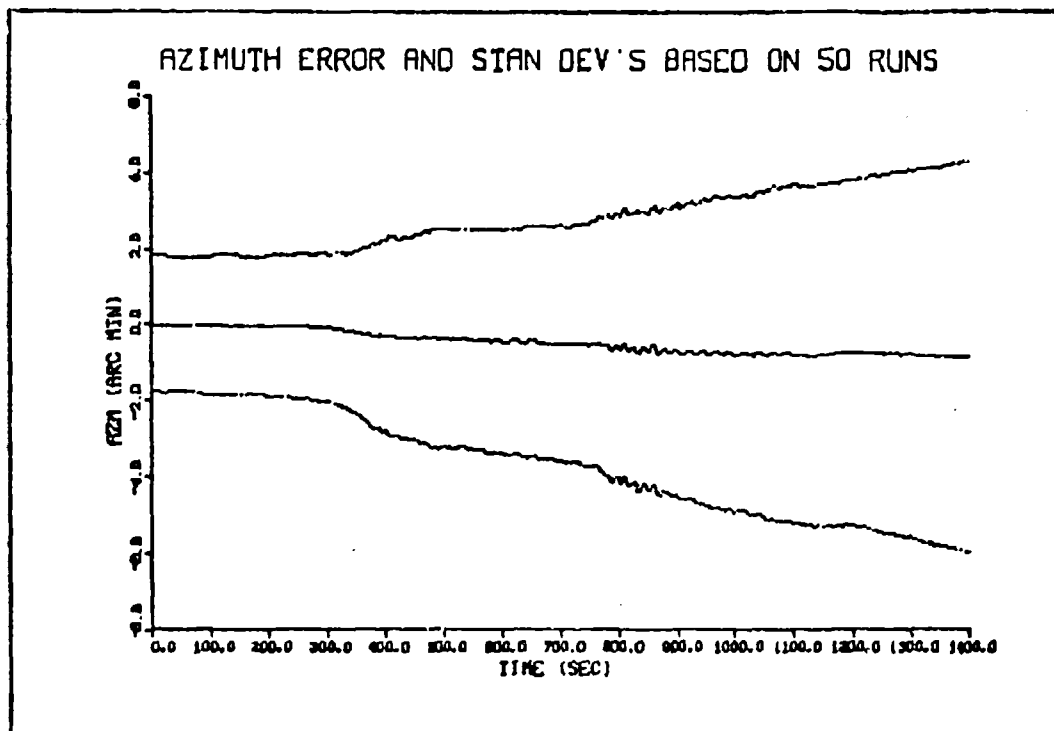


Figure 23. Mean and Standard Deviations from 50 Runs

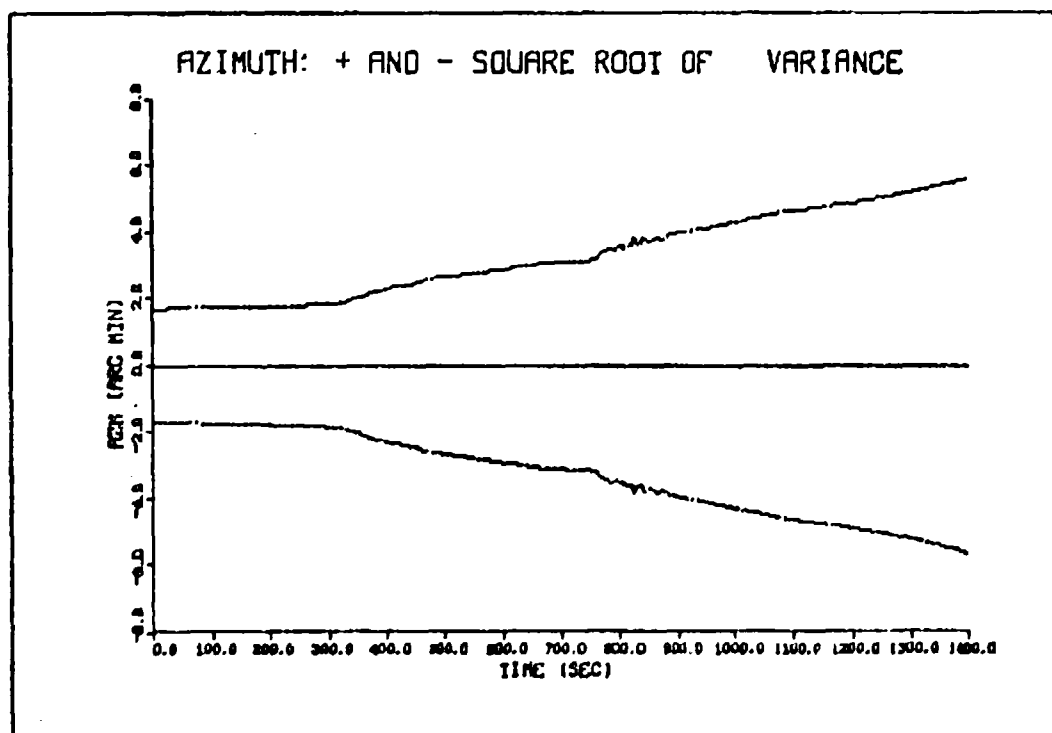


Figure 24. Square Root of Variance

method with fewer than 50 runs to set up the problems and obtain preliminary data. Also, more information is available using the truth model since, not only standard deviations, but ensemble averages of the error states can be computed. Finally, the nonlinear gyro scale factor error could be implemented in a direct fashion in the truth model, but would be difficult to account for in the covariance matrix of the filter model. Therefore, the Monte Carlo simulation method using the truth model was chosen to be used in the error analysis.

Number of Monte Carlo Runs

It is desired to keep the number of Monte Carlo runs as small as possible, but still obtain meaningful results. For problem setup and debugging one run is sufficient, but the data generated has little value since it is just one sample from a random process. Using the same F4 trajectory as in the previous comparison, the number of Monte Carlo runs was decreased from 50 to 20 runs. Two of these plots, vertical velocity and azimuth error, are shown in Figures 25 and 26. Comparing these plots, respectively, to those in Figures 17 and 23 shows some deviations, but major trends are still very much the same. Plots of the other error states show even less variation between the 50 run and the 20 run simulation. Therefore 20 run Monte Carlo simulations will be used for preliminary analysis with the number of simulations being increased to 50 for finer detail and final analysis.

Baro-Inertial Gains

One portion of the simulation program still remains to be investigated. In the development of the baro-inertial aiding equations for the vertical channel in Section II, the values of the gains K_1 , K_2 , and K_3 were arbitrarily chosen equal to magnitudes previously used in the

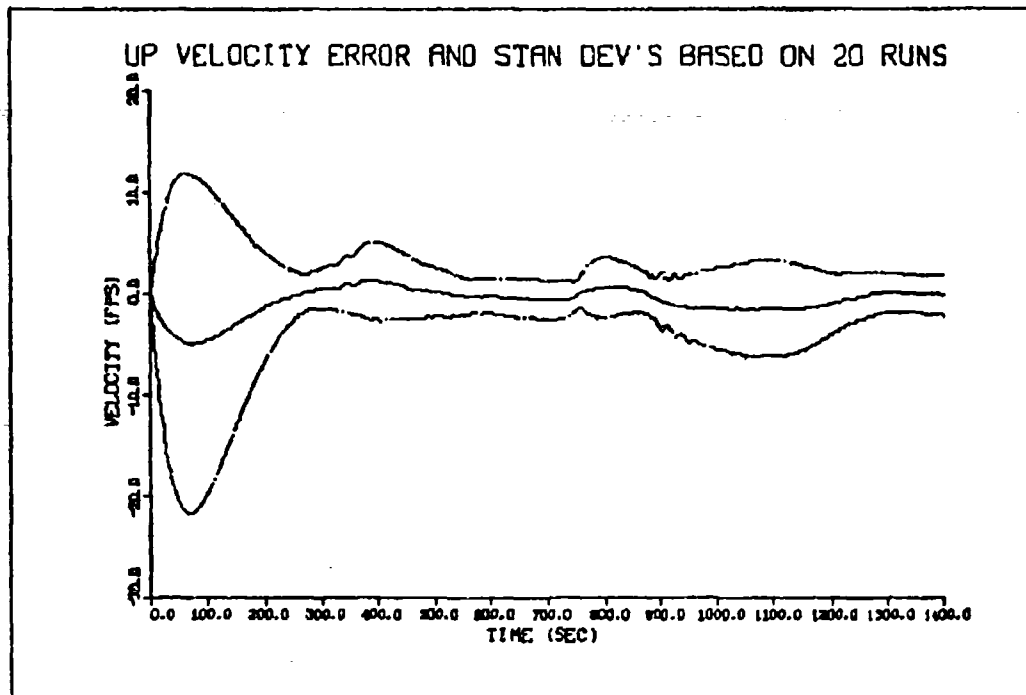


Figure 25. Mean and Standard Deviations from 20 Runs

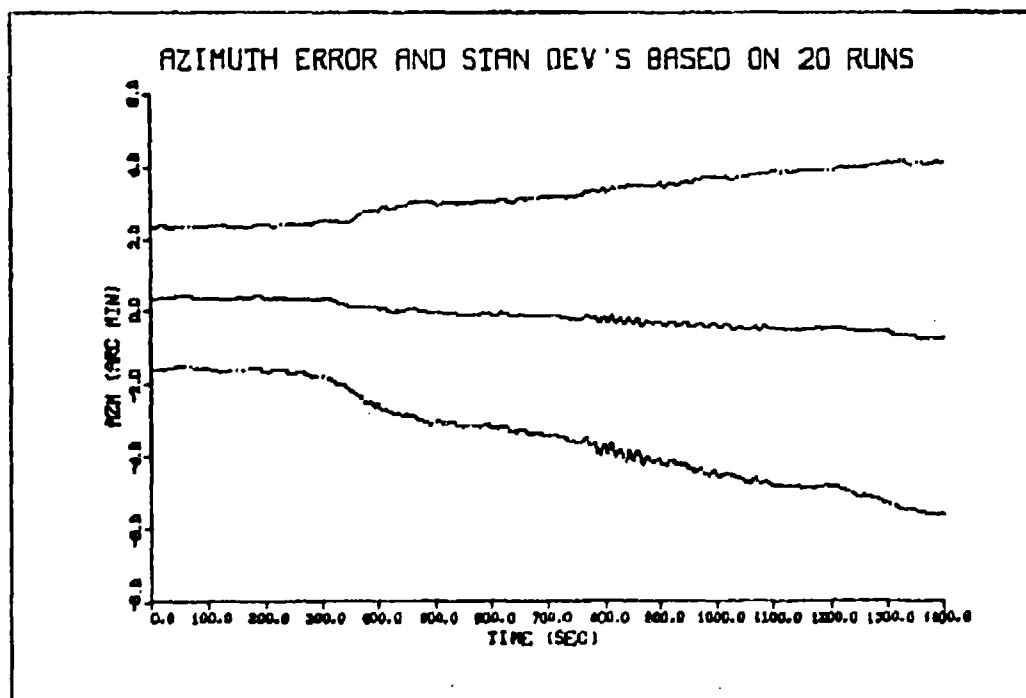


Figure 26. Mean and Standard Deviations from 20 Runs

Litton CAINS navigator (Ref 17). Referring to Figures 11 and 17, altitude and vertical velocity error, it is seen these values of gain did produce a stable vertical channel: the primary requirement of the barometric altitude aiding.

It was proposed in Reference 18 that optimizing techniques could be used to determine gains such that altitude changes could be tracked more closely. The problem encountered in applying these techniques is that the gains depend upon the strengths of the noises present in the system. Therefore, the best results would be obtained by optimizing the gains individually for each different inertial reference system. A set of gains proposed in Reference 18 for a typical inertial reference system is

$$\begin{aligned} K_1 &= 1.003 \text{ sec}^{-1} \\ K_2 &= 4.17 \times 10^{-3} \text{ sec}^{-2} \\ K_3 &= 4.39 \times 10^{-6} \text{ sec}^{-3} \end{aligned} \quad (35)$$

These values were inserted in the simulation and flown over the same F4 trajectory that was used previously. Altitude and vertical velocity errors from a 50 run Monte Carlo simulation are shown in Figures 27 and 28 respectively. Comparing these to Figures 11 and 17 shows a smaller standard deviation of the error using the gains in Equation (35). However, the new values of gains also introduce a higher frequency component in variation of the error. This higher frequency requires a smaller step size in the fifth order integrator that propagates the simulation and results in considerably longer computer run times. Although Figure 27 and 28 represented an improvement in the system error, there was no detectable difference between the corresponding plots of the

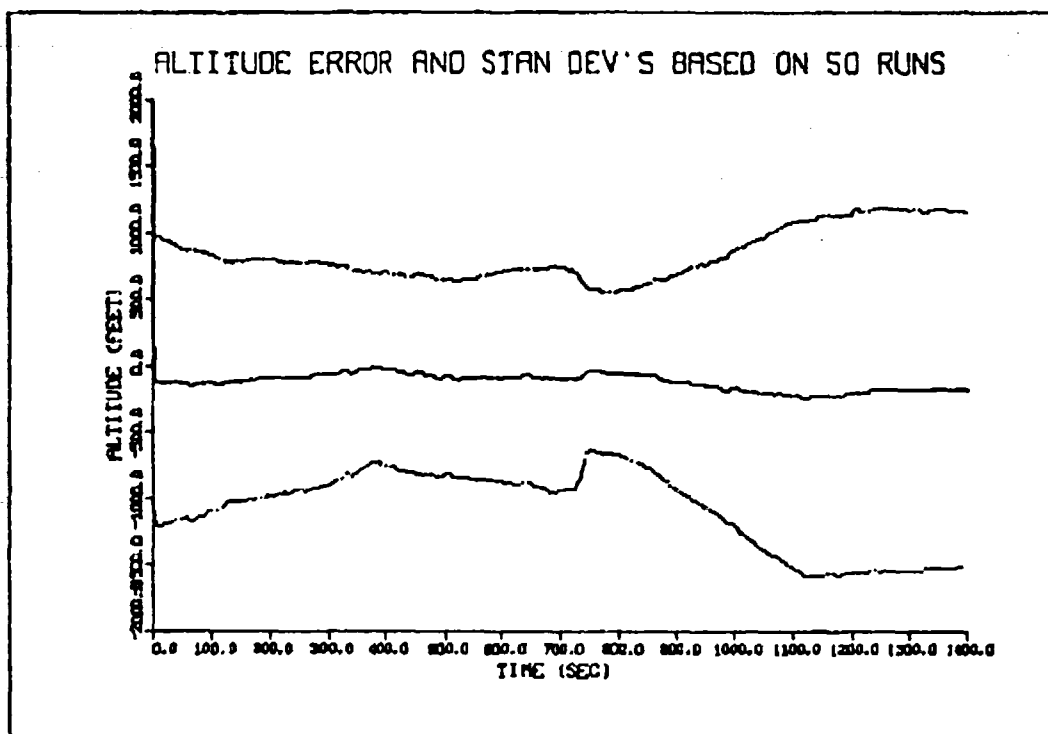


Figure 27. Altitude error using gains in Equation (35)

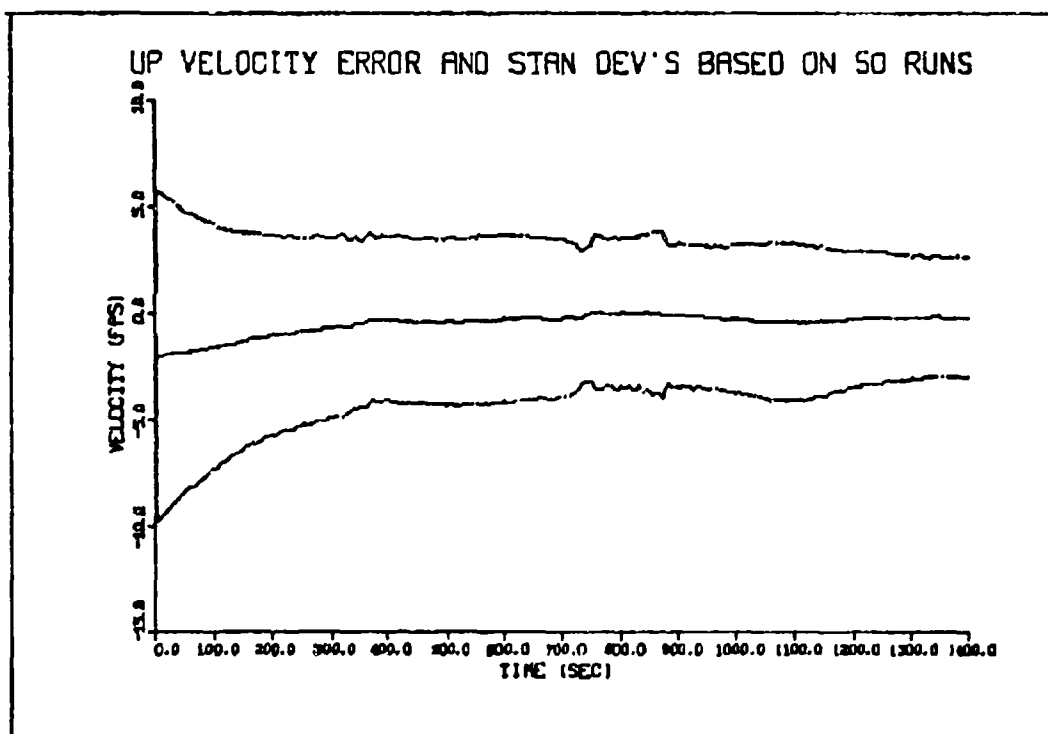


Figure 28. Up velocity error using gains in Equation (35)

other error states. Therefore, in an effort to minimize computer run time, the original gains will be used in the baro-inertial altitude aiding equations.

State-of-the-Art Error Model

The basic structure of the inertial reference system error model was developed and verified using older generation linear models of the sensors. One of the objects of this was to provide a baseline such that the improved sensors should show better error characteristics in the simulation. To verify this assertion, the state-of-the-art error model developed in Section II was driven by the same F4 trajectory used previously. The plots displayed in Figures 29 through 37 show that the standard deviations of the error states are significantly less than those in Figures 7 through 23.

In the development of the gyro scale factor nonlinearity, the peak error contribution was scaled to match empirical scale factor linearity data. The relative values of the scale factor nonlinearity and the other errors in the model suggest that the nonlinearity is not a major source of error. This was verified by using the same flight profile with a linear gyro scale factor. As expected, the ensemble average of the error states is essentially the same in each case. Since Figures 29 and 31 showed a slight tendency to deviate from a zero mean, the corresponding plots for the linear scale factor were selected and are shown in Figures 38 and 39. The results of not scaling down the original nonlinear describing function are shown in Figures 40 and 41. In both the longitude and east velocity plots shown, the ensemble averages diverge considerably from a zero mean value resulting in the nonlinearity being the dominant error source for the inertial reference system.

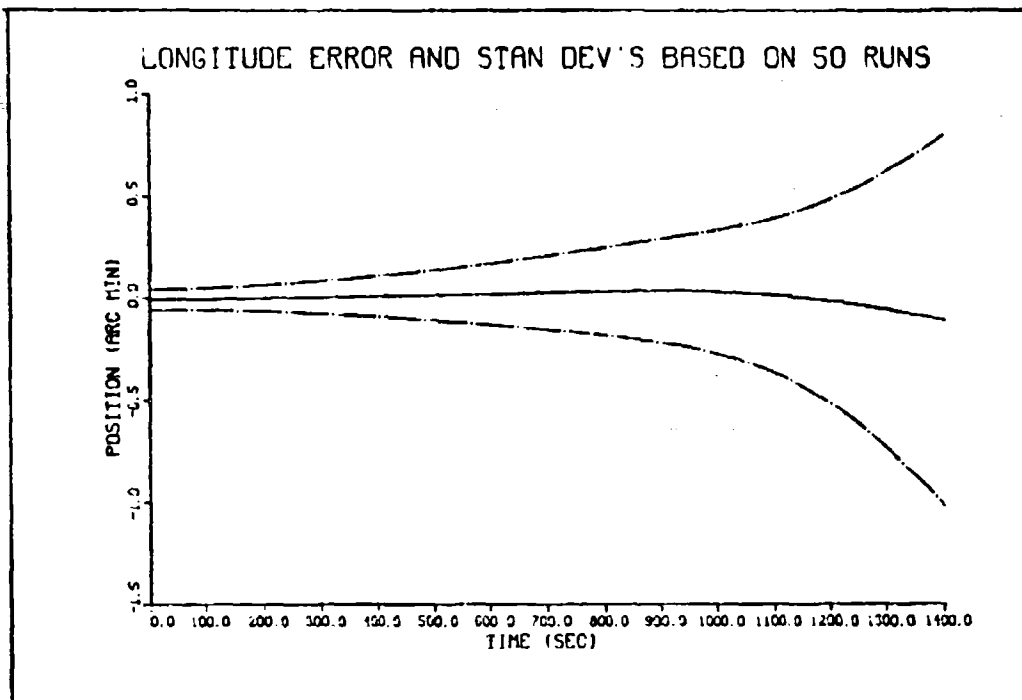


Figure 29. Error from F4 trajectory

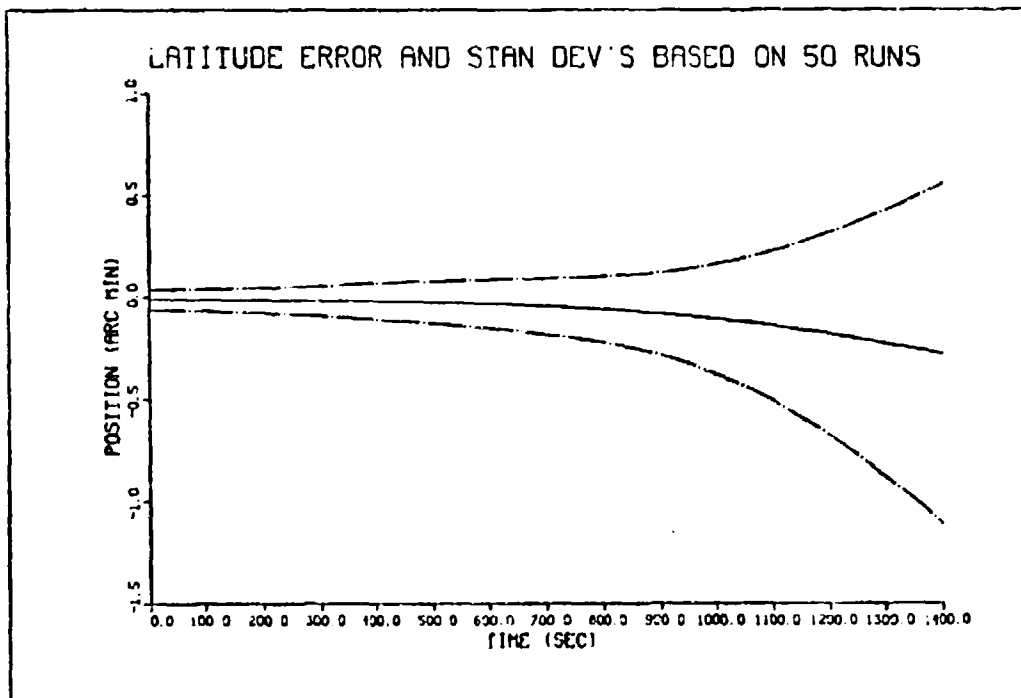


Figure 30. Error from F4 trajectory

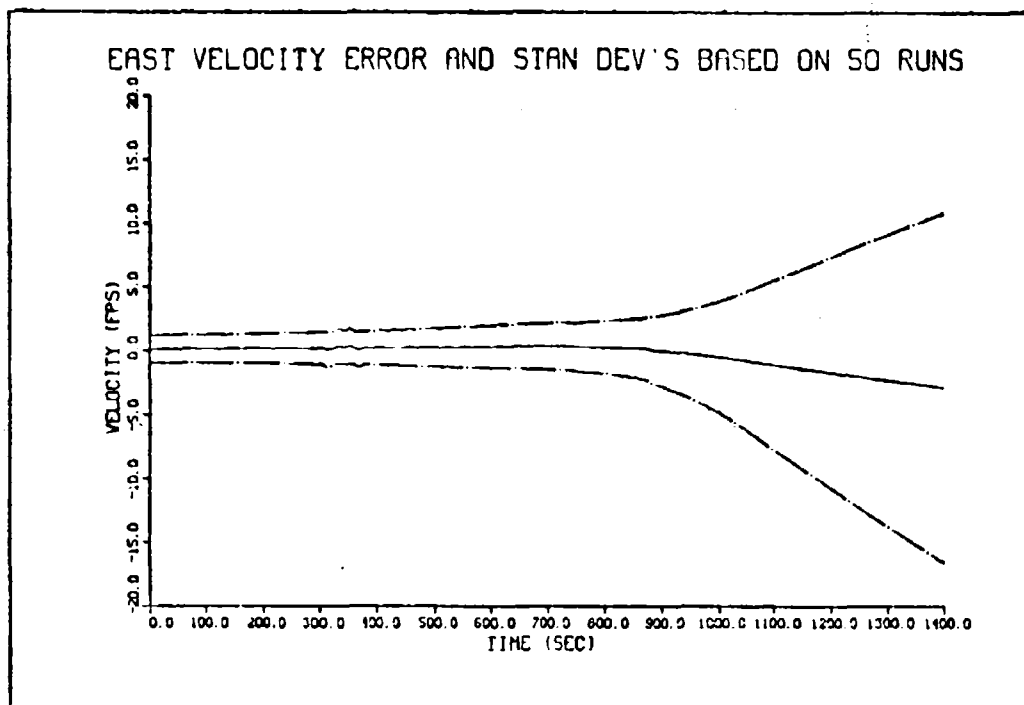


Figure 31. Error from F4 trajectory

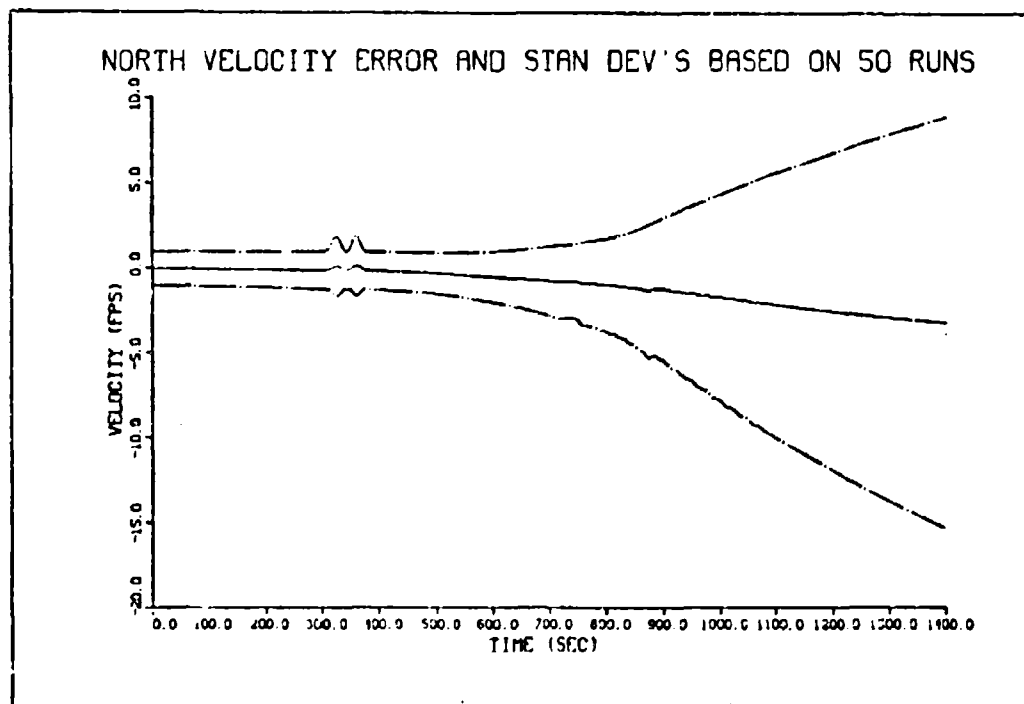


Figure 32. Error from F4 trajectory

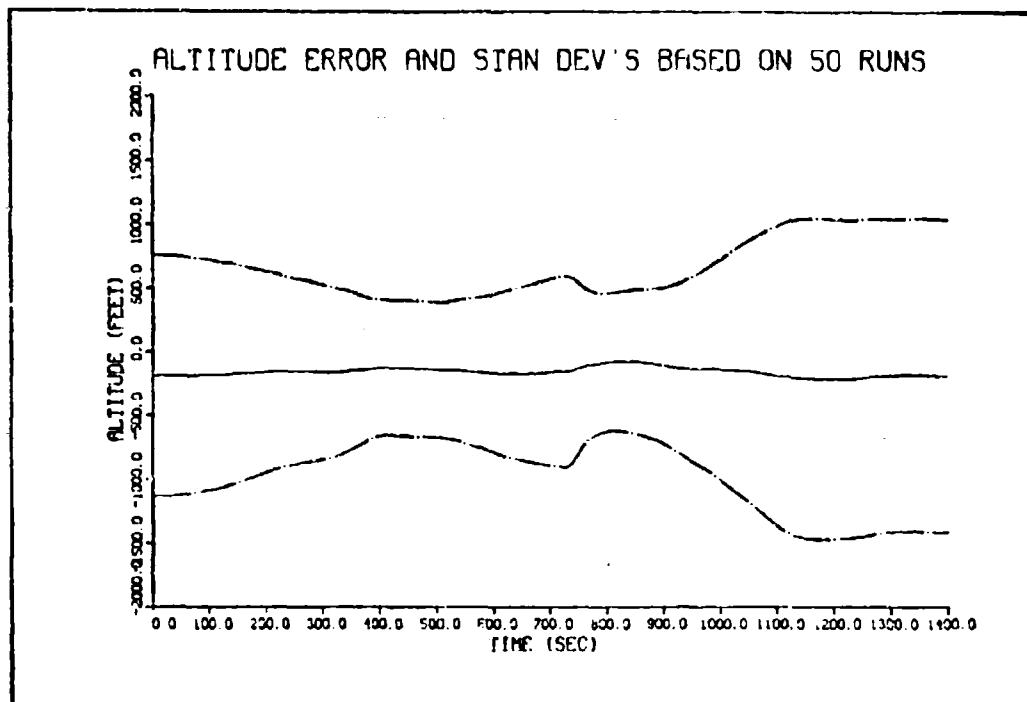


Figure 33. Error from F4 trajectory

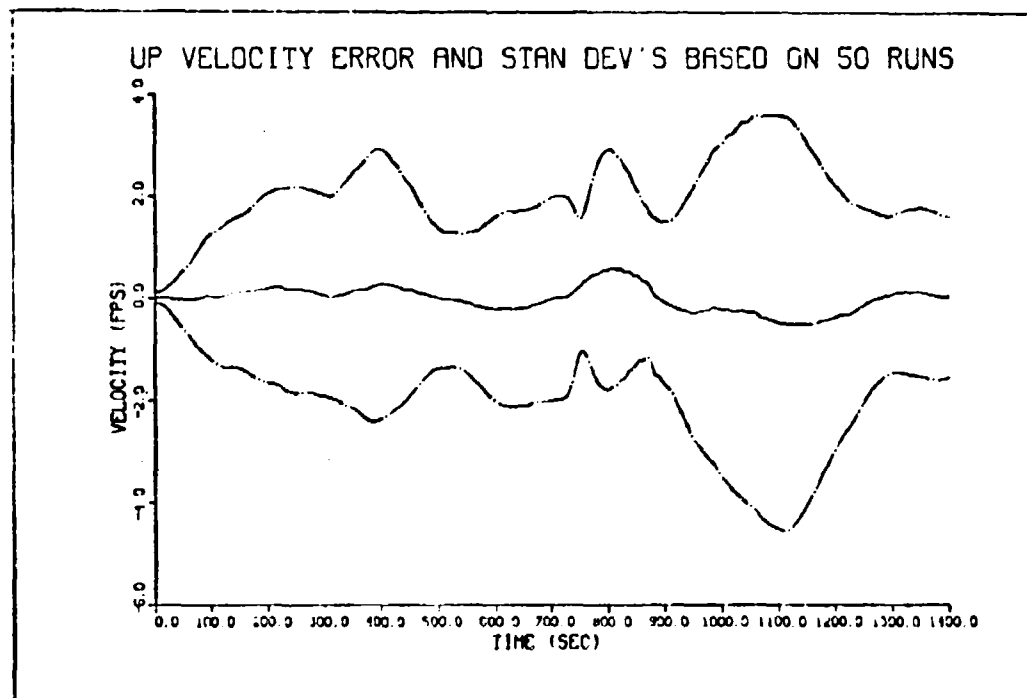


Figure 34. Error from F4 trajectory

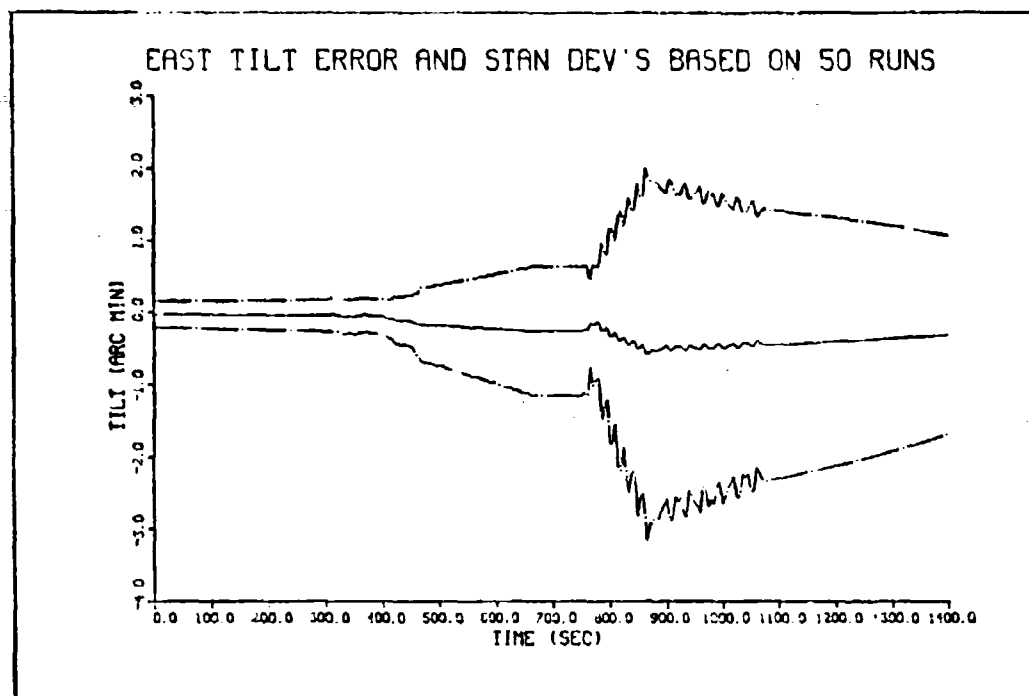


Figure 35. Error from F4 trajectory

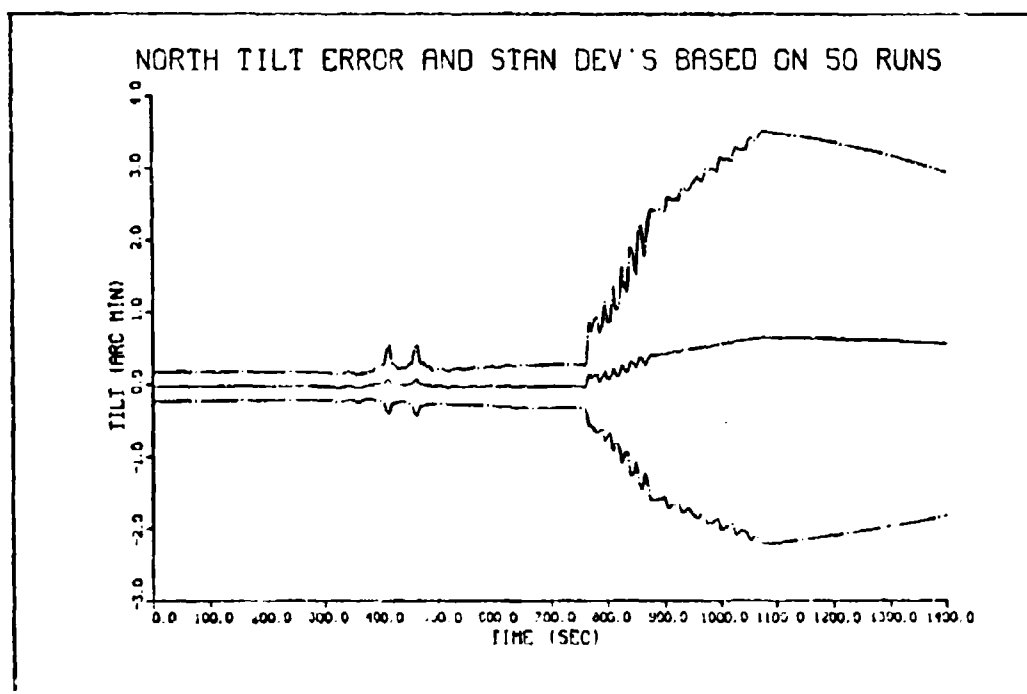


Figure 36. Error from F4 trajectory

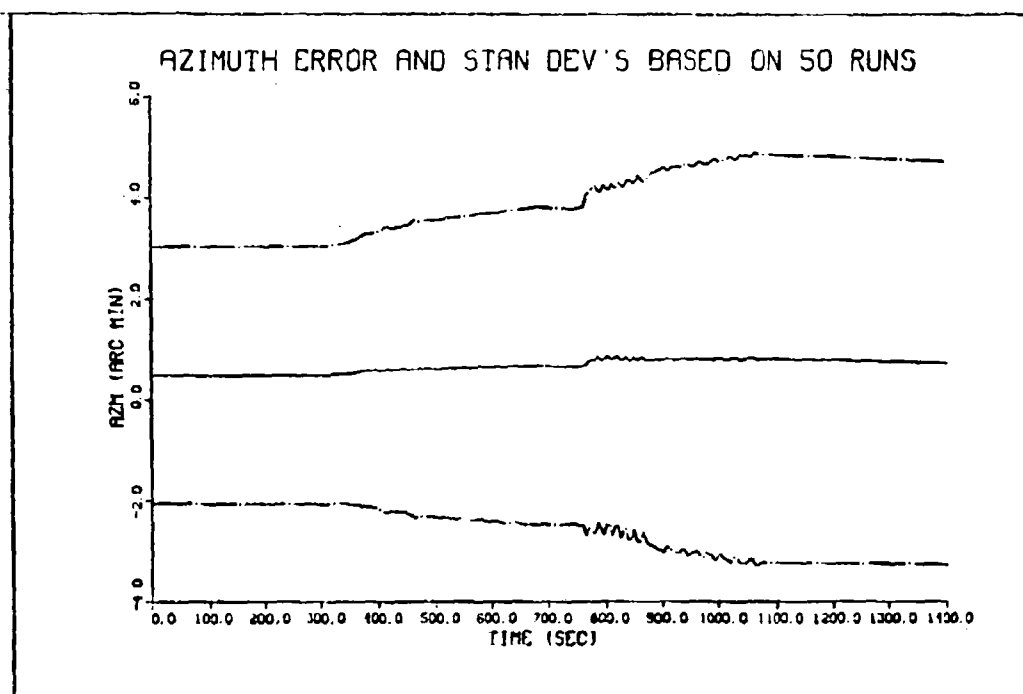


Figure 37. Error from F4 trajectory

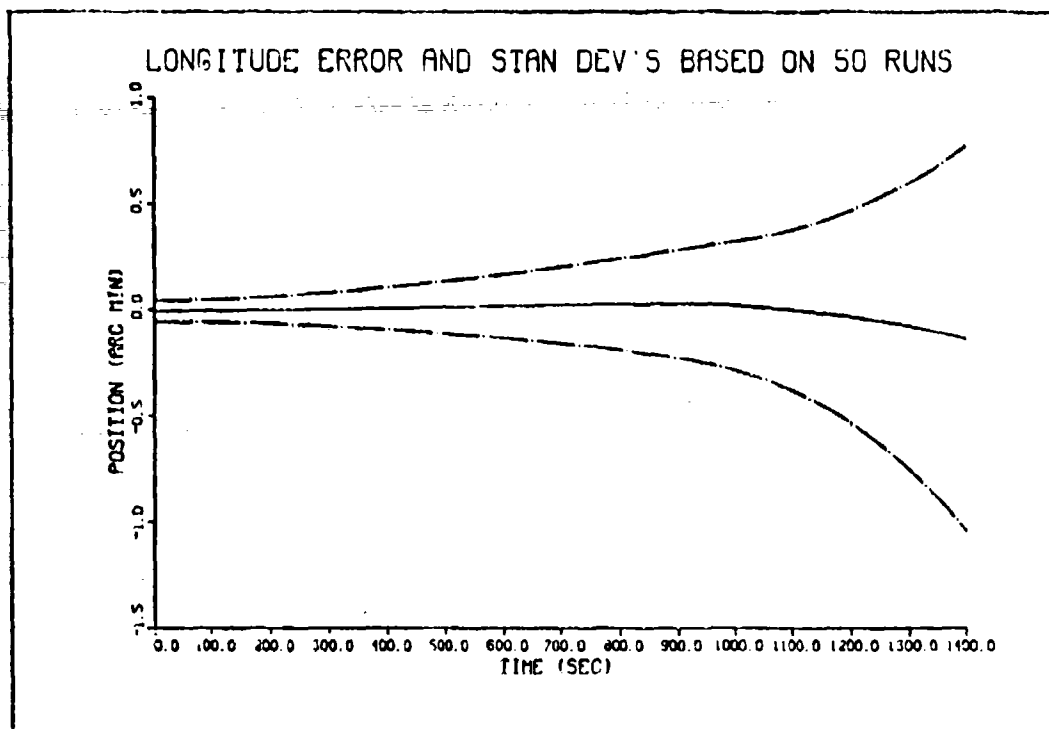


Figure 38. Error with linear gyro scale factor

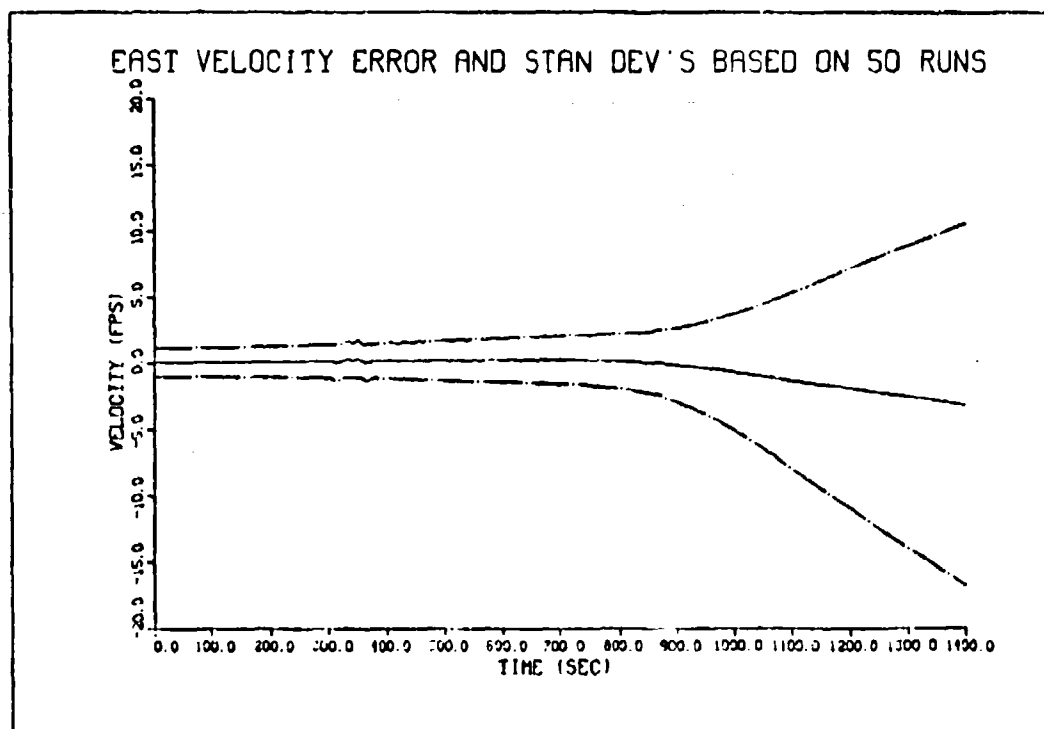


Figure 39. Error with linear gyro scale factor

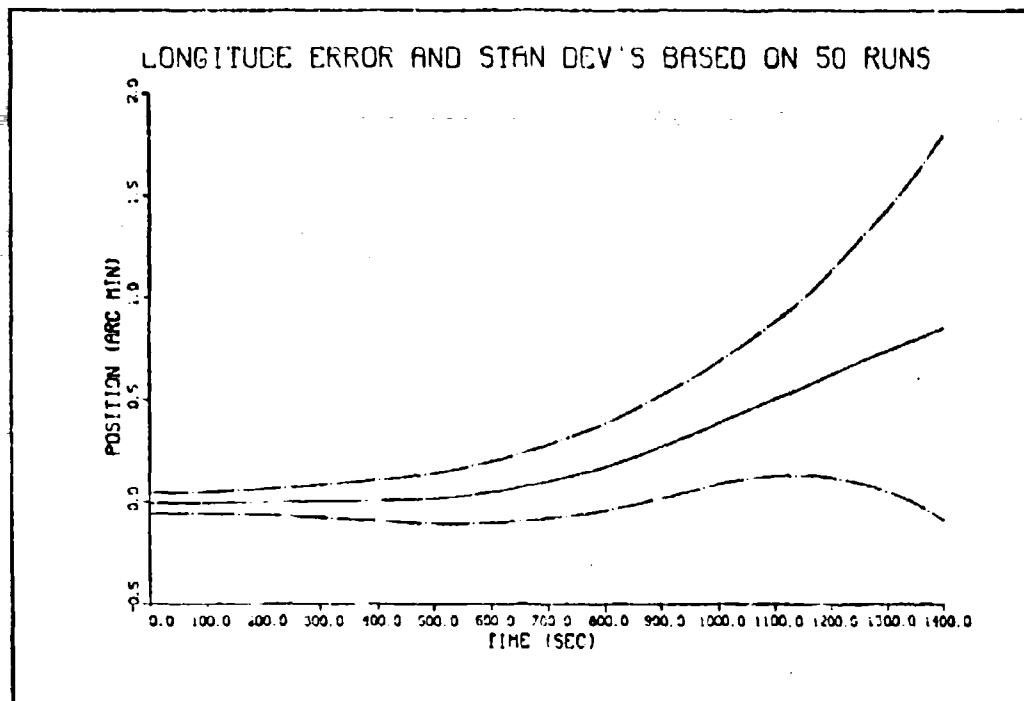


Figure 40. Error from large scale factor nonlinearity

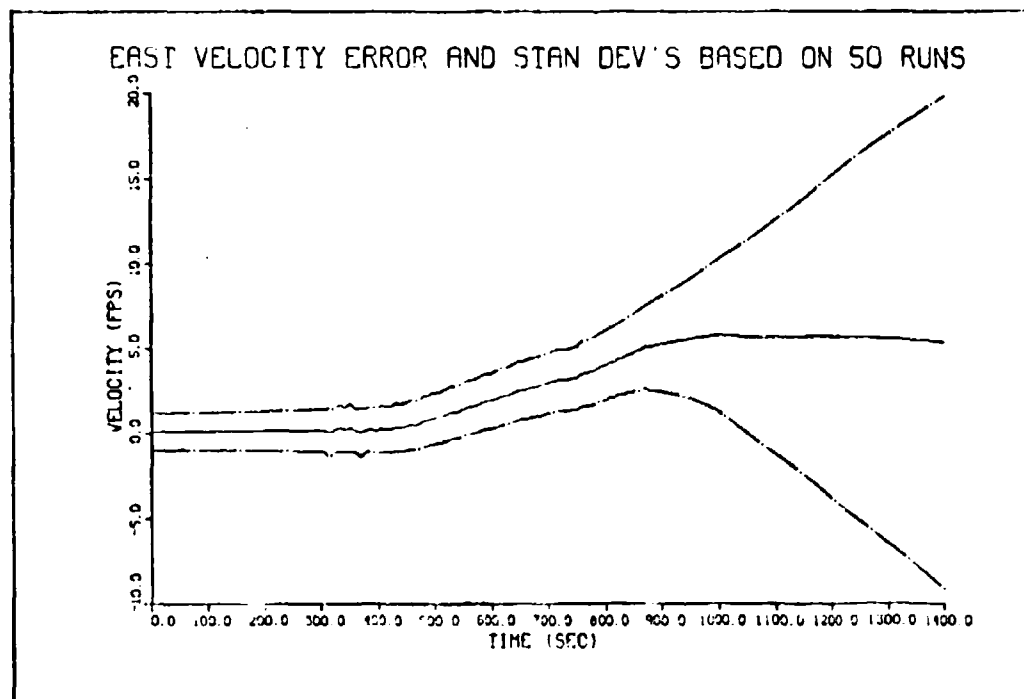


Figure 41. Error from large scale factor nonlinearity

V. Flight Profiles

The objective of the flight profile development is to provide a highly dynamic environment for the inertial sensors so that the resulting reference system errors can be studied. Air to air combat appears to be one of the most dynamic environments for an aircraft; therefore, the flight profiles will be based on that type of scenario. The approach will be, not to develop specific combat maneuvers, but to subject the sensors to loads typical of these maneuvers.

Two types of dynamic flight profiles will be developed initially. A "training" mission will be developed containing both highly dynamic and sinusoidal maneuvers. This will follow the development of a "combat" mission with more severe dynamic maneuvers and less sinusoidal content. The system errors generated by these two flight profiles will be the basis of the subsequent error analysis.

Performance

The F15 was chosen to represent today's air superiority fighter aircraft and to be the basis for the construction of flight profiles. The data in Table 12 was developed as a guideline for performance from many sources (Ref 11, 16). This table was compiled to represent maximum performance for a fighter in an air superiority role and will be used as the upper limit in the flight profile development.

Also, as an aid in constructing flight profiles, data was extracted from a tape of an F15 air-to-air combat engagement flown during aircraft combat evaluation tests (ACEVAL) at Nellis AFB in 1977 (Ref 11).

In addition to aircraft performance, the pilot's ability to sustain high accelerations must also be considered. This data was developed by the Aerospace Medical Research Laboratory and made available by

Performance	Maximum Value
Nominal Roll Rate	225 deg/sec
Roll Time Constant	0.5 sec
Forward Acceleration	1 g
Positive Turn Acceleration	7.5 g
Negative Turn Acceleration	3 g
Altitude	60,000 ft
Speed	Mach 2.5
Range	350 nm radius

Table 12. Representative Fighter Maximum Performance

Capt Robert A. Mercier (Ref 10). The average acceleration that a typical pilot can sustain while performing combat maneuvers is plotted in Figure 42. Average g's is determined by the equation

$$\text{Average g's} = \frac{\text{Accumulated g's} \times \text{Time Held}}{\text{Time in Combat}} \quad (36)$$

The pilot retains full capacity when below the lower line of the plot and passes out if average maneuver acceleration falls above the upper line. The flight profiles developed for this simulation were designed to be near the top line in the "combat" mission case and more toward the bottom line for the "training" mission.

Combat Flight Profile

The "combat" flight profile, shown in Figures 43 through 47, simulates the highly dynamic loads present during air to air combat. To conserve computer time, the mission was compressed to fifteen minutes from takeoff to landing. Each of the 50 maneuvers planned for this mission are listed in Table 13. In the table, time is specified in seconds from the start of the mission. Acceleration is divided into acceleration along the path of the flight and acceleration, generated by maneuvers, which is tangential to the flight path.

The mission starts at 38 degrees north latitude, 75 degrees west longitude, at an altitude of 200 feet. From this point the aircraft initiates a maximum performance climb up to a cruise altitude of 30,000 feet. After level off, the aircraft accelerates to supersonic airspeed and dashes toward the point of interception. The pilot looks down by performing a 45 degree roll, followed by a descent to 10,000 feet. Highly dynamic combat maneuvers are simulated at this point by

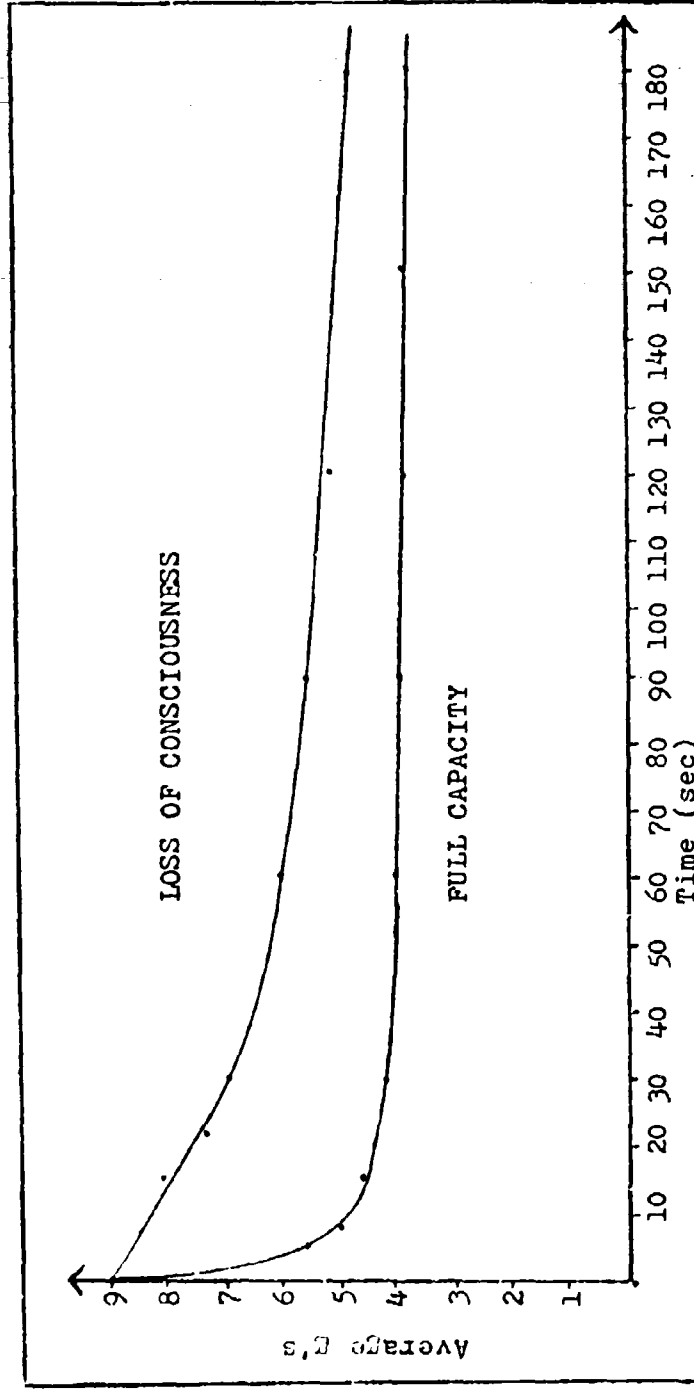


Figure 42. Acceleration tolerance during combat

Latitude/Longitude Flight Profile

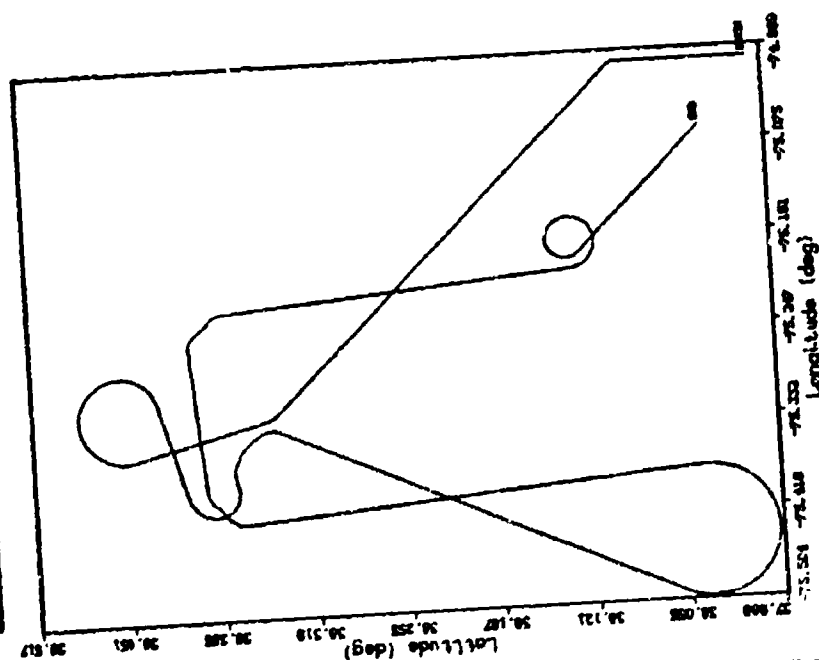


Figure 43. Combat flight profile

Altitude Flight Profile

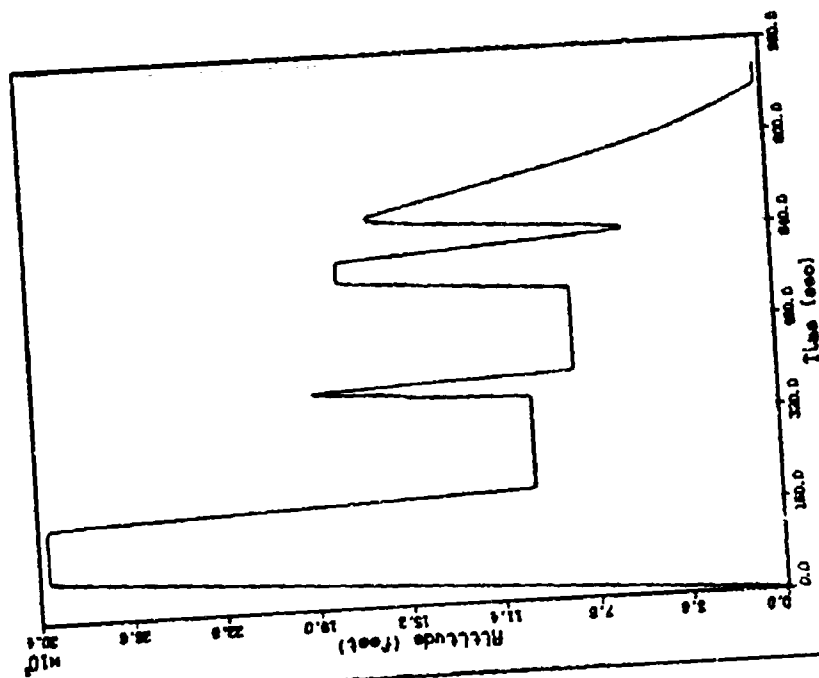


Figure 44. Combat flight profile

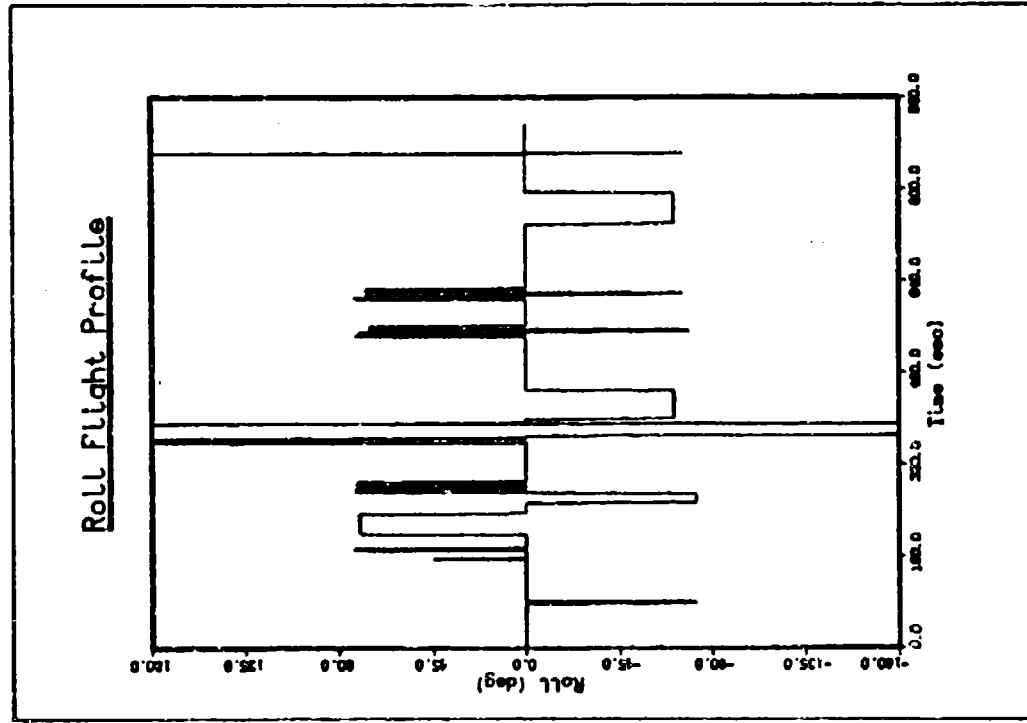


Figure 45. Combat flight profile

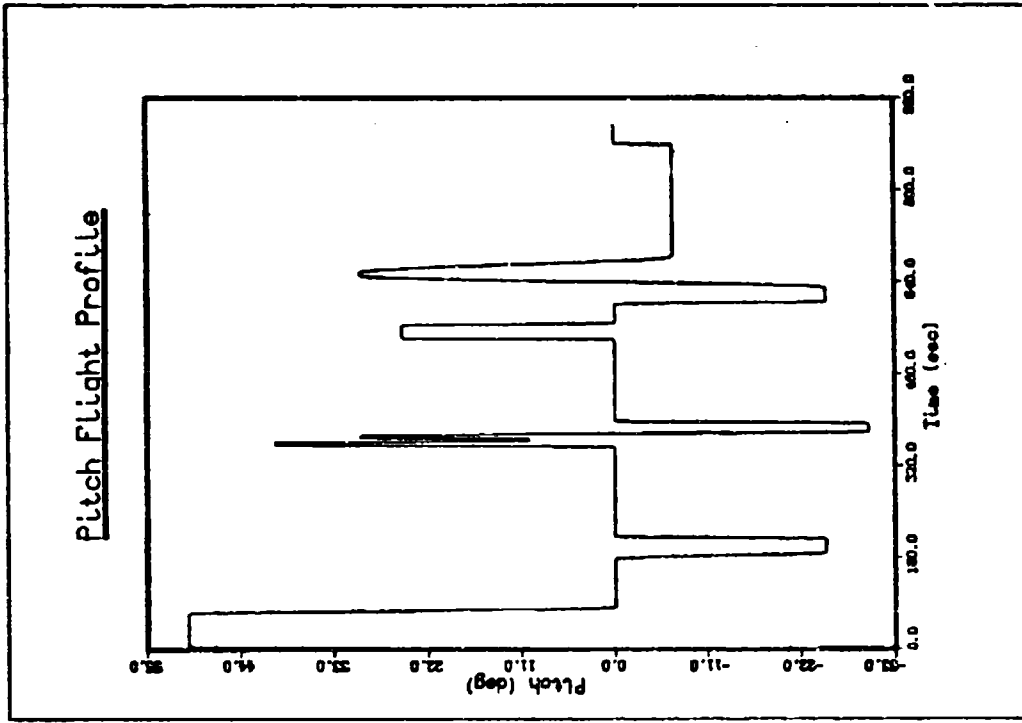


Figure 46. Combat flight profile

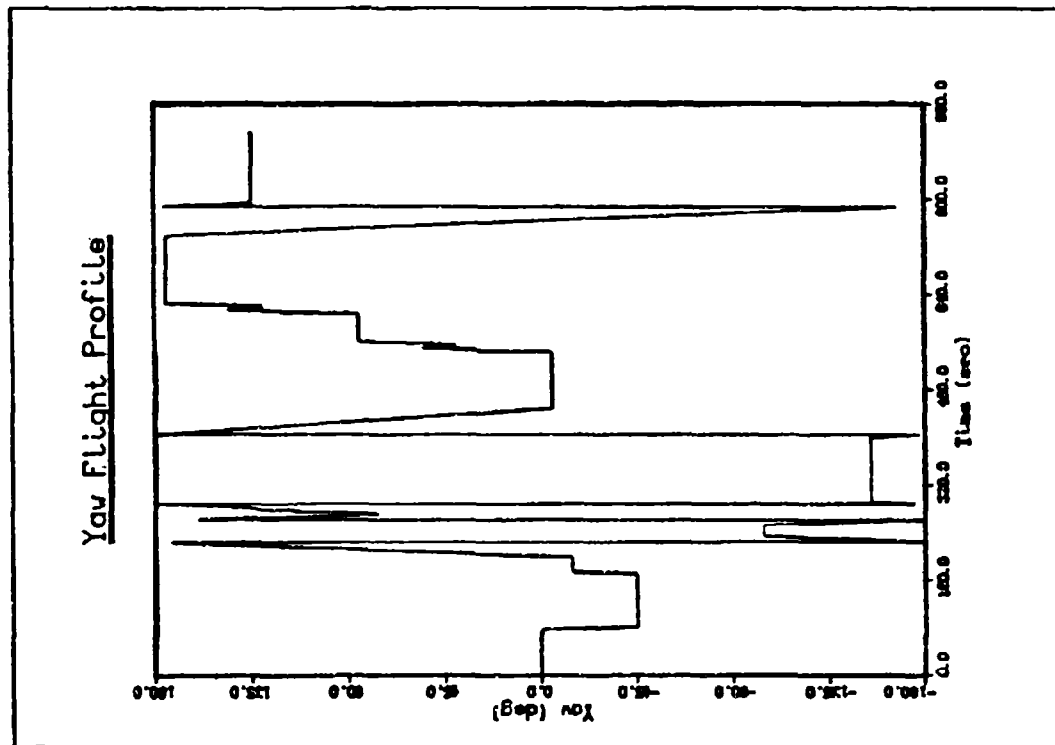


Figure 47. Combat flight profile

Segment	Time	Maneuver	Degrees	Tangent g's	Path g's
1	0.0	Pitch	50.3	7.33	0
2	5.0	Straight	0	0	0
3	61.77	Pitch	-50.3	3	0.3
4	76.77	Turn	-45	7.33	0.4
5	81.77	Straight	0	0	1.0
6	104.1	Straight	0	0	0
7	154	Roll	45	0	0
8	155	Roll	-45	0	0
9	156	Pitch	-25	3	0
10	169	Turn	30	7.33	0
11	174	Straight	0	0	0
12	190.86	Pitch	25	7.33	0
13	197	Turn	270	6	-0.1
14	252	Turn	-180	7.33	-0.3
15	271	Turn	40	7.33	-0.4
16	277	Turn	20	7.33	0
17	281	Turn	10	7.33	0
18	284	Turn	60	7.33	0
19	291	Straight	0	0	0
20	351	Pitch	40	7.33	-0.5
21	357	Roll	180	0	0
22	359	Pitch	30	7.33	0
23	364	Roll	-180	0	0
24	366	Pitch	0	7.33	0
25	369	Roll	-180	0	0

Table 13. Combat Flight Profile

Segment	Time	Maneuver	Degrees	Tangent g's	Path g's
26	371	Pitch	60	7.33	0
27	380	Straight	0	0	1
28	390	Roll	-180	0	0
29	392	Pitch	30	7.33	0
30	398	Turn	-210	3.0	0
31	450.9	Straight	0	0	-0.8
32	538	Pitch	25	6.0	0
33	542	Turn	35	6.5	-0.2
34	547	Turn	25	5.5	-0.2
35	551	Turn	-15	4.5	-0.2
36	555	Turn	45	3.5	0
37	563	Pitch	-25	4	0
38	570	Straight	0	0	0
39	600	Pitch	-25	4	0
40	607	Turn	35	6.5	0
41	611	Turn	25	4	0
42	616	Turn	-15	3.5	0
43	620	Turn	45	4	0
44	628	Pitch	55	2	0
45	652	Straight	0	0	0
46	654	Pitch	-37	1	0
47	686	Straight	0	0	0
48	737.5	Turn	-400	3	-0.111
49	859.5	Roll	360	0	0
50	877.5	Pitch	7	1.5	-0.382

Table 13. (continued)

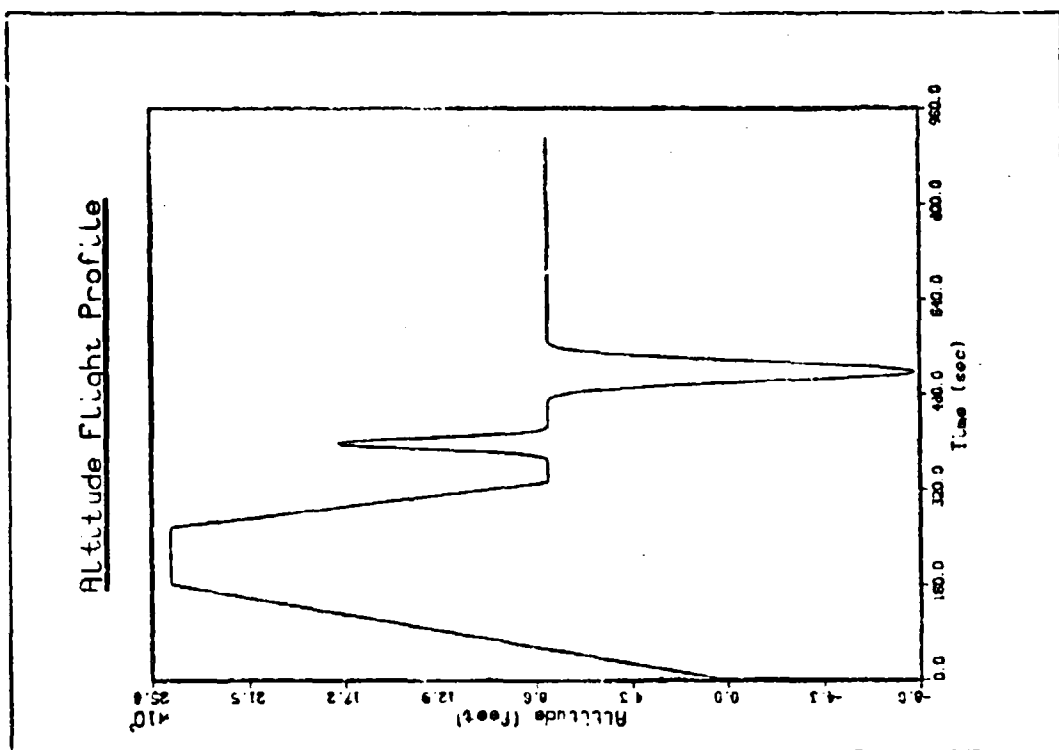
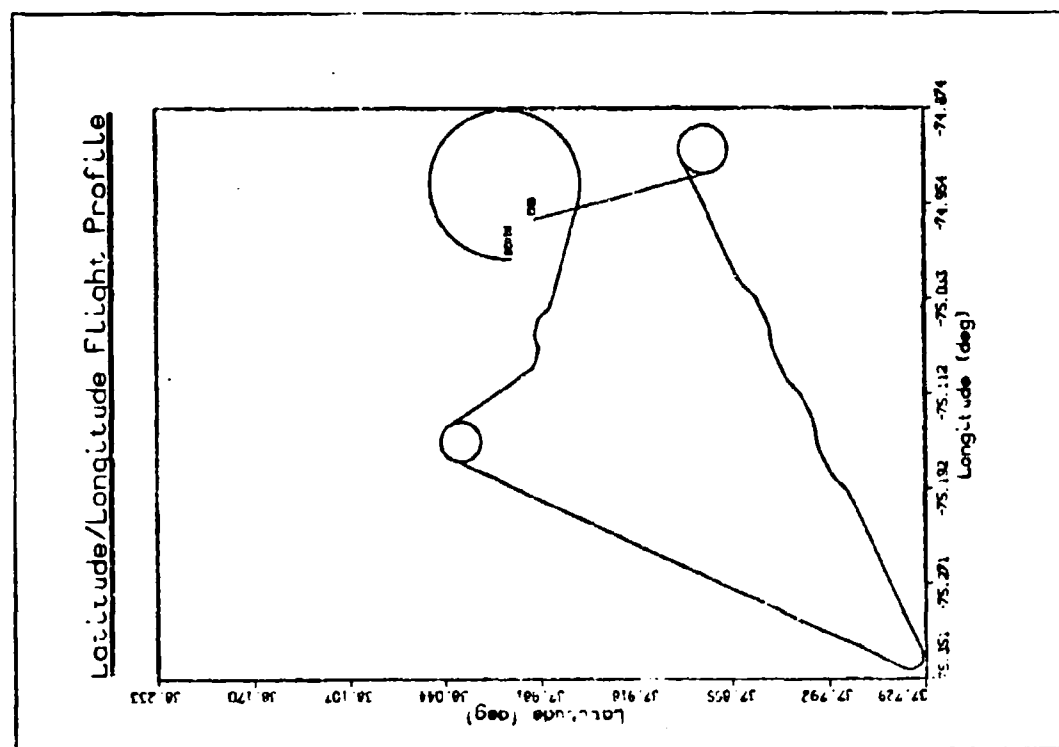
performing an arbitrary series of high acceleration vertical and horizontal turns. This is followed by a gradual descent toward home base which includes the performance of a 360 degree roll and a 400 degree turn. The mission is terminated at zero velocity near the starting point.

It should be noted that although the maximum tangential acceleration is specified the same (7.33 g's) for many maneuvers in Table 13, this is not the acceleration held throughout the turn. All of the turns in PROGEN are coordinated; therefore, tangential acceleration starts at zero with wings level and increases with roll angle until the maximum is reached. Therefore the average tangential acceleration sensed for a small turn at low airspeed would be considerably less than the average for a large turn at high speed, although the same maximum acceleration was specified for each case.

Training Flight Profile

The "training" flight profile, shown in Figures 48 through 52, represents less severe maneuvers with longer durations and more sinusoidal motion. Sinusoidal maneuvers will be performed at arbitrary frequencies to determine, in general, whether errors are compounded or just oscillate. Overall time for this profile, 15 minutes, is the same as the combat profile, but only 20 maneuvers are performed.

The starting point is the same as the combat profile, but in the training mission a gradual climbing turn, at 30 degrees of bank, is made to cruise altitude. This is followed by sine wave maneuvers; and turns, rolls, and loops of 360 degrees or more. Each maneuver is specified in Table 14. The overall errors generated by these large maneuvers will be compared to the overall errors induced by the numerous smaller maneuvers



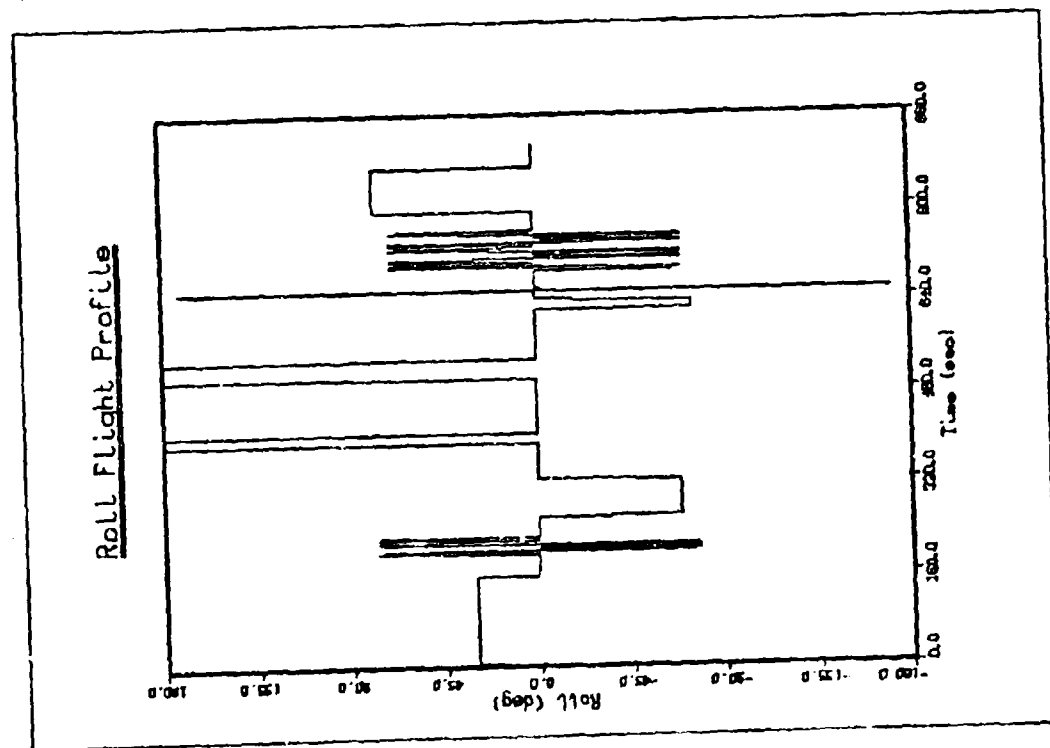


Figure 50. Training flight profile

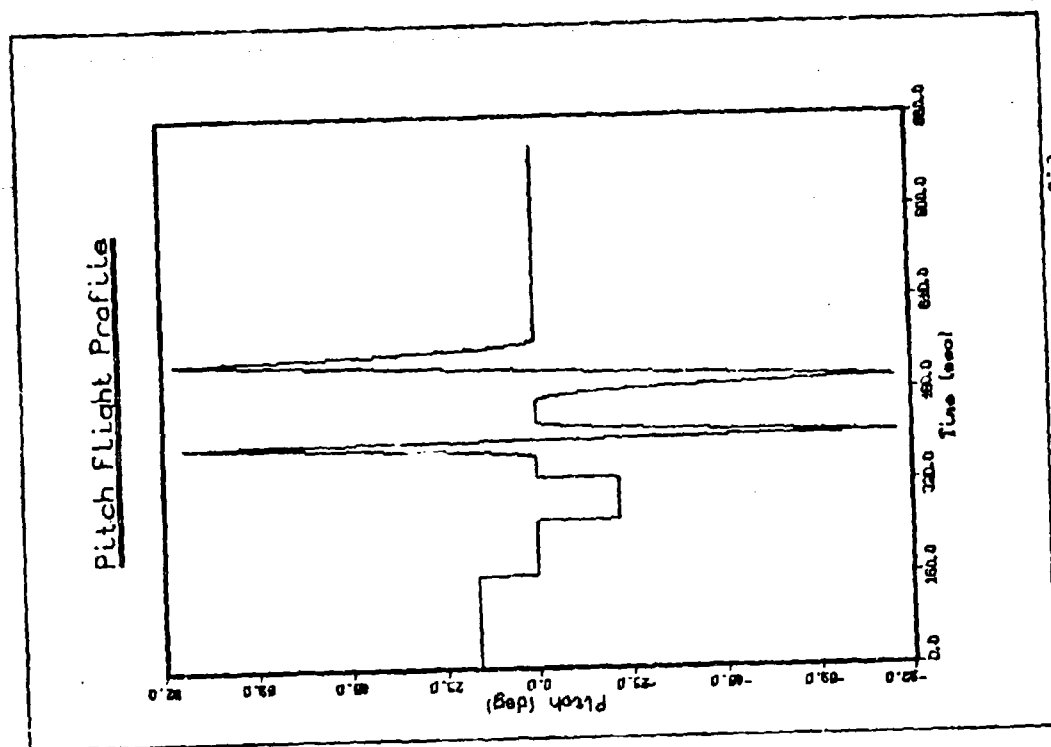


Figure 51. Training flight profile

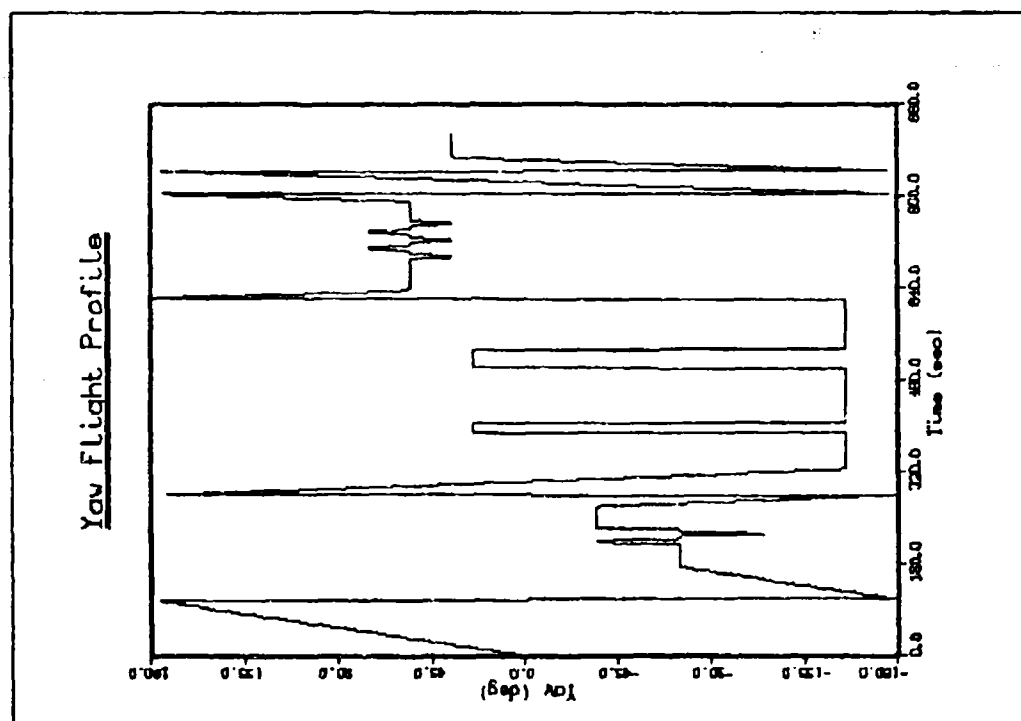


Figure 52. Training flight profile

Segment	Time	Maneuver	Degrees	Tangent g's	Path g's
1	0	Pitch	15	5.5	0.1
2	2	Turn	285	0.577	0
3	158.94	Pitch	-15	2	0.2
4	165	Straight	0	0	0
5	195	Sine	40	1	0
6	225	Straight	0	0	0
7	255	Pitch	-20	3	0.1
8	261	Turn	-480	2.5	0
9	331	Pitch	20	4	-0.2
10	335	Straight	0	0	0
11	365	Pitch	360	3.5	0
12	431	Straight	0	0	0
13	461	Pitch	-360	2	0
14	622	Turn	-140	4	0
15	652	Roll	720	0	0
16	659	Straight	0	0	0.3
17	689	Sine	-20	0	0
18	761	Straight	0	0	0
19	791	Turn	640	4.5	0
20	887	Straight	0	0	0

Table 14. Training Flight Profile

in the other flight profile.

In the development of the previous mission, the flight profile generator, PROFGEN, was found to exceed the aircraft's performance specifications during some maneuvers. This resulted in the modification of PROFGEN so that realistic trajectories could be generated. These changes will also be used here.

As with the combat mission, roll and turn maneuvers are based upon a representative roll time constant; however, the sine maneuver is not. The equation PROFGEN used to compute roll rate, $\dot{\phi}$, is

$$\dot{\phi} = \frac{64.4 v \psi \omega^2 \cos 2\omega t}{(32.2)^2 + (v \psi \omega \sin 2\omega t)^2} \quad (37)$$

where

v = Total Velocity

ψ = Maximum Heading Change

ω = Frequency of Sine Maneuver

At $t = 0$, the start of the sine maneuver, roll rate is

$$\dot{\phi} = 2 v \omega^2 / 32.2$$

which is the maximum value of Equation (37). Therefore, even if ψ and ω were chosen to conform to the aircraft's roll time constant, an unrealistic maneuver is performed since a step increase in the value of roll rate occurs at the beginning of each sine maneuver segment. The step input will have to be taken into consideration in the analysis of the errors induced by the training flight profile.

VI. Error Budget

Each type of error source will be propagated separately over a highly dynamic flight trajectory in order to determine the relative contribution of each kind of the sensor errors to the overall inertial reference system error. The "combat" flight profile will be used for this analysis since it contains more maneuvers with higher acceleration loads than the "training" flight profile. This profile should generate a broader spectrum of system errors by exciting more sensor errors.

The plots of the ensemble averages over 50 Monte Carlo runs of the error states from each error source plus and minus one standard deviation (σ) will be compared to baseline plots obtained from propagating just the initial conditions with no sensor errors. These baseline plots are shown in Figures 53 through 61. Since the initial values of tilt and azimuth errors are functions of many of the sensor errors, these initial conditions will change depending upon the particular error state being analyzed.

In contrast to the system error obtained from just the initial conditions, Figures 62 through 70 are plots of the error standard deviations as a result of the contributions of all of the error sources. These plots were developed based upon a normal long alignment. A shorter alignment, as will be shown in this section, would generate more system error.

The second column of Table 15 represents the percent of error, relative to the error generated by all the error sources, induced into the system by just the initial conditions. This percentage was estimated by comparing the maximum value of the standard deviations for each type of plot. For subsequent comparison of the contribution of each error

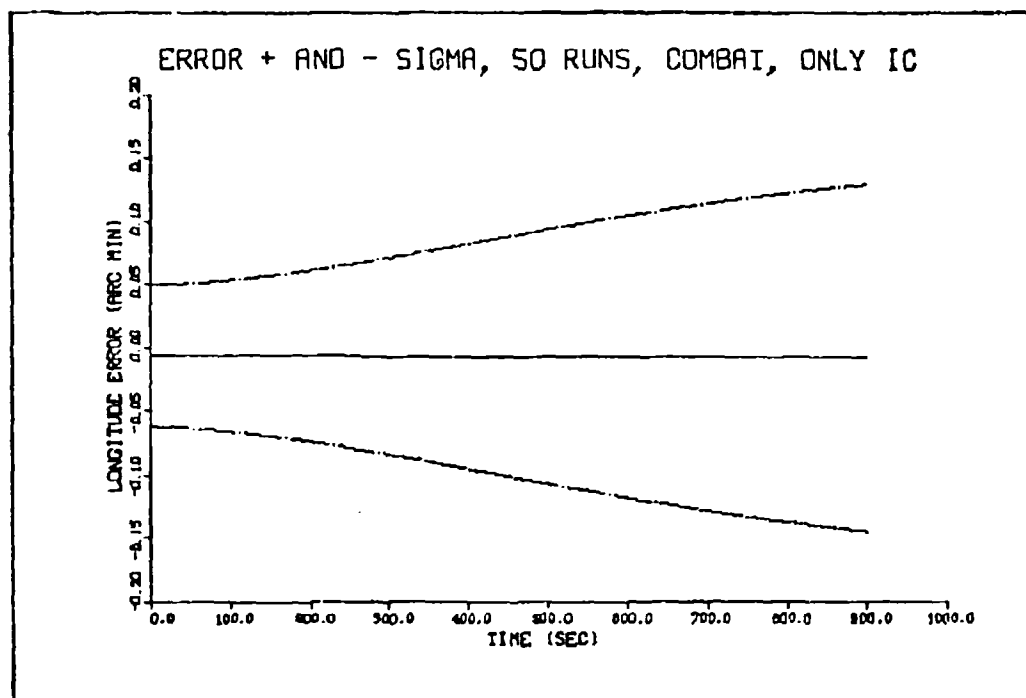


Figure 53. Longitude error state from initial conditions

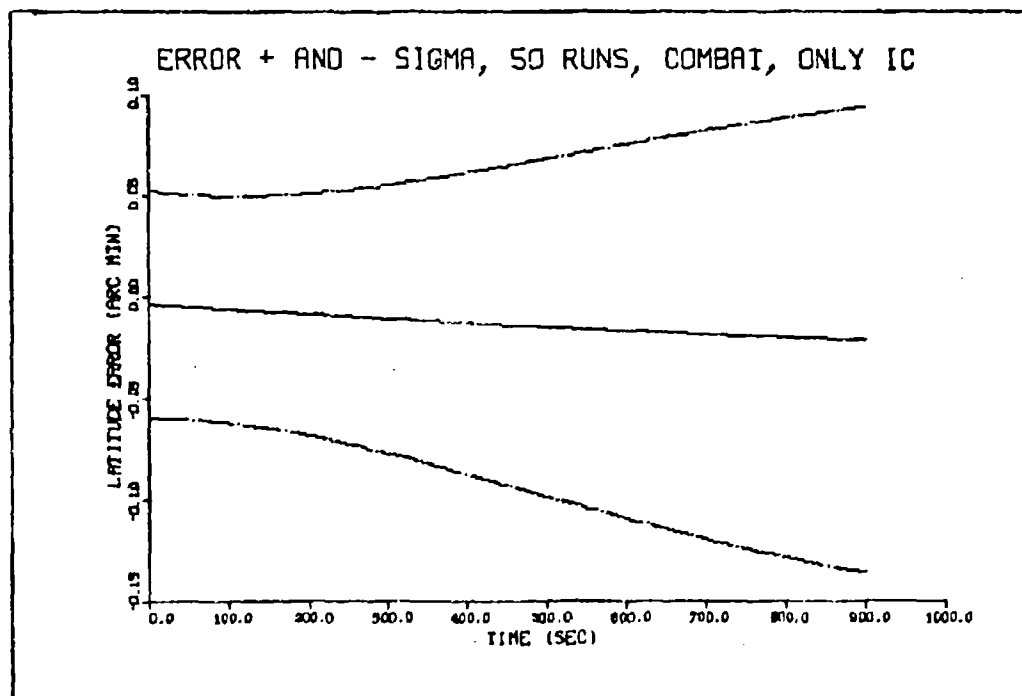


Figure 54. Latitude error state from initial conditions

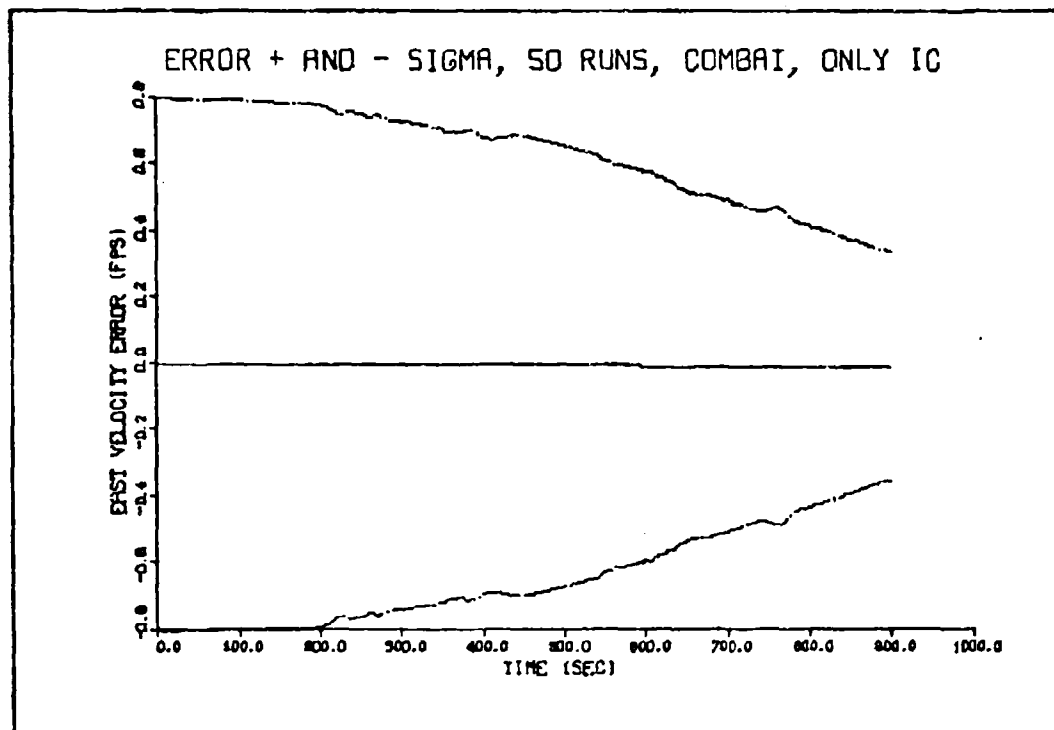


Figure 55. East vel. error state from initial conditions

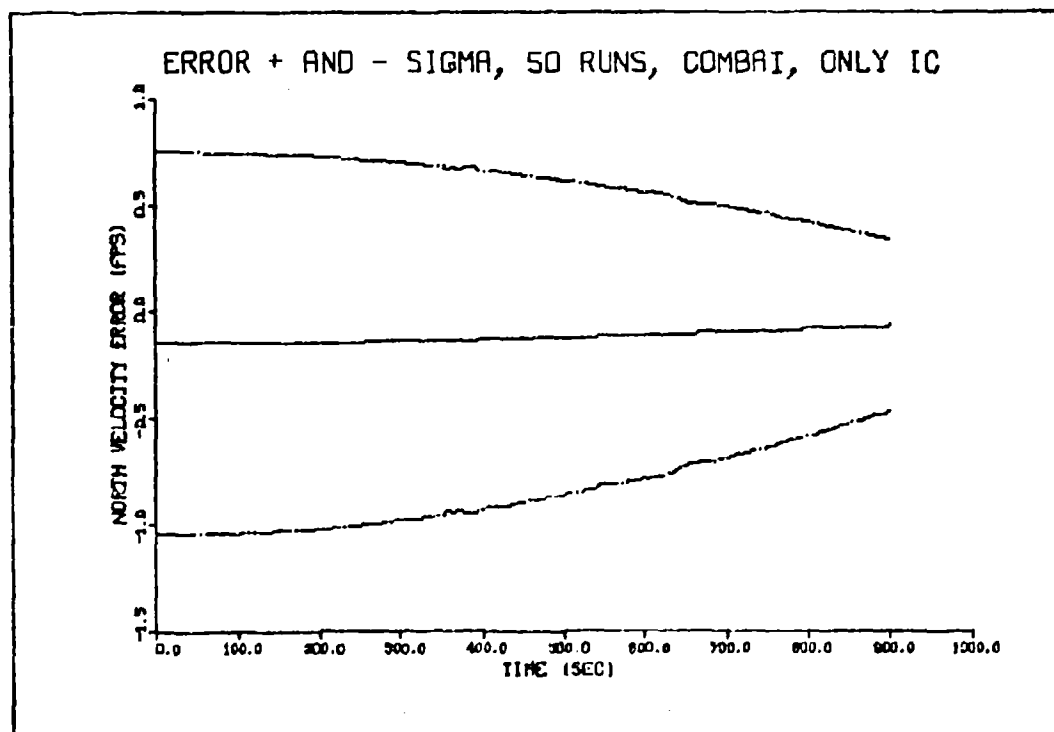


Figure 56. North vel. error state from initial conditions

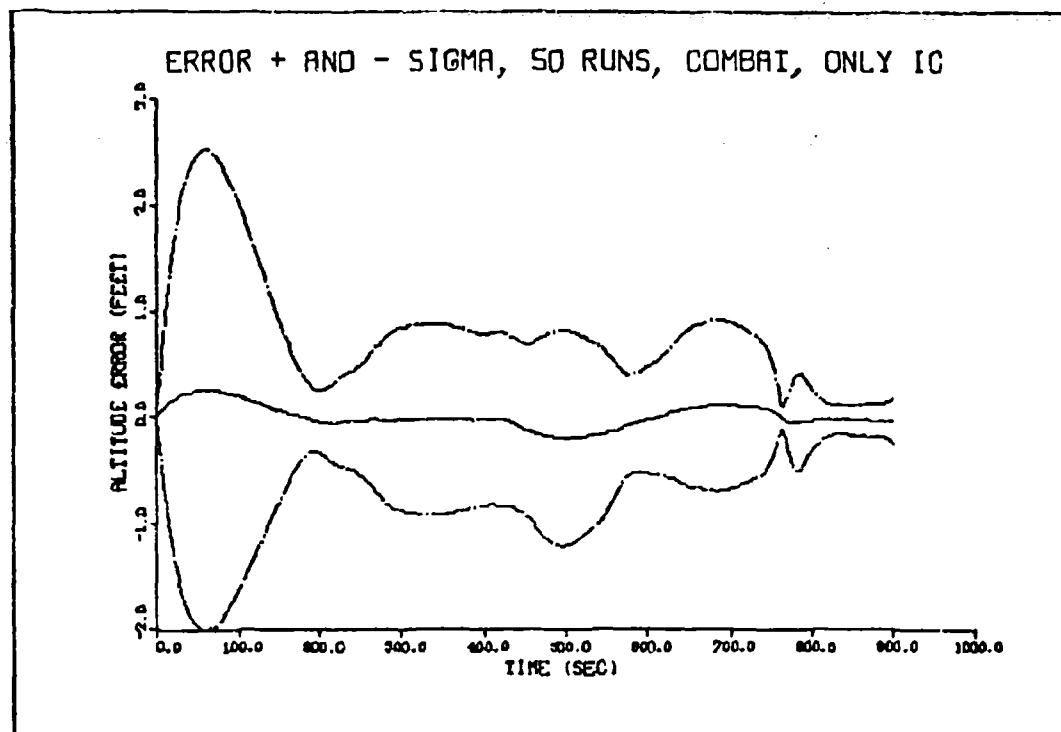


Figure 57. Altitude error state from initial conditions

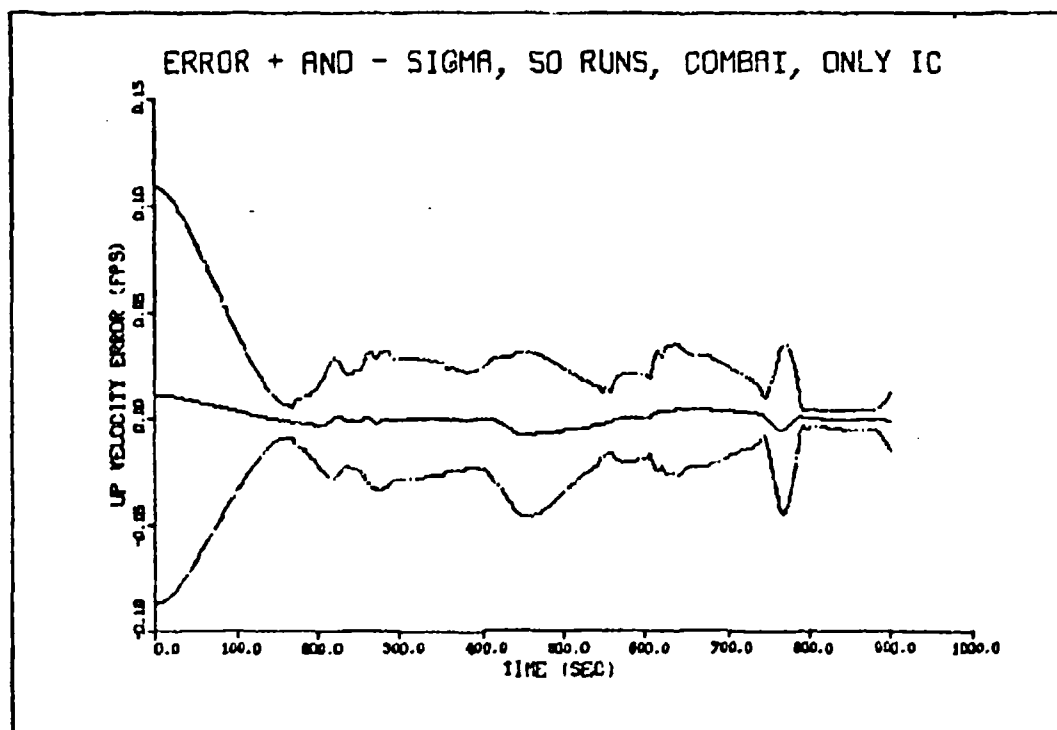


Figure 58. Up vel. error state from initial conditions

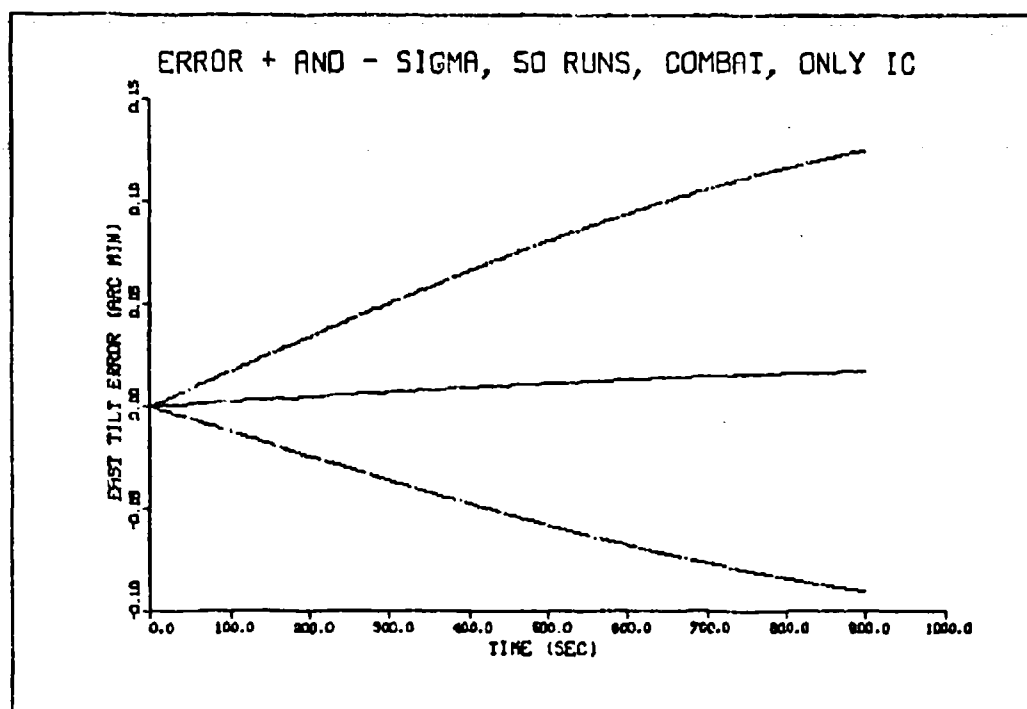


Figure 59. East tilt error state from initial conditions

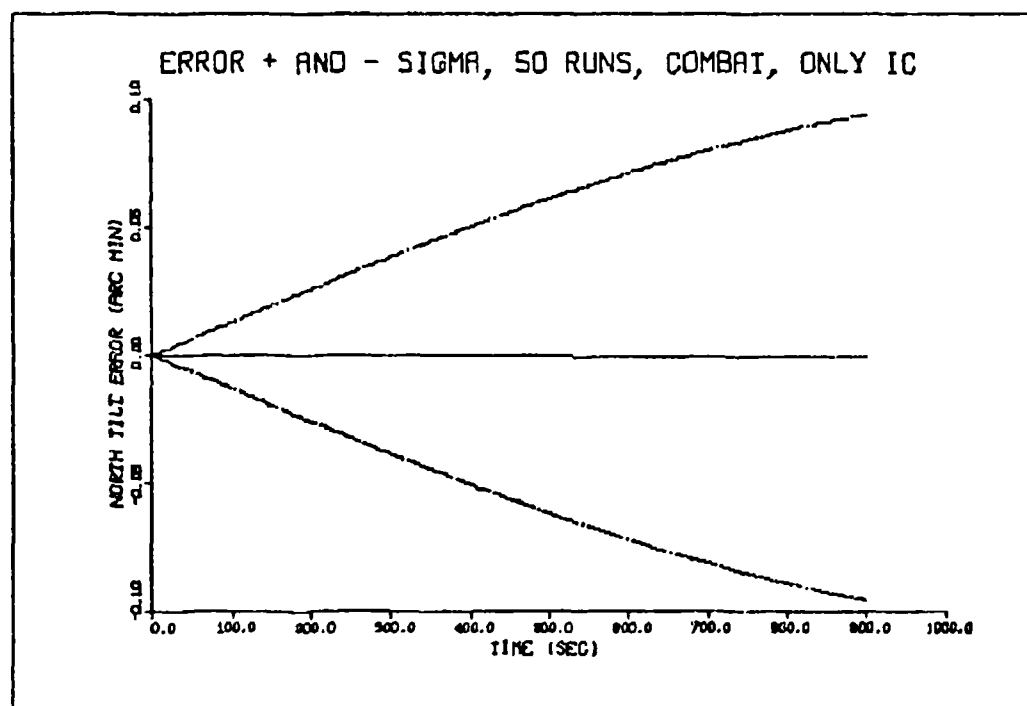


Figure 60. North tilt error state from initial conditions

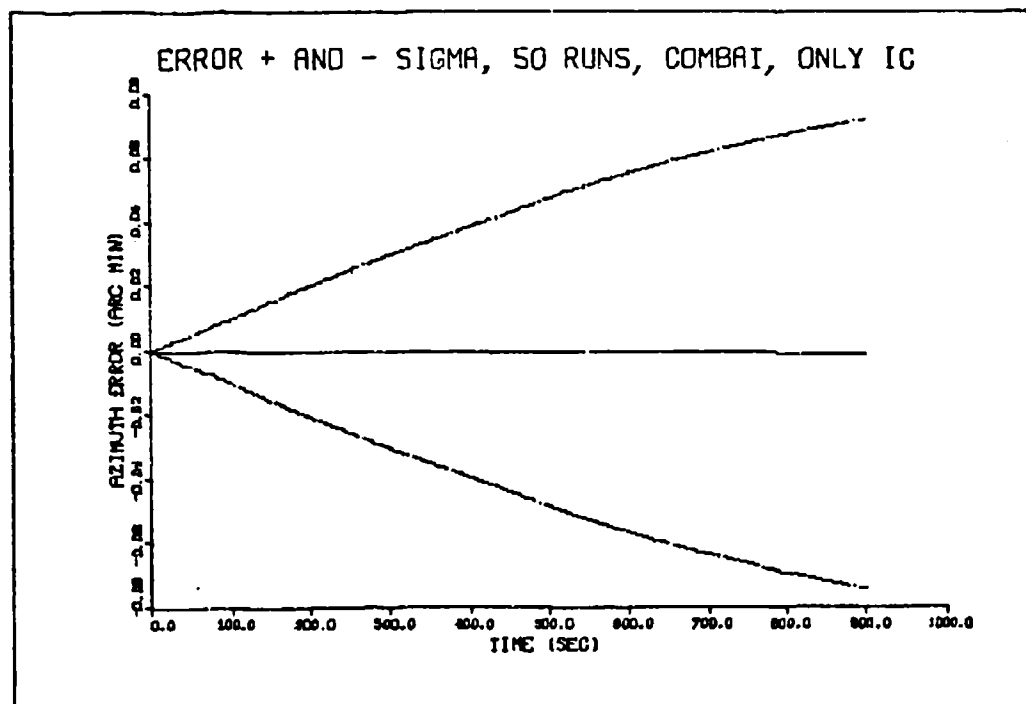


Figure 61. Azimuth error state from initial conditions

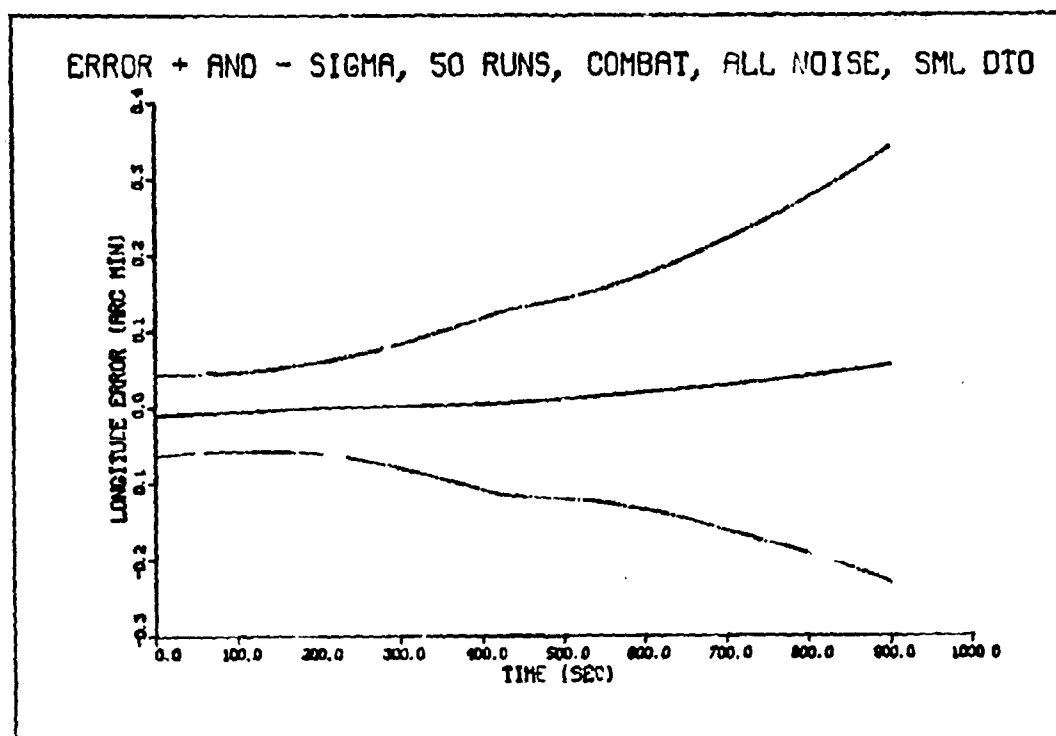


Figure 62. Longitude error state from all noise sources

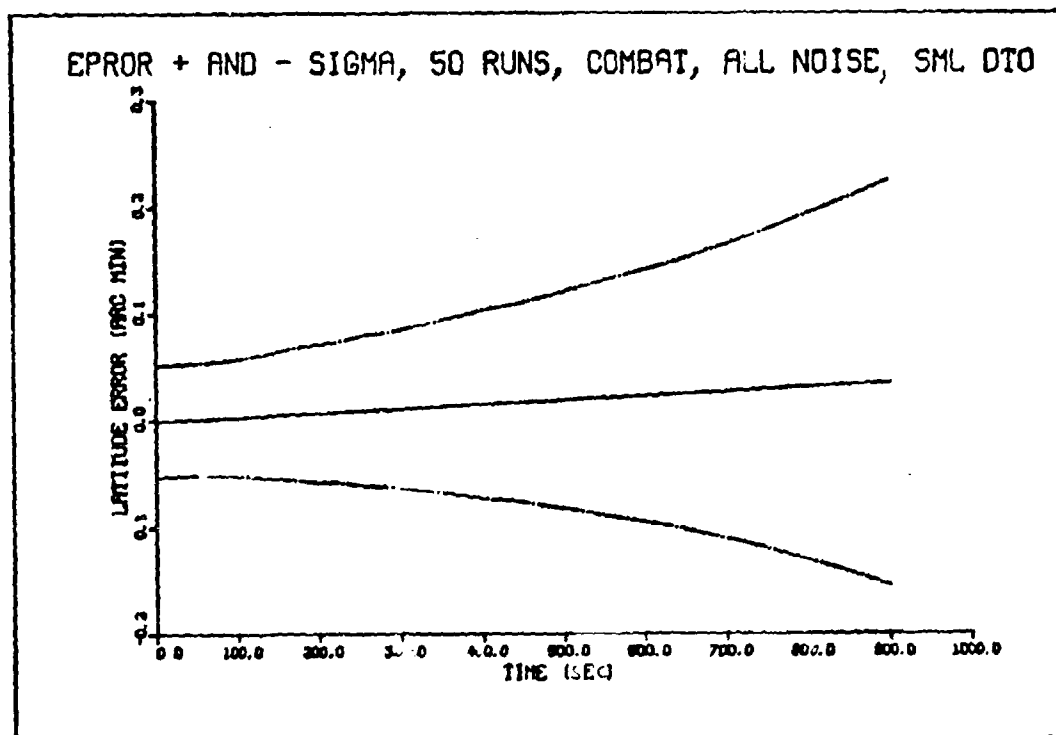


Figure 63. Latitude error state from all noise sources

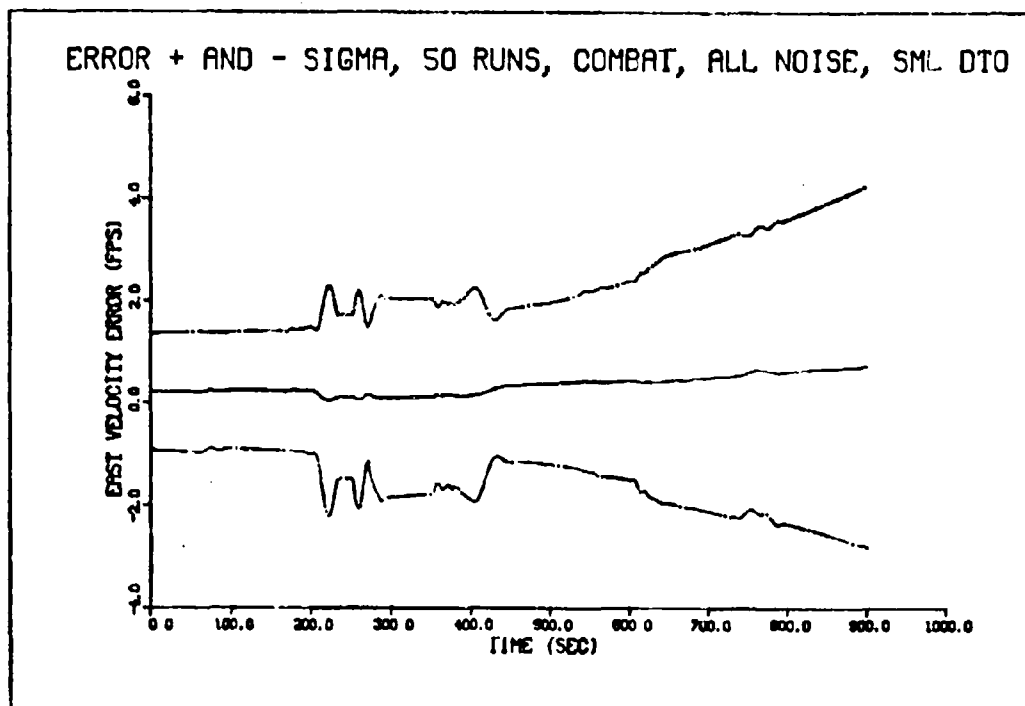


Figure 64. East vel. error state from all noise sources

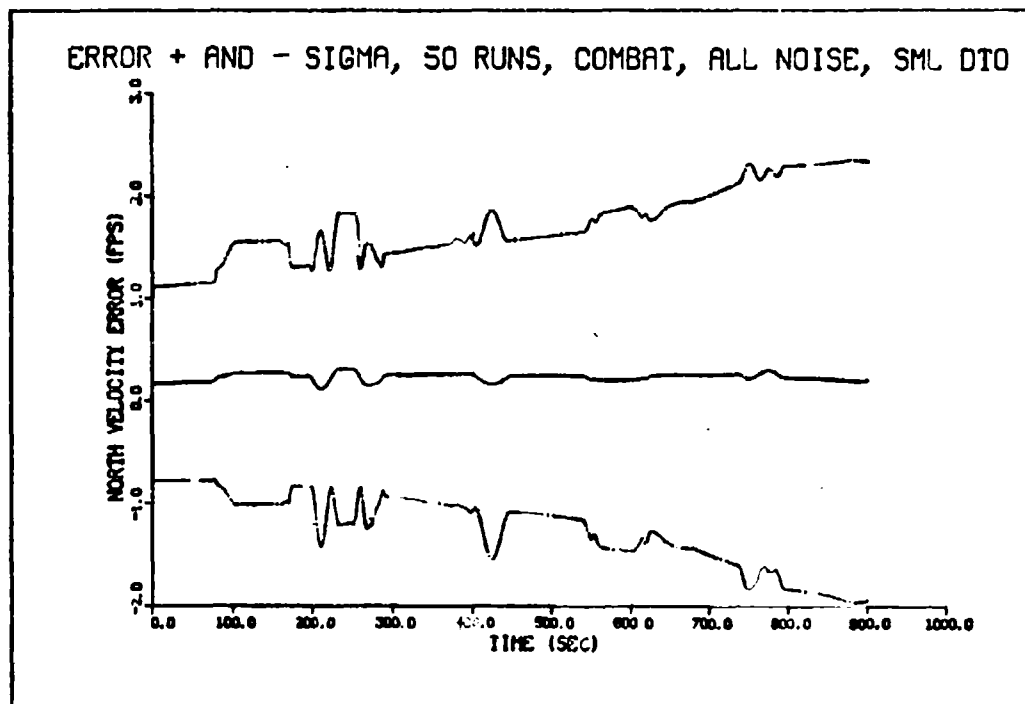


Figure 65. North vel. error state from all noise sources

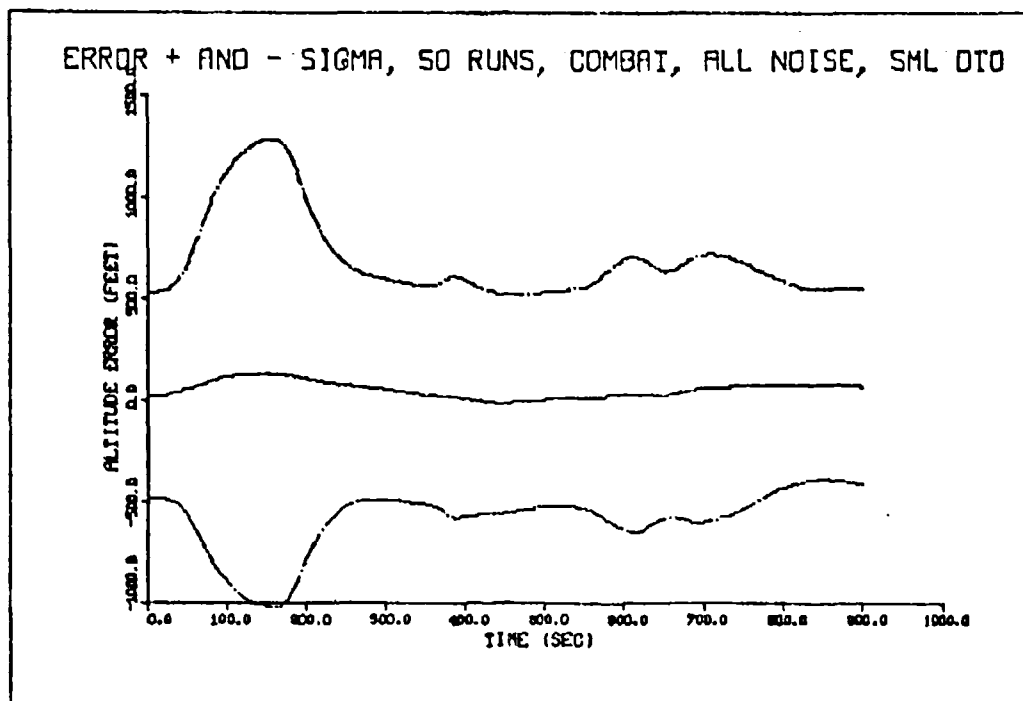


Figure 66. Altitude error state from all noise sources

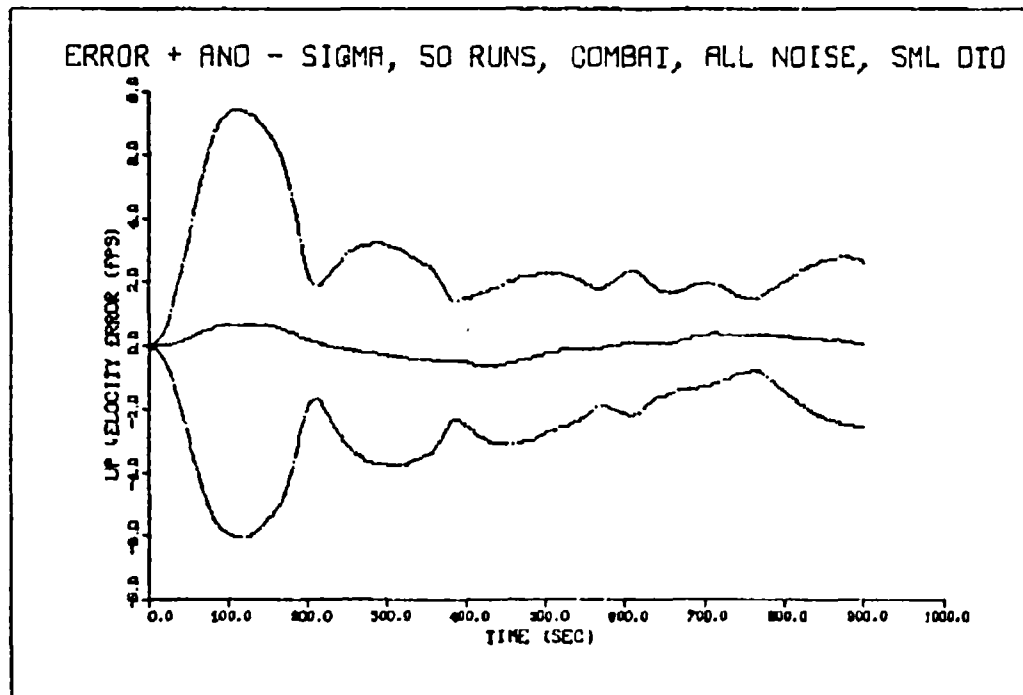


Figure 67. Up vel. error state from all noise sources

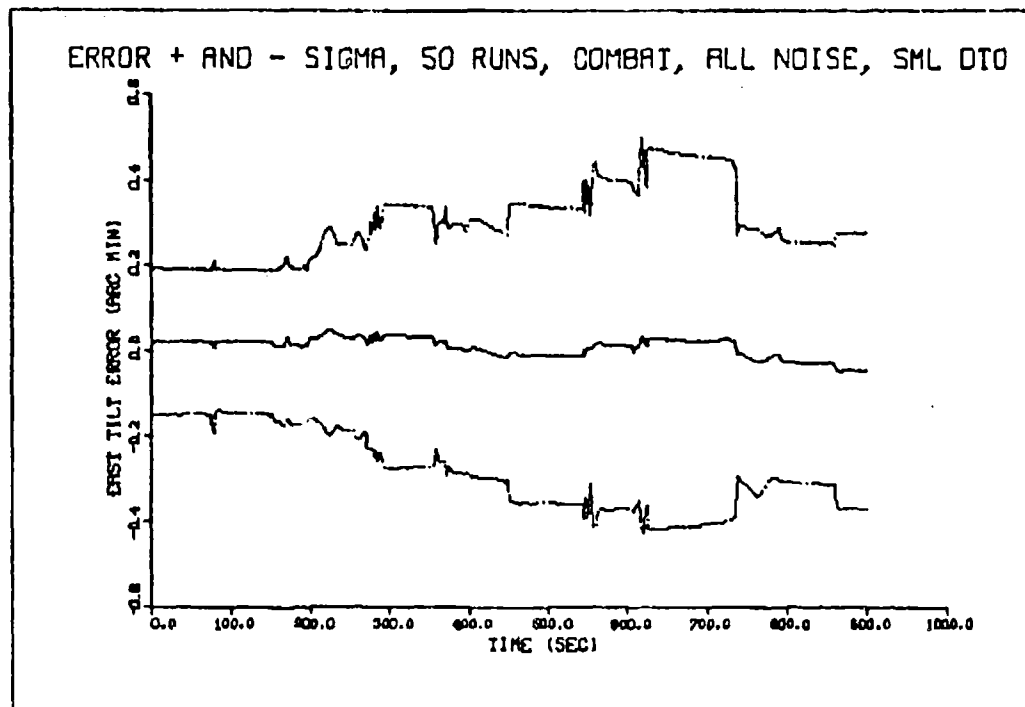


Figure 68. East tilt error state from all noise sources

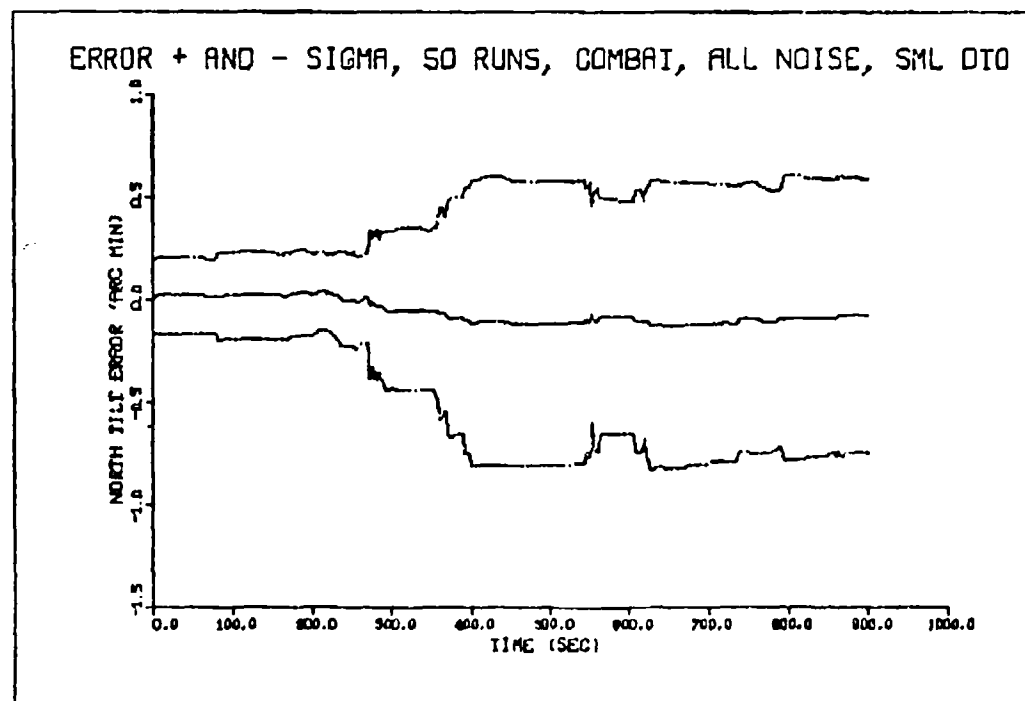


Figure 69. North tilt error state from all noise sources

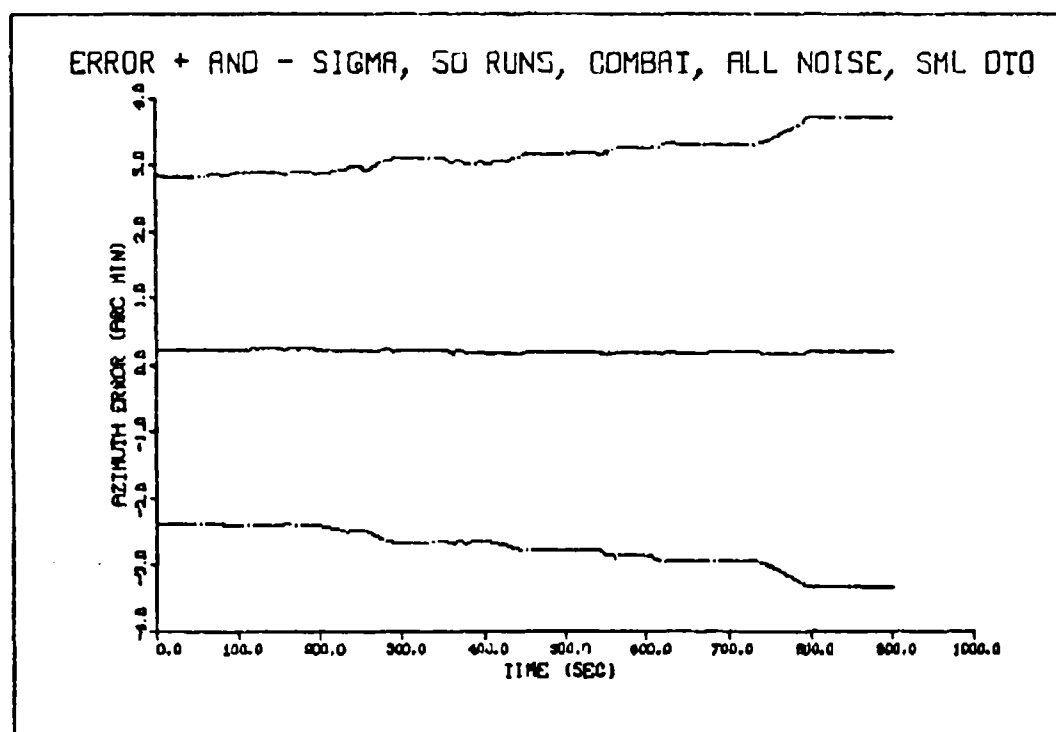


Figure 70. Azimuth error state from all noise sources

Error State	Initial Conditions	Accelerometer Errors	Gyro Errors	Barometric Errors	Gravity Errors	Short Alignment
Longitude	47.8	26.1	47.0	0.0	2.6	12.1
Latitude	59.7	19.5	33.8	5.2	15.6	12.2
East Velocity	22.9	13.6	70.0	0.7	7.9	30.8
North Velocity	40.7	34.7	52.3	2.8	14.0	30.7
Altitude	0.2	0.6	0.4	119.6	0.1	0.0
Up Velocity	1.4	4.4	4.1	120.8	1.4	0.0
East Tilt	23.6	20.3	98.4	1.6	6.7	6.9
North Tilt	13.6	10.7	80.7	0.0	5.3	7.0
Azimuth	2.1	1.8	81.1	0.1	0.8	75.7

Table 15. Percent contribution to total error

source, the maximum value obtained from propagating just the initial conditions was subtracted from the maximum obtained with the error source, then the percentage is computed. In all cases, the final value of the longitude and latitude error states are the maximum value. The vertical channel, in most instances, is compared at the peak standard deviation value resulting from the initial climb. In addition to changing the driving forces of the vertical channel, the error sources also change the damping of this closed baro-inertial loop. In some cases this results in variations that exceed the maximums obtained from the presence of all error sources, as shown in the fifth column of Table 15. Many of the standard deviations of gyro induced tilt errors reached maximum values just before the -400 degree turn at $t = 737.5$ seconds cancelled much of the error built up by turns in the opposite direction. In the cases where the initial velocity standard deviations are the maximum value, the difference between the standard deviations at the final time was the basis of comparison.

Additional tables, constructed in the same manner as Table 15, will be used for comparison of individual accelerometer errors and individual gyro error contributions to the overall system error. Since the contributions of error sources are calculated at points which best reflect their relative contribution to the overall error, and vertical channel damping is variable; the square root of the sums of the squares (RSS) of the percentages of contribution will not, in general, be 100 percent.

It should also be noted that the tables show some error sources contribute more to one of the horizontal channels than the other. This is a result of the predominately north-south orientated flight profile shown in Figure 43. Therefore, scale factor type of error sources would

cause more error in the predominant north-south direction, while misalignments would couple errors into the perpendicular, east-west direction.

Table 16 was developed to show the relative contribution of the sensor error sources to the initial alignment error of the tilt and azimuth error states. This percentage was derived from the ratio of the standard deviation induced by an individual error to that induced by all the sensor errors. These alignment error sources are not independent, since a change in heading will increase the contribution of some of the sources, while decreasing that of the others. Therefore, especially for azimuth, the RSS value of all the percentages of contribution will not necessarily be 100 percent.

In addition to these tables, a word description rather than the inclusion of a plot will be used to point out simple trends resulting from the error sources. The plots selected to illustrate more complex detail have been consolidated in Appendix H since they will be referenced in both this section and the following section.

Accelerometer Errors

The ensemble averages and standard deviations of the error states resulting from propagation of just the accelerometer over the flight trajectory are shown in Figures H-1 through H-9. With the exception of the damped vertical channel, virtually none of the dynamics of the trajectory are reflected in these error plots. The slight variations in the north velocity error correspond to large turns initialed at 197, 398 and 735.5 seconds.

Accelerometer errors, through the relationships in Equations (23) and (25), cause most of the tilt errors during initial alignment. The

Error State	Accel. Bias	Accel. Misalign	Accel. Cor. Noise	Gyro Bias	Gyro Scale Factor	Gyro Misalign	Gravity Error
East Tilt	31.2	82.4	15.3	0	0	0	47.6
North Tilt	19.5	100.0	10.0	0	0	0	35.5
Azimuth	1.2	6.2	0.6	71.2	0.7	3.8	2.4

Table 16. Percent Contribution to the Initial Conditions

resulting north tilt error, in turn, causes a small initial azimuth error due to the first term in Equation (27). The standard deviations of these initial errors, shown in Figures H-7 through H-9, remain relatively constant throughout the mission.

The third column in Table 15 shows the percentage of error (based on comparison of maximum values) that the accelerometers contribute to the overall system error. Comparison of these values to those resulting from just the initial conditions show that, in general, the accelerometer errors had a smaller adverse impact on the performance of the navigation system. However, introduction of the accelerometer errors did cause more variation of error in vertical channel as seen by comparing Figures H-5 and H-6 to Figures 47 and 48.

The contributions of each type of accelerometer error to the overall system error is shown in Table 17. Each of the error sources will be discussed.

Accelerometer Bias. Accelerometer bias, as shown in Table 16, is a factor in the initial alignment accuracy of the tilt error states and indirectly has a small effect on initial azimuth error. These three additional initial errors and the bias errors contribute to the velocity differential error equations. The resulting velocity error is then integrated to give position errors. Both position and velocity errors are terms in the tilt and azimuth differential error equations, and therefore the cycle continues.

The standard deviations of tilt and azimuth errors grow smoothly to the maximum relative relationship shown in the second column of Table 17. This same linear growth is also true for the latitude and longitude error states. The horizontal velocity standard deviations,

Error State	Bias	Scale Factor	Misalign	Second Order	Correlated Noise	White Noise
Longitude	7.8	7.8	25.2	2.6	7.5	6.1
Latitude	15.6	18.2	20.8	15.6	17.1	5.2
East Velocity	5.4	2.9	21.4	0.7	2.9	2.9
North Velocity	5.8	3.6	10.5	5.8	3.6	2.1
Altitude	0	0	0.5	0	0	0
Up Velocity	0.1	0	3.8	0	0	0.1
East Tilt	6.0	4.1	7.1	2.7	3.8	0.1
North Tilt	3.6	3.6	15.0	0.7	3.3	3.6
Azimuth	0.6	0.5	2.5	0.5	0.5	0.6

Table 17. Percent Contribution of Accelerometer Errors to Total Error

however, start at their maximum value and gradually decrease. The percent of system error contributed by these states was determined by comparison of the standard deviations at the final time. Slightly more oscillation than that observed from just the initial conditions was apparent in the vertical channel, but this contribution is insignificant relative to the total vertical error.

Accelerometer Scale Factor Error. Scale factor errors contribute about the same amount of error to the system as accelerometer bias errors, as a result of this flight trajectory. Unlike bias, the scale factor errors do not contribute to the initial tilt and azimuth alignment errors, but the standard deviations of these error states grows linearly until the maximum is about equal to the bias-induced errors.

Table 17 shows that the horizontal velocity error standard deviations for the scale factor induced errors are less than those induced by the bias errors. Yet, the position error standard deviations are equal to or greater than that caused by the bias errors. In each case, the initial velocity error standard deviation was the maximum value followed by a gradual decrease. However, the standard deviation for scale factor induced velocity error remained at a higher value longer and dropped slightly faster toward the end of the mission. Integration of the higher average velocity error resulted in more scale factor induced position error.

Accelerometer Misalignment. Misalignment is the dominant source of accelerometer induced system errors. The third column of Table 16 shows that this error source is the cause of most of the initial tilt errors and some of the initial azimuth error. Unlike the bias induced initial errors, whose standard deviation grew as the flight progressed,

these three higher initial standard deviations remained relatively constant throughout the mission.

The standard deviations of the east and north velocity errors, as shown in Table 17, are considerably higher for the misalignment induced errors than any other accelerometer error source. This relatively high velocity error would have a large impact on position error when integrated over a longer flight profile.

The oscillations produced in the vertical channel are nearly identical in size and in shape to those produced by the combination of all accelerometer errors shown in Figures H-5 and H-6.

Accelerometer Second Order Errors. Second order error sources were included in the accelerometer error model as a result of the comparison of their maximum impact on system error to that caused by other error sources. These relationships were shown in Table 6. The percentages of total error contributed by these sources, shown in Table 17, confirm that the system errors generated are not insignificant. In fact, the standard deviation of latitude errors and north velocity error contribute the same percentage of total error as accelerometer bias.

When the quadratic and cross scale factor second order error source types are considered separately, each produces the same percentage of error as the other. However, in almost every error state, the standard deviation is more when just one type of error source is present than when the two second order sources are combined. This result is not contradictory since specific force excites both of these error sources, but the quadratic error remains positive while the cross scale factor error changes sign, causing some cancellation of the error.

The second order errors cause the tilt and azimuth standard

deviations to grow linearly from zero to the maximum percentage of error shown in the fifth column of Table 17. The standard deviations of position errors start at their initial values and gradually increase, while the velocity error states gradually decrease from their initial value. The percentage of total error for each of these error states is computed based upon their relative value at the final time.

Accelerometer Correlated Noise. Correlated Noise produced a system error similar in magnitude to that of bias and scale factor induced error. Table 16 shows that this noise source also contributed a small amount of initial alignment error.

Although the relative magnitudes vary slightly, as seen in Table 17, the system plots obtained from both the accelerometer bias and correlated noise are nearly identical in shape. The tilt, azimuth and position errors gradually grow from their initial values to the maximum percentage of overall error shown in the table. The velocity errors decrease gradually from their initial standard deviations until the final time where their relative contribution is tabulated. Correlated noise causes slightly more oscillation in the vertical channel than the accelerometer bias.

Accelerometer White Gaussian Noise. Overall, the white noise contribution to the inertial reference system error is the least significant accelerometer error source. Comparison of the relative values of the columns of Table 17 shows that in several error states even second order errors were considerably greater than white noise induced system errors.

In this simulation the white noise contribution is added directly to the velocity error states. A noise sample, weighted by the time

interval between samples, is added periodically (every two seconds in this case) to simulate the driving noise. The strength of the noise used here, however, is not sufficient to alter trends established from just the initial conditions. Therefore, the velocity error standard deviations still gradually decrease from their initial values but end at a slightly higher percentage of total velocity error than those caused by just the initial conditions. Again, position, tilt and azimuth errors gradually grow to a maximum standard deviation at the final time.

Gyro Errors

Gyro errors are the dominant source of error for this strapdown inertial reference system. The system errors caused by the gyro error sources, unlike the accelerometer error sources, strongly reflect the dynamics of the flight trajectory driving the simulation program. The standard deviations of the error states generated by just the gyro errors (and initial conditions) are shown in Figures H-10 through H-18. With the exception of the position errors, each of these plots show variations due to specific maneuvers.

The gyro errors are terms in the tilt and azimuth differential equations. These error states, as seen in columns 7, 8 and 9 of Figure 4b, are multiplied by specific force and become terms in the velocity differential equations. Velocity error is integrated to give position error and both, in turn, cause more tilt error. Each integration of the induced error provides some smoothing, therefore, rapid changes in tilt error results in the gradual growth of position error shown in Figures H-10 and H-11.

Through the alignment process of nulling the east component of the earth's rotation rate, the gyro errors contribute most of the initial

azimuth error. This is reflected in the relative percentages of total initial error shown in Table 16. Figure H-18 shows that the gyro error sources cause the standard deviation of azimuth error to remain relatively constant throughout the mission. Comparison of the percentages of total error listed in Table 15 shows that this is the major source of azimuth error.

The gyro errors do not contribute to the initial tilt errors, but Figures H-16 and H-17 show that specific maneuvers cause large variations in these standard deviations leading to the maximum percentage of error shown in Table 15. This table shows the gyro error sources contribute both the largest percentage of tilt errors and the largest percentage of velocity errors. These standard deviations of east and north velocity error shown in Figures H-12 and H-13, unlike the accelerometer induced errors, have prominent variations as a result of the flight trajectory. The velocity and north tilt error standard deviations reach a maximum at the final time, while that of east tilt peaks before a large turn cancels some previously built up system errors.

The initial conditions resulted in greater position errors than those induced by the gyro errors sources. However, for a longer flight time, integration of the larger gyro induced velocity errors would result in considerably larger position errors.

Gyro error sources produced about the same amount of error in the vertical channel as the accelerometer error sources. However, this is a relatively small percentage of the total error.

The contribution of each type of gyro error to the overall error is shown in Table 18. Each of these gyro error sources will now be discussed.

Error State	Bias	Scale Factor	Misalign	White Noise	Scale Factor Nonlinearity
Longitude	13.0	10.4	30.4	5.0	0
Latitude	18.2	19.5	10.4	4.7	0
East Velocity	21.4	19.3	57.1	2.9	0.7
North Velocity	19.8	22.1	23.0	4.2	0
Altitude	0	0	0.5	0	0
Up Velocity	0	0	2.9	0.1	0
East Tilt	10.4	22.5	72.5	2.7	0
North Tilt	5.4	22.1	71.1	6.4	0
Azimuth	50.8	0.6	61.9	1.0	0

Table 18. Percent Contribution of Gyro Errors to Total Errors

Gyro Bias. Gyro bias errors are modeled as random constants in the tilt and azimuth differential equations. Therefore, these terms do not directly couple the dynamics of the flight trajectory into the error states. This type of error source causes the standard deviations of the tilt errors to grow linearly from zero to the maximum percentage shown in Table 18. Azimuth error, on the other hand, has an initial alignment error that is caused by gyro bias. Table 16 shows that this is the major source of initial azimuth error. The standard deviation of azimuth error remains constant throughout the mission and accounts for about half of the total error as seen in Table 18.

Azimuth error, multiplied by the specific forces shown in the ninth column of Figure 4b, are terms in the velocity error differential equations. Figures H-19 and H-20 show the resulting variations in the east and north velocity standard deviations. Comparison of these two plots to Figure H-12 and H-13 shows that this is the major source of variation in the standard deviation of velocity error, but does not account for its increasing trend or variations of the mean.

As is the case with most of the other error sources, the standard deviation of the gyro bias induced position error increased smoothly to the maximum percentage shown in Table 18. Also, slightly more variation was apparent in the vertical channel than obtained with just the initial conditions, but this was insignificant compared to the overall vertical error.

Gyro Scale Factor Error. The gyro scale factor errors multiplied by angular velocity are terms in the tilt and azimuth differential error equations. This directly couples some of the dynamics of the flight trajectory into these error states as shown in Figures H-21 through H-23.

The standard deviations of the tilt errors grow in steps until they represent about one fourth of the total.

From the relationship established in Equation (27), it is seen that the scale factor error multiplied by the north component of the earth's rotation rate contributes to the initial azimuth error. Table 16 shows, however, that this is a small percentage of the overall alignment error. From the initial standard deviation, as shown in Figure H-23, the azimuth error increases steadily, but has several minor variations due to specific maneuvers.

The tilt and azimuth errors multiplied by specific force are terms in the velocity differential equations. Integration results in a smooth standard deviation of velocity error that gradually decreases for the first two thirds of the mission followed by a slight increase during the final portion. The overall result is about the same percentage of velocity and position error as the gyro bias produced system error.

Gyro Misalignment. Misalignment is a dominant source of gyro error. Table 18 shows, however, that while the percentage of longitude error from this source is large, latitude error is small. This difference is due to the predominant north-south orientation of the flight trajectory shown in Figure 43. Inspection of the fundamental submatrix shown in Figure 41 shows that for a northerly heading ($C_{ey} = C_{nx} = -C_{uz} = 1$), the terms multiplying misalignment errors in the east velocity differential equation are $-\omega_z$ and ω_x while for north velocity they are ω_z and $-\omega_y$ (ω is the angular velocity of the body frame with respect to the inertial reference frame). Since roll rate is a factor in ω_x , this term is generally much higher than the other terms resulting in more east velocity and longitude error.

This directional dependence is seen explicitly in Figure H-24.

The slope of the standard deviation of east velocity error increases as the turn to a north heading is completed after 400 seconds of flight time. Figure H-24 also shows along with Figure H-25 that, while bias induced error accounted for most of the variations in the standard deviations shown in Figures H-12 and H-13, misalignment error causes the increasing trend.

Figures H-26 through H-28 show that gyro misalignments produce abrupt changes in the tilt and azimuth error states as a result of the flight trajectory. The resulting growth in the standard deviations of these error states leads to the largest percentage of overall error as shown in Table 18. Figure H-28 also shows that gyro misalignment produces a small initial azimuth error. This is error resulting from sensing earth rate during alignment.

Gyro White Gaussian Noise. As discussed in Section II, the output error of the ring laser gyro is better characterized by a white Gaussian noise component rather than by exponentially time-correlated noise or the limit thereof for long correlation time, random walk, which is typical of mechanical gyros. It is a physically wider band noise process in laser gyros than mechanical gyros. This noise directly drives the tilt and azimuth differential error equations resulting in the error shown in Figures H-29 to H-31.

The standard deviations have, as expected, an increasing trend, but also have a wavering component. This is due to the simulation program which approximates the driving noise by periodically adding noise samples weighted by the time interval between samples. A smaller time interval than two seconds used here would have produced less variations. Table 18

shows that white Gaussian noise contributes only a small percentage of the overall system error. The standard deviations of the east and north velocity errors decrease smoothly from their initial values and those of latitude and longitude gradually increase. Slightly more oscillation is apparent in the vertical channel than that caused by just the initial conditions.

Gyro Scale Factor Nonlinearity. The nonlinearity is added to the scale factor error as shown in Equation (13). Table 18 shows that the nonlinear contribution has almost no effect on the growth of the standard deviations of the error states. However, as shown in Figures H-32 through H-34, the ensemble averages of the tilt error states vary considerably as a result of the dynamics of the flight profile. The cumulative effect of these variations is a slight increase in the mean values of longitude and east velocity error, and a small decrease of the latitude and north velocity error.

The small effect of the nonlinearities on the error standard deviations was expected since the flight profile was not specifically constructed to excite this error source. None of the rolls or turns performed during this mission were designed to maintain a roll rate in the nonlinear region shown in Figure 3. The nonlinear error source was only excited while the roll rate was in transition through the region. An increase in the magnitude of the scale factor nonlinearity causes considerable deviation of the mean, but no detectable change in the growth of the standard deviations.

Barometric Altimeter Errors

Barometric altimeter errors are the dominant error source for the vertical channel. As shown in Table 15, both the altitude and up

Velocity percentages of total error are two orders of magnitude larger than that obtained from any other error source. The standard deviations of these two error states is virtually identical to Figures 66 and 67. Although this error is significant, a relatively small amount of error is coupled into the horizontal channels.

Table 15 shows that barometric errors generate more latitude error than longitude errors. Again, this is a result of the predominantly north-south orientated flight profile shown in Figure 43. Inspection of the third column of Figure 4b shows that north velocity, through the relation $\rho_e = -v_n/R$, multiplied by altitude error is a factor in the latitude error differential equation. The factor ρ_e also multiplies the vertical velocity error in the north velocity error differential equation resulting in more north velocity error than that in the east direction. More east tilt error than north tilt error is also a result of the factor ρ_e .

Gravity Errors

Gravity error sources, like the accelerometer errors, contribute directly to the initial tilt errors and indirectly (through the first term in Equation (27)) to the initial azimuth error. The relative amount of this initial contribution is shown in Table 16.

Although gravity errors contribute little to the growth of the vertical channel standard deviations, they do cause some variation in the mean values of altitude and up velocity error. This is shown in Figures H-35 and H-36. Each deflection of the mean corresponds to a large horizontal turn. Referring back to Table 7 shows a large difference in the standard deviations of the east-west and north-south deflections of gravity. This difference would cause variations in system error with a

change in the direction of flight. However, the higher strength of the east deflection of gravity also should cause more east velocity and longitude error, but Table 15 shows just the opposite. This is misleading because the entries in this table are percentages relative to the error generated by all sources. More total longitude and east velocity errors were generated than latitude and north velocity errors, which caused the apparent difference.

Short Alignment Time

The inertial reference system alignment process is assumed to occur in two steps. First, the computer determines local level by sensing the gravity vector through the accelerometers. Then an azimuth reference is found by nulling the east component of the earth's rotation rate vector as sensed by the gyros. Since the gravity vector is a relatively large quantity which can easily be detected by the accelerometers, the computer can rapidly determine the transformation necessary for a local level coordinate frame. However, this is not the case during the second portion of the alignment. The earth rate vector is relatively small which makes it difficult for the computer to determine the precise direction of zero earth rate (the east direction). The longer time the computer has to solve the problem, the more accurate the azimuth reference is.

As developed in Section II, a long alignment has tilt errors directly related to accelerometer and gravity errors, and azimuth error is mostly a function of gyro errors. To simulate a shorter alignment, the initial azimuth has an added Gaussian random sample of 3 arc min standard deviation.

The major impact of the short alignment time is shown in

Figures H-37 and H-38. These variations in the velocity standard deviations are similar to those caused by gyro bias. The ninth column in Figure 4b shows that the azimuth error multiplied by specific force is a component in the velocity differential equations. Changes in these specific forces as a result of high g turns cause the steps and peaks shown in the velocity error state plots.

The relative contribution of a short alignment time to the other error states is shown in Table 15.

Error Budget Conclusions

Table 15 shows that gyro error sources contribute the most overall error in the strapdown inertial reference system analyzed here. Although the barometric altimeter errors induce the most error in the vertical channel, relatively little of this error is coupled into the other error states. The position error resulting from just the initial conditions is more than the gyro induced position error, but the velocity errors caused by gyro error sources are considerably higher than those from the initial conditions. Therefore, a longer time of flight would result in more gyro induced position error as a result of integration of the velocity errors.

Accelerometer error sources in general did not couple any of the dynamics of the flight trajectory into the error state equation. However, each error source did cause a difference in the trend of the standard deviations of the error states. Misalignment was the major source of accelerometer induced error. It was not only the largest cause of variation of the standard deviations but was the major source of initial alignment tilt error.

The gyro error sources cause specific maneuvers in the flight

trajectory to be reflected by changes in the inertial reference system error. Again, misalignment was the major source of this error. This caused rapid variations in the tilt and azimuth error states and introduced an increasing trend in the velocity states. Gyro bias caused the most initial azimuth alignment error. This higher error coupled trajectory variations into the velocity error states. Scale factor errors induced variations in the tilt error state, but not to the extent of the gyro misalignment errors. The scale factor nonlinearity introduced variation in the error state mean values but had little cumulative effect.

Gravity errors did make a small contribution to the system error, as seen in Table 15. The amount of this error varied slightly with the direction of flight.

For the time of flight used in this simulation, a short alignment time causes a system error that is comparable to gyro bias induced error. This is because each causes a large initial azimuth error.

VII. Error Analysis

While the previous section was concerned with determining the contribution of each error source to the overall system error, this section investigates the specific maneuvers and combinations of maneuvers that particularly excite these errors. Since gyro errors induced the most significant trajectory-dependent variations in the error states, the plots of the specific contributions of each of these error sources, included in Appendix H, will be used to help determine the effects of each maneuver. These plots are a result of the "combat" flight profile shown in Figures 43 through 47.

The errors generated as a result of the "training" flight profile will then be compared to those obtained previously. This profile, as shown in Figures 48 through 52, is the same time length as the "combat" flight profile but is made up of 20 segments of longer duration with more sinusoidal content and lower accelerations.

Error Generated from Pitch Changes

The pitch-up initiated at $t = 2$ seconds produces a step increase in the standard deviation of north tilt error (Figure H-27) and a smaller increase in that of east tilt error (Figure H-27). Although these changes do not dominate over the initial tilt alignment errors (Figures 68 and 69), they clearly show how the flight trajectory interacts with the error sources. With the aircraft heading north, the pitch-up generates an angular rotation vector in the east direction. This vector is multiplied by scale factor error to become a term in the east tilt differential error equation and by misalignment error to become a term in the north tilt differential equation. More north tilt error is generated since misalignment is the predominant gyro error source. Inspection of

Figures H-21 and H-27 shows that level off, initiated at $t = 61.77$ seconds, negated most of the previous increase. Although the pitch down was made at a slower rate, it was in exactly the opposite direction as the pitch up and of longer duration. Had the aircraft turned 90 degrees before leveling off, the scale factor and misalignment induced errors would be in opposite channels than the pitch-up and not result in the cancelation previously observed.

The overall result of these two maneuvers is that during the climb some tilt errors are present in the system. These tilt errors, multiplied by specific force, are terms in the velocity differential equations. Therefore, through integration, velocity errors and subsequently position errors are generated as a result of the climb. Since position and velocity errors are factors in the tilt differential equations, a slight increase in overall tilt error would be expected in spite of the cancelling effects of these two maneuvers.

The above analysis shows two characteristics of the system error that will be prevalent, although not always explicitly stated, throughout the error analysis. First, the propagation of the error is directly dependent upon the direction of flight. A change in direction between maneuvers could cause either reinforcement or cancelling of system errors. Second, although variations in error appear to have a cancelling effect, the overall system error, through integration of the error changes into the other error states, is generally higher.

The coupling of the error states increases considerably when the direction of flight is not in a cardinal direction as above. At time $t = 156$ seconds, while the aircraft heading is 315 degrees, a -25 degree pitch change is initiated. Figures H-25 and H-27 show that small steps of about equal amplitude but in opposite directions are caused in the

standard deviations of the tilt error states. Even smaller variations result from the scale factor errors during this maneuver.

Numerous pitch changes in succession were performed in the time period from $t = 351$ until $t = 398$ seconds. A 180 degree roll was made before and after each pitch down maneuver. The aircraft was on a heading of 205 degrees during these maneuvers so both roll and pitch changes were coupled into each horizontal channel. Since a major portion of the tilt errors are due to the roll maneuvers, the specific contributions from the changes in pitch cannot be isolated in the plots. However, the major trend, as shown in Figures H-16 and H-17, is clear. The east tilt error, which had the most coordinate frame rotation because of the 180 degree roll maneuver, had a standard deviation which oscillated. On the other hand, the north tilt error, without the reversals in the relationship of the body and navigation frame, built up a substantial standard deviation of the error. The specific force generated by these pitch maneuvers, f_u , also induced small variations in the velocity error states shown in Figures H-19 and H-20.

Errors Generated from Turns

The first turn, initiated at $t = 76.77$ seconds, produced prominent changes in the standard deviations of the error states. This was a 45 degree turn which started from a north heading. The tangential acceleration, therefore, rotates from west to south-west. From Figure 4b, it is seen that west specific force, $-f_e$, multiplied by azimuth error is a term in the north velocity error differential equation. Figure H-20 shows that this relationship resulted in a step increase in this standard deviation. Little variation resulted in the east velocity error state since most of the specific force was in a westerly direction, which

is not a term in this equation.

Other gyro error sources also contributed some variation in error during this first turn. Figure H-22 shows that the standard deviation of north tilt error has a step increase resulting from the scale factor error times the roll rate into the turn. A smaller step, due to the 45 degree change in heading, in the opposite direction is generated from roll out at the turn's completion. East tilt error standard deviation (Figure H-21), on the other hand, has just one increase (following a decrease caused by a pitch maneuver) as a result of the angular velocity of the turn itself reinforced at the end by a portion of the roll out vector. The scale factor nonlinearities (Figures H-32 and H-33) also caused these same type of variations in the mean of the tilts.

The tilt error standard deviations due to gyro misalignment (Figures H-26 and H-27) have greater variations and effect each channel in the opposite way as the scale factor errors. A large step in the standard deviation of east tilt error resulted from the roll into the turn, and a smaller, opposite direction, step occurred on roll-out. The turn caused a step increase in the standard deviation of north tilt error which was reinforced by a portion of the roll-out vector.

Figure H-28 shows that the angular turn rate vector also increased the azimuth error standard deviation as a result of misalignment.

The combined effect of these error sources did cause definite variations in the standard deviations of the error states with all error sources present (Figures 64 through 70). Results similar to these, but in the opposite direction, were obtained from the 30 degree turn initiated at $t = 169$ seconds. The errors generated by these turns were relatively small compared to those induced by the larger turns.

Two of these large turns were performed in succession. The first was a 6g, 270 degree turn initiated at $t = 197$ seconds and ended at $t = 235$ seconds. This was followed by a 7.33 g, -180 degree turn initiated at $t = 252$ seconds and ended at $t = 271$ seconds. Figures H-19 and H-20 show that each of these turns induced large oscillations in the velocity standard deviations. Although the -180 turn, at 7.33 g, is generating more specific force and therefore inducing more error into the velocity differential equations; these figures show a smaller peak in this standard deviation as the heading passes 180 degrees. This shows that other factors including residual system errors from the 270 degree turn are influencing the overall system error.

Both of these large turns resulted in substantial increases in the standard deviations of azimuth and tilt errors as a result of the same factors discussed previously. However, roll-out from the -180 degree turn at $t = 271$ seconds produced a very large increase in the standard deviation of north tilt error as a result of gyro misalignment (Figure H-27). The roll-out heading of 75 degrees caused the misalignment error to couple most of the roll rate vector into the north channel.

This same effect is also very apparent in the -400 degree turn entered at $t = 737.5$ seconds with roll-out at $t = 794$ seconds. The aircraft is on a heading of 175 degrees when the turn is initiated. Figure H-26 shows a large variation in the standard deviation of east tilt error induced by misalignment during the roll-in. Again, the error is induced all in one channel because the aircraft is nearly on a cardinal heading. Also, the decrease in the standard deviation is a result of residual system error from previous maneuvers. Specifically, two series of turns, with a net result of a 180 degree right turn, were performed

just before the -400 degree turn. The roll-in to the first turn of the series at a heading of 355 degrees, and the roll-out of the last turn at a heading of 175 degrees induced reinforcing errors into the east channel as a result of misalignment. Rolling into the -400 degree turn induced the negative of these residual errors resulting in the sharp drop in the standard deviation. Rolling out of the -400 degree turn at a heading of 135 degrees induced little change, as a result of misalignment, in either the north or east tilt error states.

Errors Generated from Rolls

The 45 degree roll and back initiated at $t = 154$ seconds did not reach a high enough roll rate (based on a time constant of 0.5 seconds) and was not of long enough duration to have induced any perceptible system errors. On the other hand, the 180 degree rolls between pitch maneuvers generated substantial errors. These rolls, on a heading of 205 degrees, induced large changes in the standard deviations of the tilt error states as a result of scale factor error (Figures H-21 and H-22) and gyro misalignment (Figures H-26 and H-27) during the time $t = 357$ until $t = 390$ seconds. The rolls also produced deviations in the mean as a result of the scale factor nonlinearity (Figures H-32 and H-33).

The 360 degree roll initiated at $t = 859.5$ seconds produced some very interesting results. Figures H-21 and H-22 show steps, in opposite directions, in the standard deviations of the tilt errors as a result of gyro scale factor error. However, Figures H-26 and H-27 show no change in these error states from gyro misalignment as a result of this maneuver. At this particular heading, 135 degrees, and as a result of the residual system errors, the errors induced by misalignment in the tilt error states cancel each other. Referring to Figure 4i shows the term $C_{ey}^{\omega_x}$ in the

east tilt differential equation and the term $C_{ny} \omega_x$ in the north tilt differential equations. But at a heading of 135 degrees, these elements of the direction cosine matrix are equal. Figure 4b shows that these two differential equations are coupled by the term $-\omega_y$ times the east tilt error. It is this coupling with the same driving term and the proper initial conditions that produces the observed cancellation of errors.

Errors Generated by Acceleration Along Flight Path

The only isolated occurrence of acceleration along the flight path occurs from $t = 81.77$ until $t = 104.1$ seconds. A 1g forward acceleration is applied at a heading of 315 degrees. Figure 4b shows that north specific force, f_n , is a term in the east velocity differential equation and that west specific force, $-f_e$, is a factor in the north velocity differential equation. Therefore, it would normally be expected that an acceleration midway between these two cardinal directions would induce equal variations in each channel. But, Figures H-19 and H-20 show that this is not the case. A ramp is induced in the standard deviation of the north velocity error state, but no change is apparent in east velocity error. The last maneuver, a -45 degree turn, generated mainly west specific force. Although the acceleration along the path applies equal specific force to each channel, in the north channel it reinforces existing error while in the east channel the induced acceleration error itself is not strong enough to be predominant.

Errors Generated Using the Training Flight Profiles

The ensemble averages of the error states, plus and minus one standard deviation, resulting from propagating all the error sources over the training flight profile are shown in Figures 71 through 79.

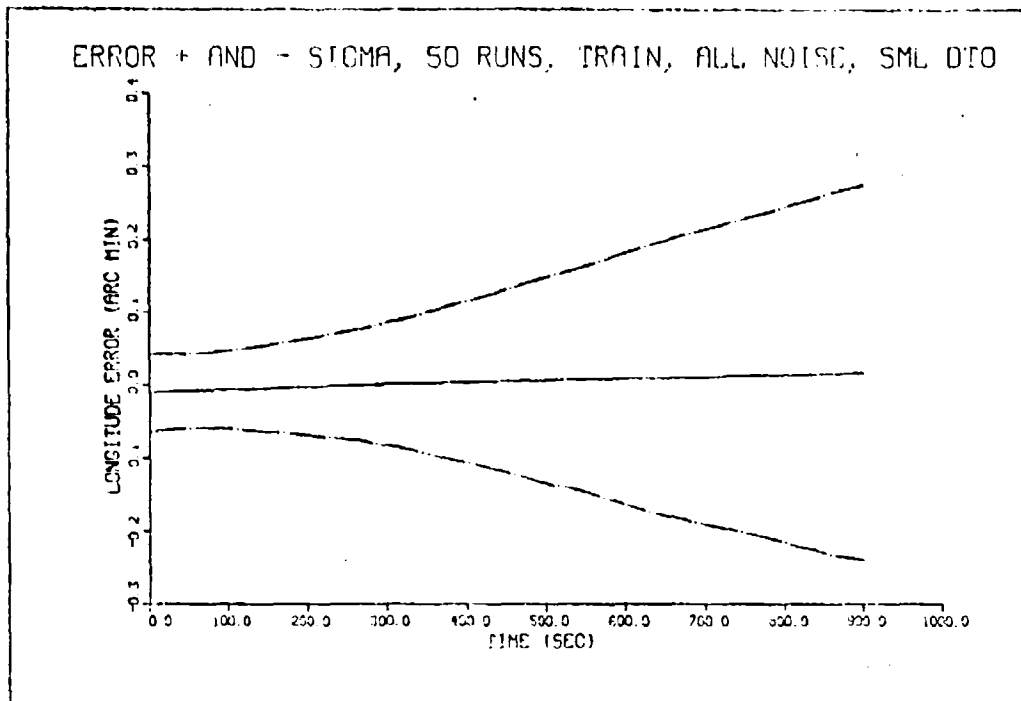


Figure 71. Longitude error state from training profile

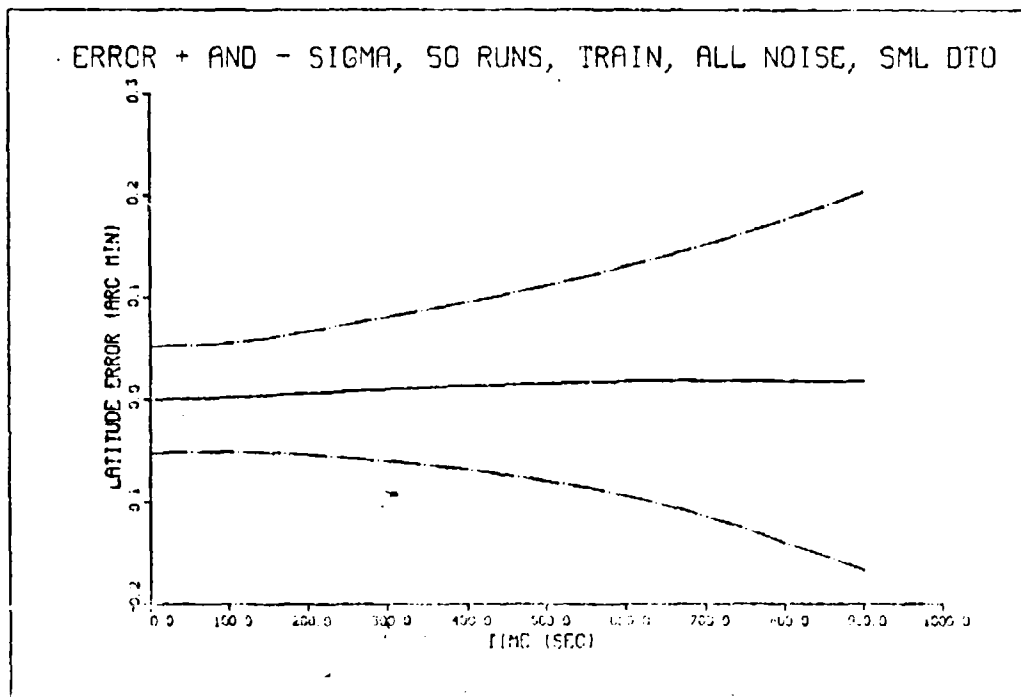


Figure 72. Latitude error state from training profile

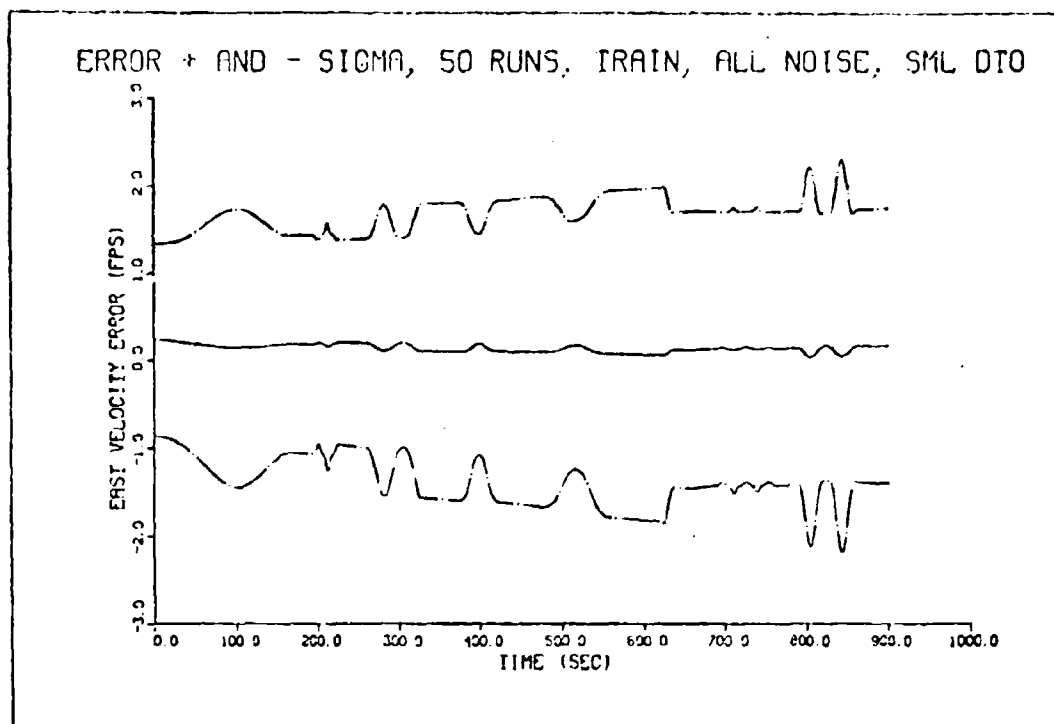


Figure 73. East vel. state from training profile

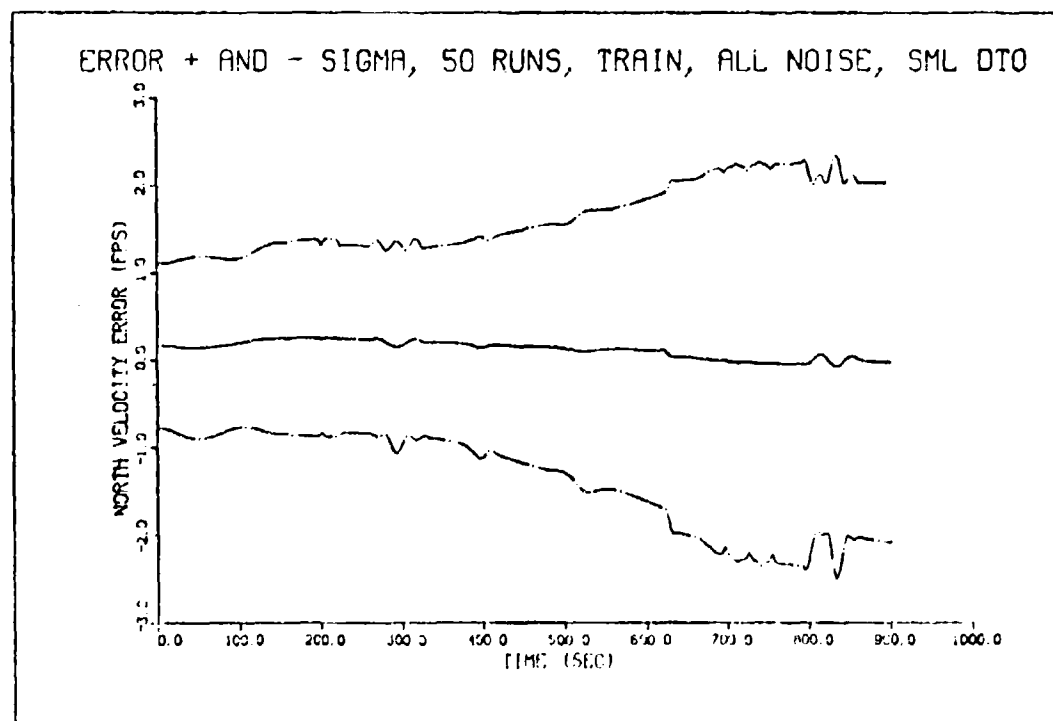


Figure 74. North vel. state from training profile

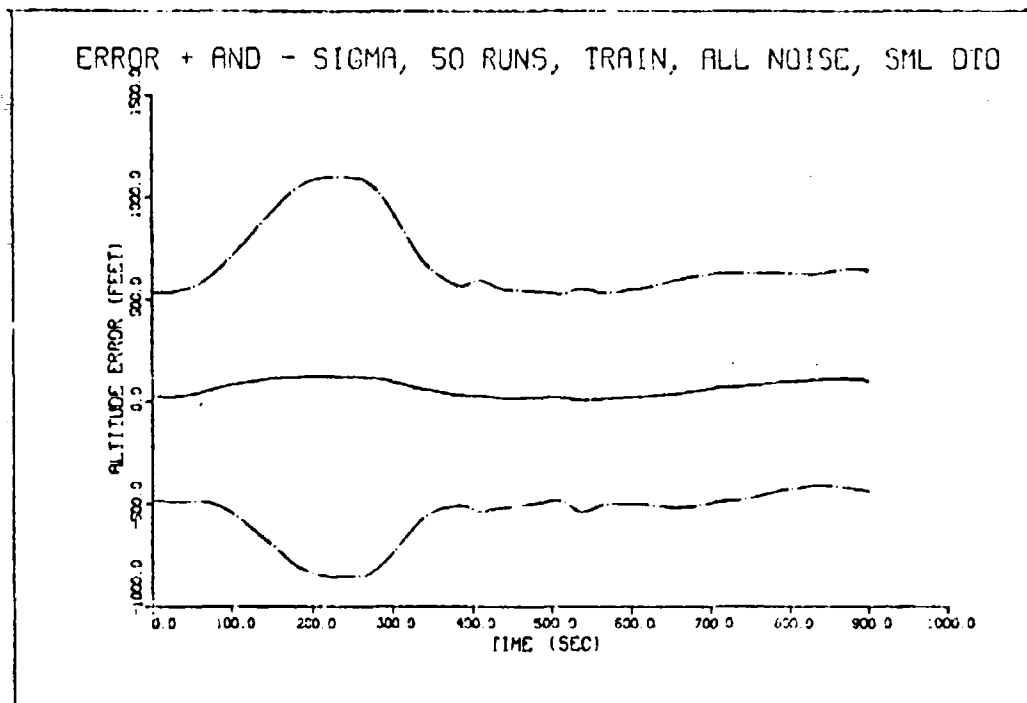


Figure 75. Altitude error state from training profile

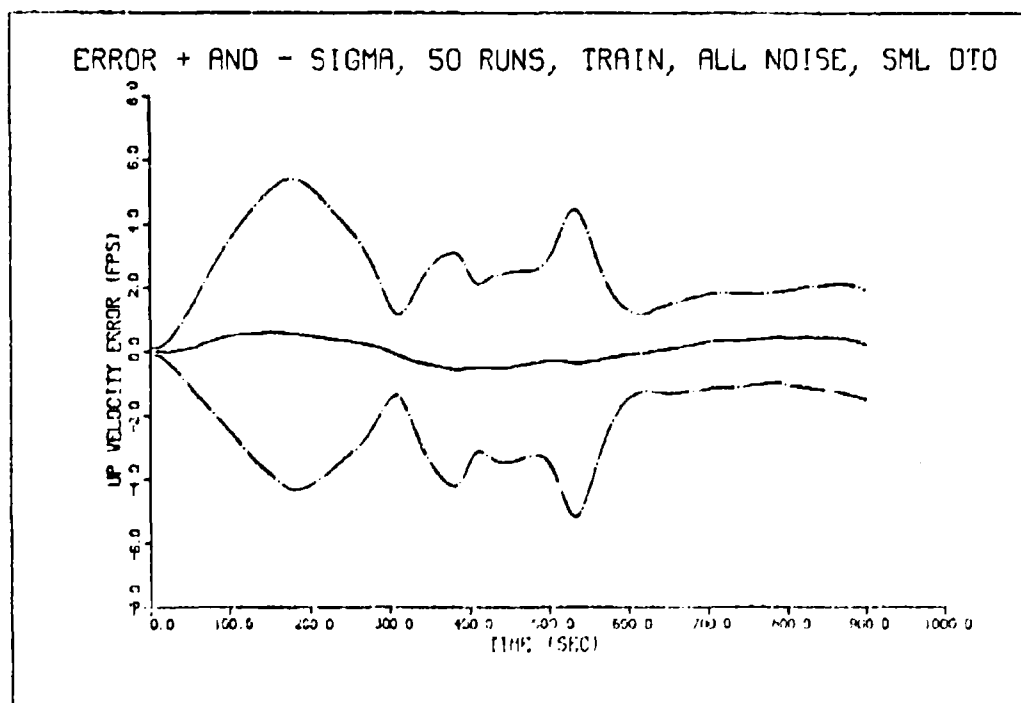


Figure 76. Up vel. error state from training profile

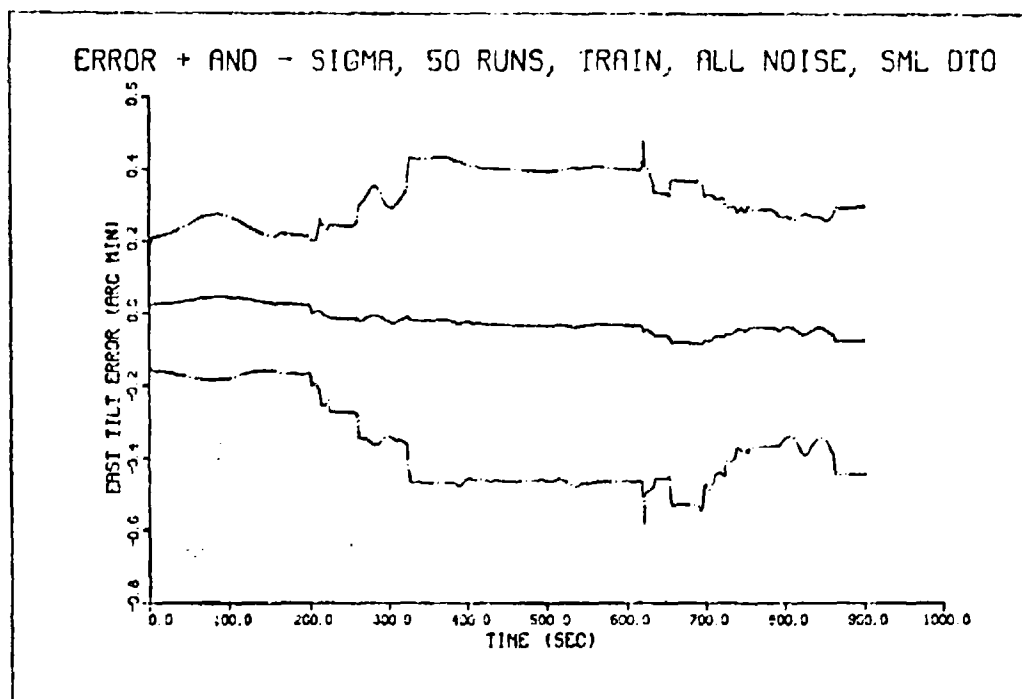


Figure 77. East tilt error state from training profile

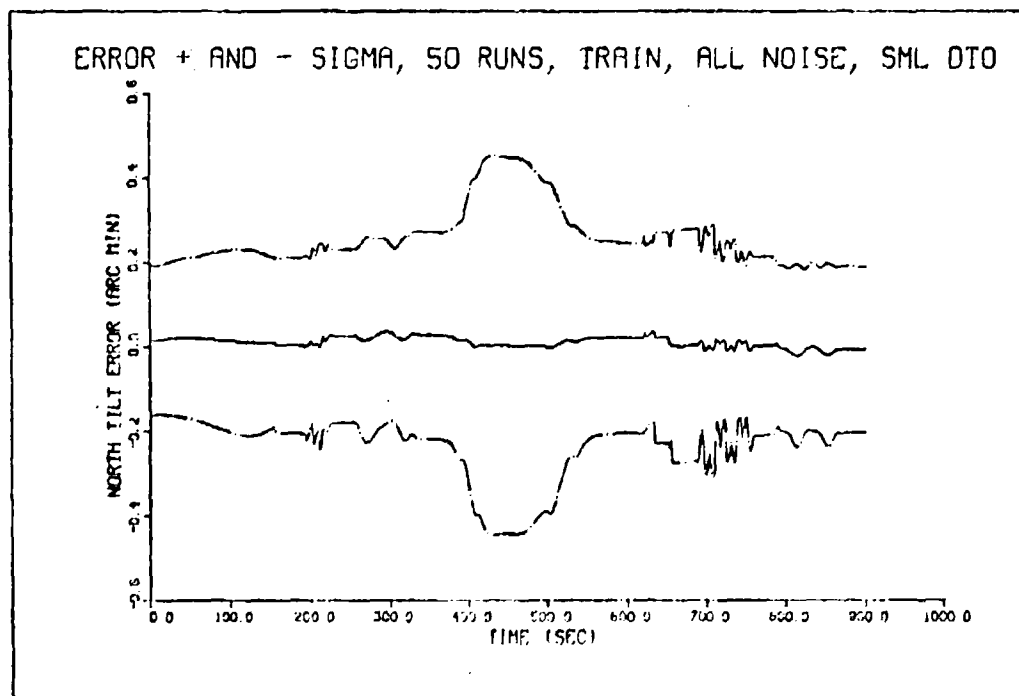


Figure 78. North tilt error state from training profile

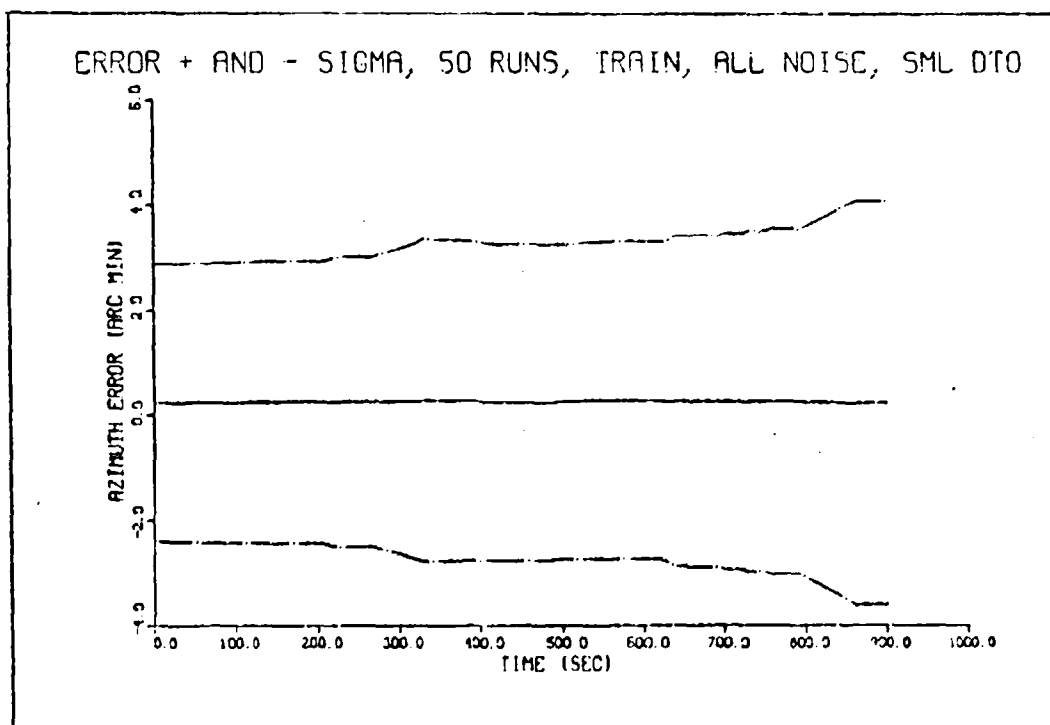


Figure 79. Azimuth error state from training profile

Comparison of these plots to the corresponding plots in Figures 62 through 70 resulting from the combat flight profile show, with the exception of the north velocity error state, that higher standard deviations of the errors are generated using the combat flight trajectory. However, the standard deviation of north velocity error for the training flight profile did remain below that of the combat profile for the first two thirds of the mission. Large maneuvers toward the end of the training flight profile caused the observed increase in velocity error.

Inspection of altitude and up velocity error plots from the training profile (Figures 75 and 76) shows lower initial peak values occurring at a later time than those induced by the combat flight profile (Figures 66 and 67). This is due to the different type of climb used to obtain initial cruise altitude. The combat profile simulates an afterburner climb to gain altitude rapidly, while a gradual, turning climb is used in the training profile. The climbing turn, unlike the straight climb in the combat mission, also generates velocity errors (Figures 73 and 74). The errors coupled into the east velocity differential error equation by north and up specific forces reinforce each other and produce a large increase in the standard deviation, while the opposite is true for east and up specific forces in the north velocity differential equations.

The tilt error states shown in Figures 77 and 78 also show some variation due to the initial turning climb. However, these changes appear small compared to the large variations shown in north tilt error from $t = 365$ until $t = 622$ seconds. During this time period, a 3.5 g loop was performed by pitching up on a heading of

205 degrees, followed by a lower, negative g loop on the same heading. Since this results in a predominately east-west oriented angular rotation vector, most of the error is generated by gyro misalignment in the north tilt error state as shown in standard deviation plotted in Figure 78. These maneuvers also cause large variations in the east velocity error state as a result of the combination of up and north specific force (Figure 73).

The remainder of the maneuvers in the training flight profile, based on the previous analysis of errors generated by the combat flight profile, produced predictable variations in the error states. The sine maneuvers, initiated at $t = 195$ seconds and $t = 689$ seconds, induced oscillatory variations in the standard deviations of the error states, but did not contribute to any large increases in system error. Figures 77 and 78 show that the 720 degree roll, initiated at $t = 652$ on a heading of 65 degrees, induced steps in the standard deviations of both east and north tilt errors. Considerable variation was induced into the velocity, tilt and azimuth error states as a result of the -480 degree, 2.5 g turn initiated at $t = 261$ seconds and, as expected, even more error was induced by the 640 degree, 4.5 g turn which started at $t = 791$ seconds.

Error Analysis Conclusions

Overall, the error analysis showed that a maneuver of longer duration, rather than high g loads, induced more system error. Relatively low acceleration (1 or 2 g) maneuvers caused little change in the error states, but a maneuver performed at two different higher acceleration loads (4.5 versus 6.5 g) induced about the same amount of tilt and azimuth error in each case. The magnitude of the variation in the

velocity error states does directly depend on the amount of specific force generated, but the cumulative effect depends upon the length of the turn.

Pitch changes generally induced the most error into the channel more closely aligned with the aircraft's heading. This is caused by gyro misalignment interacting with the pitch angular velocity vector which is perpendicular to the aircraft's heading. Scale factor errors do induce errors in the opposite channels as the misalignment generated errors, but in most cases the errors resulting from misalignment are larger. Most of the errors generated by changes in pitch directly effect the tilt errors as a result of the pitch angular velocity vector; however, the vertical specific force, f_u , also induces small variations in the velocity error states. Large, relatively high g pitch changes induce considerable system error, but a subsequent pitch change in the opposite direction of the same amount, not necessarily the same g load, cancels most of this error. However, a change in heading or attitude (especially a 180 degree roll or turn) between these maneuvers could, instead, cause these errors to reinforce each other.

Turns generate errors from three different events: roll into the turn, the turn itself, and roll out of the turn. The turns are coordinated so that some heading changes do occur during roll-in and roll-out. During the turn, the horizontal specific forces that are generated are coupled directly into the velocity differential equations by the azimuth error. This can be a considerable source of system error depending upon the amount of azimuth error and the g loads of the turn. A 180 degree turn from one cardinal heading

to another induces a step in the velocity standard deviation of the channel perpendicular to the original heading and a peak in that of the other channels. Rolls into and out of the turns, done at the performance limit of the aircraft, rather than the turn itself induce the most tilt errors. A 90 degree turn from a cardinal heading induces about the same amount of error in each channel, but a 180 degree turn induces reinforcing errors in one channel and little error in the other. Most error, as a result of gyro misalignment, is induced in the channel perpendicular to the heading as a result of the rolls into and out of the turns. Misalignment also causes a ramp in the standard deviation of azimuth error during each turn.

Isolating the roll maneuver itself proved to be very beneficial. It showed that maneuvers that are not performed on cardinal headings (those aligned with the error states) do not necessarily contribute proportional errors to each channel. While the other error sources do contribute proportion errors, the effects of the major error source, misalignment, can be cancelled depending upon the heading being flown and the previous system errors.

Maneuvers in succession that generate errors in the same direction produce more variation in the standard deviations of the error states than when each maneuver occurred separately. This effect was shown in several instances. In one case, accelerating along the flight path 45 degrees between cardinal headings only produced changes in the velocity standard deviations of the one channel. This was a result of reinforcement of the specific force generated during the previous turn.

The second flight profile did not generate quite as much overall

system error as the first one. However, each of the longer duration maneuvers did produce large system errors. It did show that a faster climb produces more vertical channel error and that sine type maneuvers produce oscillatory variations in the error states but do not contribute to significant growth in the error states. This profile also highlighted the fact that the effect of induced errors can be cancelled by performing the same maneuver in the opposite direction but not necessarily with the same acceleration loads.

VIII. Conclusions and Recommendations

Conclusions

This study evolved into two distinct phases. The first phase was the development of the error model and the computer simulation of a state-of-the-art strapdown inertial reference system, while the second phase was an analysis of the errors induced into this inertial system when driven over a highly dynamic trajectory.

A Monte Carlo simulation was chosen in preference to a covariance analysis so that computer resources could be used more efficiently. This also allowed the gyro scale factor nonlinearity to be included explicitly in the error model. A 50 run Monte Carlo simulation produced almost identical results as a covariance analysis and ran in about the same amount of computer time. Fewer than 50 runs were used for problem set up and to obtain preliminary results.

The Honeywell GG1342 ring laser gyro error model was used to represent a state-of-the-art gyro since it was recently flight tested in the A7-E. The Bell Model XI accelerometer error model was chosen because this instrument is in wide use today and has better error characteristics than the accelerometer currently being used in the Ring Laser Gyro Navigator (RLGN) with the GG1342.

Two highly dynamic flight profiles were constructed from representative performance characteristics of the F15 in its air superiority role. The more intricate "combat" flight profile was used for most of the error analysis, while the "training" flight profile was used for comparison of the overall effects of two different scenarios.

The basic result obtained from the error budget was that the gyro error sources contributed the most to overall system error.

These gyro error sources also directly coupled most of the dynamics of the flight trajectory into the variations of the system error. Misalignment was the major source of error for both the gyros and the accelerometers. Accelerometer errors caused more initial alignment error in the tilt error states than gravity errors, while gyro errors and short alignment times were responsible for most of the initial alignment errors in the azimuth error states.

Analysis of the errors generated by propagating the error model over the flight trajectories showed that, in general, a long duration medium acceleration maneuver induced more system error than a series of arbitrary maneuvers of higher accelerations. Moreover, maneuvers that occur in succession and generate reinforcing errors generally induce more system error than each maneuver separately. Also, the same maneuver performed in opposite directions produces less overall errors than performing the maneuver just once. Performance of a maneuver between cardinal headings does not necessarily induce proportional errors in each channel. One of the major contributors to system error, misalignment, can generate errors in the tilt error states that, through interaction between the tilt differential error equations, cancel themselves out. This depends upon the heading of the aircraft and the previous system errors.

Recommendations

The investigation done here was an initial step toward gaining a fundamental knowledge of the propagation of errors through a strapdown inertial reference system as a result of highly dynamic trajectories. Considerable effort was expended in setting up the complete simulation package and incorporating the stochastic error models and error equations

into the simulation. Since the general simulation program used here, SOFE, is very well documented, and the subroutines implementing the strapdown inertial reference system error model are essentially self-documenting, these should provide a solid foundation for future study in this area.

The flight profile generator, PROFGEN, has some definite disadvantages. Primarily, it does not model the dynamics of the aircraft. For highly maneuverable aircraft this causes some problems, especially in the performance of roll maneuvers. Two modifications to PROFGEN were made, one to include a roll-only maneuver and another to provide a realistic roll time constant for turns and rolls, but more changes need to be made. Out-of-plane maneuvers cannot be simulated effectively since changes in pitch, rolls and turns must be specified in separate profile segments. It is therefore recommended that another profile generator be considered for follow-on study in this area.

This study did identify the major causes of system error for the particular gyro and accelerometer model used here. Further study should include the incorporation of other ring laser gyro and accelerometer error models into the simulation to determine if these errors are typical of the particular models chosen or of a state-of-the-art model in general. This should be accompanied by a sensitivity study in which defining parameters are increased and decreased.

It was noted during this investigation that particular maneuvers reinforced errors while others cancelled some system error. More data needs to be generated and more extensive analysis is necessary in order to provide firm guidelines as to which maneuvers should be employed or avoided when possible. Also, the various types of

optimal aiding should be explored to determine the reduction of system error caused by each in this highly dynamic environment.

Bibliography

1. Aronowitz, Frederick. "The Laser Gyro," Laser Applications, Vol.1. New York: Academic Press, 1971.
2. Bachman, K.L. and R.J. Skoyles. Ring Laser Gyro Navigator Flight Test. Honeywell Pamphlet No. 41095, presented at the Guidance and Navigation Symposium, Holloman AFB, New Mexico, October 1979.
3. Bell, Jack W. Electronics Engineer. Personal correspondence. Air Force Avionics Laboratory, Wright-Patterson AFB, Ohio, January 17, 1980.
4. Britting, K.R. Inertial Navigation System Analysis. New York: John Wiley and Sons, Inc., 1971.
5. Culpepper, Mark A., et.al. Laboratory Tests of the Bell Model-XI Accelerometer. ADTC-TR-77-50. Eglin AFB, Florida: Armament Development and Test Center, 1977.
6. Feldman, Richard E. SOFEPL: A Plotting Post-Processor for "SOFE", User's Manual. UDRI-TR-78-88. Dayton, Ohio: University of Dayton Research Institute, 1978.
7. Maybeck, Peter S. "Performance Analysis of a Particularly Simple Kalman Filter," Journal of Guidance and Control, 1: 391-96 (November-December 1978).
8. -----. Stochastic Models, Estimation, and Control, Volume 1. New York: Academic Press, 1979.
9. Mercier, Robert A. Chief, Effectiveness Analysis Group. Personal interview. Air Force Flight Dynamics Laboratory, Wright-Patterson AFB, Ohio, June 17, 1980.
10. -----. Extracted data from ACEVAL tape no. 7299C2. Nellis AFB, Nevada, 1977.
11. Musick, Stanton H. PROFGEN - A Computer Program for Generating Flight Profiles. AFAL-TR-76-247. Wright-Patterson AFB, Ohio: Air Force Avionics Laboratory, November 1976.
12. -----. SOFE: A Generalized Digital Simulation for Optional Filter Evaluation User's Manual. AFAL-TM-78-19. Wright-Patterson AFB, Ohio: Air Force Avionics Laboratory, June 1978.
13. Pinson, J.C. "Inertial Guidance for Cruise Vehicles," Guidance and Control of Aerospace Vehicles, edited by C.T. Leondes. New York: McGraw-Hill Book Company, 1963.
14. Reynolds, Richard H. "Deterministic Analysis of the Effects of Sensor or Strapped-Down IIRs Performance." Unpublished MS Thesis. School of Engineering, Air Force Institute of Technology, Wright-Patterson AFB, Ohio, December 1979.

15. Sinha, Prasun K. Integrated GPS/Strapdown Inertial Simulation Computer Program. IR-253. Cambridge, Massachusetts: Intermetrics Incorporated, December 1977.
16. T.O. 1F-15A-1. Flight Manual. Warner-Robins AFB, Georgia: Air Force Logistics Command, December 1, 1979 (Ch.1 March 1, 1980).
17. Widnall, William S. and Peter A. Grundy. Inertial Navigation System Error Models. TR-03-73 Technical Report for 6585th Test Group, Holloman AFB, New Mexico. Cambridge, Massachusetts: Intermetrics Incorporated, May 1973.
18. Widnall, William S. and Prasun K. Sinha. "Optimizing the Gains of the Baro-Inertial Vertical Channel," Journal of Guidance and Control, 3: 172-78 (March-April 1980).

Appendix A

SOFE: A Generalized Digital Simulation for Optional Filter Evaluation (Ref 12)

SOFE was developed as an efficient general purpose simulation program for the design of Kalman filters. Although filter design was beyond the context of this thesis, SOFE was used for both the generation of a Monte Carlo simulation using a truth model, and for covariance propagation of the error state equations for a filter based on the truth model and having no input measurements.

The basic SOFE program contains 34 routines which perform input/output, problem setup, run setup, numerical integration, and run termination. Nine additional subroutines must be written by the user of the program to specify the problem to be simulated. These nine routines supply derivatives, measurements, truth model fluctuations, and trajectory data. All of the programming was set up to be efficient in both the use of core and time. This was done by dense packing arrays and vectors into a single array, using singly subscripted variables, using sparse matrix storage techniques, and exploiting the symmetric properties of some of the matrices.

A truth model in SOFE is a direct implementation of the error state equations. The 9 subroutines and data required to develop the truth model are shown in Appendix F. Differential equations for the model, without the driving noises, are propagated through time by a fifth order Runge-Kutta integrator. At intervals specified by the user of the program, the integration is stopped to allow for measurement updates, the addition of noise to the truth model, feedback,

output, or whatever is specified by the program user. A subroutine, GAUSS, is provided in SOFE for generating random Gaussian samples. SOFE was implemented in this simulation to stop integration just for the addition of noise to the truth model and to generate output. No measurements or feedback were used.

The filter model in SOFE is implemented by specifying both the filter error state equations and the initial covariance matrix. Propagation of the filter error state equations by the integrator is much the same as the propagation of the homogeneous truth error state equations. However, rather than periodically adding noise to the states, the covariance of the error, $P(t)$, is also propagated forward in time by numerically integrating the equation

$$\dot{P}(t) = F(t)P(t) + P(t)F(t)^T + Q(t) \quad (A-1)$$

corresponding to the state equation $\dot{\underline{x}}(t) = F(t)\underline{x}(t) + \underline{w}(t)$, where

$F(t)$ = fundamental matrix

$Q(t)$ = white driving noise matrix

such that $E(\underline{w}(t)\underline{w}^T(t + \tau)) = Q(t)\delta(\tau)$

The 9 subroutines and data necessary to implement a filter model are shown in Appendix G. A complete explanation of Equation (A-1) and filter models can be found in Reference 8.

Out of the 9 user written subroutines available in SOFE, only 6 were utilized in this simulation. USRIN, which is only called once by SOFE for problem initialization, was used to read in time constants and initial standard deviations of the error states. Subroutine TRAJ was used only to specify some constants, since an external flight

trajectory was generated. Subroutines XFDOT and XSDOT specify the homogeneous differential equations of the filter model and truth model. These two subroutines were essentially the same in this case since a full order filter was used. Subroutine SNOYS is used in conjunction with the truth model. It is called at intervals to inject noise into the appropriate states to simulate the driving noise, $w(t)$. Subroutine FQGEN is used to specify Equation (A-1) for the propagation of the covariance matrix associated with the filter model. All of these subroutines, except USRIN, are called at the beginning of each Monte Carlo run, through a FORTRAN ENTRY statement, to initialize data or variables particular to that routine.

In addition to supplying 9 subroutines, 37 parameters are entered through a list called PRDATA in CDC NAMELIST FORMAT. These are parameters which remain fixed throughout the simulation. They specify the problem content, control input and output, and regulate the numerical integration.

APPENDIX B

SOFE SUBROUTINES FOR ERROR ANALYSIS

```
SUBROUTINE AMEND(IRUN,T,NF,NS,NXTJ,XF,XS,XTRAJ)
DIMENSION XF(NF),XS(NS),XTRAJ(NXTJ)
RETURN
ENTRY AMEND0
RETURN
END
```

```
SUBROUTINE ESTIX(IRUN,T,NF,NS,NXTJ,XF,XS,XTRAJ,NTR,PF)
DIMENSION XF(NF),XS(NS),XTRAJ(NXTJ),PF(NTR)
RETURN
ENTRY ESTIX0
RETURN
END
```

```
SUBROUTINE FQGEN(IRUN,T,NF,NS,NXTJ,XF,XS,XTRAJ,
&NZF,NZQ,F,Q)
DIMENSION XF(NF),XS(NS),XTRAJ(NXTJ),F(NZF),Q(NZQ)
RETURN
ENTRY FQGEN0
RETURN
END
```

```
SUBROUTINE HRZ(IRUN,T,NF,NS,NXTJ,XF,XS,XTRAJ,NTR,PF,IMEAS,
&M,H,R,ZRES)
DIMENSION XF(NF),XS(NS),H(NF),XTRAJ(NXTJ),PF(NTR)
RETURN
ENTRY HRZ0
RETURN
END
```

```
SUBROUTINE SNOYS(IRUN,T,NF,NS,NXTJ,XF,XS,XTRAJ)
```

```
COMMON/SNOIS/SDWS(60),SDWS(13),SDWFO(1)
COMMON/TCSYS/TAUS(3),DIST(4)
COMMON/TRJCOM/RE,G,OMEGA,E,RK1,RK2,RK3
DIMENSION XF(NF),XS(NS),XTRAJ(NXTJ)
```

```
VGND=SQRT(XTRAJ(8)**2+XTRAJ(9)**2)
DT=T-TOLD
SRDT=SQRT(DT)
```

```
STDEV=SDWS(1)*SRDT
XS(7)=XS(7)+GAUSS(0.0,STDEV)
STDEV=SDWS(2)*SRDT
XS(8)=XS(8)+GAUSS(0.0,STDEV)
STDEV=SDWS(3)*SRDT
XS(9)=XS(9)+GAUSS(0.0,STDEV)
```

```

15  STDEV=SDWS(4)*SROT
    XS(4)=XS(4)+GAUSS(0.0,STDEV)
    STDEV=SDWS(5)*SROT
    XS(5)=XS(5)+GAUSS(0.0,STDEV)
    STDEV=SDWS(6)*SROT
    XS(6)=XS(6)+GAUSS(0.0,STDEV)
20  STDEV=SDWS(7)*SQRT(2.*DT/TAUS(1))
    XS(26)=XS(26)+GAUSS(0.0,STDEV)
    STDEV=SDWS(8)*SQRT(2.*DT/TAUS(2))
    XS(27)=XS(27)+GAUSS(0.0,STDEV)
    STDEV=SDWS(9)*SQRT(2.*DT/TAUS(3))
    XS(28)=XS(28)+GAUSS(0.0,STDEV)
30  STDEV=SDWS(10)*SQRT(2.*DT*VGND/DIST(1))
    XS(56)=XS(56)+GAUSS(0.0,STDEV)
40  STDEV=SDWS(11)*SQRT(2.*DT*VGND/DIST(2))
    XS(58)=XS(58)+GAUSS(0.0,STDEV)
    STDEV=SDWS(12)*SQRT(2.*DT*VGND/DIST(3))
    XS(59)=XS(59)+GAUSS(0.0,STDEV)
    STDEV=SDWS(13)*SQRT(2.*DT*VGND/DIST(4))
    XS(60)=XS(50)+GAUSS(0.0,STDEV)
50  CONTINUE
    ENTRY SNOYSO
    TOLD=T
    RETURN
    END

SUBROUTINE TRAJ(IRUN,T,NF,NS,NXTJ,XF,XS,XTRAJ)
COMMON/TRJCOM/RE,G,OMEGA,E,RK1,RK2,RK3
DIMENSION XF(NF),XS(NS),XTRAJ(NXTJ)
DIMENSION TITLE(20)
DIMENSION SEGLNT(50),RESTRT(50),ITURN(50),NPATH(50),PACC(50)
DIMENSION TACC(50),HEAD(50),PIT(50),DTQ(50),MODE(50)
DIMENSION ERROR(50),HMAX(50),HMIN(50)
RETURN
ENTRY TRAJD

READ (3) TITLE,TODAY,CLOCK
READ (3) IPR03,NSEGT,LLMECH,TSTART,VTO,PHEAD0,PITO,
& ALFA0,LAT0,LON0,ALTO,IPRNT,IRITE,IPLOT,ROLRAT,LUNIT
READ (3) SEGLNT,RESTRT,ITURN,NPATH,PACC,TACC,HEAD,
& PIT,DTQ,MODE,ERROR,HMAX,HMIN
IF (IRUN.GT.1) GO TO 10

CALL PACCON(44,1)
WRITE (6,100) TITLE,TODAY,CLOCK
100 FORMAT(1X,7HTITLE: ,20A4/1X,7HDATE: ,A10/1X,7HTIME: ,A10)

PRINT*," IPR03: ",IPR03
PRINT*," NSEGT: ",NSEGT
PRINT*," LLMECH:",LLMECH
PRINT*," TSTART:",TSTART

```

```

PRINT*, " VTO: ", VTO
PRINT*, " PHEAD: ", PHEAD
PRINT*, " PITCH: ", PITCH
PRINT*, " ALFA: ", ALFA
PRINT*, " IPRNT: ", IPRNT
PRINT*, " IRITE: ", IRITE
PRINT*, " IPLOT: ", IPLOT
PRINT*, " ROLRAT: ", ROLRAT
PRINT*, " LUNIT: ", LUNIT
PRINT*, " "
PRINT*, " SEGLNT: ", SEGLNT
PRINT*, " RESTR: ", RESTR
PRINT*, " ITURN: ", ITURN
PRINT*, " NPATH: ", NPATH
PRINT*, " PACC: ", PACC
PRINT*, " TACC: ", TACC
PRINT*, " HEAD: ", HEAD
PRINT*, " PITCH: ", PIT
PRINT*, " DTO: ", DTO
PRINT*, " MODE: ", MODE
PRINT*, " ERROR: ", ERROR
PRINT*, " HMAX: ", HMAX
PRINT*, " HMIN: ", HMIN

```

10 CONTINUE

```

RE=20925640.
G=32.0881576
OMEGA=.72921151E-4
E=1./293.3

```

C STANDARD K VALUES ARE K1=3.E-2, K2=3.E-4, K3=1.E-6

C OPTIMAL K VALUES ARE K1=1.003, K2=4.17E-3, K3=4.39E-6

```

RK1=3.E-2
RK2=3.E-4
RK3=1.E-6
RETURN
END

```

```

SUBROUTINE USRIN
COMMON/SNGIS/SDWSD(60),SDWS(13),SDWFO(1)
COMMON/TCSYS/TAUS(3),DIST(4)
NAMELIST/INS/TAUS,DIST,SDWSD,SDWS,SDWFO

```

```

CALL PAGCON(60,1)
PRINT*, " X(1) EAST LONGITUDE"
PRINT*, " X(2) NORTH LATITUDE"
PRINT*, " X(3) ALTITUDE (UP)"
PRINT*, " X(4) EAST VELOCITY"
PRINT*, " X(5) NORTH VELOCITY"

```

```

PRINT#," X(6)  VERTICAL VELOCITY"
PRINT#," X(7)  EAST ATTITUDE      "
PRINT#," X(8)  NORTH ATTITUDE     "
PRINT#," X(9)  UP ATTITUDE        "
PRINT#," X(10) INTEGRAL OF VERTICAL CHANNEL ERROR "
PRINT#," X(11) X GYRO DRIFT RATE  "
PRINT#," X(12) Y GYRO DRIFT RATE  "
PRINT#," X(13) Z GYRO DRIFT RATE  "
PRINT#," X(14) X GYRO SCALE FACTOR "
PRINT#," X(15) Y GYRO SCALE FACTOR "
PRINT#," X(16) Z GYRO SCALE FACTOR "
PRINT#," X(17) X GYRO MISALIGN ABOUT Y "
PRINT#," X(18) X GYRO MISALIGN ABOUT Z "
PRINT#," X(19) Y GYRO MISALIGN ABOUT X "
PRINT#," X(20) Y GYRO MISALIGN ABOUT Z "
PRINT#," X(21) Z GYRO MISALIGN ABOUT X "
PRINT#," X(22) Z GYRO MISALIGN ABOUT Y "
PRINT#," X(23) X ACCELEROMETER  BIAS "
PRINT#," X(24) Y ACCELEROMETER  BIAS "
PRINT#," X(25) Z ACCELEROMETER  BIAS "
PRINT#," X(26) X ACCELEROMETER 60 SEC BIAS "
PRINT#," X(27) Y ACCELEROMETER 60 SEC BIAS "
PRINT#," X(28) Z ACCELEROMETER 60 SEC BIAS "
PRINT#," X(29) X ACCELEROMETER INPUT QUADRATIC (X AXIS) "
PRINT#," X(30) Y ACCELEROMETER CROSS QUADRATIC (X AXIS) "
PRINT#," X(31) Z ACCELEROMETER CROSS QUADRATIC (X AXIS) "
PRINT#," X(32) X ACCELEROMETER CROSS QUADRATIC (Y AXIS) "
PRINT#," X(33) Y ACCELEROMETER INPUT QUADRATIC (Y AXIS) "
PRINT#," X(34) Z ACCELEROMETER CROSS QUADRATIC (Y AXIS) "
PRINT#," X(35) X ACCELEROMETER CROSS QUADRATIC (Z AXIS) "
PRINT#," X(36) Y ACCELEROMETER CROSS QUADRATIC (Z AXIS) "
PRINT#," X(37) Z ACCELEROMETER INPUT QUADRATIC (Z AXIS) "
PRINT#," X(38) X ACCELEROMETER CROSS SCALE FACTOR (X,Y) "
PRINT#," X(39) Y ACCELEROMETER CROSS SCALE FACTOR (X,Y) "
PRINT#," X(40) Z ACCELEROMETER CROSS SCALE FACTOR (X,Y) "
PRINT#," X(41) X ACCELEROMETER CROSS SCALE FACTOR (X,Z) "
PRINT#," X(42) Y ACCELEROMETER CROSS SCALE FACTOR (X,Z) "
PRINT#," X(43) Z ACCELEROMETER CROSS SCALE FACTOR (X,Z) "
PRINT#," X(44) X ACCELEROMETER CROSS SCALE FACTOR (Y,Z) "
PRINT#," X(45) Y ACCELEROMETER CROSS SCALE FACTOR (Y,Z) "
PRINT#," X(46) Z ACCELEROMETER CROSS SCALE FACTOR (Y,Z) "
PRINT#," X(47) X ACCELEROMETER SCALE FACTOR "
PRINT#," X(48) Y ACCELEROMETER SCALE FACTOR "
PRINT#," X(49) Z ACCELEROMETER SCALE FACTOR "
PRINT#," X(50) X ACCELEROMETER MISALIGN ABOUT Y "
PRINT#," X(51) X ACCELEROMETER MISALIGN ABOUT Z "
PRINT#," X(52) Y ACCELEROMETER MISALIGN ABOUT X "
PRINT#," X(53) Y ACCELEROMETER MISALIGN ABOUT Z "
PRINT#," X(54) Z ACCELEROMETER MISALIGN ABOUT X "
PRINT#," X(55) Z ACCELEROMETER MISALIGN ABOUT Y "
PRINT#," X(56) BAR PRES "

```

```

PRINT*, " X(57) BAR SCALE FACTOR "
PRINT*, " X(58) EAST DEFL GRAVITY "
PRINT*, " X(59) NDR DEFL GRAVITY "
PRINT*, " X(60) GRAVITY ANOMALY "

```

```

READ(5,INS)
WRITE(6,100) TAUS,DIST,SDWSO,SDWS,SDWFO
RETURN

```

```

100 FORMAT("1"5(//)T10"TRUTH MODEL DATA-BASE FROM
&NAMELIST INS: "
&//T15"TIME CONSTANTS, TAUS "
&/T20,3G14.7
&//T15"CORRELATION DISTANCE, DIST "
&/T20,4G14.7
&//T15"SDWS")
&/10(//T20,6G14.7)
&//T15"SDWS"
&/2(//T20,6G14.7)/T20,6G14.7
&//T15"SDWFO"
&/T20,1G14.7)
END

```

```

SUBROUTINE XFDOT(IRUN,T,NF,NS,NXTJ,XF,XS,XTRAJ,NTR,P=XDOT)
COMMON/TRJCOM/RE,G,OMEGA,E,RK1,RK2,RK3
COMMON/SNOIS/SDWSO(60),SDWS(13),SDWFO(1)
DIMENSION XF(NF),XDOT(NF),XS(NS),XTRAJ(NXTJ),P=(NTR)
XDOT(1)=0.
RETURN
ENTRY XFDOTO
XF(1)=0.
RETURN
END

```

```

SUBROUTINE XSDOT(IRUN,T,NF,NS,NXTJ,XF,XS,XTRAJ,XDOT)
DIMENSION XF(NF),XS(NS),XTRAJ(NXTJ),XDOT(NS)

```

```

COMMON/TCSYS/TAUS(3),DIST(4)
COMMON/SNOIS/SDWSO(60),SDWS(13),SDWFO(1)
COMMON/TRJCOM/RE,G,OMEGA,E,RK1,RK2,RK3

```

C 16 TRAJECTORY INPUTS FROM PROFGEN

```

RLAT=XTRAJ(1)
RLON=XTRAJ(2)
ALPHA=XTRAJ(3)
ALT=XTRAJ(4)
ROL=XTRAJ(5)
PIT=XTRAJ(6)
YAW=XTRAJ(7)
VN=XTRAJ(8)
VE=-XTRAJ(9)

```

```

VU=XTRAJ(10)
FN=XTRAJ(11)
FE=-XTRAJ(12)
FU=XTRAJ(13)
DROL=XTRAJ(14)
DPIT=XTRAJ(15)
DYAW=XTRAJ(16)

```

```

VGND=SQRT(VN**2+VE**2)
SLAT=SIN(RLAT)
CLAT=COS(RLAT)
TLAT=SLAT/CLAT
OMEGAN=OMEGA*CLAT
OMEGAU=OMEGA*SLAT
SX=SIN(ROL)
CX=COS(ROL)
SY=SIN(PIT)
CY=COS(PIT)
SZ=SIN(YAW)
CZ=COS(YAW)
SA=SIN(ALPHA)
CA=COS(ALPHA)
SLON=SIN(RLON)
CLON=COS(RLON)

```

C RHO IS THE ANGULAR VELOCITY OF THE NAV FRAME WRT EARTH

```

RHOE=-VN/RE
RHON=VE/RE
RHOU=VE*TLAT/RE

```

C WE-WN-WU ARE THE ANGULAR VELOCITY OF THE NAV FRAME WRT
C INERTIAL FRAME COORDINATIZED IN THE NAV FRAME (E-N-U)

```

WE=RHOE
WN=RHON+OMEGAN
WU=RHOU+OMEGAU

```

C COMPONENTS OF THE PINSON MATRIX

```

RKZ=VU/RE
RLAT2=2.*RLAT
F42=2.*(OMEGAN*VN+OMEGAU*VU)+RHON*VN/(CLAT**2)
F43=RHOU*RHOE+RHON*RKZ
F44=-RHOE*TLAT-RKZ
F52=-2.*OMEGAN*VE-RHON*VE/CLAT**2
F53=RHON*RHOU-RHOE*RKZ
F63=2.*G/RE-RHON**2-RHOE**2
F72=WN+RHOU*TLAT

```

C TRANSFORMATION FROM NAV FRAME (E-N-U) TO BODY FRAME (X-Y-Z)


```

CXE=SZ*CY
CXN=CZ*CY
CXU=SY
CYE=SZ*SY*SX+CZ*CX
CYN=CZ*SY*SX-SZ*CX
CYU=-CY*SX
CZE=-CZ*SX+SZ*SY*CX
CZN=CZ*SY*CX+SZ*SX
CZU=-CY*CX

```

C TRANSFORMATION FROM BODY FRAME (X-Y-Z) TO NAV FRAME (E-N-U)

```

CEX=CXE
CEY=CYE
CEZ=CZE
CNX=CXN
CNY=CYN
CNZ=CZN
CUX=CXU
CUY=CYU
CUZ=CZU

```

C SPECIFIC FORCE IN THE BODY FRAME

```

FX=CXN*FN+CXE*FE+CXU*FU
FY=CYN*FN+CYE*FE+CYU*FU
FZ=CZN*FN+CZE*FE+CZU*FU

```

C ANGULAR VELOCITY OF BODY FRAME WRT INERTIAL FRAME
C COORDINATIZED IN THE BODY FRAME

```

WX=CXE*WE+CXN*WN+CXU*WU+OROL
WY=CYE*WE+CYN*WN+CYU*WU+DPIT
WZ=CZE*WE+CZN*WN+CZU*WU+OYAW

```

C INSERT 2.5 PPM SCALE FACTOR NONLINEARITY

```

XSFNL=0.0
YSFNL=0.0
ZSFNL=0.0
AWX=ABS(WX)
AWY=ABS(WY)
AWZ=ABS(WZ)
IF((AWX.GT.2.4434609).OR.(AWX.LT.1.3962634)) GO TO 20
XSFNL=9.11997E-6*WX**2-3.50189E-5*AWX+3.11166E-5
20 IF((AWY.GT.2.4434609).OR.(AWY.LT.1.3962634)) GO TO 30
YSFNL=9.11997E-6*WY**2-3.50189E-5*AWY+3.11166E-5
30 IF((AWZ.GT.2.4434609).OR.(AWZ.LT.1.3962634)) GO TO 40
ZSFNL=9.11997E-6*WZ**2-3.50189E-5*AWZ+3.11166E-5

```

40 CONTINUE

XDOT(1)=XS(2)*RHOU/CLAT-XS(3)*RHON/(RE*CLAT)+XS(4)/
E(RF*CLAT)

XDOT(2)=XS(3)*RHOE/RE+XS(5)/RE

XDOT(3)=-R<1*XS(3)+XS(6)+XS(56)*RK1+XS(57)*RK1*ALT

XDOT(4)=XS(2)*F42+XS(3)*F43+XS(4)*F44+XS(5)*(4J+OMEGAU)

E-XS(6)*(WN+OMEGAN)-XS(8)*FU+XS(9)*FN

E+XS(23)*CFX+XS(24)*CEY+XS(25)*CEZ

E+XS(26)*CEX+XS(27)*CEY+XS(28)*CEZ

E+XS(29)*CEX*FX*FX+XS(30)*CEY*FX*FX+XS(31)*CEZ*FX*FX

E+XS(32)*CEX*FY*FY+XS(33)*CEY*FY*FY+XS(34)*CEZ*FY*FY

E+XS(35)*CEX*FZ*FZ+XS(36)*CEY*FZ*FZ+XS(37)*CEZ*FZ*FZ

E+XS(38)*CEX*FX*FY+XS(39)*CEY*FX*FY+XS(40)*CEZ*FX*FY

E+XS(41)*CEX*FX*FZ+XS(42)*CEY*FX*FZ+XS(43)*CEZ*FX*FZ

E+XS(44)*CEX*FY*FZ+XS(45)*CEY*FY*FZ+XS(46)*CEZ*FY*FZ

E+XS(47)*CEX*FX+XS(48)*CEY*FY+XS(49)*CEZ*FZ

E-XS(50)*CEX*FZ+XS(51)*CEX*FY+XS(52)*CEY*FZ

E-XS(53)*CEY*FX-XS(54)*CEZ*FY+XS(55)*CEZ*FX+XS(58)

XDOT(5)=XS(2)*F52+XS(3)*F53-XS(4)*2.*WU-XS(5)*RKZ

E+XS(6)*RHOE+XS(7)*FU-XS(9)*FE

E+XS(23)*CNX+XS(24)*CNY+XS(25)*CNZ

E+XS(26)*CNX+XS(27)*CNY+XS(28)*CNZ

E+XS(29)*CNX*FX*FX+XS(30)*CNY*FX*FX+XS(31)*CNZ*FX*FX

E+XS(32)*CNX*FY*FY+XS(33)*CNY*FY*FY+XS(34)*CNZ*FY*FY

E+XS(35)*CNX*FZ*FZ+XS(36)*CNY*FZ*FZ+XS(37)*CNZ*FZ*FZ

E+XS(38)*CNX*FX*FY+XS(39)*CNY*FX*FY+XS(40)*CNZ*FX*FY

E+XS(41)*CNX*FX*FZ+XS(42)*CNY*FX*FZ+XS(43)*CNZ*FX*FZ

E+XS(44)*CNX*FY*FZ+XS(45)*CNY*FY*FZ+XS(46)*CNZ*FY*FZ

E+XS(47)*CNX*FX+XS(48)*CNY*FY+XS(49)*CNZ*FZ

E-XS(50)*CNX*FZ+XS(51)*CNX*FY+XS(52)*CNY*FZ

E-XS(53)*CNY*FX-XS(54)*CNZ*FY+XS(55)*CNZ*FX+XS(59)

XDOT(6)=-XS(2)*2.*OMEGAU*VE+XS(3)*(F63-RK2)+XS(4)*2.*WN

E-XS(5)*2.*RHOE-XS(7)*FN+XS(8)*FE-XS(10)

E+XS(23)*CUX+XS(24)*CUY+XS(25)*CUZ

E+XS(26)*CUX+XS(27)*CUY+XS(28)*CUZ

E+XS(29)*CUX*FX*FX+XS(30)*CUY*FX*FX+XS(31)*CUZ*FX*FX

E+XS(32)*CUX*FY*FY+XS(33)*CUY*FY*FY+XS(34)*CUZ*FY*FY

E+XS(35)*CUX*FZ*FZ+XS(36)*CUY*FZ*FZ+XS(37)*CUZ*FZ*FZ

E+XS(38)*CUX*FX*FY+XS(39)*CUY*FX*FY+XS(40)*CUZ*FX*FY

E+XS(41)*CUX*FX*FZ+XS(42)*CUY*FX*FZ+XS(43)*CUZ*FX*FZ

E+XS(44)*CUX*FY*FZ+XS(45)*CUY*FY*FZ+XS(46)*CUZ*FY*FZ

E+XS(47)*CUX*FX+XS(48)*CUY*FY+XS(49)*CUZ*FZ

E-XS(50)*CUX*FZ+XS(51)*CUX*FY+XS(52)*CUY*FZ

E-XS(53)*CUY*FX-XS(54)*CUZ*FY+XS(55)*CUZ*FX

E+XS(56)*RK2+XS(57)*RK2*ALT+XS(60)

XDOT(7)=-XS(3)*RHOE/RE-XS(5)/RE+XS(8)*WU-XS(9)*WN

```

E+XS(11)*CEX+XS(12)*CEY+XS(13)*CFZ
E+(XS(14)+XSFNL)*CEX*WX+(XS(15)+YSFNL)*CEY*WY
E+(XS(16)+ZSFNL)*CEZ*WZ
E+XS(17)*CEX*WZ-XS(18)*CEX*WY-XS(19)*CEY*WZ
E+XS(20)*CEY*WX+XS(21)*CEZ*WY-XS(22)*CEZ*WX

```

```

XDOT(8)=-XS(2)*OMEGAJ-XS(3)*RHON/RE+XS(4)/RE-XS(7)*WJ
E+XS(9)*WE+XS(11)*CNX+XS(12)*CNY+XS(13)*CNZ
E+(XS(14)+XSFNL)*CNX*WX+(XS(15)+YSFNL)*CNY*WY
E+(XS(16)+ZSFNL)*CNZ*WZ
E+XS(17)*CNX*WZ-XS(18)*CNX*WY-XS(19)*CNY*WZ
E+XS(20)*CNY*WX+XS(21)*CNZ*WY-XS(22)*CNZ*WX

```

```

XDOT(9)=XS(2)*F92-XS(3)*RHOU/RE+XS(4)*TLAT/RE+XS(7)*WN
E-XS(8)*WE+XS(11)*CUX+XS(12)*CUY+XS(13)*CUZ
E+(XS(14)+XSFNL)*CUX*WX+(XS(15)+YSFNL)*CUY*WY
E+(XS(16)+ZSFNL)*CUZ*WZ
E+XS(17)*CUX*WZ-XS(18)*CUX*WY-XS(19)*CUY*WZ
E+XS(20)*CUY*WX+XS(21)*CUZ*WY-XS(22)*CUZ*WX

```

```

XDOT(10)=XS(3)*RK3-XS(56)*RK3-XS(57)*RK3*ALT

```

```

DO 2 I=11,25
2 XDOT(I)=0.

```

```

XDOT(26)=-XS(26)/TAUS(1)
XDOT(27)=-XS(27)/TAUS(2)
XDOT(28)=-XS(28)/TAUS(3)

```

```

DO 4 I=29,55
4 XDOT(I)=0.

```

```

XDOT(56)=-XS(56)*VGND/DIST(1)
XDOT(57)=0.
XDOT(58)=-XS(58)*VGND/DIST(2)
XDOT(59)=-XS(59)*VGND/DIST(3)
XDOT(60)=-XS(60)*VGND/DIST(4)
RETURN

```

```

ENTRY XSDOTO
DO 11 I=1,6
11 XS(I)=GAUSS(0.,SDWSO(I))
DO 13 I=11,22
13 XS(I)=GAUSS(0.,SDWSO(I))
DO 15 I=23,55
15 XS(I)=GAUSS(0.,SDWSO(I))
DO 17 I=56,57
17 XS(I)=GAUSS(0.,SDWSO(I))
DO 19 I=58,60
19 XS(I)=GAUSS(0.,SDWSO(I))

```

C SET STEADY STATE AND CORRELATED INITIAL CONDITIONS

```

ALT=XTRAJ(4)
RLAT=XTRAJ(1)
OMEGAN=OMEGA*COS(RLAT)
OMEGAU=OMEGA*SIN(RLAT)
RANHEAD=GAUSS(.0,1.8138)
CHEAD=COS(RANHEAD)
SHEAD=SIN(RANHEAD)

```

```

XS(3)=XS(56)+XS(57)*ALT
XS(7)=-((XS(23)/G+XS(26)/G+XS(35)*G+XS(50))*CHEAD
E      +((XS(24)/G+XS(27)/G+XS(36)*G-XS(52))*SHEAD
E      - XS(59)/G
XS(8)= ((XS(24)/G+XS(27)/G+XS(36)*G-XS(52))*CHEAD
E      +((XS(23)/G+XS(26)/G+XS(35)*G+XS(50))*SHEAD
E      + XS(58)/G
XS(9)=(XS(8)*OMEGAU
E      + (XS(12)-XS(15)*OMEGAN*SHEAD+XS(19)*OMEGAU
E      + XS(20)*OMEGAN*CHEAD)*CHEAD
E      + (XS(11)+XS(14)*OMEGAN*CHEAD-XS(17)*OMEGAU
E      + XS(18)*OMEGAN*SHEAD)*SHEAD)/OMEGAN
XS(10)=(2.*G/RE)*XS(3)-XS(25)-XS(28)-XS(37)*G*G+XS(49)*G
E      + XS(50)

```

```

RETURN
END

```

TRUTH MODEL FOR HONEYWELL GG1342 RLG AND BELL MOD 11 ACCELEROMETER

```

$PRDATA
NF=1, NS=60, TF=900., DTPRNT=150., DTN3YS=2., DTPRPL=9.,
LPRXF=.F., LPRLT=.F., LPRDG=.F., LPP=.T., NXTJ=16, LXTJ=.T.,
M=0, LPRXTJ=.T., _CC=.T., DTCCPL=2., IPASS=50,
$

```

60*0.

1*0.

1,1,1.

0,0,0.

\$INS TAUS(1)=60.,60.,60.,

\$IST(1)=1519025.8,60761.0333,60761.0333,364566.19,

\$OWSD(1)=1.67944E-5, 1.67944E-5, 28.877513 ,

```

1.      , 1.      , 1.      E-1,
5.      E-4, 5.      E-4, 9.      E-4,

```

1. E-2,
 3.87850E-8, 3.87850E-8, 3.87850E-8,
 5. E-6, 5. E-6, 5. E-6,
 2.5 E-5, 2.5 E-5, 2.5 E-5,
 2.5 E-5, 2.5 E-5, 2.5 E-5,
 4.55375E-4, 4.55375E-4, 4.55375E-4,
 2.254 E-4, 2.254 E-4, 2.254 E-4,
 2.79503E-9, 2.79503E-9, 2.79503E-9,
 2.79503E-9, 2.79503E-9, 2.79503E-9,
 2.79503E-9, 2.79503E-9, 2.79503E-9,
 6.21118E-9, 6.21118E-9, 6.21118E-9,
 6.21118E-9, 6.21118E-9, 6.21118E-9,
 6.21118E-9, 6.21118E-9, 6.21118E-9,
 1.58113E-5, 1.58113E-5, 1.58113E-5,
 4.84813E-5, 4.84813E-5, 4.84813E-5,
 4.84813E-5, 4.84813E-5, 4.84813E-5,
 5. E+2, 3. E-2, 8.372 E-4,
 5.474 E-4, 1.127 E-3,

SDWS(1)= 5.81776E-7, 5.81776E-7, 5.81776E-7,
 1.61 E-4, 1.61 E-4, 1.61 E-4,
 4.11522E-5, 4.11522E-5, 4.11522E-5,
 5. E+2, 8.372 E-4, 5.474 E-4,
 1.127 E-3,

SDWFO(1)=1.,4

1.

1,0,0,3437.7467
 2,0,0,3437.7467
 3,0,0,1.
 4,0,0,1.
 5,0,0,1.
 6,0,0,1.
 7,0,0,3437.7467
 8,0,0,3437.7467
 9,0,0,3437.7467
 0,0,0,0.

TIME (SEC)
 LONGITUDE ERROR
 POSITION *ARC MIN*
 LATITUDE ERROR
 POSITION *ARC MIN*
 ALTITUDE ERROR
 ALTITUDE *FEET*
 EAST VELOCITY ERROR
 VELOCITY *FPS*
 NORTH VELOCITY ERROR
 VELOCITY *FPS*
 UP VELOCITY ERROR
 VELOCITY *FPS*

FAST TILT
TILT *ARC MIN*
NORTH TILT
TILT *ARC MIN*
AZIMUTH ERROR
AZH *ARC MIN*

Appendix C

PROFGEN: A Computer Program for Generating Flight Profiles (Ref 11)

PROFGEN is a six degree of freedom flight profile generating program that computes position, velocity, acceleration, attitude, and attitude rate of an aircraft flying a specified route over an ellipsoidal earth. It does not model the aerodynamics of the aircraft; therefore the body coordinate frame is coincident with the coordinate frame of the flight path. This results in the inability to simulate maneuvers that require side slip, an angle of attack, or crabbing motion.

Four basic maneuvers are included in PROFGEN:

- Climb or Dive
- Coordinated Turns
- Sinusoidal Heading Changes
- Straight Flights

The aircraft may accelerate during any of these maneuvers. Flight profiles are constructed by concatenating up to 50 of the basic maneuvers. Different types of aircraft are represented by the rates and accelerations specified for each maneuver.

The earth model in PROFGEN is an ellipsoid having values based on the DOD World Geodetic System 1972. Gravity is a function of both latitude and altitude with both radial and level components.

PROFGEN uses a fifth order polynomial to control roll rate. The body frame gradually rolls up to the maximum roll rate with respect to the navigation frame, then gradually rolls out to the desired

roll angle. For a given maximum roll rate, a smaller desired roll angle produces a greater roll acceleration. In an effort to avoid abnormally high accelerations in rolling to small angles, PROFGEN's maximum roll rate for horizontal turns, $\dot{\phi}_H$, is

$$\dot{\phi}_H = \dot{\phi}_M(1 - e^{-n}) \quad (C-1)$$

where

n = Normal Turn Acceleration in g's

$\dot{\phi}_M$ = Maximum Roll Rate

For low acceleration (small g) turns, only a small bank angle is required and a lower maximum roll rate, through Equation (C-1), is used to achieve this angle. For higher acceleration horizontal turns, however, the maximum roll rate remains essentially unchanged as the roll angle approaches 90 degrees.

The result of using Equation (C-1) and the fifth order polynomial to control roll rate is that an arbitrary time constant is being used to control roll acceleration which does not necessarily reflect the dynamics of the aircraft. Calculations based on the aircrafts roll time constant were added to PROFGEN to correct this problem.

Roll rate, $\dot{\phi}$, is determined from

$$\dot{\phi} = \dot{\phi}_M(1 - e^{-t/\tau}) \quad (C-2)$$

where

$\dot{\phi}_M$ = Maximum Roll Rate

τ = Roll Time Constant

t = Time

Integrating (C-2) to obtain instantaneous roll angle, ϕ , at time t results in

$$\phi = \dot{\phi}_M(t + \tau e^{-t/\tau - \tau}) \quad (C-3)$$

Substituting $e^{-t/\tau} = 1 - t/\tau + t^2/2\tau$ gives

$$\phi \approx \dot{\phi}_M t^2/2\tau \quad (C-4)$$

Solving for t yields

$$t = |2\tau\phi/\dot{\phi}_M|^{0.5} \quad (C-5)$$

which is the approximate time necessary to achieve a given roll rate. It is assumed that the same time constant τ , applies for roll out; therefore, twice the time given in Equation (C-5) will be needed to achieve a desired roll angle.

Using the fifth order polynomial in PROFGEN, the time to complete a roll, $2t$, is given by

$$2t = 15\phi/8\dot{\phi}_H \quad (C-6)$$

Substituting Equation (C-5) into (C-6) yields

$$\dot{\phi}_H = 15\phi/16|2\tau\phi/\dot{\phi}_M|^{0.5} \quad (C-7)$$

Thus, the maximum horizontal roll rate, $\dot{\phi}_H$, will now be computed based upon the roll time constant, τ , for a desired roll angle, ϕ , and maximum roll rate, $\dot{\phi}_M$. This overall effect will be to change the slope of the fifth order polynomial so that the body frame rolls out at the desired roll angle at a time that is approximately (to second order) consistent

with the aircraft's roll time constant.

It was felt that the four basic maneuvers were overly restrictive, especially for the fighter aircraft used in this simulation. Therefore, PROFGEN was modified to include a fifth, roll-only, maneuver.

A listing of the necessary changes to the program is shown in Appendix D. It was also necessary to modify the output of PROFGEN to include roll rate, pitch rate, and yaw rate. These changes are also included in the appendix.

PROFGEN would be a more effective flight profile generator if additional modifications were made. For the sine maneuver, initial roll rate as shown in Equation 38 is not realistic. Also, fighter aircraft seldom maneuver in just the horizontal or vertical planes. Although PROFGEN has the capability to initiate turns from various pitch angles, a more realistic maneuver would be to initiate pitch changes from arbitrary roll angles. Finally, the method of storing samples of the flight trajectory data during the turn maneuver should be changed. The roll into and out of a turn should be sampled at a different rate than the turn itself. Presently, in order to correctly sample the faster dynamics of the rolls, computer resources are expended by sampling the turn itself at a higher rate than necessary.

APPENDIX D

PROFGEN UPDATE FOR ROLL ONLY MANEUVER

```

*IDENT MOREOUT
*I PROFGEN.1399
    CALL ETADOT(ETAXDOT,ETAYDOT,ETAZDOT)
*I AUG78.58
    2,ETAXDOT,ETAYDOT,ETAZDOT
*I PROFGEN.1724
    WRITE(6,101) TOFF,TON,RMAX
*I PROFGEN.1741
    WRITE(6,101) TOFF,TON,RMAX
*I PROFGEN.1748
    WRITE(6,101) TOFF,TON,RMAX
*I PROFGEN.1756
    WRITE(6,101) TOFF,TON,RMAX
*I PROFGEN.1764
    101 FORMAT(5X,16HROLLUP STOPS AT ,G20.10/,5X,
        820HROLL DOWN STARTS AT ,G20.10/,5X,17HMAX ROLL RATE IS ,G20.10)
*I PROFGEN.1686
    EQUIVALENCE (FIXED(2),RADPRD)
*I PROFGEN.1700
    RMAX=RRHORZ/RADPRD
*IDENT ROLLTC
*I PROFGEN.160
    RRHORZ=0.
*O APR80.9
    IF (ITURN.EQ.2) ROLANG(ISEG)=ATAN(TACC(ISEG)/32.2/COS(ETAY(DAY)))
    IF (ITURN.EQ.2) TRTC=SQRT(ABS(2.*RTC*ROLANG(ISEG)/ROLRAT))
    IF (ITURN.EQ.2) RRHORZ=ABS(15.*ROLANG(ISEG)/(15.*TRTC))
    IF (ITURN.EQ.2.AND.RRHORZ.GT.ROLRAT) RRHORZ=ROLRAT
*O AUG78.5
    COMMON /PRBLK/PRBLK(15)
*I APR80.6
    EQUIVALENCE (PRBLK(15),RTC)
*I AUG78.6
    C    PRBLK(15) RTC, ROLL TIME CONSTANT
*O FEB80.75
    COMMON /PITCH/PITCH(50)    /PRBLK/PRBLK(15)
*I FEB80.92
    EQUIVALENCE (PRBLK(15),RTC)
*I FEB80.105
    2,RTC
*O AUG78.64
    COMMON /PITCH/PITCH(50)    /PRBLK/PRBLK(15)    /SEGMENT/SEGMENT(50)
*I AUG78.65
    EQUIVALENCE (PRBLK(15),RTC)
*I NOV79.47
    2,RTC
*I NOV79.53

```

```

      5,RTC/0.5/
*IDENT ROLL
*I PROGEN.128
      COMMON /ROLANG/ROLANG(50)
*I PROGEN.168
      IF (ITURN.EQ.5) TRTC=SQRT(ABS(2.*RTC*ROLANG(ISEG)/ROLRAT))
      IF (ITURN.EQ.5) RRHORZ=ABS(15.*ROLANG(ISEG)/(15.*TRTC))
      IF (ITURN.EQ.5.AND.RRHORZ.GT.ROLRAT) RRHORZ=ROLRAT
      IF (ITURN.EQ.5) CALL TSTUP5(TDONE)
      IF (ITURN.EQ.5) TURNOUN=0.
      IF (ITURN.EQ.5) RRCDIFF=+1.
*O PROGEN.176
      GO TO (40,50,60,70,80),ITURN
*I PROGEN.222
C
C
C      *** ROLL-ONLY MANEUVER ***
C
C
      80  H=HLIMIT(T,TF,H,HMN)
          CALL HLIMS(H,RRCDIFF)
          CALL KUTMER(N,T,X,+1,F,MDE,ERR,HMX,HYN)
          IF (T.GE.TDONE) TRNDUN=1.
          CALL OUT(T,TI,IPANT,IRITE,IPLAT)
          IF (T.LT.TF) GO TO 80
          RETURN
*I PROGEN.414
      COMMON /ROLANG/ROLANG(50)
*I PROGEN.433
      4  ,ROLANG/50*G./
*I FEB80.47
      IF(TURN(ISEG).EQ.5) WRITE (6,700) TEMP5
*I FEB80.20
      COMMON /ROLANG/ROLANG(50)
*I FEB80.42
      TEMP5=ROLANG(ISEG)/RADPRO
*I FEB80.65
      700  FORMAT(5X,76HTHIS FLIGHT SEGMENT IS A ROLL-ONLY MANEUVER WITH A DE
          *SIZED CHANGE-IN-ROLL OF,612.5,9H DEGREES.)
*I PROGEN.866
      SUBROUTINE HLIMS(H,RRCDIFF)
C
C**  HLIMS ADJUSTS THE STEP SIZE IN A ROLL-ONLY MANEUVER
C**  SO THAT THE PROGRAM WILL PAUSE AT TDONE WHEN THE
C**  AIRCRAFT IS FINISHING A ROLL-ONLY MANEUVER.
C
      COMMON /SUPLE/SUPLE(11)
C
      EQUIVALENCE (SUPLE(1),T)
      EQUIVALENCE (SUPLE(2),TF)
      EQUIVALENCE (SUPLE(5),TDONE)

```

```

C
C
C      TRANSFER TO PROPER SUBSEGMENT
      IF (T.LT.TDONE) GO TO 10
      IF (T.GE.TDONE.AND.T.LT.TF) GO TO 20
C
C      SET RRCDEF AND LIMIT H IF NECESSARY
10  CONTINUE
      H=HCHOP(H,T,TDONE)
      RETURN
20  CONTINUE
      RRCDEF=0.
      RETURN
      END
*I PROGEN.1063
      COMMON /R/LANG/ROLANG(50)
*I PROGEN.1081
      ROLANG(I)=ROLANG(I)*RADPRD
*I FEB80.94
      INTEGER RESTRT,PATH(2),TRNTYP(5),TURN
*I FEB80.95
*I FEB80.101
      DATA TRNTYP/4HVERT,4HHORZ,4HSINE,4HSTRT,4HROLL/
*I FEB80.107
      2,ROLANG
*I PROGEN.1263
      GO TO (10,20,30,10,10),ITURN
*I FEB80.77
      COMMON /R/LANG/ROLANG(50)
*I APR80.36
      COMMON /R/LANG/ROLANG(50)
*I PROGEN.1448
      IF (ITURN.EQ.5) GO TO 20
*I PROGEN.1469
C
C      ROLL RATE COMMAND FOR A ROLL-ONLY MANEUVER
20  ROLDTC=0.
      T1=TDONE-TI
      TE=T-TI
      IF (RRCDEF.EQ.+1.) ROLDTC= TE*TE*(TE-T1)*((TE-T1)/(T1+4)
      ROLDTC=ROLDTC*SIGN(1.,ROLANG(1SEG))*16.*RRHORZ
      RETURN
*I PROGEN.1770
      SUBROUTINE TSTOP5(TDONE)
C
C**  PRIOR TO EACH ROLL-ONLY MANEUVER, TSTOP5 COMPUTES THE TIME
C**  AT WHICH THE CHANGE IN ROLL ANGLE WILL EQUAL "ROLANG". IF
C**  AND WHEN SUCH TIME IS REACHED, THE MANEUVER IS COMPLETE AND
C**  THE ROLL RATE IS SWITCHED OFF IN SUBROUTINE FLPTH.
C
      COMMON /S/PLE/SOPL*(11)

```

```
COMMON /ROLANG/ROLANG(50)
COMMON /FIXED/FIXED(16)
```

```
EQUIVALENCE (FIXED(2),RADPRO)
EQUIVALENCE (SUPL(2),TF)
EQUIVALENCE (SUPL(3),TI)
EQUIVALENCE (SUPL(6),ISFG)
EQUIVALENCE (SUPL(11),RRHORZ)
```

```
C
DT=ABS((15.*ROLANG(ISFG))/(8.*RRHORZ))
TDONE=TI+DT
RMAX=RRHORZ/RADPRO
WRITE (6,100) TDONE,RMAX
IF (TDONE.GT.TF) WRITE (6,200)
IF (TDONE.GT.TF) TDONE=TF
100 FORMAT(5X,47HTHE DESIRED CHANGE-IN-ROLL IS ACHIEVED AT TIME=,
6G20.10,/,5X,15HMAX ROLL RATE =,6G20.10)
RETURN
200 FORMAT(5X,46HTHE SEGMENT LENGTH IS NOT LONG ENOUGH FOR ROLL)
END
*0 PROFGEN.1323
IF (TURN(I).LT.1 .OR. TURN(I).GT.5) IERR(11)=1
```

Appendix E

Older generation strapdown laser gyro
and accelerometer model used in the
development of the truth and filter
models in Appendices E and F. (Ref7)

State	Initial Variance (P_{T0})	Driving Noise (Q_t)
Basic INS		
Position Errors	$(1500\text{ft})^2$	0
Velocity Errors	$(2\text{ft/sec})^2$	0
Attitude Errors	$(0.5 \text{ mrad})^2$	$7.6 \times 10^{-11} \text{ rad}^2/\text{sec}$
Accelerometers		
Bias	$(250 \mu\text{g})^2$	0
Scale Factor Errors	$(500 \text{ PPM})^2$	0
Input axis misalign	$(10 \text{ arc sec})^2$	0
Correlated Noise		
$T_1 = 60 \text{ min}$	$(40 \mu\text{g})^2$	$2P_{to}/T_1$
$T_2 = 15 \text{ min}$	$(20 \mu\text{g})^2$	$2P_{to}/T_2$
Gyros		
Drift Rate Bias	$(0.09 \text{ deg/hr})^2$	$1.47 \times 10^{-18} \text{ rad}^2/\text{sec}^3$
Scale Factor Error	$(100 \text{ PPM})^2$	0
Input Axis Misalign	$(6 \text{ arc sec})^2$	0

APPENDIX F

SOFE SUBROUTINES FOR TRUTH MODEL

```
SUBROUTINE AMEND(IRUN,T,NF,NS,NXTJ,XF,XS,XTRAJ)
DIMENSION XF(NF),XS(NS),XTRAJ(NXTJ)
RETURN
ENTRY AMEND0
RETURN
END
```

```
SUBROUTINE ESTIX(IRUN,T,NF,NS,NXTJ,XF,XS,XTRAJ,NTR,PF)
DIMENSION XF(NF),XS(NS),XTRAJ(NXTJ),PF(NTR)
RETURN
ENTRY ESTIX0
RETURN
END
```

```
SUBROUTINE FQGEN(IRUN,T,NF,NS,NXTJ,XF,XS,XTRAJ,
&NZF,NZQ,F,Q)
DIMENSION XF(NF),XS(NS),XTRAJ(NXTJ),F(NZF),Q(NZQ)
RETURN
ENTRY FQGEN0
RETURN
END
```

```
SUBROUTINE HRZ(IRUN,T,NF,NS,NXTJ,XF,XS,XTRAJ,NTR,PF,IMEAS,
&H,H,R,ZRES)
DIMENSION XF(NF),XS(NS),H(NF),XTRAJ(NXTJ),PF(NTR)
RETURN
ENTRY HRZ0
RETURN
END
```

```
SUBROUTINE SNOYS(IRJN,T,NF,NS,NXTJ,XF,XS,XTRAJ)
```

```
COMMON/SNOIS/SDWS(45),SDWS(13),SDWFO(1)
COMMON/TCSYS/TAUS(6),DIST(4)
COMMON/TRJCOM/RE,G,OMEGA,E,RK1,RK2,RK3
DIMENSION XF(NF),XS(NS),XTRAJ(NXTJ)
```

```
VGND=SQRT(XTRAJ(8)**2+XTRAJ(9)**2)
DT=T-TOLD
SRDT=SQRT(DT)
```

```
STDEV=SDWS(2)*SRDT
XS(7)=XS(7)+GAUSS(0.0,STDEV)
STDEV=SDWS(3)*SRDT
XS(8)=XS(8)+GAUSS(0.0,STDEV)
STDEV=SDWS(4)*SRDT
XS(9)=XS(9)+GAUSS(0.0,STDEV)
```



```

STDEV=SDWS(5)*SRDT
XS(10)=XS(10)+GAUSS(0.0,STDEV)
STDEV=SDWS(6)*SRDT
XS(11)=XS(11)+GAUSS(0.0,STDEV)
STDEV=SDWS(7)*SRDT
XS(12)=XS(12)+GAUSS(0.0,STDEV)
STDEV=SDWS(8)*SQRT(2.*DT/TAUS(1))
XS(25)=XS(25)+GAUSS(0.0,STDEV)
STDEV=SDWS(9)*SQRT(2.*DT/TAUS(2))
XS(26)=XS(26)+GAUSS(0.0,STDEV)
STDEV=SDWS(10)*SQRT(2.*DT/TAUS(3))
XS(27)=XS(27)+GAUSS(0.0,STDEV)
STDEV=SDWS(11)*SQRT(2.*DT/TAUS(4))
XS(28)=XS(28)+GAUSS(0.0,STDEV)
STDEV=SDWS(12)*SQRT(2.*DT/TAUS(5))
XS(29)=XS(29)+GAUSS(0.0,STDEV)
STDEV=SDWS(13)*SQRT(2.*DT/TAUS(6))
XS(30)=XS(30)+GAUSS(0.0,STDEV)
STDEV=SDWS(14)*SQRT(2.*DT*VGND/DIST(1))
XS(40)=XS(40)+GAUSS(0.0,STDEV)
STDEV=SDWS(15)*SQRT(2.*DT*VGND/DIST(2))
XS(42)=XS(42)+GAUSS(0.0,STDEV)
STDEV=SDWS(16)*SQRT(2.*DT*VGND/DIST(3))
XS(43)=XS(43)+GAUSS(0.0,STDEV)
STDEV=SDWS(17)*SQRT(2.*DT*VGND/DIST(4))
XS(44)=XS(44)+GAUSS(0.0,STDEV)
ENTRY SNOYSO
TOLD=T
RETURN
END

```

```

SUBROUTINE TRAJ(IRUN,T,NF,NS,NXTJ,XF,XS,XTRAJ)
COMMON/TRJCOM/RE,G,OMEGA,E,RK1,RK2,RK3
DIMENSION XF(NF),XS(NS),XTRAJ(NXTJ)
DIMENSION TITLE(20)
RETURN
ENTRY TRAJ

```

```

READ (3) TITLE,TODAY,CLOCK
READ (3) IPR03,NSEGT,LLMECH,TSTART,VTO,PHEAD,PITO,
& ALFAD,LATD,LONG,ALTD,IPRNT,IRITE,IPL0T,ROLRAT,LUNIT
READ (3) SEGLNT,RESTR1,TURN,NPATH,PACC,TACC,HEAD,
& PIT,DT0,MODE,ERROR,HMAX,HMIN
IF (IPUN.GT.1) GO TO 10

```

```

PRINT*, " "
WRITE (6,100) TITLE,TODAY,CLOCK
100 FORMAT(1X,7HTITLE: ,20A4/1X,7HDATE: ,A10/1X,7HTIME: ,A10)

PRINT*, " IPR03: ",IPR03
PRINT*, " NSEGT: ",NSEGT

```

```

PRINT*, " LLMECH: ", LLMECH
PRINT*, " ISTART: ", ISTART
PRINT*, " VTO: ", VTO
PRINT*, " PHEADO: ", PHEADO
PRINT*, " PITHCO: ", PITHO
PRINT*, " ALFAD: ", ALFAD
PRINT*, " IPENT: ", IPENT
PRINT*, " IRITE: ", IRITE
PRINT*, " IPLOT: ", IPLOT
PRINT*, " ROLRAT: ", ROLRAT
PRINT*, " LUNIT: ", LUNIT

```

```

PRINT*, " SEGLNT: ", SEGLNT
PRINT*, " RESTRT: ", RESTRT
PRINT*, " TJRN: ", TJRN
PRINT*, " NPATH: ", NPATH
PRINT*, " PACC: ", PACC
PRINT*, " TACC: ", TACC
PRINT*, " HEAD: ", HEAD
PRINT*, " PIT: ", PIT
PRINT*, " DTO: ", DTO
PRINT*, " MODE: ", MODE
PRINT*, " ERROR: ", ERROR
PRINT*, " HMAX: ", HMAX
PRINT*, " HMIN: ", HMIN

```

10 CONTINUE

```

RE=20925640.
G=32.0881576
OMEGA=.72921151E-4
E=1./298.3

```

C STANDARD K VALUES ARE K1=3.E-2, K2=3.E-4, K3=1.E-6

C OPTIMAL K VALUES ARE K1=1.003, K2=4.17E-3, K3=4.39E-6

```

RK1=3.E-2
RK2=3.E-4
RK3=1.E-6
RETURN
END

```

```

SUBROUTINE USRIN
COMMON/SNDIS/SDWSO(45),SDWS(18),SDWFO(1)
COMMON/TCSYS/TAUS(6),DIST(4)
NAMELIST/INS/TAUS,DIST,SDWSO,SDWS,SDWFO

```

```

PRINT*, " "
PRINT*, " X(1) EAST LONGITUDE"
PRINT*, " X(2) NORTH LATITUDE"
PRINT*, " X(3) ALTITUDE (UP)"

```

```

PRINT*, " X(4)  EAST VELOCITY"
PRINT*, " X(5)  NORTH VELOCITY"
PRINT*, " X(6)  VERTICAL VELOCITY"
PRINT*, " X(7)  EAST ATTITUDE      "
PRINT*, " X(8)  NORTH ATTITUDE     "
PRINT*, " X(9)  UP ATTITUDE        "
PRINT*, " X(10) X GYRO DRIFT RATE  "
PRINT*, " X(11) Y GYRO DRIFT RATE  "
PRINT*, " X(12) Z GYRO DRIFT RATE  "
PRINT*, " X(13) X GYRO SCALE FACTOR "
PRINT*, " X(14) Y GYRO SCALE FACTOR "
PRINT*, " X(15) Z GYRO SCALE FACTOR "
PRINT*, " X(16) X GYRO MISALIGN ABOUT Y "
PRINT*, " X(17) X GYRO MISALIGN ABOUT Z "
PRINT*, " X(18) Y GYRO MISALIGN ABOUT X "
PRINT*, " X(19) Y GYRO MISALIGN ABOUT Z "
PRINT*, " X(20) Z GYRO MISALIGN ABOUT X "
PRINT*, " X(21) Z GYRO MISALIGN ABOUT Y "
PRINT*, " X(22) X ACCEL NONREPEAT BIAS "
PRINT*, " X(23) Y ACCEL NONREPEAT BIAS "
PRINT*, " X(24) Z ACCEL NONREPEAT BIAS "
PRINT*, " X(25) X ACCEL 60 MIN BIAS  "
PRINT*, " X(26) Y ACCEL 60 MIN BIAS  "
PRINT*, " X(27) Z ACCEL 60 MIN BIAS  "
PRINT*, " X(28) X ACCEL 15 MIN BIAS  "
PRINT*, " X(29) Y ACCEL 15 MIN BIAS  "
PRINT*, " X(30) Z ACCEL 15 MIN BIAS  "
PRINT*, " X(31) X ACCEL SCALE FACTOR "
PRINT*, " X(32) Y ACCEL SCALE FACTOR "
PRINT*, " X(33) Z ACCEL SCALE FACTOR "
PRINT*, " X(34) X ACCEL MISALIGN ABOUT Y "
PRINT*, " X(35) X ACCEL MISALIGN ABOUT Z "
PRINT*, " X(36) Y ACCEL MISALIGN ABOUT X "
PRINT*, " X(37) Y ACCEL MISALIGN ABOUT Z "
PRINT*, " X(38) Z ACCEL MISALIGN ABOUT X "
PRINT*, " X(39) Z ACCEL MISALIGN ABOUT Y "
PRINT*, " X(40) BAR PRES  "
PRINT*, " X(41) BAR SCALE FACTOR  "
PRINT*, " X(42) EAST DEFL GRAVITY  "
PRINT*, " X(43) NOR  DEFL GRAVITY  "
PRINT*, " X(44) GRAVITY ANOMALY  "
PRINT*, " X(45) VERTICAL ACCEL ERROR"

```

```

READ(5,INS)
WRITE(6,100) TAUS,DIST,SDWSO,SDWS,SDWFO
RETURN
100  FORMAT("1"5(//)10"FILTER MODEL DATA-BASE FROM
&NAMELIST INS: "
&//115"TIME CONSTANTS, TAUS "
&//20.6614.7
&//115"CORRELATION DISTANCE, DIST "

```

```

E/T20,4G14.7
E//T15"SDWS")
E/7(/T20,6G14.7)/T20,3G14.7
E//T15"SDWS"
E/3(/T20,5G14.7)/T20,3G14.7
E//T15"SDWF0"
E/T20,1G14.7)
END

```

```

SUBROUTINE XF00T(IRUN,T,NF,NS,NXTJ,XF,XS,XTRAJ,NTR,PF,XDOT)
COMMON/TRJCOM/RE,G,OMEGA,E,RK1,RK2,RK3
COMMON/SNOIS/SDWSJ(45),SDWS(18),SDWFO(1)
DIMENSION XF(NF),XDOT(NF),XS(NS),XTRAJ(NXTJ),PF(NTR)
XDOT(1)=0.
RETURN
ENTRY XF00T0
XF(1)=0.
RETURN
END

```

```

SUBROUTINE XS00T(IRUN,T,NF,NS,NXTJ,XF,XS,XTRAJ,XDOT)
DIMENSION XF(NF),XS(NS),XTRAJ(NXTJ),XDOT(NS)

```

```

COMMON/TCSYS/TAUS(6),DIST(4)
COMMON/SNOIS/SDWSJ(45),SDWS(18),SDWFO(1)
COMMON/TRJCOM/RE,G,OMEGA,E,RK1,RK2,RK3

```

C 16 TRAJECTORY INPUTS FROM PROFGEN

```

RLAT=XTRAJ(1)
RLON=XTRAJ(2)
ALPHA=XTRAJ(3)
ALT=XTRAJ(4)
ROL=XTRAJ(5)
PIT=XTRAJ(6)
YAW=XTRAJ(7)
VN=XTRAJ(8)
VE=-XTRAJ(9)
VU=XTRAJ(10)
FN=XTRAJ(11)
FE=-XTRAJ(12)
FU=XTRAJ(13)
OROL=XTRAJ(14)
OPIT=XTRAJ(15)
OYAW=XTRAJ(16)

VCND=SQRT(VN**2+VE**2)
SLAT=SIN(RLAT)
CLAT=COS(RLAT)
TLAT=SLAT/CLAT
OMEGAN=OMEGA*CLAT

```

```

OMEGAU=OMEGA*SLAT
SX=SIN(ROL)
CX=COS(ROL)
SY=SIN(PIT)
CY=COS(PIT)
SZ=SIN(YAW)
CZ=COS(YAW)
SA=SIN(ALPHA)
CA=COS(ALPHA)
SLON=SIN(RLON)
CLON=COS(RLON)

```

C RHO IS THE ANGULAR VELOCITY OF THE NAV FRAME WRT EARTH

```

RHOE=-VN/RE
RHON=VE/RE
RHOU=VE*TLAT/RE

```

C WE-WN-WU ARE THE ANGULAR VELOCITY OF THE NAV FRAME WRT
C INERTIAL FRAME COORDINATIZED IN THE NAV FRAME (E-N-U)

```

WE=RHOE
WN=RHON+OMEGAN
WU=RHOU+OMEGAU

```

C COMPONENTS OF THE 9 X 9 MATRIX

```

RKZ=VU/RE
RLAT2=2.*RLAT
F42=2.*(OMEGAN*VN+OMEGAU*VU)+RHON*VN/(CLAT**2)
F43=RHOU*RHOE+RHON*RKZ
F44=-RHOE*TLAT-RKZ
F52=-2.*OMEGAN*VE-RHON*VE/CLAT**2
F53=RHON*RHOE-RHOU*RKZ
F63=2.*G/RE-RHON**2-RHOE**2
F92=4N+RHOJ*TLAT

```

C TRANSFORMATION FROM NAV FRAME (E-N-U) TO BODY FRAME (X-Y-Z)

```

CXE=SZ*CY
CXN=CZ*CY
CXU=SY
CYE=SZ*SY*SX+CZ*CX
CYN=CZ*SY*SX-SZ*CX
CYU=-CY*SX
CZE=-CZ*SX+SZ*SY*CX
CZN=CZ*SY*CX+SZ*SX
CZU=-CY*CX

```

C TRANSFORMATION FROM BODY FRAME (X-Y-Z) TO NAV FRAME (E-N-U)

CEX=CXE
 CEY=CYE
 CEZ=CZE
 CNX=CNX
 CNY=CYN
 CNZ=CNZ
 CUX=CUX
 CUY=CUY
 CUZ=CUZ

C SPECIFIC FORCE IN THE BODY FRAME

FX=CNX*FN+CXE*FE+CXU*FU
 FY=CYN*FN+CYE*FE+CYU*FU
 FZ=CNZ*FN+CZE*FE+CUZ*FU

C ANGULAR VELOCITY OF BODY FRAME WRT INERTIAL FRAME C COORDINATIZED IN THE BODY FRAME

WX=CXE*WE+CNX*WN+CXU*WU+DROL
 WY=CYE*WE+CYN*WN+CYU*WU+DPIT
 WZ=CZE*WE+CNZ*WN+CUZ*WU+DYAW

XDOT(1)=XS(2)*RHOU/CLAT-XS(3)*RHON/(RE*CLAT)+XS(4)/
 E(RE*CLAT)
 XDOT(2)=XS(3)*RHOE/RE+XS(5)/RE
 XDOT(3)=-R<1*XS(3)+XS(6)+XS(40)*RK1+XS(41)*RK1*ALT

XDOT(4)=XS(2)*F42+XS(3)*F43+XS(4)*F44+XS(5)*(WJ+OMEGAU)
 E-XS(6)*(WN+OMEGAN)-XS(8)*FU+XS(9)*FN
 E+XS(22)*CEX+XS(23)*CEY+XS(24)*CEZ
 E+XS(25)*CEX+XS(26)*CEY+XS(27)*CEZ
 E+XS(28)*CEX+XS(29)*CEY+XS(30)*CEZ
 E+XS(31)*CEX*FX+XS(32)*CEY*FY+XS(33)*CEZ*FZ
 E-XS(34)*CEX*FZ+XS(35)*CEX*FY+XS(36)*CEY*FZ
 E-XS(37)*CEY*FX-XS(38)*CEZ*FY+XS(39)*CEZ*FX+XS(42)

XDOT(5)=XS(2)*F52+XS(3)*F53-XS(4)*2.*WU-XS(5)*RKZ
 E+XS(6)*RHOE+XS(7)*FU-XS(9)*FE
 E+XS(22)*CNX+XS(23)*CNY+XS(24)*CNZ
 E+XS(25)*CNX+XS(26)*CNY+XS(27)*CNZ
 E+XS(28)*CNX+XS(29)*CNY+XS(30)*CNZ
 E+XS(31)*CNX*FX+XS(32)*CNY*FY+XS(33)*CNZ*FZ
 E-XS(34)*CNX*FZ+XS(35)*CNX*FY+XS(36)*CNY*FZ
 E-XS(37)*CNY*FX-XS(38)*CNZ*FY+XS(39)*CNZ*FX+XS(43)

XDOT(6)=-XS(2)*2.*OMEGAU*VE+XS(3)*(F63-R<2)+XS(4)*2.*WN
 E-XS(5)*2.*RHOE-XS(7)*FN+XS(8)*FE
 E+XS(22)*CUX+XS(23)*CUY+XS(24)*CUZ

```

E+XS(25)*CUX+XS(26)*CUIY+XS(27)*CUIZ
E+XS(28)*CUX+XS(29)*CUIY+XS(30)*CUIZ
E+XS(31)*CUX*FX+XS(32)*CUIY*FY+XS(33)*CUIZ*FZ
E-XS(34)*CUX*FZ+XS(35)*CUX*FY+XS(36)*CUIY*FZ
E-XS(37)*CUIY*FX-XS(38)*CUIZ*FY+XS(39)*CUIZ*FX
E+XS(40)*RK2+XS(41)*RK2*ALT+XS(44)
E-XS(45)

```

```

XDOT(7)=-XS(3)*RHDE/RE-XS(5)/RE+XS(8)*WU-XS(9)*WN
E+XS(10)*CEX+XS(11)*CEY+XS(12)*CEZ
E+XS(13)*CEX*WX+XS(14)*CEY*WY+XS(15)*CEZ*WZ
E+XS(16)*CEX*WZ-XS(17)*CEX*WY-XS(18)*CEY*WZ
E+XS(19)*CEY*WX+XS(20)*CEZ*WY-XS(21)*CEZ*WX

```

```

XDOT(8)=-XS(2)*OMEGA J-XS(3)*RHON/RE+XS(4)/RE-XS(7)*WJ
E+XS(9)*WE+XS(10)*CNX+XS(11)*CNY+XS(12)*CNZ
E+XS(13)*CNX*WX+XS(14)*CNY*WY+XS(15)*CNZ*WZ
E+XS(16)*CNX*WZ-XS(17)*CNX*WY-XS(18)*CNY*WZ
E+XS(19)*CNY*WX+XS(20)*CNZ*WY-XS(21)*CNZ*WX

```

```

XDOT(9)=XS(2)*F92-XS(3)*RHOU/RE+XS(4)*TLAT/RE+XS(7)*4N
E-XS(8)*WE+XS(10)*CUX+XS(11)*CUIY+XS(12)*CUIZ
E+XS(13)*CUX*WX+XS(14)*CUIY*WY+XS(15)*CUIZ*WZ
E+XS(16)*CUX*WZ-XS(17)*CUX*WY-XS(18)*CUIY*WZ
E+XS(19)*CUIY*WX+XS(20)*CUIZ*WY-XS(21)*CUIZ*WX

```

```

2 DO 2 I=10,24
  XDOT(I)=0.

```

```

XDOT(25)=-XS(25)/TAUS(1)
XDOT(26)=-XS(26)/TAUS(2)
XDOT(27)=-XS(27)/TAUS(3)
XDOT(28)=-XS(28)/TAUS(4)
XDOT(29)=-XS(29)/TAUS(5)
XDOT(30)=-XS(30)/TAUS(6)

```

```

4 DO 4 I=31,39
  XDOT(I)=0.

```

```

XDOT(40)=-XS(40)*VGND/DIST(1)
XDOT(41)=0.
XDOT(42)=-XS(42)*VGND/DIST(2)
XDOT(43)=-XS(43)*VGND/DIST(3)
XDOT(44)=-XS(44)*VGND/DIST(4)
XDOT(45)=XS(3)*RK3-XS(40)*RK3-XS(41)*RK3*ALT
RETURN

```

```

ENTRY XSDOT0

```

```

10 DO 10 I=1,45
  XS(I)=CAUSS(0.,SD*SD(I))

```

RETURN
END
TRUTH MODEL FOR PREVIOUS GENERATION INERTIAL REF SYSTEM

\$PRDATA

NF=1, NS=45, TF=1400., DTPRNT=150., DTPRPL=15., DTNDYS=15.,
LPRXF=.T., LPRLT=.F., LPRDG=.F., LPP=.T., NXTJ=16, LXTJ=.T.,
M=0, LPRXTJ=.T., LCC=.T., DTCCPL=3., IPASS=50,3

45*0.

1*0.

1,1,1.

0,0,0.

\$INS TAUS(1)=3600.,3600.,3600.,900.,900.,900.,

DIST(1)=1519025.8,60761.0333,60761.0333,364566.19,

SDWS(1)=7.16823E-5, 7.16923E-5, 1.5 E+3,
9.55765E-8, 9.55765E-8, 9.55765E-8,
.5E-3, .5E-3, .5E-3,
4.36332E-7, 4.36332E-7, 4.36332E-7,
100.E-6, 100.E-6, 100.E-6,
2.90888E-5, 2.90888E-5, 2.90888E-5,
2.90888E-5, 2.90888E-5, 2.90888E-5,
8.05E-3, 8.05E-3, 8.05E-3,
1.288E-3, 1.288E-3, 1.288E-3,
6.44E-4, 6.44E-4, 6.44E-4,
500.E-6, 500.E-6, 500.E-6,
4.84813E-5, 4.84813E-5, 4.84813E-5,
4.84813E-5, 4.84813E-5, 4.84813E-5,
5.E+2, 3.E-2, 8.372E-4,
5.474E-4, 1.127E-3, 1.E-2,

SDWS(1)= 2.25 E-2,
8.71779E-6, 8.71779E-6, 8.71779E-6,
1.21243E-9, 1.21243E-9, 1.21243E-9,
1.288 E-3, 1.288 E-3, 1.288 E-3,
6.44 E-4, 6.44 E-4, 6.44 E-4,
5. E+2, 8.372 E-4, 5.474 E-4,
1.127 E-3, 1.5 E-1,

SDWFO(1)=1.,3

.0166667

1,0,0,3437.7467

2,0,0,3437.7467

3,0,0,1.
4,0,0,1.
5,0,0,1.
6,0,0,1.
7,0,0,3437.7467
8,0,0,3437.7467
9,0,0,3437.7467
0,0,0,0.

TIME (MIN)

LONGITUDE ERROR
POSITION *ARC MIN*
LATITUDE ERROR
POSITION *ARC MIN*
ALTITUDE ERROR
ALTITUDE *FEET*
EAST VELOCITY ERROR
VELOCITY *FPS*
NORTH VELOCITY ERROR
VELOCITY *FPS*
UP VELOCITY ERROR
VELOCITY *FPS*
EAST TILT
TILT *ARC MIN*
NORTH TILT
TILT *ARC MIN*
AZIMUTH ERROR
AZM *ARC MIN*

APPENDIX G

SOFE SUBROUTINES FOR FILTER MODEL

```
SUBROUTINE AMEND(IRUN,T,NF,NS,NXTJ,XF,XS,XTRAJ)
DIMENSION XF(NF),XS(NS),XTRAJ(NXTJ)
RETURN
ENTRY AMEND0
RETURN
END
```

```
SUBROUTINE ESTIX(IRUN,T,NF,NS,NXTJ,XF,XS,XTRAJ,NTR,P=)
DIMENSION XF(NF),XS(NS),XTRAJ(NXTJ),PF(NTR)
RETURN
ENTRY ESTIX0
RETURN
END
```

```
SUBROUTINE FGEN(IRUN,T,NF,NS,NXTJ,XF,XS,XTRAJ,
*NZF,NZO,F,QF)
DIMENSION XF(NF),XS(NS),XTRAJ(NXTJ),F(NZF),QF(NZO)
```

```
COMMON/TCSYS/TAUF(6),DIST(4)
COMMON/FNDIS/SDWFO(45),QFIN(16),SDWSO(1)
COMMON/TRJCOM/RE,G,OMEGA,E,RK1,RK2,RK3
COMMON/C1/CXE,CXN,CXJ,CYE,CYN,CYU,CZE,CZN,CZJ
COMMON/C2/CEX,CEY,CEZ,CNX,CNY,CNZ,CUX,CUY,CJZ
COMMON/C4/SLAT,CLAT,TLAT,SLX,CX,SY,CY,CZ,SA,CA,SLON,CLON
COMMON/C5/RLAT,RLON,ALPHA,ALT,ROLL,PITCH,YAW,VN,VE,VJ
COMMON/C6/VGND,OMEGAN,OMEGAU,RHOE,RHON,RHOU,RKZ
COMMON/C7/WE,WV,WU,WX,WY,WZ
COMMON/C8/F42,F43,F44,F52,F53,F63,F92
COMMON/C9/FX,FY,FZ,FN,FE,FU
```

```
F(1)=RHOU/CLAT
F(2)=-RHON/(RE*CLAT)
F(3)=1./(RE*CLAT)
F(4)=RHOE/RE
F(7)=F42
F(8)=F43
F(9)=F44
F(10)=OMEGAU+WU
F(11)=-OMEGAN-WN
F(12)=-FU
F(13)=FN
F(14)=CEX
F(15)=CEY
F(16)=CEZ
F(17)=CNX
F(18)=CNY
F(19)=CNZ
```

F(20)=CEX
 F(21)=CEY
 F(22)=CEZ
 F(23)=CEX*FX
 F(24)=CEY*FY
 F(25)=CEZ*FZ
 F(26)=-CEX*FZ
 F(27)=CEX*FY
 F(28)=CEY*FZ
 F(29)=-CEY*FX
 F(30)=-CEZ*FY
 F(31)=CEZ*FX
 F(33)=F52
 F(34)=F53
 F(35)=-2.*WU
 F(36)=-RKZ
 F(37)=RHDE
 F(38)=FU
 F(39)=-FE
 F(40)=CNX
 F(41)=CNY
 F(42)=CNZ
 F(43)=CNX
 F(44)=CNY
 F(45)=CNZ
 F(46)=CNX
 F(47)=CNY
 F(48)=CNZ
 F(49)=CNX*FX
 F(50)=CNY*FY
 F(51)=CNZ*FZ
 F(52)=-CNX*FZ
 F(53)=CNX*FY
 F(54)=CNY*FZ
 F(55)=-CNY*FX
 F(56)=-CNZ*FY
 F(57)=CNZ*FX
 F(59)=-2.*OMEGAU*VE
 F(60)=F63-RKZ
 F(61)=2.*WN
 F(62)=-2.*RHDE
 F(64)=-FN
 F(65)=FE
 F(66)=CUX
 F(67)=CUY
 F(68)=CUZ
 F(69)=CUX
 F(70)=CUY
 F(71)=CUZ
 F(72)=CUX
 F(73)=CUY

F(74)=CUZ
 F(75)=CUX*FX
 F(76)=CUX*FY
 F(77)=CUZ*FZ
 F(78)=-CUX*FZ
 F(79)=CUX*FY
 F(80)=CUX*FZ
 F(81)=-CUX*FX
 F(82)=-CUX*FY
 F(83)=CUZ*FX
 F(84)=CUZ*FY
 F(85)=RK2*ALT
 F(87)=-RHDE/RE
 F(89)=WU
 F(90)=-WN
 F(91)=CEX
 F(92)=CEY
 F(93)=CEZ
 F(94)=CEX*FX
 F(95)=CEY*FY
 F(96)=CEZ*FZ
 F(97)=CEX*WZ
 F(98)=-CEX*WY
 F(99)=-CEY*WZ
 F(100)=CEY*WX
 F(101)=CEZ*WY
 F(102)=-CEZ*WX
 F(103)=-OMEGA
 F(104)=-RHON/RE
 F(106)=-WU
 F(107)=WE
 F(108)=CNX
 F(109)=CNY
 F(110)=CNZ
 F(111)=CNX*WX
 F(112)=CNY*WY
 F(113)=CNZ*WZ
 F(114)=CNX*FZ
 F(115)=-CNX*WY
 F(116)=-CNY*WZ
 F(117)=CNY*WX
 F(118)=CNZ*WY
 F(119)=-CNZ*WX
 F(120)=F92
 F(121)=-RHOU/RE
 F(122)=TLAT/RE
 F(123)=WN
 F(124)=-WE
 F(125)=CUX
 F(126)=CUX
 F(127)=CUZ
 F(128)=CUX*WX

```

F(129)=CUX*WY
F(130)=CUZ*WZ
F(131)=CUX*WZ
F(132)=-CUX*WY
F(133)=-CUX*WZ
F(134)=CUX*WX
F(135)=CUZ*WY
F(136)=-CUZ*WX
F(137)=-1./TAUF(1)
F(138)=-1./TAUF(2)
F(139)=-1./TAUF(3)
F(140)=-1./TAUF(4)
F(141)=-1./TAUF(5)
F(142)=-1./TAUF(6)
F(143)=-VGND/DIST(1)
F(144)=-VGND/DIST(2)
F(145)=-VGND/DIST(3)
F(146)=-VGND/DIST(4)
F(150)=RK1*ALT
F(152)=-RK3*ALT

```

```

DO 5 I=13,16
5 QF(I)=QFIN(I)*VGND
RETURN

```

```

ENTRY FQGEN0
DO 10 I=1,12
10 QF(I)=QFIN(I)
F(5)=1./RE
F(6)=1.
F(32)=1.
F(58)=1.
F(63)=-1.
F(84)=RK2
F(86)=1.
F(88)=-1./RE
F(105)=1./RE
F(147)=RK3
F(148)=-RK1
F(149)=RK1
F(151)=-RK3
RETURN
END

```

```

SUBROUTINE HRZ(IRUN,T,NF,NS,NXTJ,XF,XS,XTRAJ,NTR,PF,IMEAS,
*M,H,R,ZRES)
DIMENSION XF(NF),XS(NS),H(NF),XTRAJ(NXTJ),PF(NTR)
RETURN
ENTRY HRZ0
RETURN
END

```

```

SUBROUTINE SNOYS(IRUN,T,NF,NS,NXTJ,XF,XS,XTRAJ)
COMMON/ENDIS/SOWEN(45),DEFIN(16),SOWSO(1)
COMMON/ICSYS/TAUF(5),DIST(4)
DIMENSION XF(NF),XS(NS),XTRAJ(NXTJ)
ENTRY SNOYSO
RETURN
END

```

```

SUBROUTINE TRAJ(IRUN,T,NF,NS,NXTJ,XF,XS,XTRAJ)
COMMON/TRJCOM/RF,G,OMEGA,E,RK1,RK2,RK3
DIMENSION XF(NF),XS(NS),XTRAJ(NXTJ)
DIMENSION TITLE(20)
DIMENSION SEGLNT(50),RESTRT(50),ITURN(50),NPATH(50),PACC(50)
DIMENSION TACC(50),HEAD(50),PIT(50),DTO(50),MODE(50)
DIMENSION ERROR(50),HMAX(50),HMIN(50)
RETURN
ENTRY TRAJJ

```

```

READ (3) TITLE,TODAY,CLOCK
READ (3) IPROB,NSEGT,LLMECH,TSTART,VTO,PHEAD,PITO,
& ALFAD,LATD,LOND,ALTD,IPRNT,IRITE,IPLT,POLRAT,LUNIT
READ (3) SEGLNT,RESTRT,ITURN,NPATH,PACC,TACC,HEAD,
& PIT,DTO,MODE,ERROR,HMAX,HMIN
IF (IRUN.GT.1) GO TO 10

```

```

CALL PAGCON(44,1)
WRITE (6,100) TITLE,TODAY,CLOCK
100 FORMAT(1X,7HTITLE: ,20A4/1X,7HDATE: ,A10/1X,7HTIME: ,A10)

```

```

PRINT*," IPROB: ",IPROB
PRINT*," NSEGT: ",NSEGT
PRINT*," LLMECH: ",LLMECH
PRINT*," TSTART: ",TSTART
PRINT*," VTO: ",VTO
PRINT*," PHEAD: ",PHEAD
PRINT*," PITCH: ",PITO
PRINT*," ALFAD: ",ALFAD
PRINT*," IPRNT: ",IPRNT
PRINT*," IRITE: ",IRITE
PRINT*," IPLT: ",IPLT
PRINT*," POLRAT: ",POLRAT
PRINT*," LUNIT: ",LUNIT
PRINT*," "
PRINT*," SEGLNT: ",SEGLNT
PRINT*," RESTRT: ",RESTRT
PRINT*," ITURN: ",ITURN
PRINT*," NPATH: ",NPATH
PRINT*," PACC: ",PACC
PRINT*," TACC: ",TACC
PRINT*," HEAD: ",HEAD

```

```

PRINT*, " PITCH: ", PIT
PRINT*, " DTD: ", DTD
PRINT*, " MODE: ", MODE
PRINT*, " ERROR: ", ERROR
PRINT*, " HMAX: ", HMAX
PRINT*, " HMIN: ", HMIN
10 CONTINUE

```

```

RE=20925640.
G=32.0841576
OMEGA=.72921151E-4
E=1./298.3

```

C STANDARD K VALUES ARE K1=3.E-2, K2=3.E-4, K3=1.E-6

C OPTIMAL K VALUES ARE K1=1.003, K2=4.17E-3, K3=4.39E-6

```

RK1=3.E-2
RK2=3.E-4
RK3=1.E-6
RETURN
END

```

```

SUBROUTINE USRIN
COMMON/FNOIS/SDWFO(45),QFIN(16),SDWSO(1)
COMMON/TCSYS/TAUF(6),DIST(4)
NAMELIST/INF/TAUF,DIST,SDWFO,QFIN,SDWSO

```

```

PRINT*, " "
PRINT*, " X(1)  EAST LONGITUDE"
PRINT*, " X(2)  NORTH LATITUDE"
PRINT*, " X(3)  ALTITUDE (UP)"
PRINT*, " X(4)  EAST VELOCITY"
PRINT*, " X(5)  NORTH VELOCITY"
PRINT*, " X(6)  VERTICAL VELOCITY"
PRINT*, " X(7)  EAST ATTITUDE      "
PRINT*, " X(8)  NORTH ATTITUDE     "
PRINT*, " X(9)  UP ATTITUDE        "
PRINT*, " X(10) X GYRO DRIFT RATE  "
PRINT*, " X(11) Y GYRO DRIFT RATE  "
PRINT*, " X(12) Z GYRO DRIFT RATE  "
PRINT*, " X(13) X GYRO SCALE FACTOR "
PRINT*, " X(14) Y GYRO SCALE FACTOR "
PRINT*, " X(15) Z GYRO SCALE FACTOR "
PRINT*, " X(16) X GYRO MISALIGN ABOUT Y "
PRINT*, " X(17) X GYRO MISALIGN ABOUT Z "
PRINT*, " X(18) Y GYRO MISALIGN ABOUT X "
PRINT*, " X(19) Y GYRO MISALIGN ABOUT Z "
PRINT*, " X(20) Z GYRO MISALIGN ABOUT X "
PRINT*, " X(21) Z GYRO MISALIGN ABOUT Y "
PRINT*, " X(22) X ACCEL NONREPEAT BIAS "

```

```

PRINT*, " X(23) Y ACCEL NONREPEAT BIAS "
PRINT*, " X(24) Z ACCEL NONREPEAT BIAS "
PRINT*, " X(25) X ACCEL 60 MIN BIAS "
PRINT*, " X(26) Y ACCEL 60 MIN BIAS "
PRINT*, " X(27) Z ACCEL 60 MIN BIAS "
PRINT*, " X(28) X ACCEL 15 MIN BIAS "
PRINT*, " X(29) Y ACCEL 15 MIN BIAS "
PRINT*, " X(30) Z ACCEL 15 MIN BIAS "
PRINT*, " X(31) X ACCEL SCALE FACTOR "
PRINT*, " X(32) Y ACCEL SCALE FACTOR "
PRINT*, " X(33) Z ACCEL SCALE FACTOR "
PRINT*, " X(34) X ACCEL MISALIGN ABOUT Y "
PRINT*, " X(35) X ACCEL MISALIGN ABOUT Z "
PRINT*, " X(36) Y ACCEL MISALIGN ABOUT X "
PRINT*, " X(37) Y ACCEL MISALIGN ABOUT Z "
PRINT*, " X(38) Z ACCEL MISALIGN ABOUT X "
PRINT*, " X(39) Z ACCEL MISALIGN ABOUT Y "
PRINT*, " X(40) BAR PRES "
PRINT*, " X(41) BAR SCALE FACTOR "
PRINT*, " X(42) EAST DEFL GRAVITY "
PRINT*, " X(43) NOR DEFL GRAVITY "
PRINT*, " X(44) GRAVITY ANOMALY "
PRINT*, " X(45) VERTICAL ACCEL ERROR "

```

```

      READ(5, INF)
      WRITE(6, 100) TAUF, DIST, SDWFO, QFIN, SDWSO
      RETURN
100  FORMAT("1"5(//)T10"FILTER MODEL DATA-BASE FROM
      &NAMELIST INF: "
      &//T15"TIME CONSTANTS, TAUF "
      &/T20,6G14.7
      &//T15"CORRELATION DISTANCE, DIST "
      &/T20,4G14.7
      &//T15"SDWFO"
      &/7(//T20,6G14.7)/T20,3G14.7
      &//T15"QFIN"
      &/3(//T20,5G14.7)/T20,3G14.7
      &//T15"SDWSO"
      &/T20,6G14.7)
      END

```

```

SUBROUTINE XSDOT(IRUN,T,NF,NS,NXTJ,XF,XS,XTRAJ,XDOT)
COMMON/TRJCOM/RE,G,OMEGA,E,RK1,RK2,RK3
COMMON/ENDIS/SDWFO(45),QFIN(16),SDWSO(1)
DIMENSION XF(NF),XDOT(NF),XS(NS),XTRAJ(NXTJ)
XDOT(1)=0.
RETURN
ENTRY XSDOTO
XS(1)=0.
RETURN
END

```



```
SUBROUTINE XDOT(IRUN,T,NF,NS,NXTJ,XF,XS,XTRAJ,NTR,PF,XDOT)
DIMENSION XF(NF),XS(NS),XTRAJ(NXTJ),XDOT(NS),PF(NTR)
```

```
COMMON/TCSYS/TAUF(6),DIST(4)
COMMON/FNOIS/SOWFO(45),QFIN(16),SDWSO(1)
COMMON/TRJCO1/RE,C,OMEGA,E,RK1,RK2,RK3
COMMON/C1/CXF,CXN,CXU,CYF,CYN,CYU,CZE,CZN,CZU
COMMON/C2/CEX,CEY,CEZ,CNX,CNY,CNZ,CUX,CUY,CUZ
COMMON/C4/SLAT,CLAT,TLAT,SX,CX,SY,CY,SZ,CZ,SA,CA,SLON,CLON
COMMON/C5/RLAT,RLON,ALPHA,ALT,ROLL,PITCH,YAW,VN,VE,VU
COMMON/C6/VGND,OMEGAN,OMEGAU,RHON,RHOU,RKZ
COMMON/C7/W,E,WX,WY,WZ
COMMON/C8/F42,F43,F44,F52,F53,F54,F92
COMMON/C9/FX,FY,FZ,FN,FE,FU
```

C 16 TRAJECTORY INPUTS FROM PROFGEN

```
RLAT=XTRAJ(1)
RLON=XTRAJ(2)
ALPHA=XTRAJ(3)
ALT=XTRAJ(4)
ROLL=XTRAJ(5)
PITCH=XTRAJ(6)
YAW=XTRAJ(7)
VN=XTRAJ(8)
VE=-XTRAJ(9)
VU=XTRAJ(10)
FN=XTRAJ(11)
FE=-XTRAJ(12)
FU=XTRAJ(13)
DROLL=XTRAJ(14)
DPITCH=XTRAJ(15)
DYAW=XTRAJ(16)
```

```
VGND=SQRT(VN**2+VE**2)
SLAT=SIN(RLAT)
CLAT=COS(RLAT)
TLAT=SLAT/CLAT
OMEGAN=OMEGA*CLAT
OMEGAU=OMEGA*SLAT
SX=SIN(ROLL)
CX=COS(ROLL)
SY=SIN(PITCH)
CY=COS(PITCH)
SZ=SIN(YAW)
CZ=COS(YAW)
SA=SIN(ALPHA)
CA=COS(ALPHA)
SLON=SIN(RLON)
CLON=COS(RLON)
```

C RHO IS THE ANGULAR VELOCITY OF THE NAV FRAME WRT EARTH

RHOE=-VN/RE
RHON=VE/RE
RHOU=VE*TLAT/RE

C WE-WN-WU ARE THE ANGULAR VELOCITY OF THE NAV FRAME WRT
C INERTIAL FRAME COORDINATIZED IN THE NAV FRAME (E-N-U)

WE=RHOE
WN=RHON+OMEGAN
WU=RHOU+OMEGAU

C COMPONENTS OF THE 9 X 9 MATRIX

RKZ=VU/RE
RLAT2=2.*RLAT
F42=2.*(OMEGAN*VN+OMEGAU*VU)+RHON*VN/(CLAT**2)
F43=RHOU*RHOE+RHON*RKZ
F44=-RHOE*TLAT-RKZ
F52=-2.*(OMEGAN*VE-RHON*VE/CLAT**2)
F53=RHON*RHOU-RHOE*RKZ
F63=2.*G/RE-RHON**2-RHOE**2
F92=WN+RHOU*TLAT

C TRANSFORMATION FROM NAV FRAME (E-N-U) TO BODY FRAME (X-Y-Z)

CXE=SZ*CY
CXN=CZ*CY
CXU=SY
CYE=SZ*SY*SX+CZ*CX
CYN=CZ*SY*SX-SZ*CX
CYU=-CY*SX
CZE=-CZ*SX+SZ*SY*CX
CZN=CZ*SY*CX+SZ*SX
CZU=-CY*CX

C TRANSFORMATION FROM BODY FRAME (X-Y-Z) TO NAV FRAME (E-N-U)

CEX=CXE
CEY=CYE
CEZ=CZE
CNX=CXN
CNY=CYN
CNZ=CZN
CUX=CXU
CUY=CYU
CUZ=CZU

C SPECIFIC FORCE IN THE BODY FRAME

$FX = CXN * FN + CXP * FE + CXU * FU$
 $FY = CYN * FN + CYE * FE + CYU * FU$
 $FZ = CZN * FN + CZE * FE + CZU * FU$

C ANGULAR VELOCITY OF BODY FRAME WRT INERTIAL FRAME
 C COORDINATIZED IN THE BODY FRAME

$WX = CXE * WE + CXN * WN + CXU * WU + OPOLL$
 $WY = CYE * WE + CYN * WN + CYU * WU + OPITCH$
 $WZ = CZE * WE + CZN * WN + CZU * WU + DYAW$

$XDOT(1) = XF(2) * RHOU / CLAT - XF(3) * RHON / (RE * CLAT) + XF(4) /$
 $S(RE * CLAT)$
 $XDOT(2) = XF(3) * RHOE / RE + XF(5) / RE$
 $XDOT(3) = -R(1) * XF(3) + XF(6) + XF(40) * RK1 + XF(41) * RK1 * ALT$

$XDOT(4) = XF(2) * F42 + XF(3) * F43 + XF(4) * F44 + XF(5) * (WU + OMEGAU)$
 $S - XF(6) * (WN + OMEGAN) - XF(8) * FU + XF(9) * FN$
 $S + XF(22) * CEX + XF(23) * CEY + XF(24) * CEZ$
 $S + XF(25) * CEX + XF(26) * CEY + XF(27) * CEZ$
 $S + XF(28) * CEX + XF(29) * CEY + XF(30) * CEZ$
 $S + XF(31) * CEX * FX + XF(32) * CEY * FY + XF(33) * CEZ * FZ$
 $S - XF(34) * CEX * FZ + XF(35) * CEX * FY + XF(36) * CEY * FZ$
 $S - XF(37) * CEY * FX - XF(38) * CEZ * FY + XF(39) * CEZ * FX + XF(42)$

$XDOT(5) = XF(2) * F52 + XF(3) * F53 - XF(4) * 2. * WU - XF(5) * RKZ$
 $S + XF(6) * RHOE + XF(7) * FU - XF(9) * FE$
 $S + XF(22) * CNX + XF(23) * CNY + XF(24) * CNZ$
 $S + XF(25) * CNX + XF(26) * CNY + XF(27) * CNZ$
 $S + XF(28) * CNX + XF(29) * CNY + XF(30) * CNZ$
 $S + XF(31) * CNX * FX + XF(32) * CNY * FY + XF(33) * CNZ * FZ$
 $S - XF(34) * CNX * FZ + XF(35) * CNX * FY + XF(36) * CNY * FZ$
 $S - XF(37) * CNY * FX - XF(38) * CNZ * FY + XF(39) * CNZ * FX + XF(43)$

$XDOT(6) = -XF(2) * 2. * OMEGAU * VE + XF(3) * (F63 - RK2) + XF(4) * 2. * WN$
 $S - XF(5) * 2. * RHOE - XF(7) * FN + XF(8) * FE$
 $S + XF(22) * CUX + XF(23) * CUY + XF(24) * CUZ$
 $S + XF(25) * CUX + XF(26) * CUY + XF(27) * CUZ$
 $S + XF(28) * CUX + XF(29) * CUY + XF(30) * CUZ$
 $S + XF(31) * CUX * FX + XF(32) * CUY * FY + XF(33) * CUZ * FZ$
 $S - XF(34) * CUX * FZ + XF(35) * CUX * FY + XF(36) * CUY * FZ$
 $S - XF(37) * CUY * FX - XF(38) * CUZ * FY + XF(39) * CUZ * FX$
 $S + XF(40) * RK2 + XF(41) * RK2 * ALT + XF(44)$
 $S - XF(45)$

$XDOT(7) = -XF(3) * RHOE / RE - XF(5) / RE + XF(8) * WU - XF(9) * WN$
 $S + XF(10) * CEX + XF(11) * CEY - XF(12) * CEZ$
 $S + XF(13) * CEX * WX + XF(14) * CEY * WY + XF(15) * CEZ * WZ$

```

E+XF(16)*CFX*WZ-XF(17)*CFX*WY-XF(18)*CFY*WZ
E+XF(19)*CFY*WX+XF(20)*CEZ*WY-XF(21)*CEZ*WX

```

```

XDOT(8)=-XF(2)*OMEGAU-XF(3)*RHON/RE+XF(4)/RE-XF(7)*WJ
E+XF(9)*WE+XF(10)*CNX+XF(11)*CNY+XF(12)*CNZ
E+XF(13)*CNX*WX+XF(14)*CNY*WY+XF(15)*CNZ*WZ
E+XF(16)*CNX*WZ-XF(17)*CNX*WY-XF(18)*CNY*WZ
E+XF(19)*CNY*WX+XF(20)*CNZ*WY-XF(21)*CNZ*WX

```

```

XDOT(9)=XF(2)*F92-XF(3)*RHOU/RE+XF(4)*TLAT/RE+XF(7)*WN
E-XF(8)*WE+XF(10)*CUX+XF(11)*CUY+XF(12)*CUZ
E+XF(13)*CUX*WX+XF(14)*CUY*WY+XF(15)*CUZ*WZ
E+XF(16)*CUX*WZ-XF(17)*CUX*WY-XF(18)*CUY*WZ
E+XF(19)*CUY*WX+XF(20)*CUZ*WY-XF(21)*CUZ*WX

```

```

DO 2 I=10,24
2 XDOT(I)=0.

```

```

XDOT(25)=-XF(25)/TAUF(1)
XDOT(26)=-XF(26)/TAUF(2)
XDOT(27)=-XF(27)/TAUF(3)
XDOT(28)=-XF(28)/TAUF(4)
XDOT(29)=-XF(29)/TAUF(5)
XDOT(30)=-XF(30)/TAUF(6)

```

```

DO 4 I=31,39
4 XDOT(I)=0.

```

```

XDOT(40)=-XF(40)*VGND/DIST(1)
XDOT(41)=0.
XDOT(42)=-XF(42)*VGND/DIST(2)
XDOT(43)=-XF(43)*VGND/DIST(3)
XDOT(44)=-XF(44)*VGND/DIST(4)
XDOT(45)=XF(3)*RK3-XF(40)*RK3-XF(41)*RK3*ALT
RETURN

```

```

ENTRY XFDDTD
RETURN
END

```

THREE AXIS RLG FILTER MODEL

```

$PRDATA
NF=45, NS=1, TF=1400., DTPRPL=15., NXTJ=16, LPP=.T.,
NZF=152, NZO=16, LPRXS=.F., LPRXF=.T., LPRLT=.F., LPRDG=.T.,
LXTJ=.T., DTPRNT=150.,M=0, LPRXTJ=.T.,
LCC=.T., DICCP=5.,
1, 2, 1, 3, 1, 4, 2, 3, 2, 5,
3, 6, 4, 2, 4, 3, 4, 4, 4, 5,
4, 6, 4, 3, 4, 9, 4, 22, 4, 23,
4, 24, 4, 25, 4, 26, 4, 27, 4, 28,
4, 29, 4, 30, 4, 31, 4, 32, 4, 33,

```

4,34, 4,35, 4,36, 4,37, 4,38,
 4,39, 4,42, 5, 2, 5, 3, 5, 4,
 5, 5, 5, 6, 5, 7, 5, 9, 5,22,
 5,23, 5,24, 5,25, 5,26, 5,27,
 5,28, 5,29, 5,30, 5,31, 5,32,
 5,33, 5,34, 5,35, 5,36, 5,37,
 5,38, 5,39, 5,43, 6, 2, 6, 3,
 6, 4, 6, 5, 6,45, 6, 7, 6, 8,
 6,22, 6,23, 6,24, 6,25, 6,26,
 6,27, 6,28, 6,29, 6,30, 6,31,
 6,32, 6,33, 6,34, 6,35, 6,36,
 6,37, 6,38, 6,39, 6,40, 6,41,
 6,44, 7, 3, 7, 5, 7, 8, 7, 9,
 7,10, 7,11, 7,12, 7,13, 7,14,
 7,15, 7,16, 7,17, 7,18, 7,19,
 7,20, 7,21, 8, 2, 8, 3, 8, 4,
 8, 7, 8, 9, 8,10, 8,11, 8,12,
 8,13, 8,14, 8,15, 8,16, 8,17,
 8,18, 8,19, 8,20, 8,21, 9, 2,
 9, 3, 9, 4, 9, 7, 9, 8, 9,10,
 9,11, 9,12, 9,13, 9,14, 9,15,
 9,16, 9,17, 9,18, 9,19, 9,20,
 9,21, 25,25, 26,26, 27,27, 28,28,
 29,29, 30,30, 40,40, 42,42, 43,43,
 44,44, 45, 3, 3, 3, 3,40, 3,41,
 45,40, 45,41

7, 7, 8, 8, 9, 9, 10,10,
 11,11, 12,12, 25,25, 26,26, 27,27,
 28,28, 29,29, 30,30, 40,40, 42,42,
 43,43, 44,44,

1*0.

45*0.

1,1,5.13235E-9
 2,2,5.13235E-9
 3,3,2.25E+6
 4,4,9.13486E-15
 5,5,9.13486E-15
 6,6,9.13486E-15
 7,7,.25E-6
 8,8,.25E-6
 9,9,.25E-6
 10,10,1.90385E-13
 11,11,1.90385E-13
 12,12,1.90385E-13
 13,13,1.E-8
 14,14,1.E-8
 15,15,1.E-8

15,16,8.46158E-10
 17,17,8.46158E-10
 18,18,8.46158E-10
 19,19,8.46158E-10
 20,20,8.46158E-10
 21,21,8.46158E-10
 22,22,6.48025E-5
 23,23,6.48025E-5
 24,24,6.48025E-5
 25,25,1.65894E-6
 26,26,1.65894E-6
 27,27,1.65894E-6
 28,28,4.14736E-7
 29,29,4.14736E-7
 30,30,4.14736E-7
 31,31,2.5E-7
 32,32,2.5E-7
 33,33,2.5E-7
 34,34,2.35043E-9
 35,35,2.35043E-9
 36,36,2.35043E-9
 37,37,2.35043E-9
 38,38,2.35043E-9
 39,39,2.35043E-9
 40,40,2.5E+5
 41,41,9.E-4
 42,42,7.00903E-7
 43,43,2.99646E-7
 44,44,1.27012E-6
 45,45,1.E-4
 0,0,0.

SINF TAUF(1)=3600.,3600.,3600.,900.,900.,900.,

DIST(1)=1519025.8,60761.0333,60761.0333,364566.19,

SOWFO(1)=7.16823E-5, 7.16823E-5, 1.5 E+3,
 9.55765E-8, 9.55765E-8, 9.55765E-8,
 .5E-3, .5E-3, .5E-3,
 4.36332E-7, 4.36332E-7, 4.36332E-7,
 100.E-6, 100.E-6, 100.E-6,
 2.90888E-5, 2.90888E-5, 2.90888E-5,
 2.90888E-5, 2.90888E-5, 2.90888E-5,
 8.05E-3, 8.05E-3, 8.05E-3,
 1.288E-3, 1.288E-3, 1.288E-3,
 6.44E-4, 6.44E-4, 6.44E-4,
 500.E-6, 500.E-6, 500.E-6,
 4.84813E-5, 4.84813E-5, 4.84813E-5,
 4.84813E-5, 4.84813E-5, 4.84813E-5,
 5.E+2, 3.E-2, 8.372E-4,

5.474E-4, 1.127E-3, 1.E-2,

DEFIN(1)=7.6E-11, 7.6E-11, 7.6E-11,
1.47E-18, 1.47E-18, 1.47E-18,
9.21635E-10, 9.21635E-10, 9.21635E-10,
9.21635E-10, 9.21635E-10, 9.21635E-10,
.3291583, 2.30708E-11, 9.86312E-12,
6.96789E-12,
SD450(1)=1.53

1.

0.1,1,3437.7467
0.2,2,3437.7467
0.3,3,1.
0.4,4,1.
0.5,5,1.
0.6,6,1.
0.7,7,3437.7467
0.8,8,3437.7467
0.9,9,3437.7467
0,0,0,0.

TIME (SEC)

LONGITUDE ERROR
POSITION *ARC MIN*
LATITUDE ERROR
POSITION *ARC MIN*
ALTITUDE ERROR
ALTITUDE *FEET*
EAST VELOCITY ERROR
VELOCITY *FPS*
NORTH VELOCITY ERROR
VELOCITY *FPS*
UP VELOCITY ERROR
VELOCITY *FPS*
EAST TILT
TILT *ARC MIN*
NORTH TILT
TILT *ARC MIN*
AZIMUTH ERROR
AZIM *ARC MIN*

Appendix H

Plots of ensemble averages of error states, plus and minus one standard deviation, as a result of specific sensor errors.

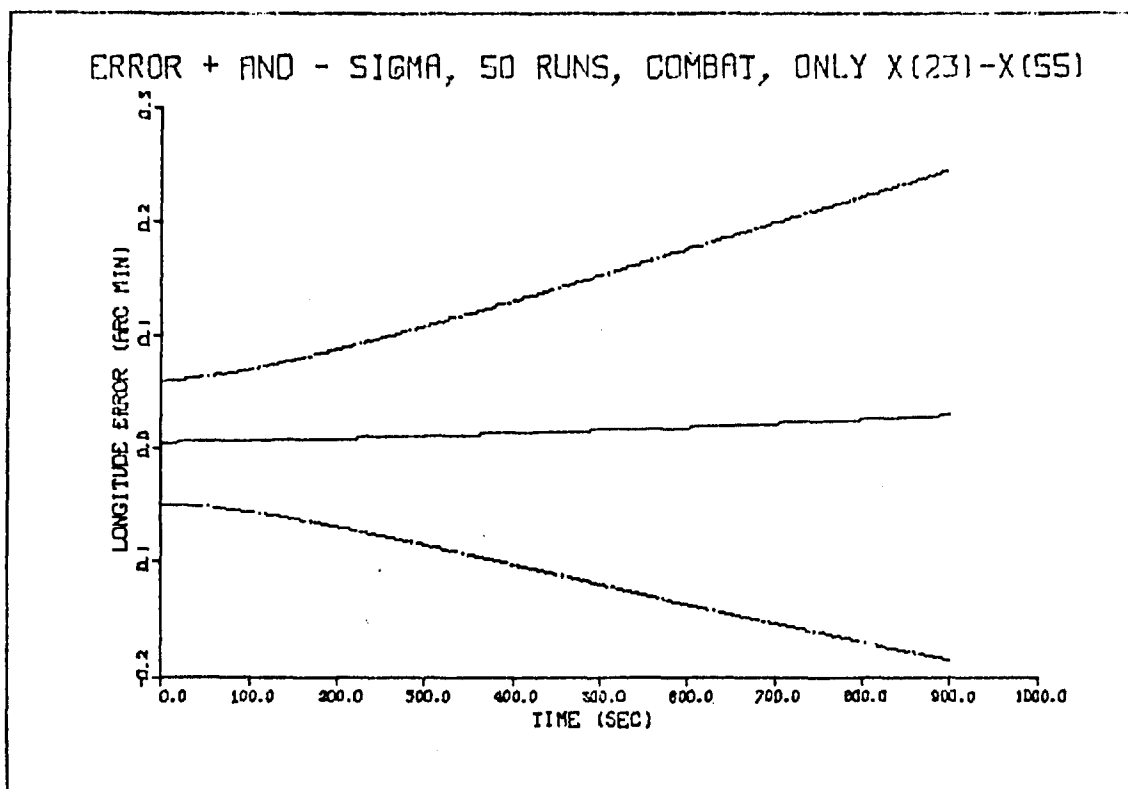


Figure H-1. Longitude error state from accelerometer noise

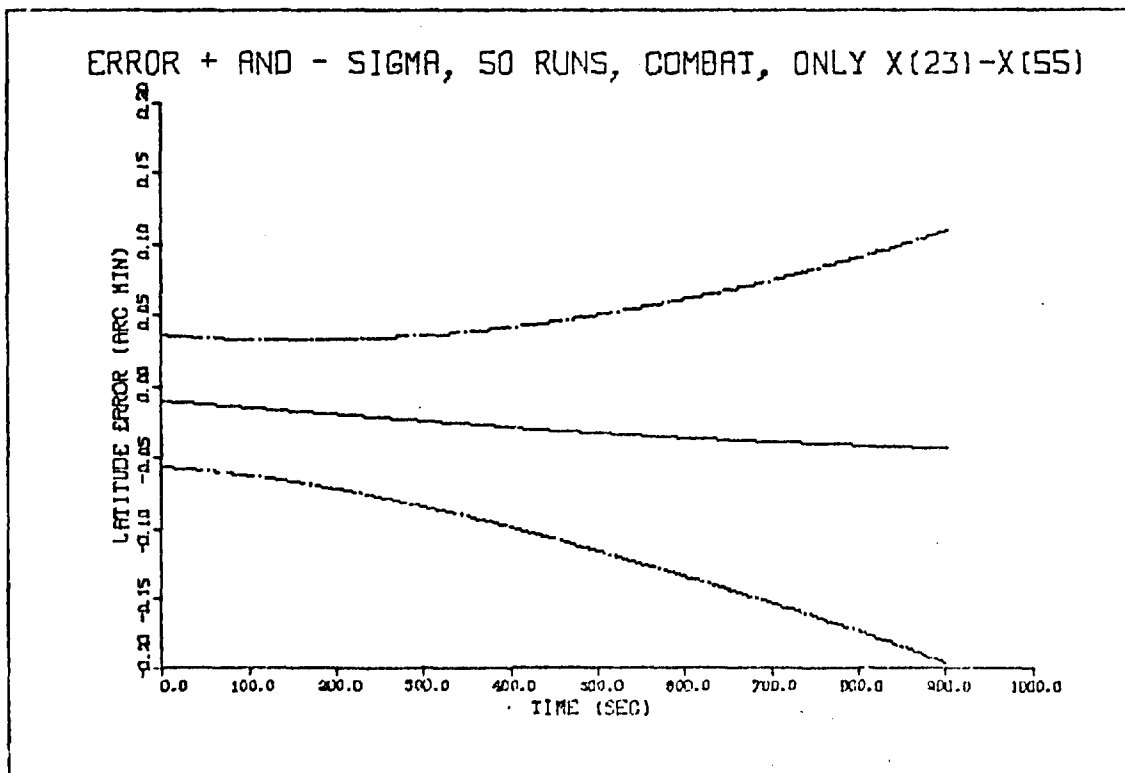


Figure H-2. Latitude error state from accelerometer noise

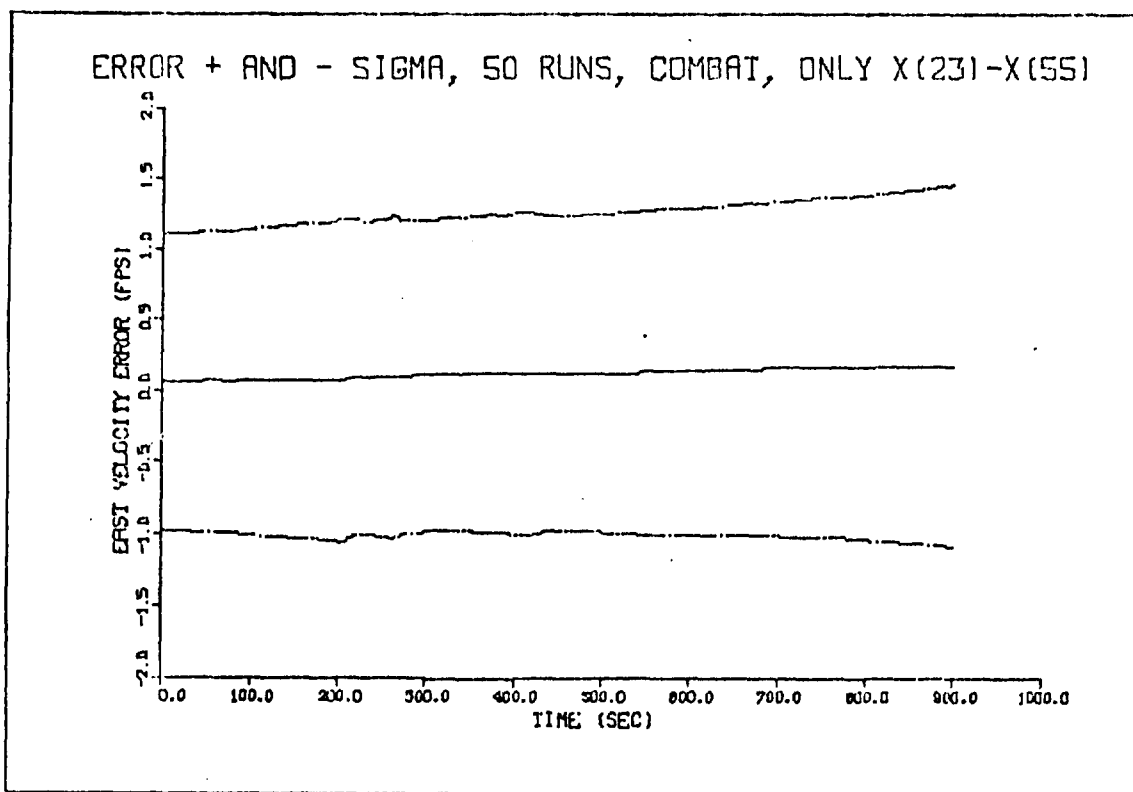


Figure H-3. East vel. error state from accelerometer noise

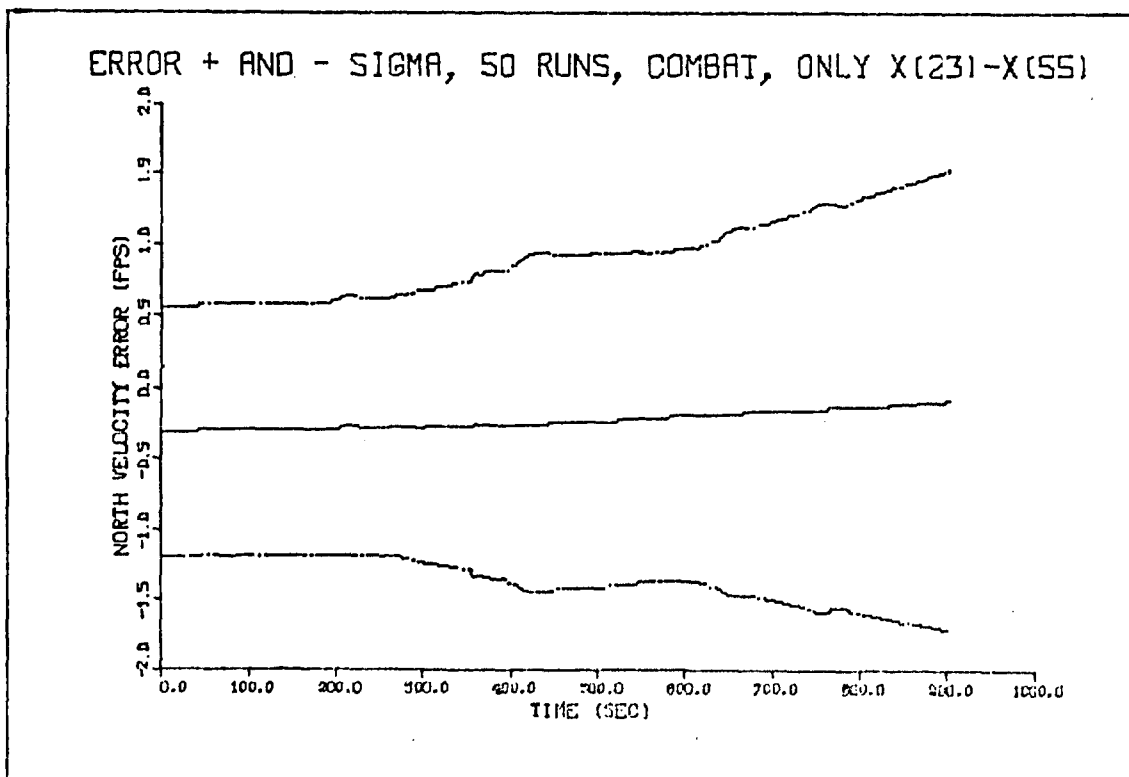


Figure H-4. North vel. error state from accelerometer noise

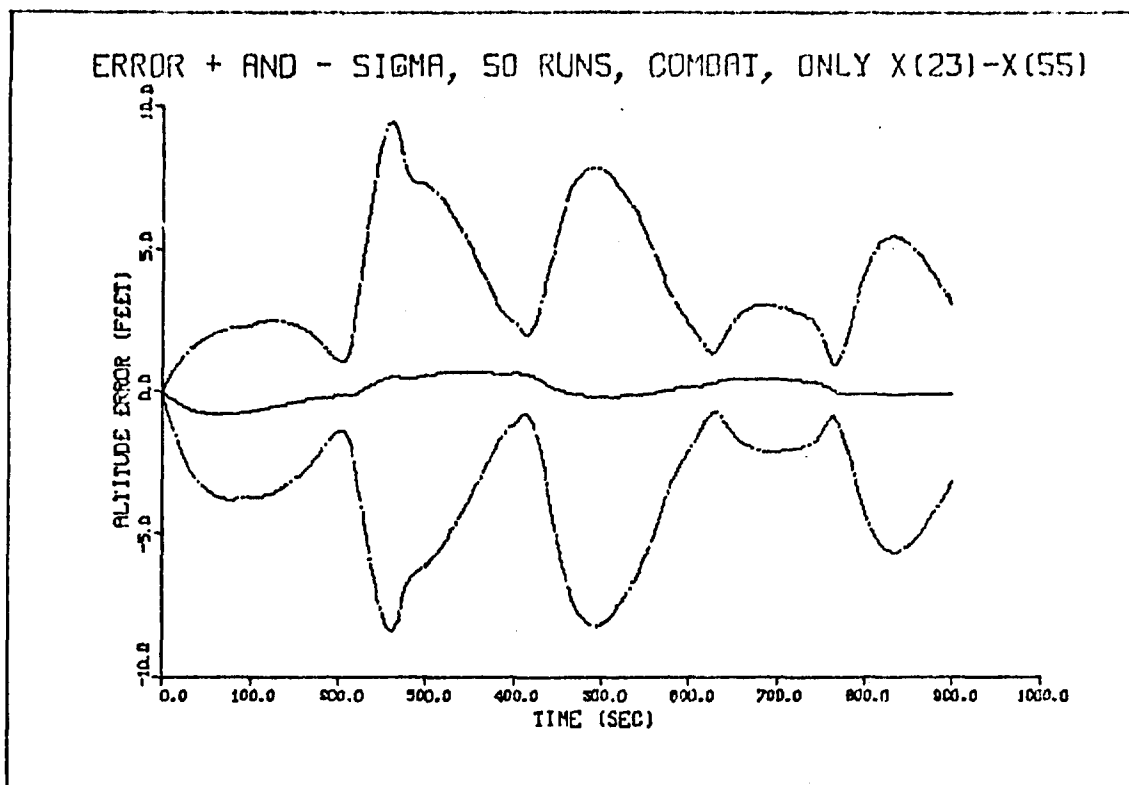


Figure H-5. Altitude error state from accelerometer noise

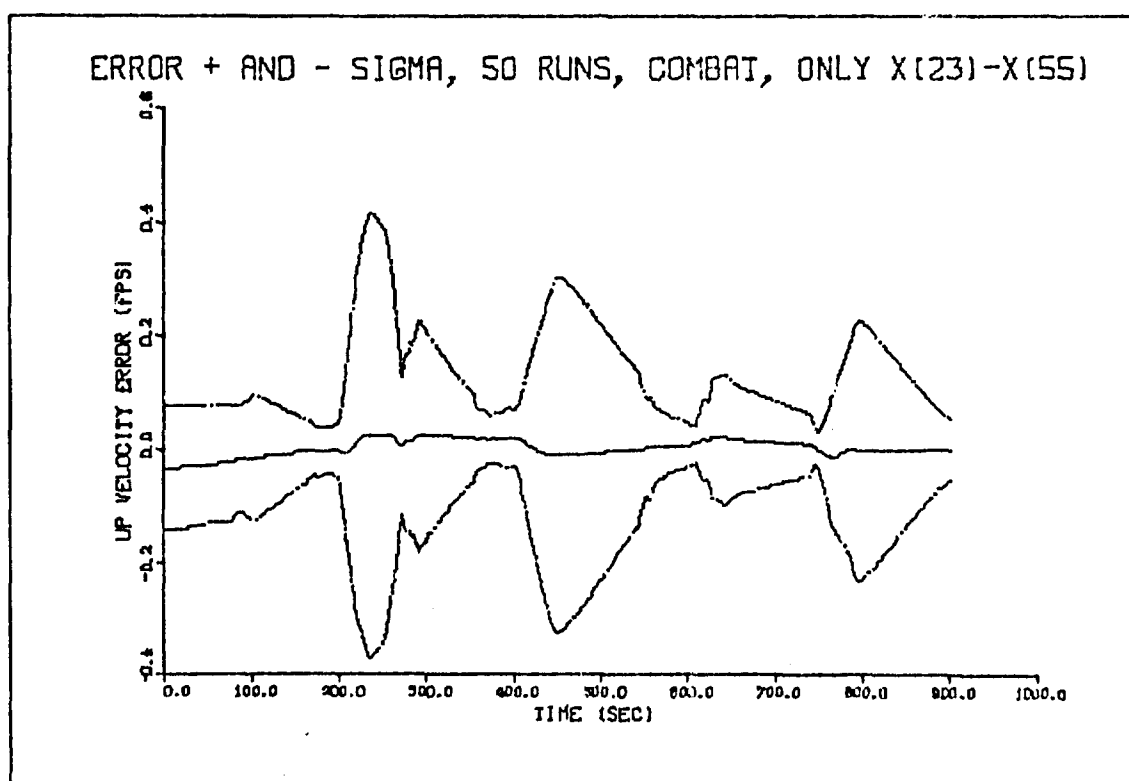


Figure H-6. Up vel. error state from accelerometer noise

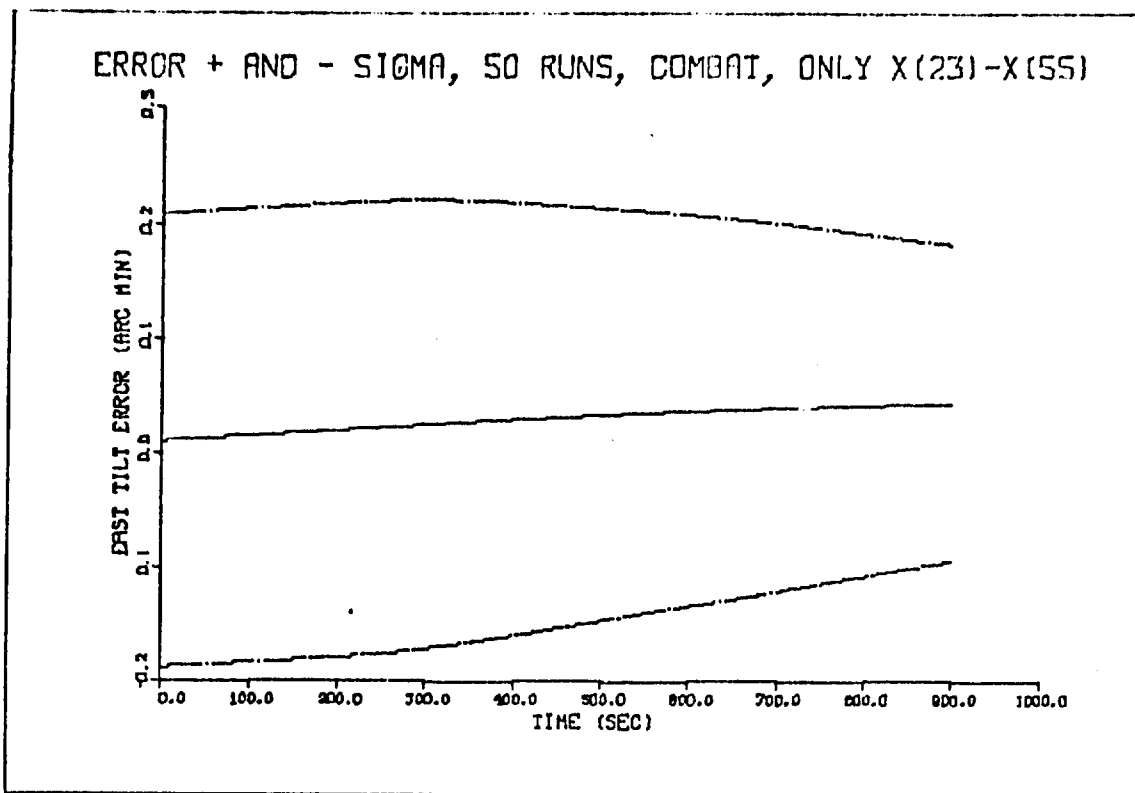


Figure H-7. East tilt error state from accelerometer noise

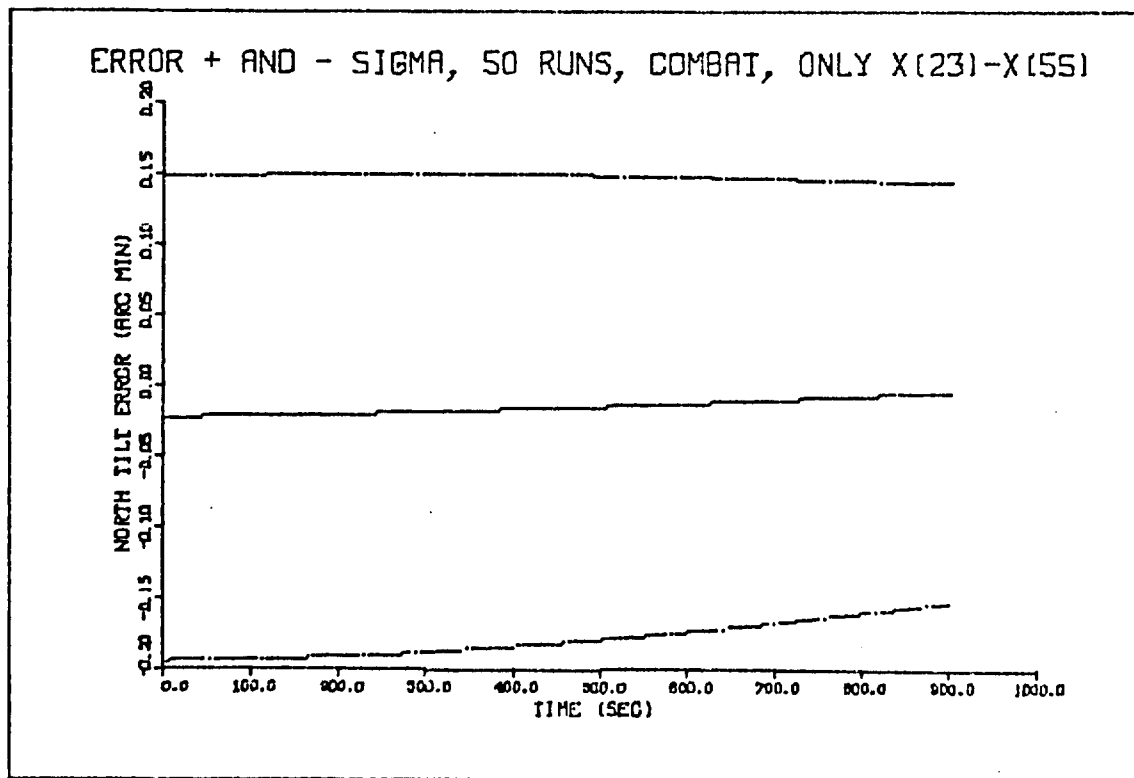


Figure H-8. North tilt error state from accelerometer noise

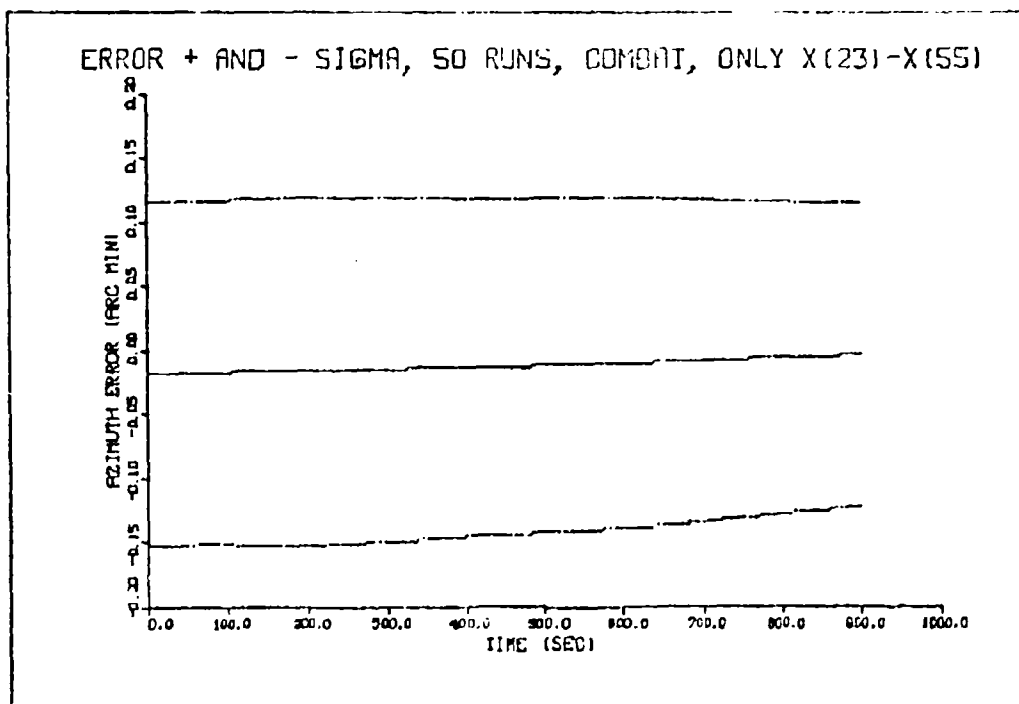


Figure H-9. Azimuth error state from accelerometer noise

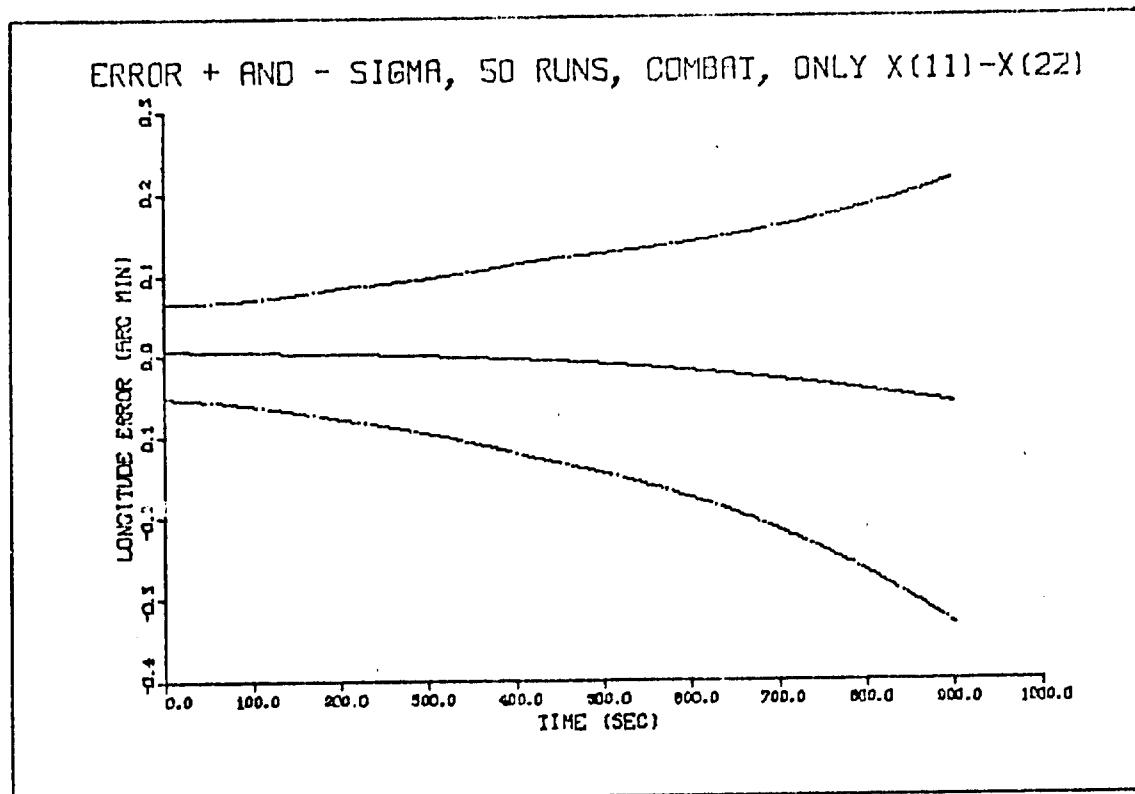


Figure H-10. Longitude error state from gyro noise

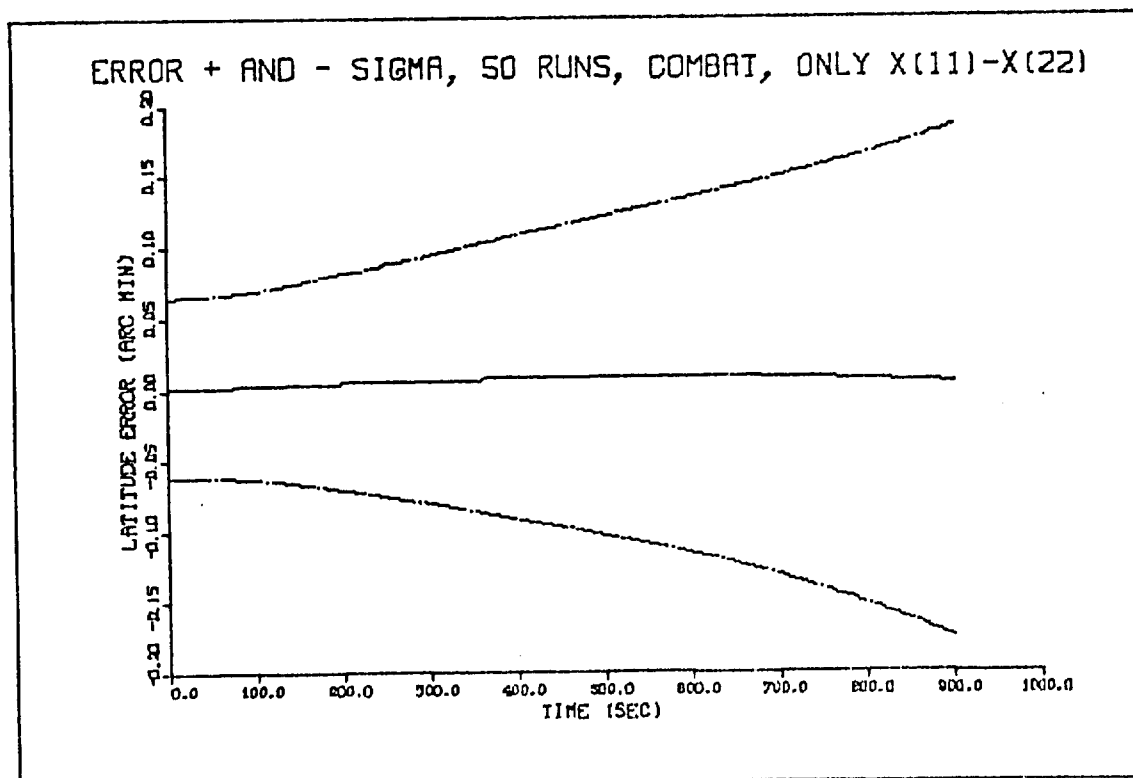


Figure H-11. Latitude error state from gyro noise

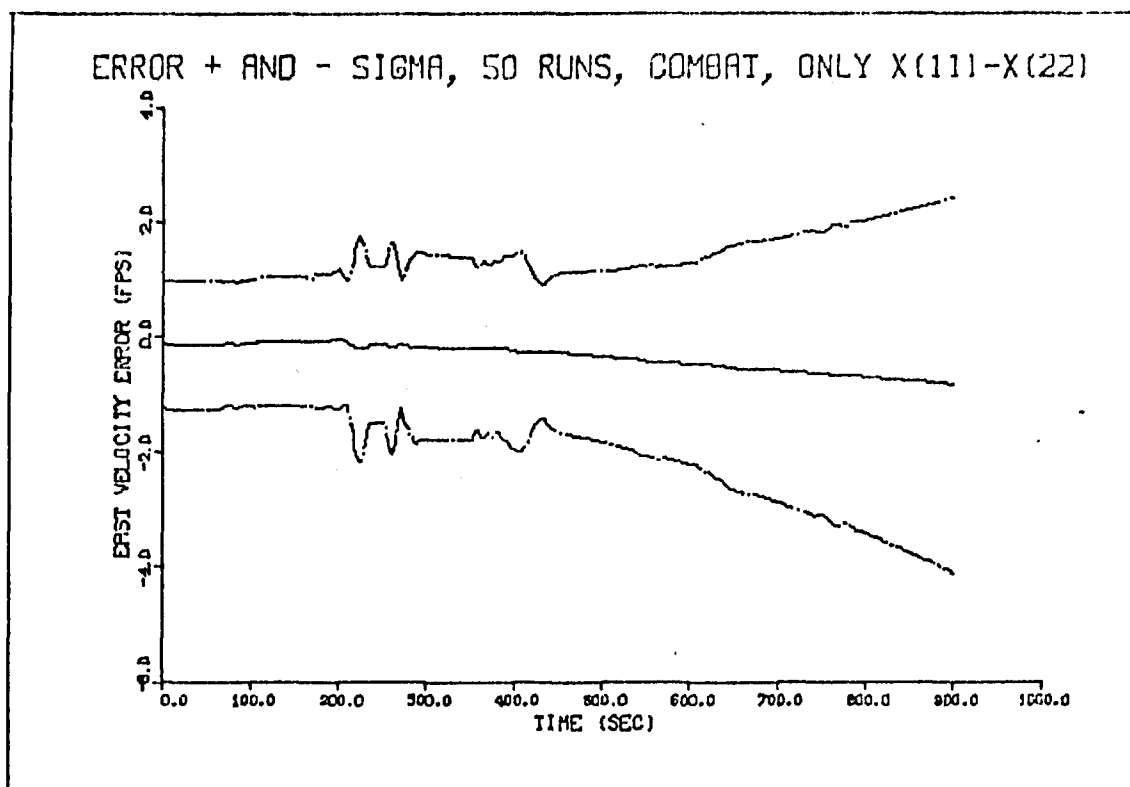


Figure H-12. East vel. error state from gyro noise

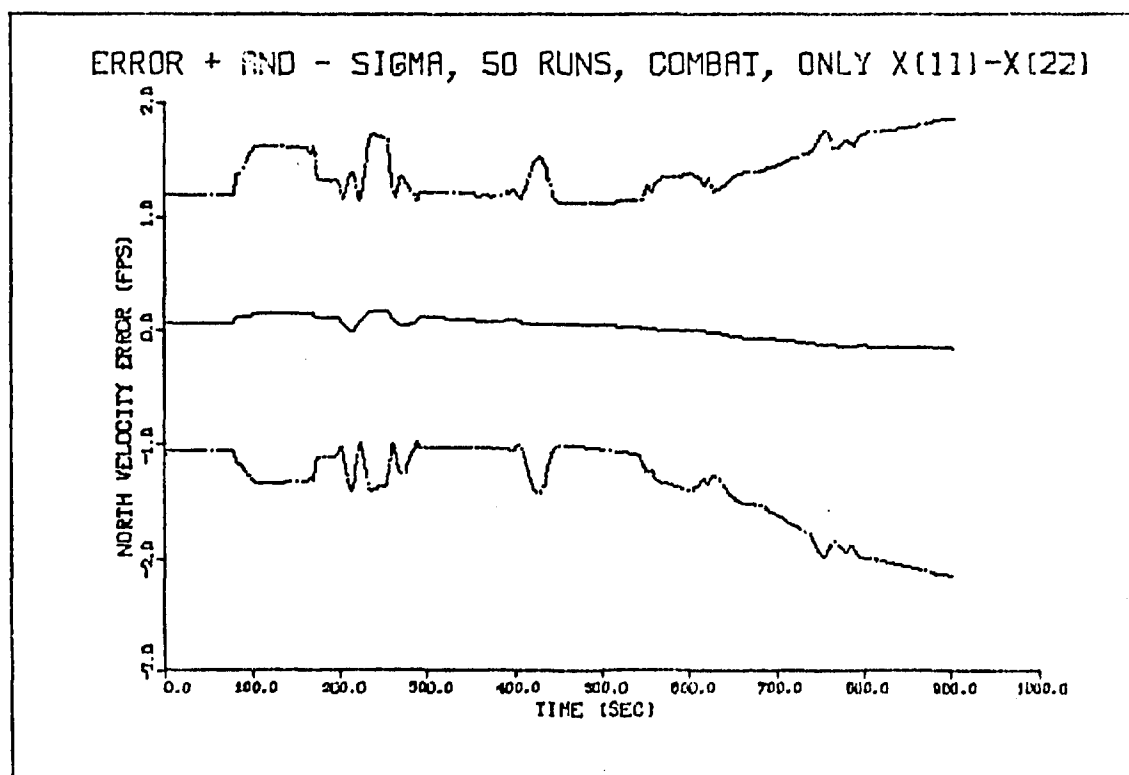


Figure H-13. North vel. error state from gyro noise

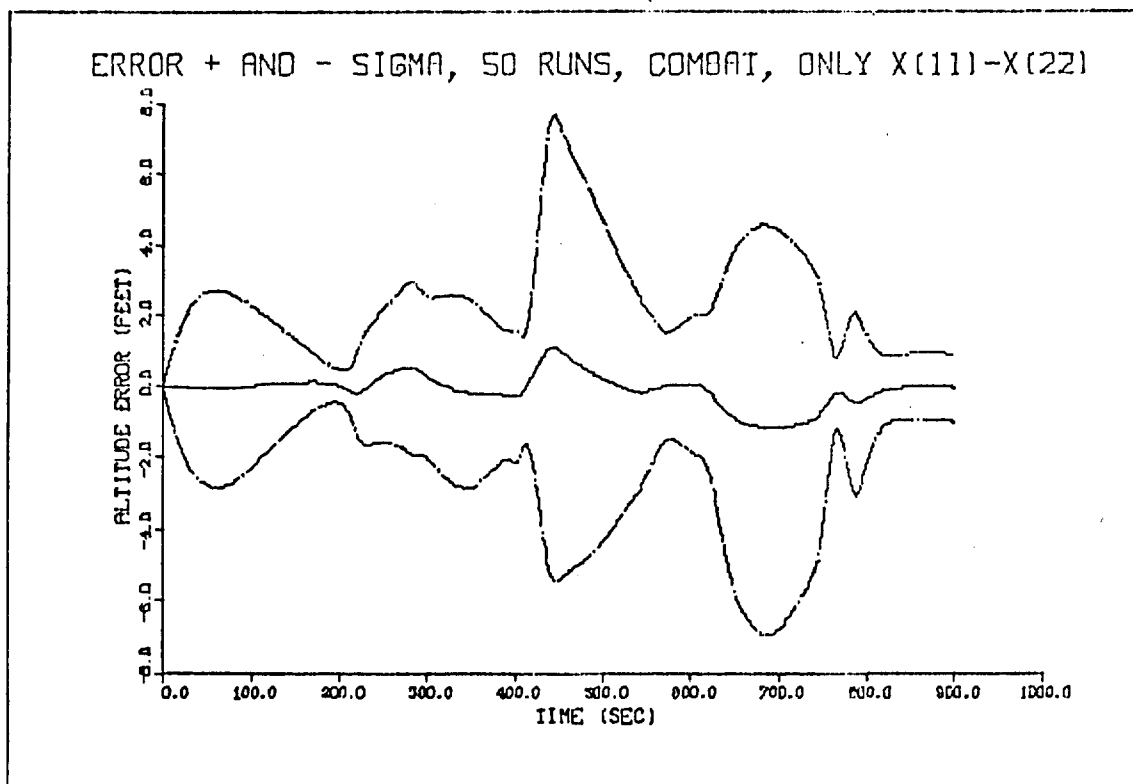


Figure H-14. Altitude error state from gyro noise

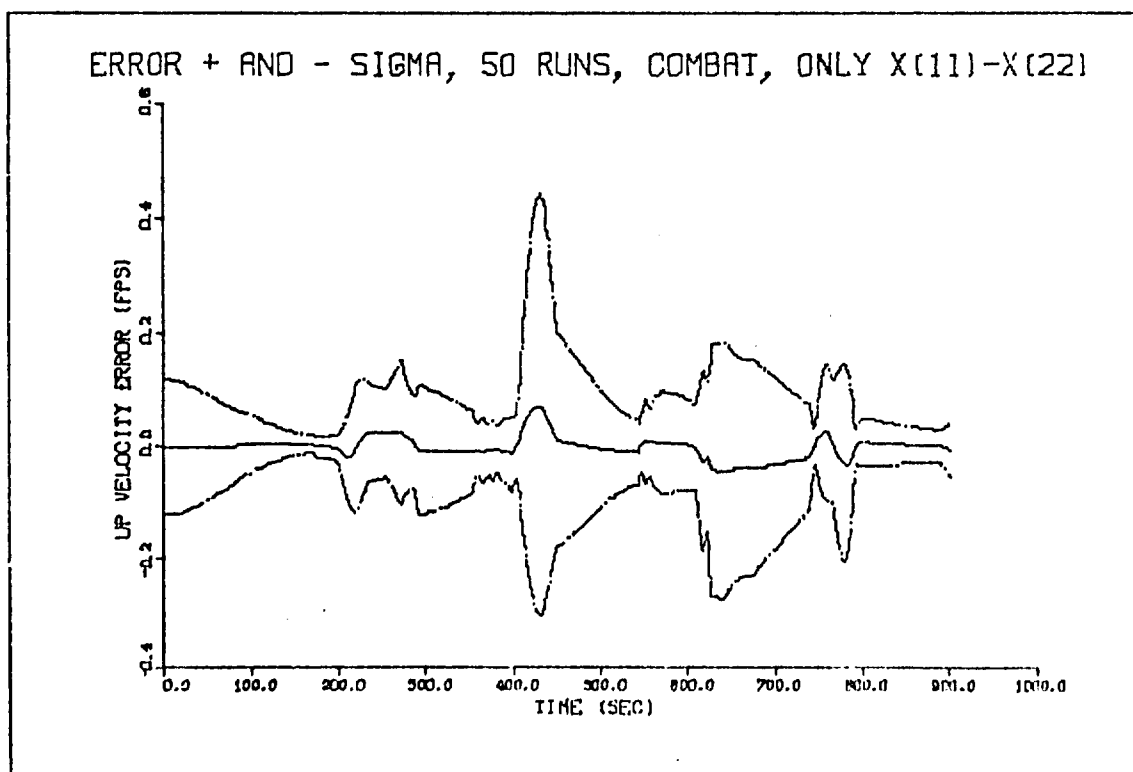


Figure H-15. Up vel. error state from gyro noise

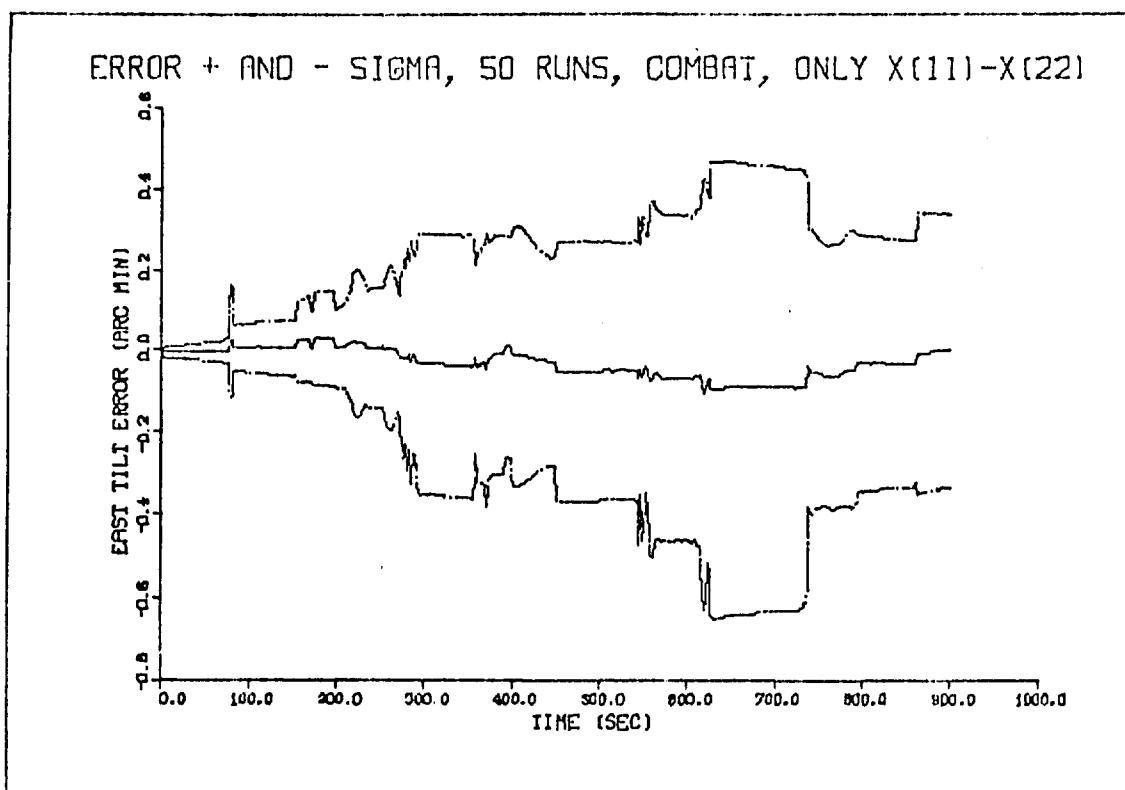


Figure H-16. East tilt error state from gyro noise

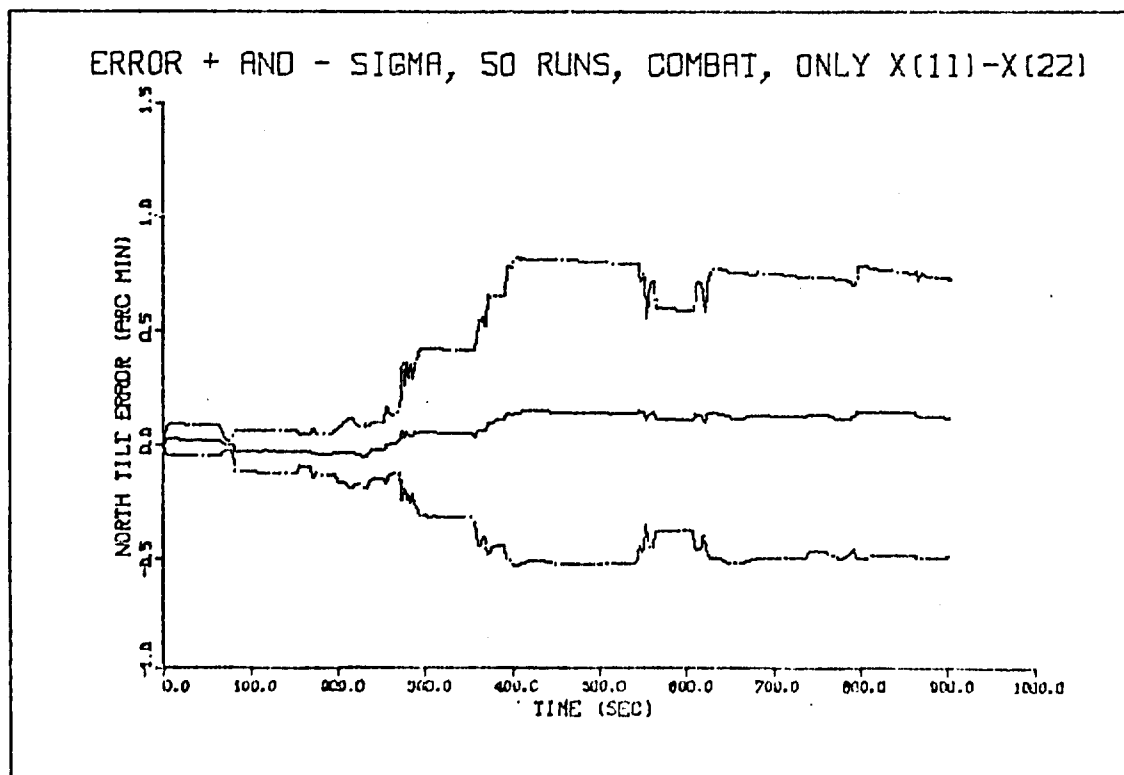


Figure H-17. North tilt error state from gyro noise

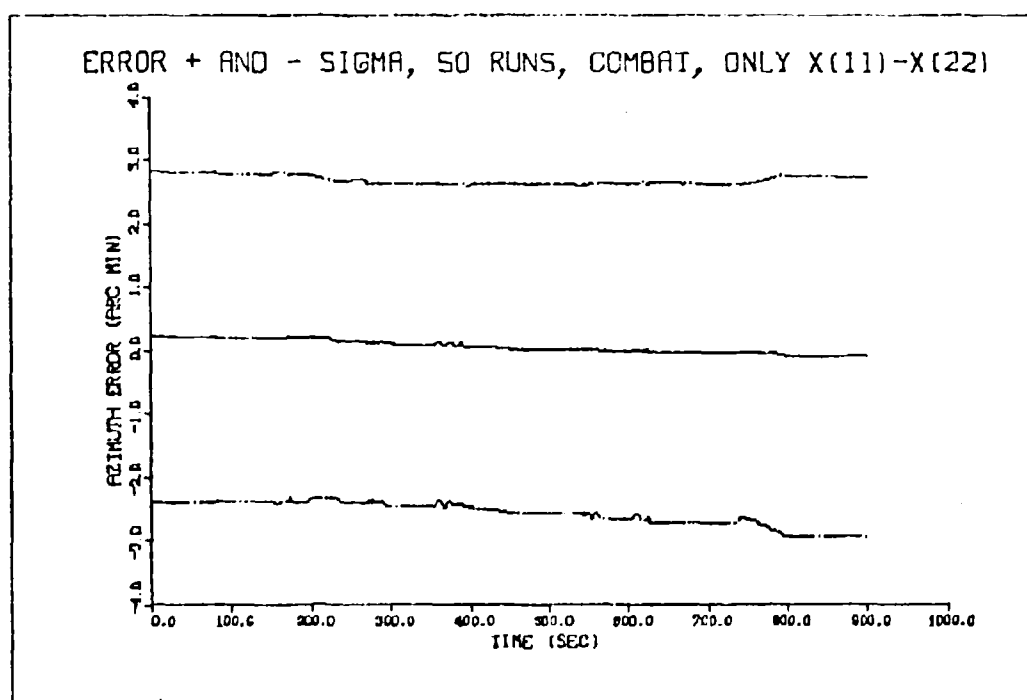


Figure H-18. Azimuth error state from gyro noise

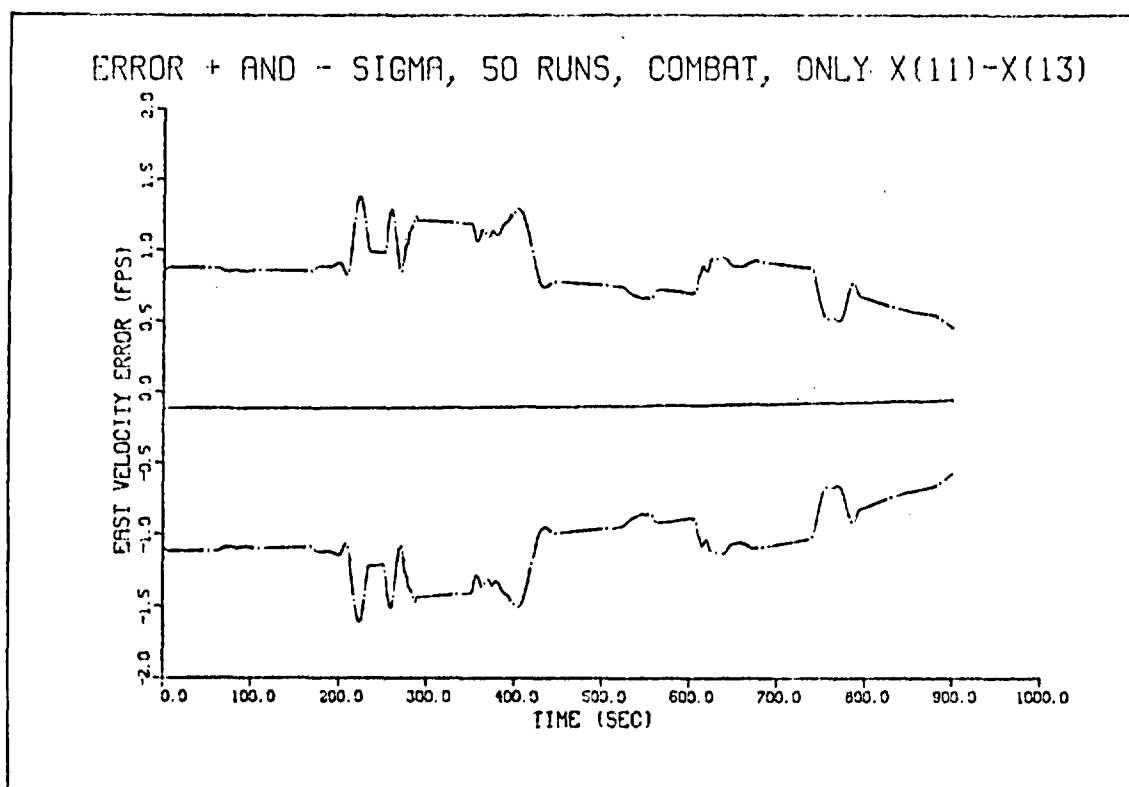


Figure H-19. East vel. error state from gyro bias

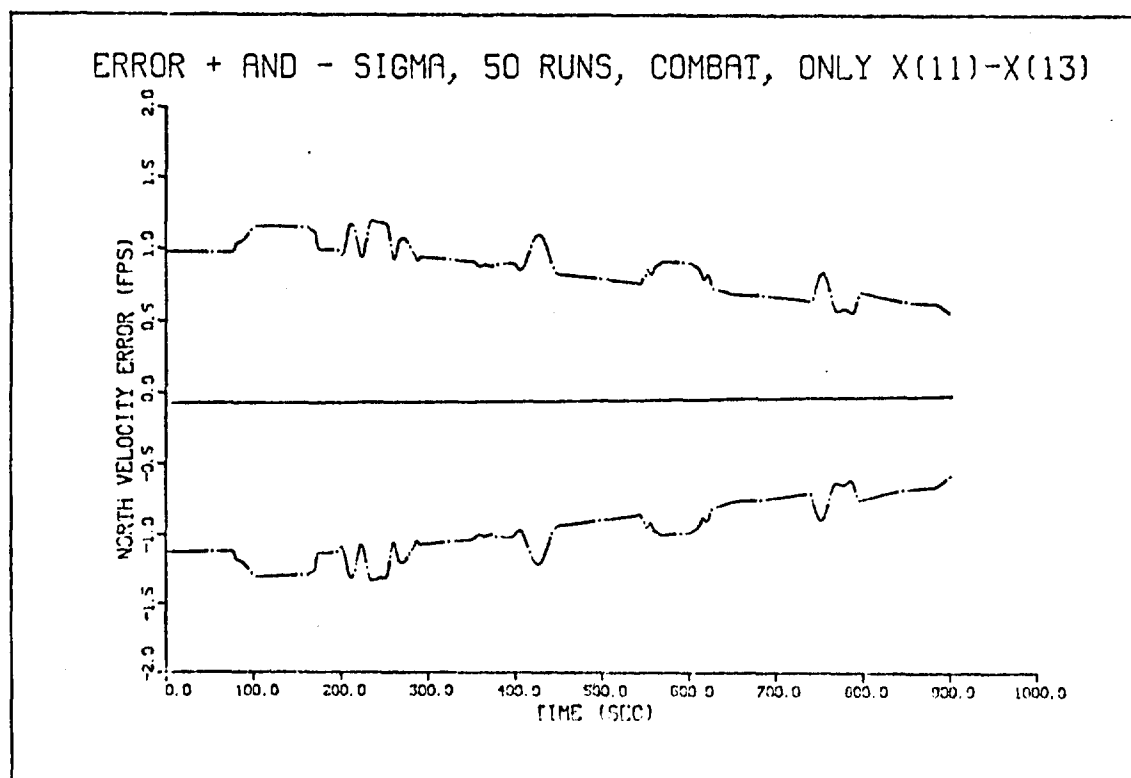


Figure H-20. North vel. error state from gyro bias

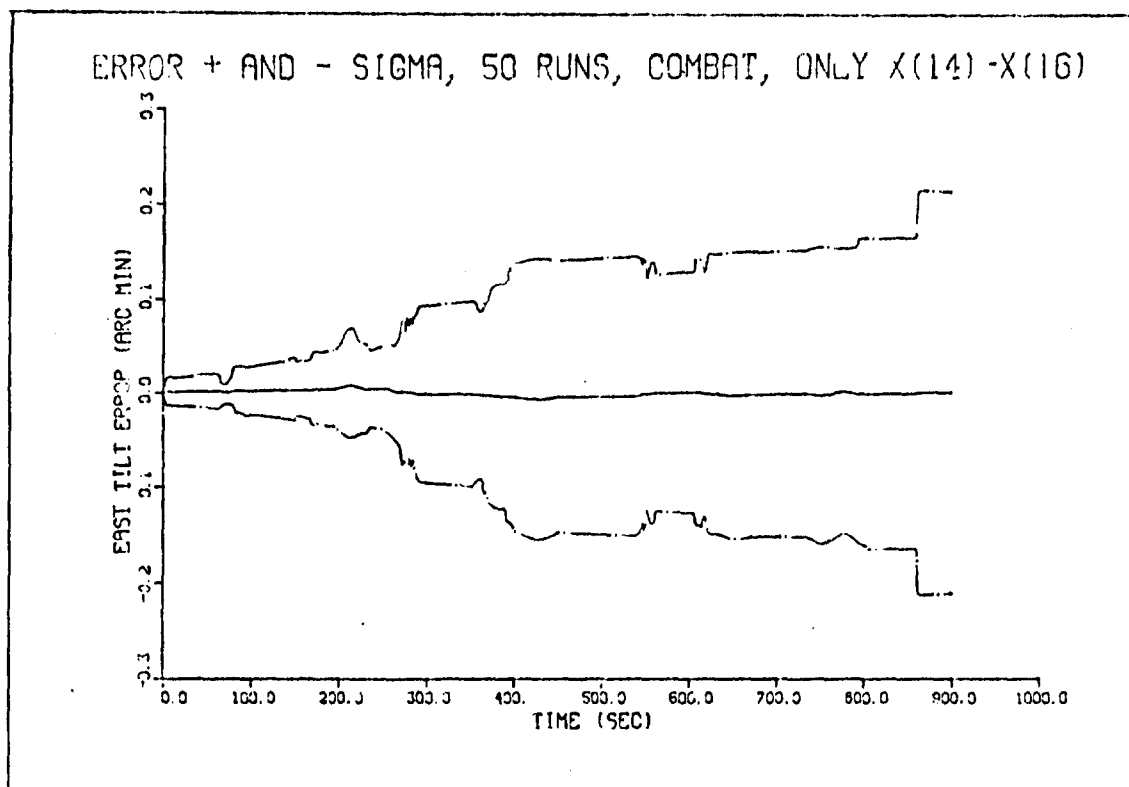


Figure H-21. East tilt error state from gyro scale factor

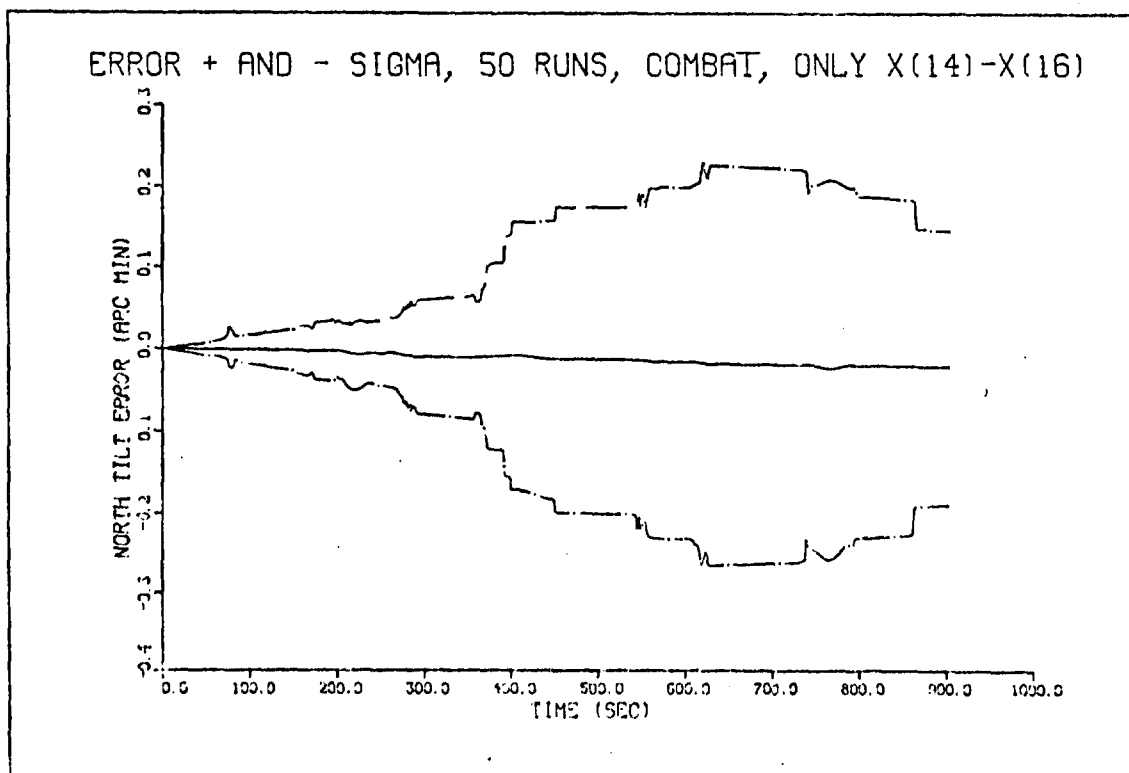


Figure H-22. North tilt error state from gyro scale factor

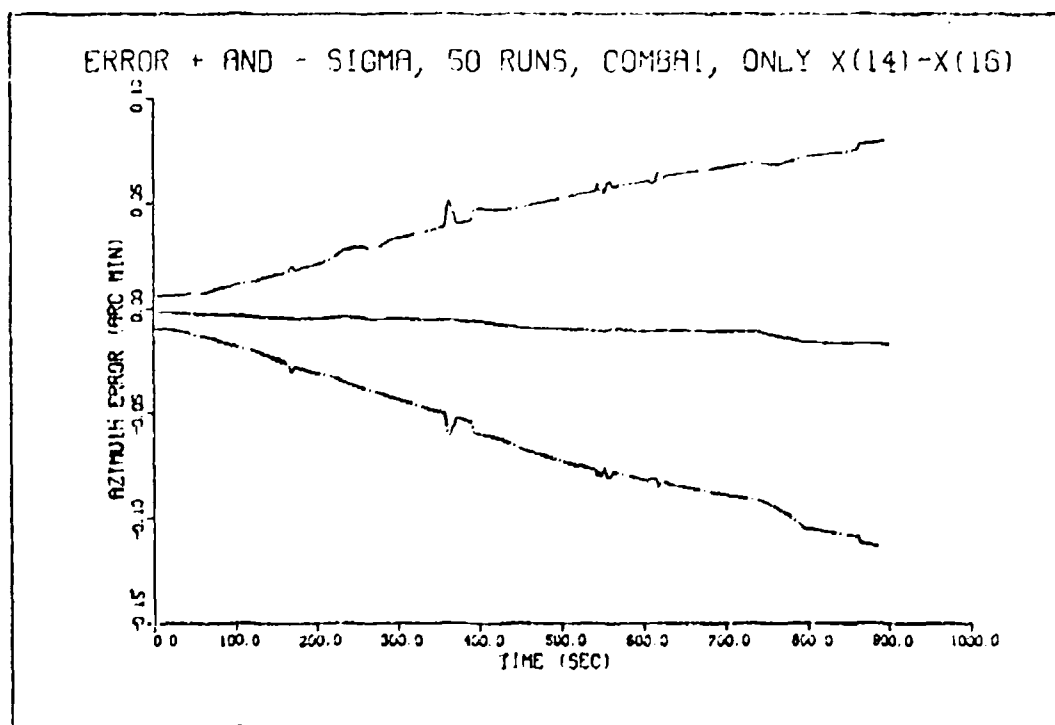


Figure n-23. Azimuth error state from gyro scale factor

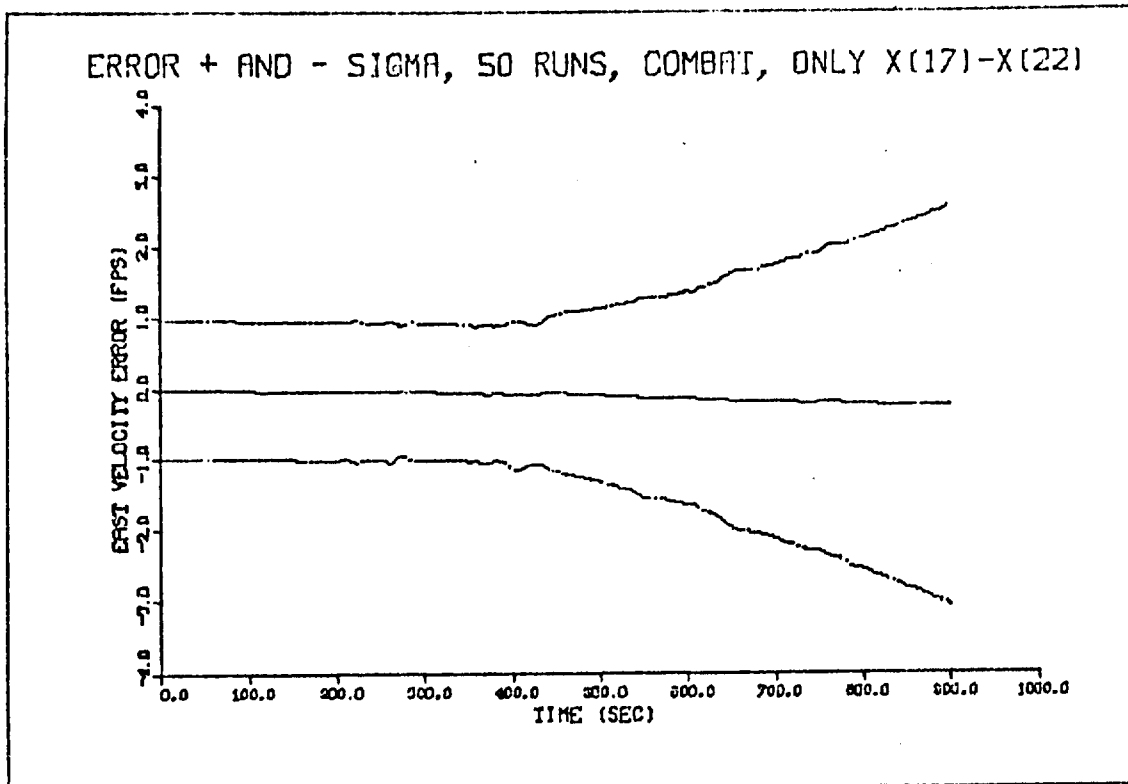


Figure H-24. East vel. error state from gyro misalignment

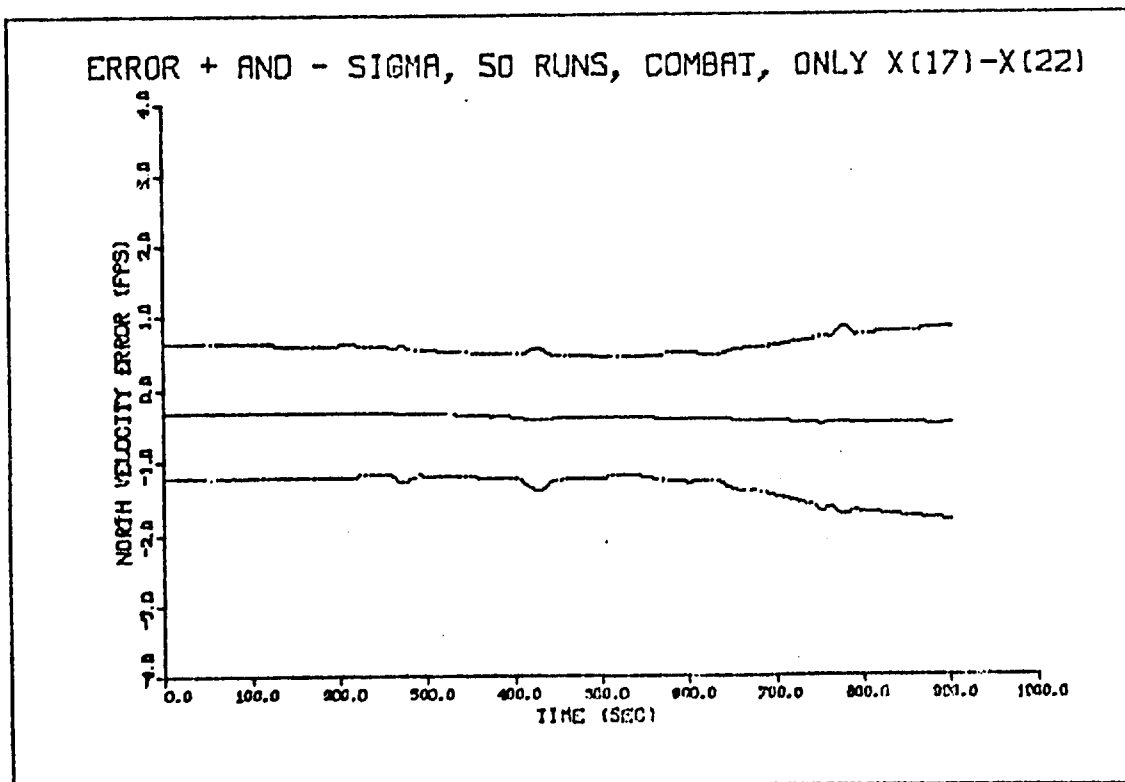


Figure H-25. North vel. error state from gyro misalignment

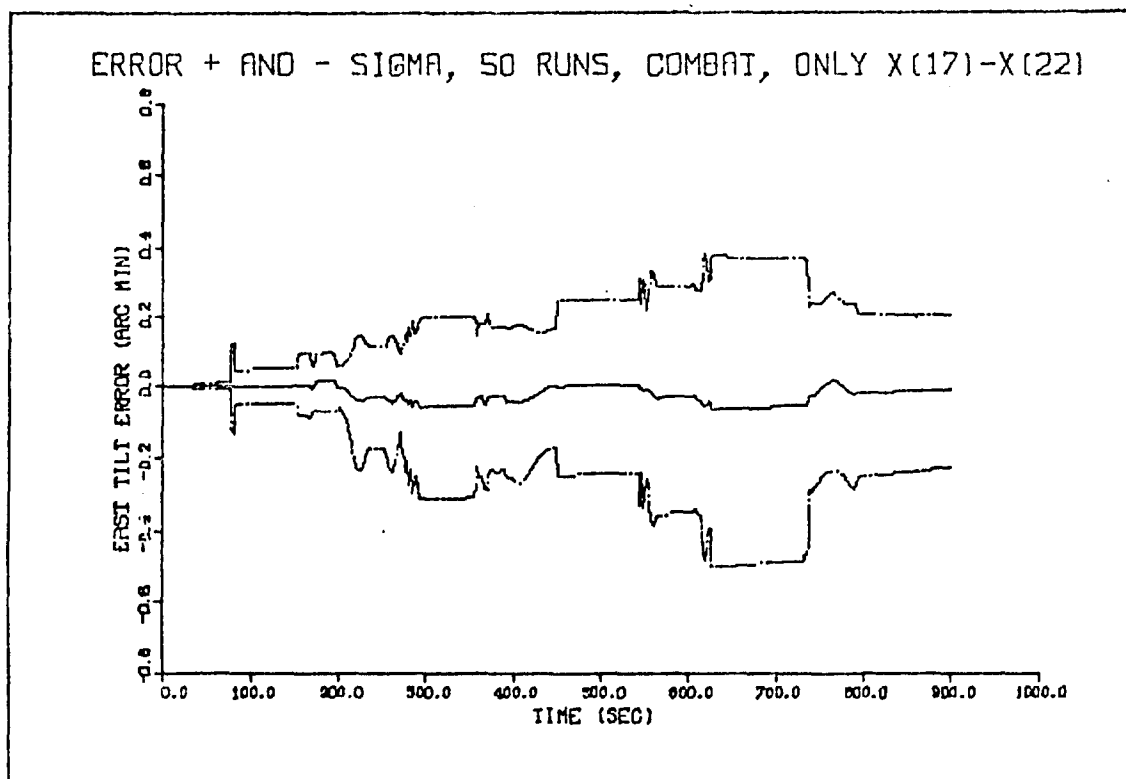


Figure H-26. East tilt error state from gyro misalignment

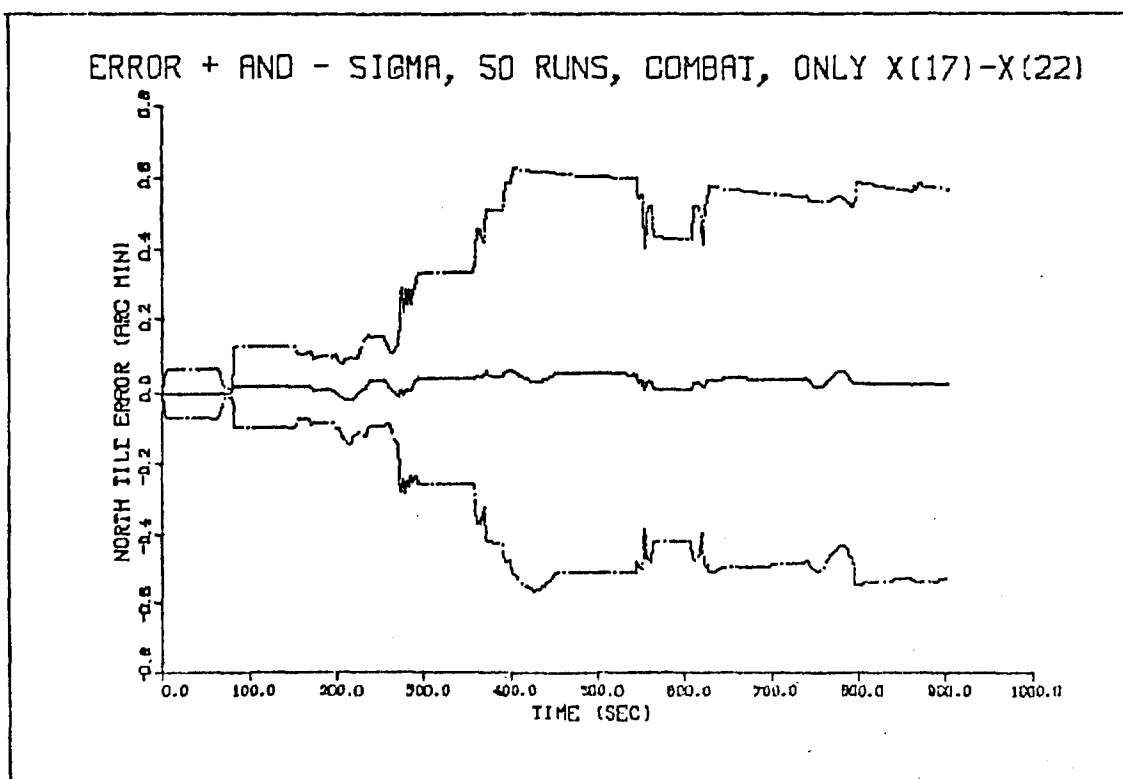


Figure H-27. North tilt error state from gyro misalignment

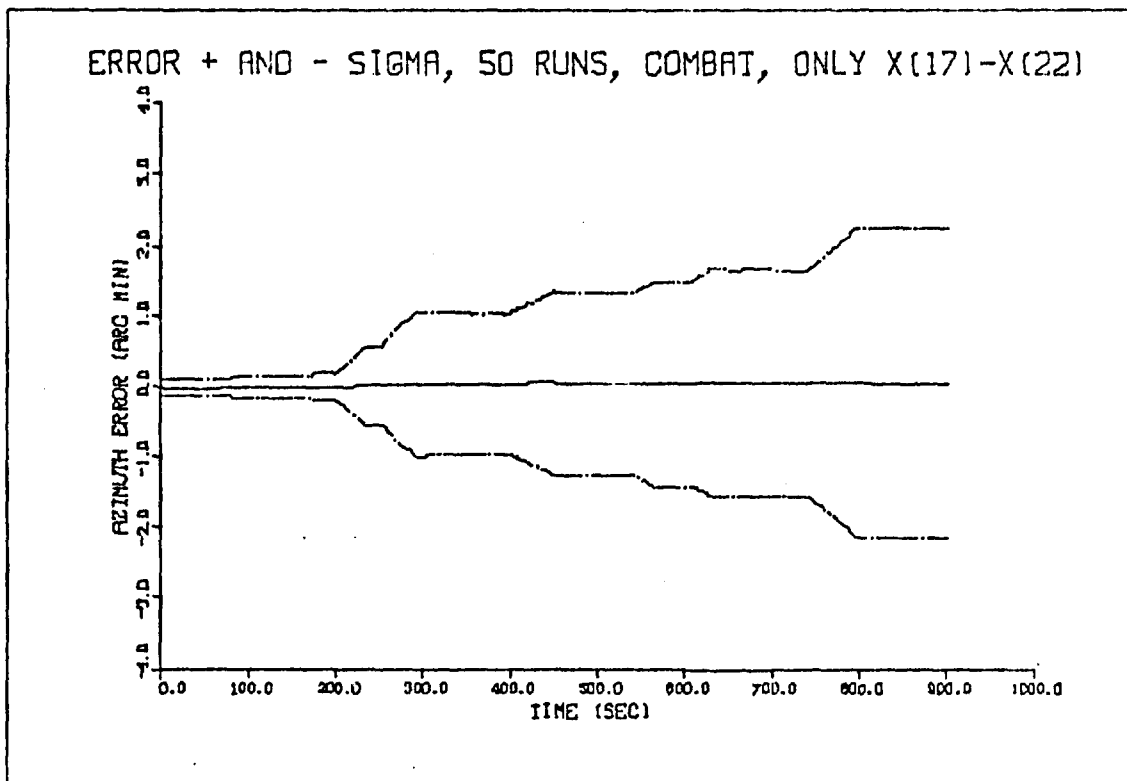


Figure H-28. Azimuth error state from gyro misalignment

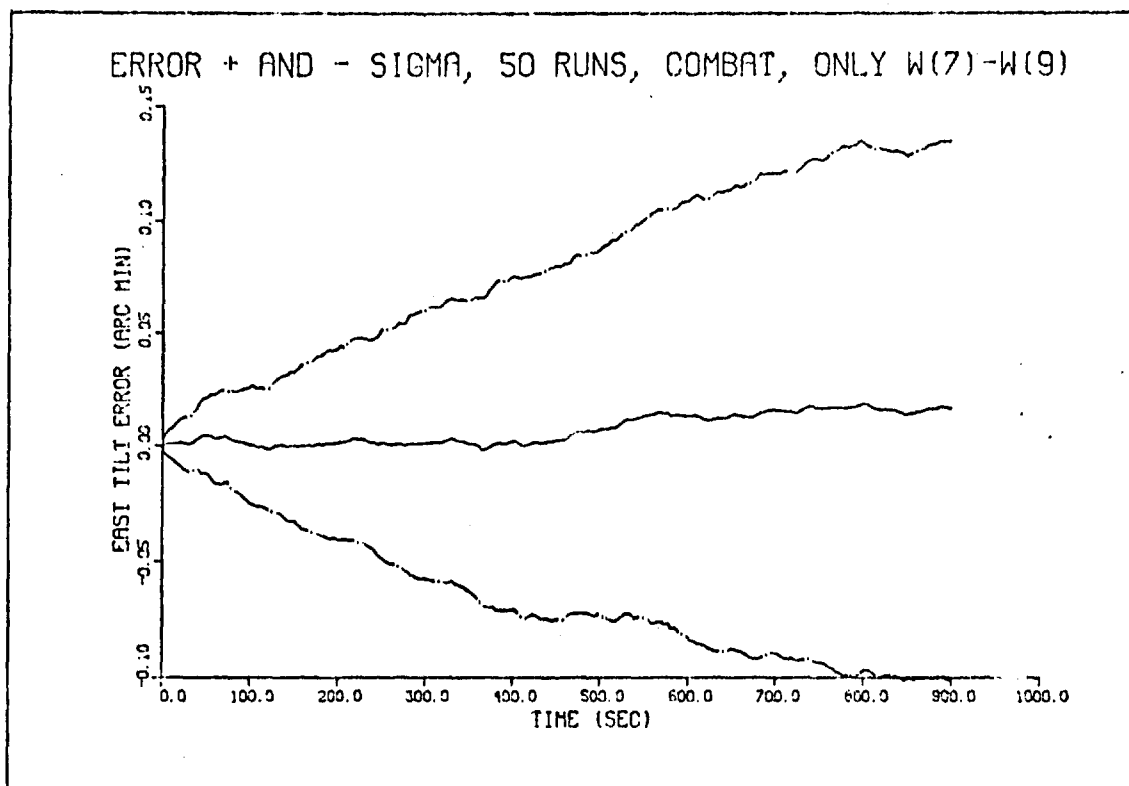


Figure H-29. East tilt error state from gyro white noise

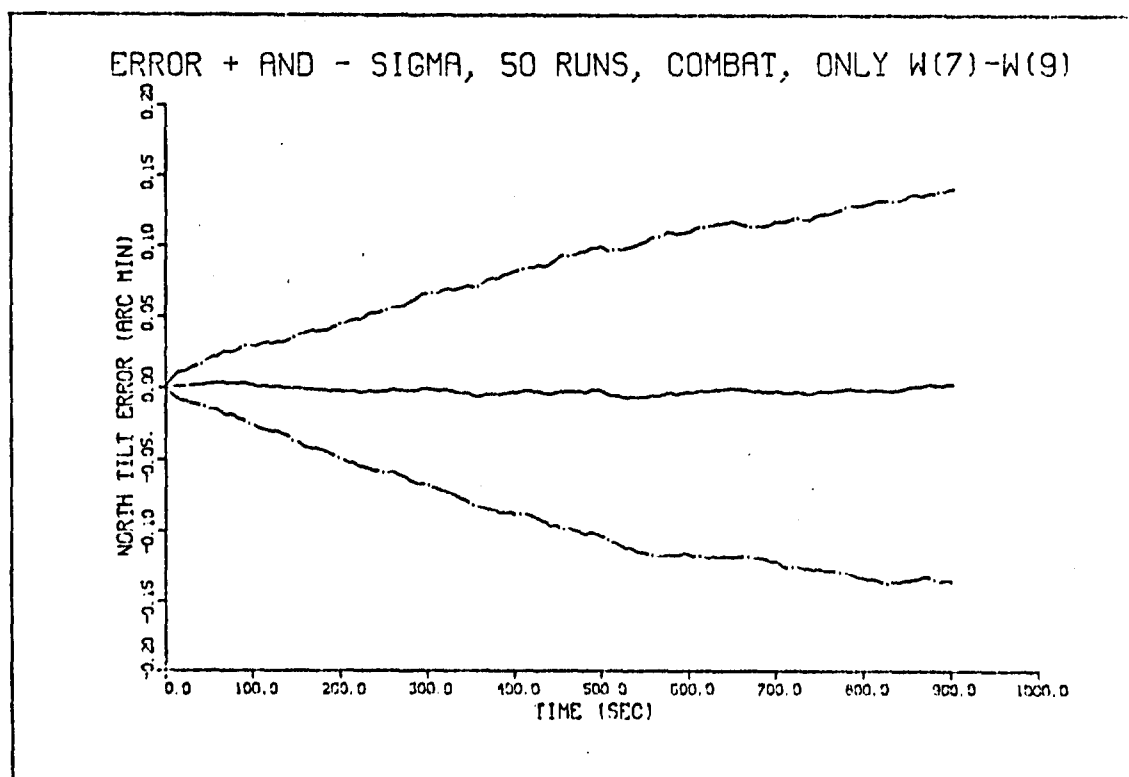


Figure H-30. North tilt error state from gyro white noise

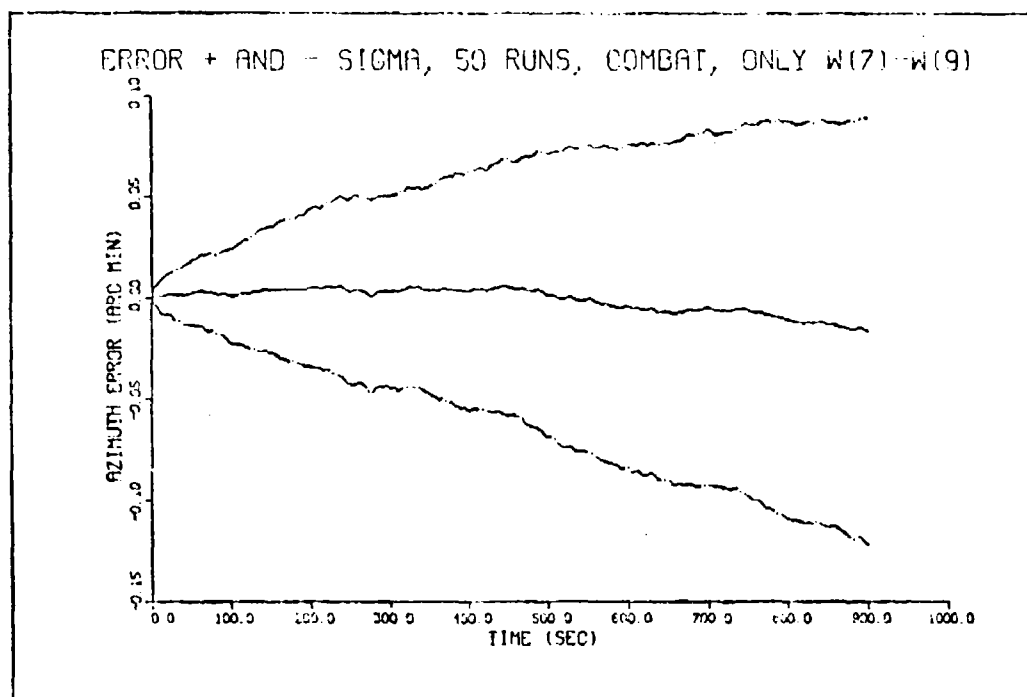


Figure H-31. Azimuth error state from gyro white noise

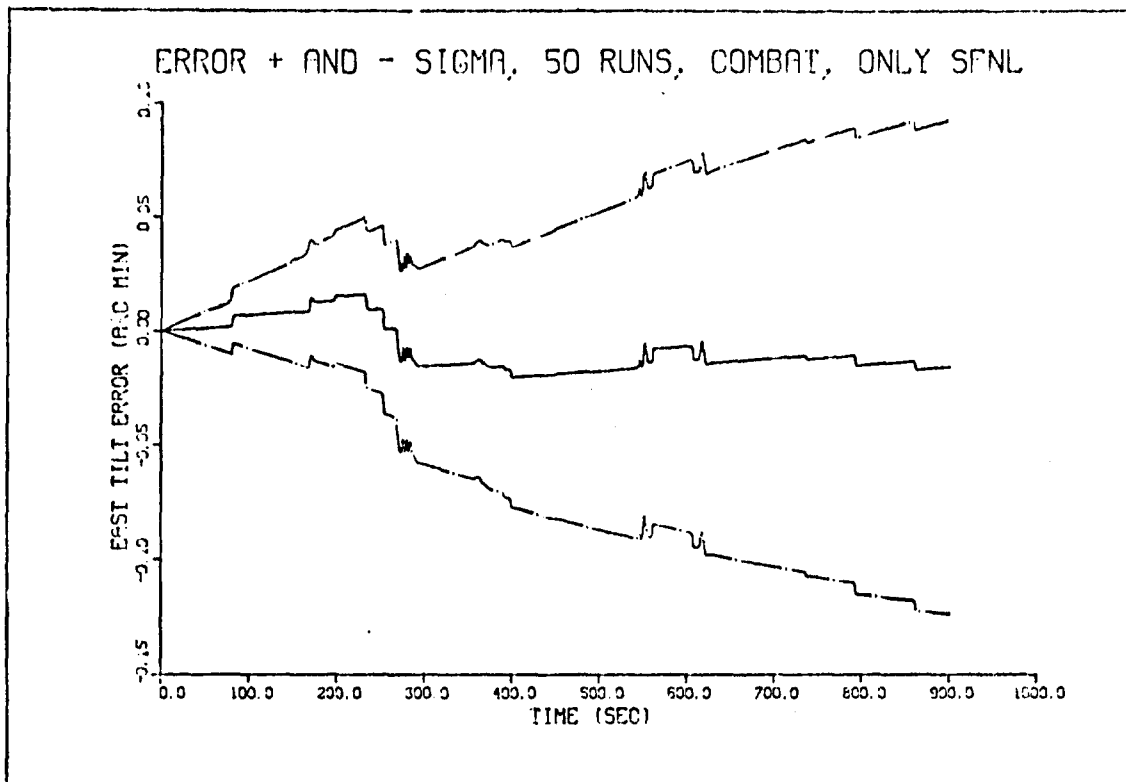


Figure H-32. East tilt error state from gyro S.F. nonlinearity

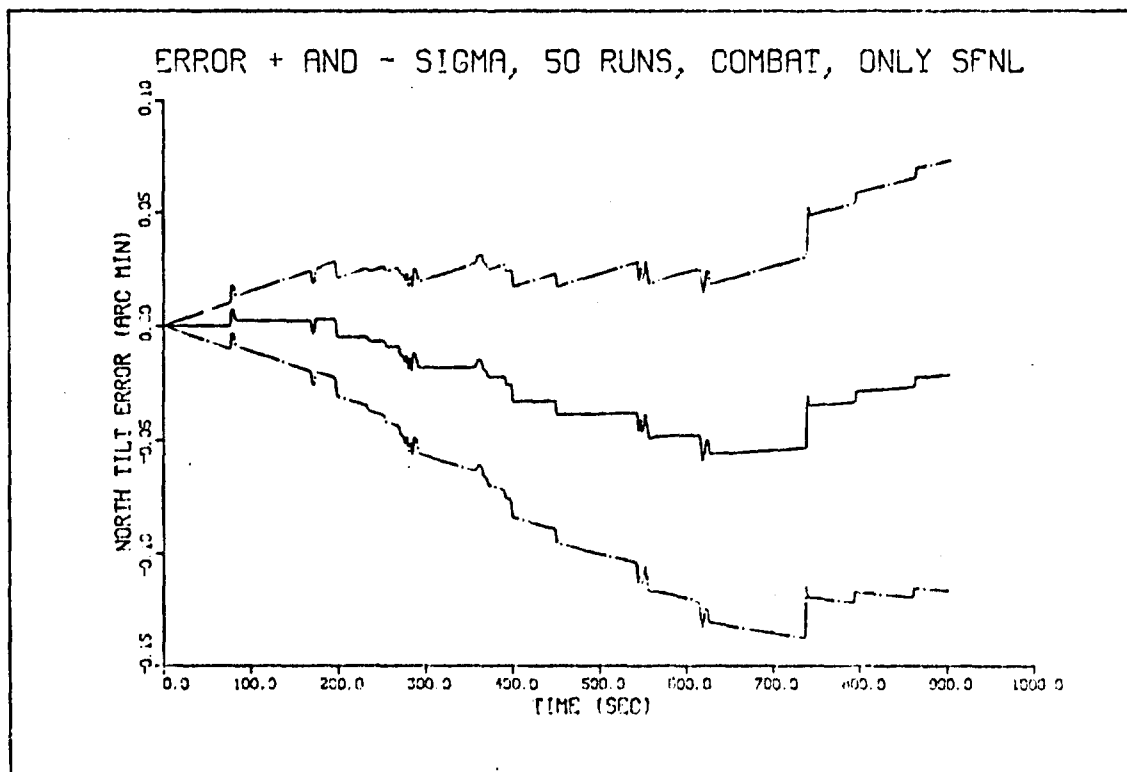


Figure H-33. North tilt error state from gyro S.F. nonlinearity

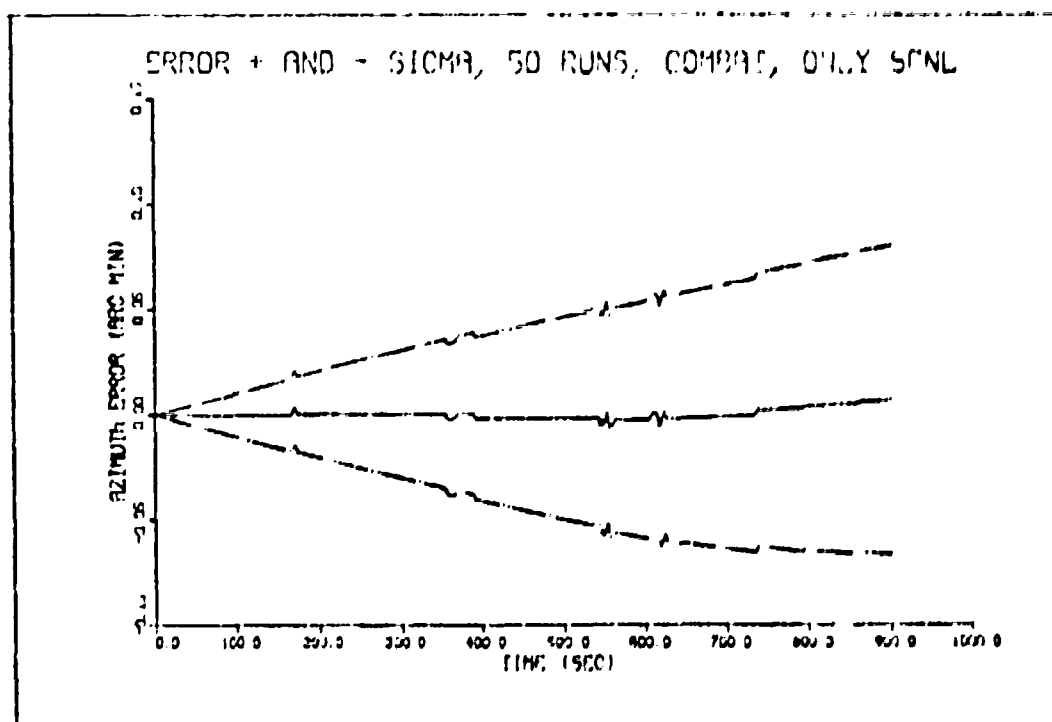


Figure H-34. Azimuth error state from gyro S.F. nonlinearity

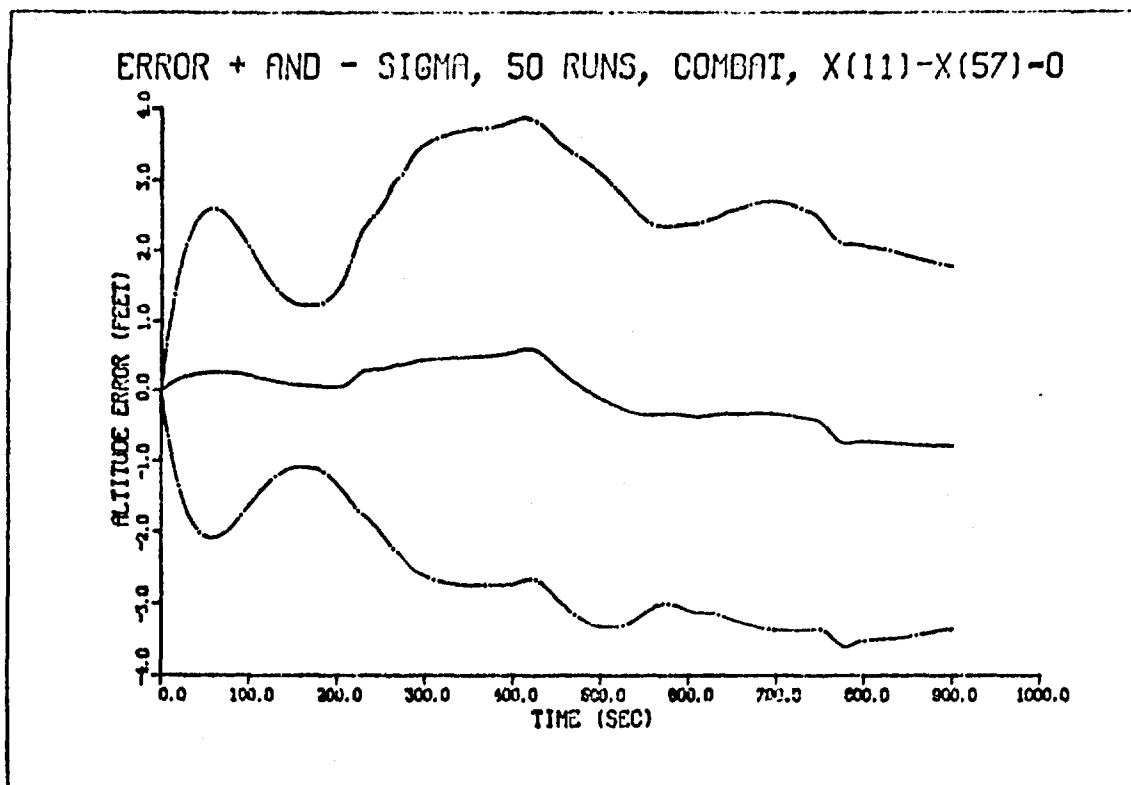


Figure H-35. Altitude error state from gravity error sources

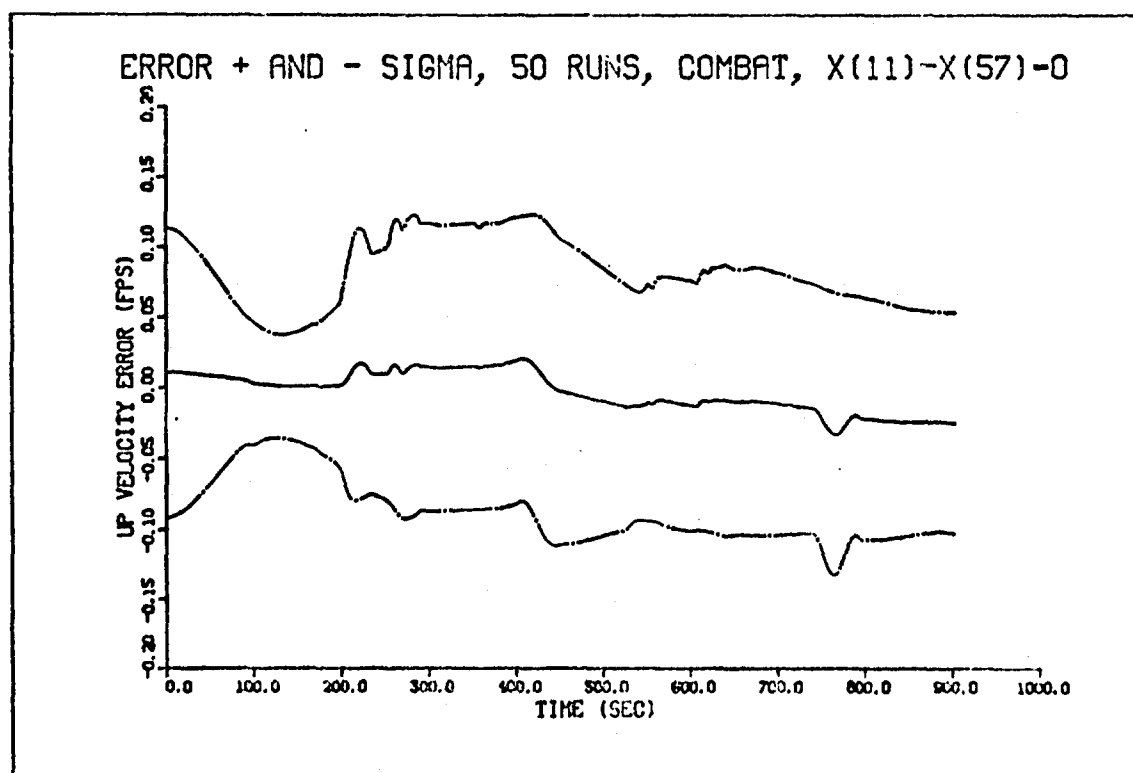


Figure H-36. Up vel. error state from gravity error sources

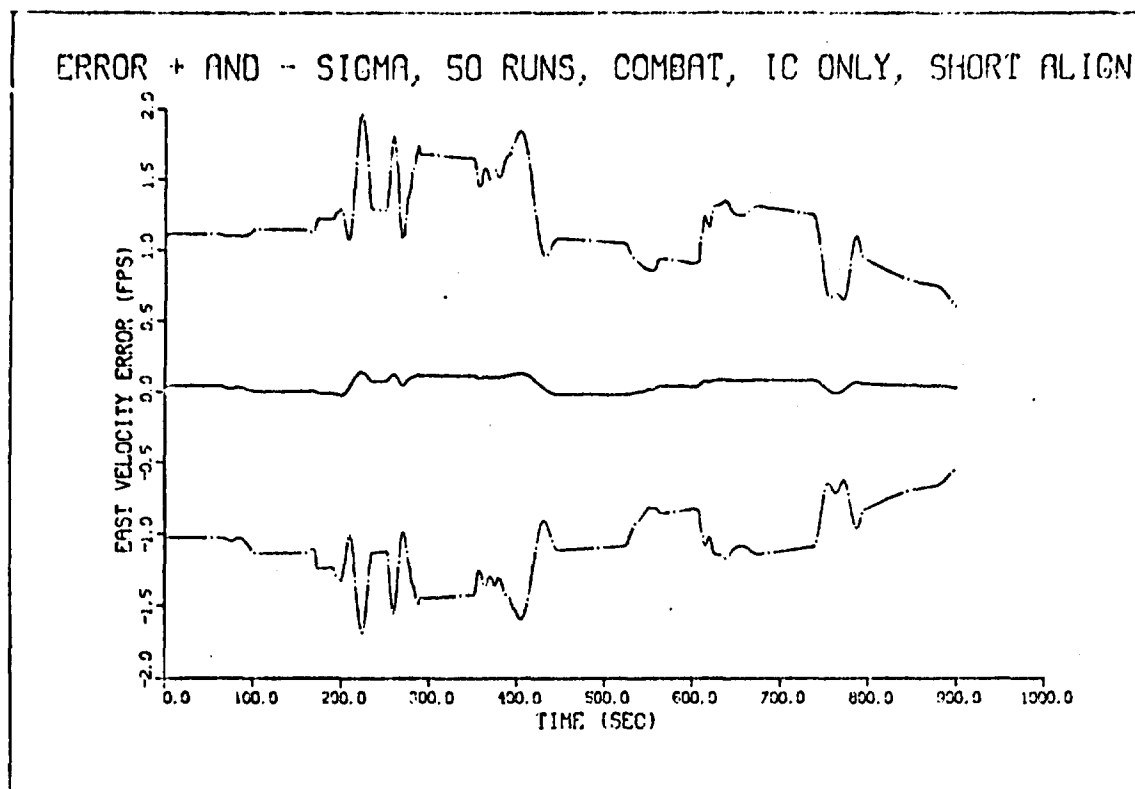


Figure H-37. East vel. error state from short alignment

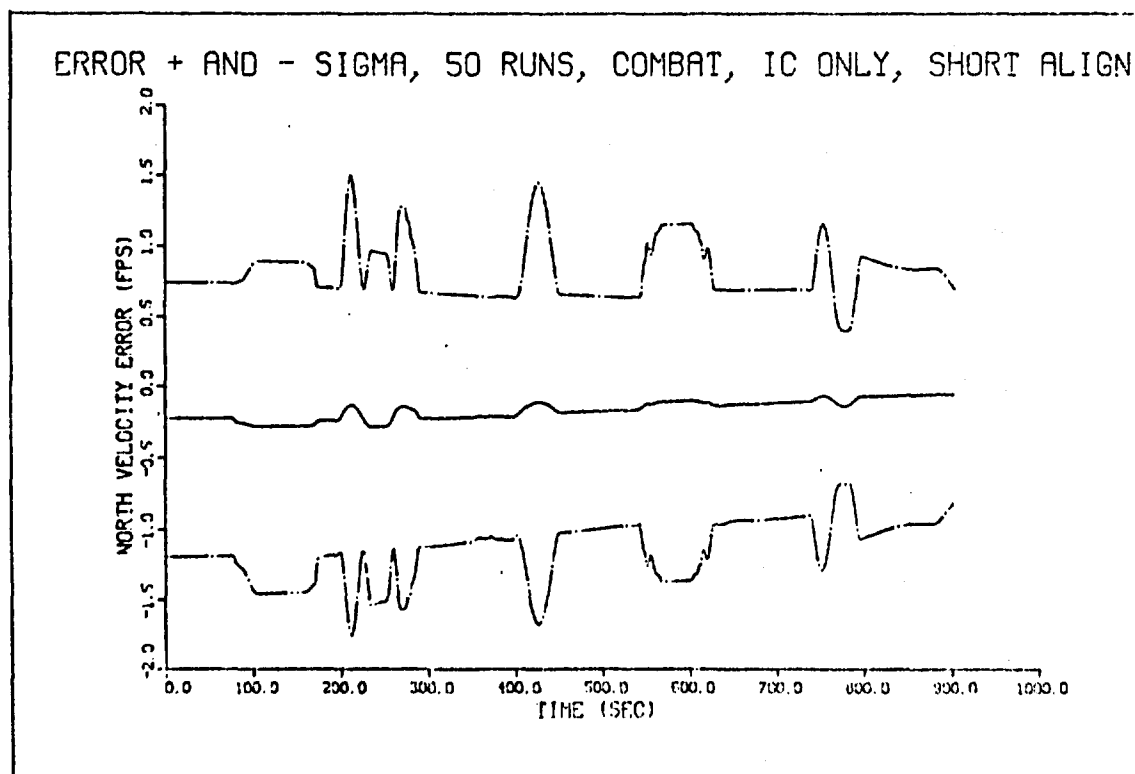


Figure H-38. North vel. error state from short alignment

VITA

Capt John E. Ryan began his Air Force career in September 1962 by attending a one year electronics technical school at Keesler Air Force Base, Mississippi. This was followed by a 2-1/2 year assignment to Celle, Germany as a Radio Relay Equipment Repairman. During a break in service he attended St. John Fisher College, Rochester, New York from 1966 to 1968 and graduated with distinction from the University of Rochester in June 1970 with a B.S. in Electrical Engineering. After completing Officer Training School in July 1973, Capt Ryan went on to navigation training and an assignment to Dover Air Force Base, Delaware. At Dover, he was a C-5 Navigator, Flight Simulator Instructor and Standardization/Evaluation Flight Examiner. Capt Ryan entered the Air Force Institute of Technology in June 1979 and is completing the Guidance and Control sequences for a M.S. in Electrical Engineering. He is a member of the Tau Beta Pi and Eta Kappa Nu associations.

Permanent address: 41 Quentin Road
Rochester, New York

UNCLASSIFIED

SECURITY CLASSIFICATION OF THIS PAGE (When Data Entered)

REPORT DOCUMENTATION PAGE		READ INSTRUCTIONS BEFORE COMPLETING FORM
1. REPORT NUMBER AFIT/GE/EE/80D-38	2. GOVT ACCESSION NO. AD-A100 825	3. RECIPIENT'S CATALOG NUMBER
4. TITLE (and Subtitle) SENSITIVITY STUDY OF STRAPDOWN INERTIAL SENSORS IN HIGH PERFORMANCE APPLICATIONS		5. TYPE OF REPORT & PERIOD COVERED MS Thesis
		6. PERFORMING ORG. REPORT NUMBER
7. AUTHOR(s) John E. Ryan Capt USAF		8. CONTRACT OR GRANT NUMBER(s)
9. PERFORMING ORGANIZATION NAME AND ADDRESS Air Force Institute of Technology (AFIT-EN) Wright-Patterson AFB, Ohio 45433		10. PROGRAM ELEMENT, PROJECT, TASK AREA & WORK UNIT NUMBERS
11. CONTROLLING OFFICE NAME AND ADDRESS AFWAL/AARA Wright-Patterson AFB, Ohio 45433		12. REPORT DATE December 1980
		13. NUMBER OF PAGES 222
14. MONITORING AGENCY NAME & ADDRESS (if different from Controlling Office)		15. SECURITY CLASS. (of this report) Unclassified
		15a. DECLASSIFICATION/DOWNGRADING SCHEDULE
16. DISTRIBUTION STATEMENT (of this Report) Approved for public release; distribution unlimited		
17. DISTRIBUTION STATEMENT (of the abstract entered in Block 20, if different from Report)		
18. SUPPLEMENTARY NOTES <p style="text-align: center;">Approved for public release; IAW AFR190-17 <i>Fredric C. Lynch</i> Fredric C. Lynch, Major, USAF Director of Public Affairs</p> <div style="text-align: right;">16 JUN 1981</div>		
19. KEY WORDS (Continue on reverse side if necessary and identify by block number) Strapdown Inertial Reference System Ring Laser Gyro Error Analysis Flight Profiles Monte Carlo Simulation Covariance Analysis Gimballess		
20. ABSTRACT (Continue on reverse side if necessary and identify by block number) This study uses a computer simulation of a strapdown laser gyro inertial reference system to analyze the errors generated as a result of highly dynamic flight profiles. A stochastic error model using state-of-the-art inertial sensors is developed in detail and implemented in software. SOFE, a generalized simulation program, was used to implement both a Monte Carlo simulation and a covariance analysis. The Monte Carlo method was selected to perform the error analysis. Two highly dynamic flight trajectories were		

DD FORM 1 JAN 73 1473

EDITION OF 1 NOV 65 IS OBSOLETE

UNCLASSIFIED

SECURITY CLASSIFICATION OF THIS PAGE (When Data Entered)

UNCLASSIFIED

SECURITY CLASSIFICATION OF THIS PAGE (When Data Entered)

Block 20. (CONTINUED)

developed using the flight profile generator, PROMGEN. The PROMGEN program itself was modified to include an aircraft roll time constant and a roll-only maneuver. The errors generated in the inertial reference system as a result of these flight trajectories were investigated. Both an error budget and an analysis of the maneuvers inducing these errors were accomplished. Gyro error sources induced the most system error and coupled the dynamics of the flight trajectory into the variations of the error. Misalignment was found to be the major cause of both the accelerometer and gyro induced error. Successive maneuvers were found that reinforced system errors and other maneuvers were found that cancelled these errors. Also, some cases were found where the amount of system error varied with a change in heading.

UNCLASSIFIED

SECURITY CLASSIFICATION OF THIS PAGE (When Data Entered)